

In Situ Investigation of the Martian Surface: Quantification of
Dust Coverages in Gale crater and Abrasion Marks in Jezero
crater

Thomas Lee Jones Henley, B.Sc. (Hons) & B.Sc.

Submitted as partial fulfillment of the requirements for the degree of:

Master of Science

Faculty of Mathematics and Science, Brock University

St. Catharines, Ontario

© Thomas Lee Jones Henley, 2023

Abstract

In situ measurements by Mars rover missions contribute to our understanding of surface geochemistry, past-depositional environments, and climate conditions that may have once supported life. Microscopic cameras capture high-resolution images of the surface allowing observations of contemporary surface and atmospheric processes. This thesis investigates microscopic images of rock surfaces to (1) measure the abundances of airfall dust covering horizontal surfaces in Gale crater, and (2) measure tool marks preserved in abrasion patches from Jezero crater. The research goals are to understand which variables are influencing surface deposits of airfall dust, and how target surface mineralogy is affecting tool mark preservation.

Previous studies have relied on orbital measurements of atmospheric opacity to study the seasonal suspension of Martian dust. Chapter 4 includes the longest single recording of surface dust coverages to date (~6 Mars Years) and contributes to the few studies that have quantified dust abundance at the surface. Using methods developed by Schmidt et al. (2018), dust coverages from 697 Mars Hand Lens Imager (MAHLI) microscopic images ranged from 0.4% to 76.6% and mirrored the results from atmospheric studies. Results indicate dust coverages decline in proximity to active aeolian dune deposits and increase with elevation. Airfall dust coverages on rocks increase annually as Mars enters a New Year (Solar longitude, L_s , ~ 0) and gradually decrease towards perihelion (L_s 251°) when seasonal winds are strongest.

To examine unweathered rock interiors, the Mars 2020 mission uses a rock abrader to remove ~10 mm of surface coatings and rinds. Operation complications including flaws in rock (e.g., cracks, vugs, and voids) and shifting of the outcrop during abrasion, have caused 5 failed abrasion attempts. To better understand how physical properties influence the abrasion process,

radial abrasion marks preserved in 10 successful abrasion patches were measured, relating abundance to mineralogy. Targets rich in primary igneous materials (i.e., crater floor targets) preserve greater counts and shorter abrasion lengths, compared to softer, sulfate- and carbonate- cemented sedimentary materials (i.e., delta front targets). The observations and results from this study will hopefully improve the prodapt algorithm that controls drilling parameters during abrasion and prevent future failed abrasion attempts.

Key Words: Mars, Mars dust, rock abrasion, Gale crater, Jezero crater

Acknowledgements

I would like to take this opportunity to express my sincere appreciation to all the people that have supported me throughout my master's thesis. First and foremost, I would like to thank my brilliant and supportive supervisor, Dr. Mariek Schmidt. I appreciate your guidance throughout my thesis, and your patience with my, what were often, “out there questions.” Despite lockdown, you have helped to provide me with the full graduate experience, allowing me to travel, meet, and collaborate with some of the most intelligent scientists in our field today. This work was also supported by MSL and M2020 Participating Scientist grants to Dr. Schmidt by the Canadian Space Agency (CSA). I would also like to thank my committee members, Drs. Frank Fueten and Richard Cheel, for their help and collaboration throughout this thesis. Thank you to Dr. Kevin Turner as well. To Dr. Kevin Turner, who helped me to plot dust data in QGIS, thank you for your advice at the beginning of my thesis.

I would like to thank the incredible friends, both life-long and those I have met throughout my studies, for your unwavering support and comradery throughout my time as a graduate student. To the Grimsby lads (a.k.a the Association of Sirs, and the Slav Squad) and their parents, we have grown so much together, and you have molded me into the Man I am today. Thank you for both humbling and encouraging me throughout life, and my time as a graduate student. Michelle Pearce and Josh Labrie, I thank you for your patience and writing expertise all those times I interrupted your work when I needed help putting my thoughts into words.

The list of everyone I would like to acknowledge exceeds the appropriate length for a thesis acknowledgements section, however, to those who were not directly named, I thank you for your support and guidance throughout my studies.

Finally, I would like to thank my beautiful Mother, Susan E. Henley, and incredibly handsome Father, Brian A. Henley, for their guidance through life. You have not only shown me what unconditional love truly is but have taught me “that if it’s to be, it truly is up to me.” I love you with all my heart and hope my efforts throughout this thesis have made you proud.

Table of Contents

Abstract

Acknowledgements

Table of Contents

List of Figures

List of Tables

List of Acronyms

Chapter 1: Overview	1
1.1. Surface accumulations of airfall dust in Gale crater	2
1.2. Variable tool mark preservation in the abrasion surfaces in Jezero crater	3
1.3. Thesis Format	4
1.4 References	5
Chapter 2: Literature Review	8
2.1 Geologic Background	8
2.2 Martian Atmosphere	11
2.3 Mars Seasons	13
2.4 Particle Mobility and Wind Generation	15
2.5 Dust Composition and Origin	17
2.6 Gale crater	19
2.6.1 Mount Sharp / Aeolis Mons	21
2.7 Isidis Planitia and the Nili Fossae	25
2.8 Jezero crater	26
2.8.1 Máaz Formation	27
2.8.2 Séítah Formation	28

2.9 Shenandoah Formation	31
2.10 References	33
Chapter 3: Methods	51
3.1 Rover Instrumentation	51
3.1.1 Curiosity Rover MSL	51
3.1.2 Perseverance Rover	54
3.2 Surface Dust Coverages in Gale crater	59
3.2.1 Image Acquisition and Selection	59
3.2.2 Target Selection and Assigning Target Type	60
3.2.3 Dust Measuring Methods	60
3.2.4 Final Dust Abundance in APXS FOV	67
3.2.5 Mapping and Classifying Dust Data	67
3.2.6 Sources of Error	67
3.3 Abrasion Mark Mapping in Jezero crater	68
3.3.1 Image Acquisition and Selection	68
3.3.2 Mineral Mapping	72
3.3.3 Measuring Abrasions	78
3.5 References	81
Chapter 4: Surface dust coverages on rock targets in Gale crater: Influence of seasonal wind variability, elevation and proximity to aeolian sand fields.	85
4.1 Abstract:	85
4.2 Introduction:	86
4.3 Methods	89
4.3.1 Method 1	91

4.3.2 Method 2	91
4.3.3 Method 3	92
4.3.4 Target Type	92
4.4 Results	93
4.4.1 Annual Dust Descriptions	100
4.5 Discussion	102
4.6 Conclusion	110
4.7 Acknowledgements	111
4.8 References	112
Chapter 5: Quantification of tool marks in abrasion patches of Jezero crater: Comparison of mineralogy and material properties between rocks of the crater floor and delta front.	121
5.1 Abstract	121
5.2 Introduction.....	122
5.2.1 Rock Abrasion	123
5.2.2 Rover Traverse and M2020 Campaigns.....	126
5.3 Methods	128
5.3.1 Rover Instrumentation.....	128
5.3.2 Abrasion Mark Mapping.....	130
5.3.3 Mineral Mapping.....	132
5.3.4. Vectorizing ROIs	134
5.3.5 Clipping Abrasion Marks to ROI and Measurements.....	135
5.4 Results	137
5.4.1 Abrasion Mark Measurements.....	154
5.4.2 Geochemistry and Mineralogy	154

5.4.3 Comparison between Abrasion Marks and Geochemistry/Mineralogy	155
5.4.4 Proclastic Level and Primary Igneous Mineral Abundance	155
5.5 Discussion	158
5.6 Conclusion	161
5.7 Acknowledgements	162
5.8 References	162
Chapter 6: Thesis Conclusion	166
6.1. Overview	166
6.2. Surficial dust accumulation in Gale crater	166
6.3. Abrasion mark mapping Jezero crater	169
6.4. Significance of this Research	169
6.4.1. Chapter 4: Dust Coverages from Gale crater	170
6.4.2. Chapter 5: Abrasion Mark Mapping	171
6.5. Future Work	172
References	173

List of Figures

Figure 1-1: (A). MSL Curiosity rover in Gale crater, Mars (NASA/JPL-Caltech). (B) Model of the M2020 Perseverance rover and Ingenuity helicopter on display at JPL-Caltech in Pasadena, California (Author for scale, photo by Dr. Mariek Schmidt).

Figure 2-1: (A.) Mars Orbiter Laser Altimeter (MOLA) global elevation map of Mars with various regions of interest labeled in white. The white box around the Medusa Fossae Formation provides global context for Figure 2-5. (B.) Inset map displaying the heavily cratered Noachian terrain surrounding Hellas basin (left of white line) and the smoother, less frequently cratered volcanic Hesperian aged plains (right of white line).

Figure 2-3: Mars' orbit around the Sun subdivided into seasonal quadrants according to equinox. The orbital eccentricity and sizes of Mars and the Sun are not to scale. The red square and circle indicate aphelion and perihelion respectively. The white halo represents the “Non-Dusty” season described by Haberle et al. (2017; Ls 0-135°). The grey halo represents the “Dusty” season (Ls 135-360°).

Figure 2-4: Illustration of aeolian sediment transport. Winds cause saltation of 50-100 μm grains. Finer grains (<50 μm) are lofted and suspended long-term in the atmosphere. Collisions between saltating grains and larger (50-100 μm), immobile material aid in lofting fine particles or result in modified saltation trajectories (Adapted from Nickling & Neuman, 2009).

Figure 2-5: MOLA shaded relief image displaying the geographical extent of the Medusa Fossae Formation (Red; Ojha et al. (2018).

Figure 2-6: (A.) Digital elevation model (DEM) the Martian surface, displaying Olympus Mons, the highest elevation (white star), and Hellas impact basin, the lowest elevation (white circle). (B.) Mars DEM showing location of Gale crater in relation to Elysium Planitia and the heavily cratered Southern highlands. (C.) HiRISE image of Gale crater with the four main geomorphic units: ejecta blanket (purple), crater rim (red), crater floor (green) and the central mound (yellow). The white triangle indicates the Curiosity landing site (Schwenzer et al. 2012).

Figure 2-7: (A.) HiRISE image of Gale crater. (B.) HiRISE image of the area of operations (AO) for Mars Science Laboratory (MSL). The white line indicates the rovers traverse (sol 0 to 3344), with red numbers indicating the first sol of each Mars year. Coloured outlines indicate the surface features used to assign the Legacy names used in this study. (C.) Zoomed in view of MSL's MY34 and MY35 AO. The white arrow shows the general direction of Curiosity's travel.

Figure 2-8: Stratigraphic column or rocks encountered by the MSL Curiosity rover in Gale crater. Inclined boundaries between members and lithologies result from elevation differences of observed contact. The geomorphically defined names for Vera Rubin Ridge (blue) and Glen Torridon (red), and their associated lithologies. (Modified from Fedo et al., 2022).

Figure 2-9: (A.) MOLA elevation map displaying the locations of the Nili Fossae, Isidis Planitia and Syrtis Major. (B.) HiRISE image of Jezero crater displaying the locations of the two inflowing (blue) deltas and single outflowing (red) channel.

Figure 2-10: (A.) HiRISE image of Jezero crater's western delta. The white line indicates the M2020 Perseverance rover's traverse to date with white circles indicating key observation points. (B.) Inset map displaying the location of Crater Floor campaign. Members and outcrops of the Séítah (red) and Máaz (blue) formations are labeled in white. Abrasion patch names are coloured according to formation. (C.) Inset map displaying the location of outcrops investigated during the Crater Floor campaign. Abrasion target names are displayed in yellow.

Figure 3-1: Mastcam image of Curiosity's rover arm showing the location of MAHLI and the DRT (image courtesy of NASA JPL/Caltech).

Figure 3-2: MAHLI image of Curiosity taken from the extended rover arm. White arrow displays the location of the ChemCam aboard the mast unit (NASA JPL/Caltech).

Figure 3-3: PIXL sensor before attaching it to the RA of the Perseverance Rover at NASA's jet Propulsion Laboratory in Pasadena California (NASA JPL/Caltech).

Figure 3-4: Configuration schematic of the SCS turret highlighting other instruments installed on the RA. Labelled are the SHERLOC-WATSON camera, Cored, PIXL, gDRT and the Facility Contact Sensor (Moeller et al., 2020).

Figure 3-5: Rotary-Percussive Drill bit (left) and the radial chisel mark pattern (Courtesy NASA/JPL-Caltech).

Figure 3-6: (A.) Highest resolution original focus merge image for ChemCam target Babbitt (Sol 2029 Babbitt; 2029MH0001930000801501R00_DXXX) with a standoff height of 1.8 cm. Red ellipses show locations of some ChemCam LIBS burn marks. (B.) Image from Panel A. changed to 8-bit greyscale. The light-coloured dust pixels were selected using Method 1 (red). The selected pixels measured to be 7.61% within the 17mm APXS FOV (white circle). (C.) The dark-coloured pixels were selected using Method 1 (red). The selected pixels measured to be 20.8% for the APXS FOV. The combined Method 1 dust coverage is 28.41%).

Figure 3-7: (A.) Highest resolution original focus merge image for ChemCam target Babbitt (Sol 2029 Babbitt; 2029MH0001930000801501R00_DXXX) with a standoff height of 1.8 cm. (B.) BeFunky.com edited image (edited from A.) Edges of dust particles are more pronounced following image editing. (C.) Figure 3-10: Dust pixel selection (29.843%) using Image J and following Method 2. Dust particles cover 25.6%% of the 17mm APXS FOV (white circle).

Figure 3-8: BeFunky.com editing of the highest resolution original focus merge image for ChemCam target Babbitt (Sol 2029 Babbitt; 2029MH0001930000801501R00_DXXX) with a standoff height of 1.8 cm. (B.) Binary colour image created in Adobe Photoshop using Method 3. The dust pixels identified in the edited BeFuky.com image have been changed to lime green while the underlying rock surface is changed to black. (C.) Selection of all dusty particles (38.1% areal dust coverage) using ImageJ and following Method 3. Dust particles cover 28.4% of the 17mm APXS FOV (white circle).

Figure 3-9: Graphic map showing the locations (red dots) where Perseverance collected and sealed 18 sample tubes to be returned to Earth. Red squares show the abrasion patch associated with each core sample (images to the right of each abrasion), excluding Montpezat (sol 346) and the Observation Mountain regolith samples (sol ~630; NASA JPL/Caltech)

Figure 3-10: SHERLOC-WATSON image (SIF_0617_0721745943_003FDR_N0301172SRLC08027_0000LMJ01) of the Uganik Island (sol 614) abrasion patch where abrasion marks are barely visible.

Figure 3-11: Guillaumes (sol 167) abrasion target with co-registered PIXL scan. Each blue point represents a ~120 μm PMC and the pink-blue line encloses the map area (Background MCC image: PCW_0167_0681701844_000RCM_N00600000631116810003075J05)

Figure 3-12: Montpezat (Sol 347) abrasion and associated PIXL 3-line scan. Each blue point represents an ~120 μm PIXL PMC. The red square surrounds a lightly coloured mineral that PMCs 201, 202 and 203 (green circles) likely missed due to the distance between lines (Background MCC image: PCW_0347_0697754573_000RCM_N00929821225528370003075J01.png). A secondary square PIXL scan was used to measure mineral abundance to compare with preserved abrasion marks.

Figure 3-13: Dourbes (Sol 257) abrasion patch and the co-registered PIXL scan and MCC image (PCW_0257_0689790669_000RCM_N00800000890639430006075J01). A $\text{TiO}_2\text{-Cr}_2\text{O}_3$ RGB colour mixed image overlays the MCC image. (A.) Shows all the PIXL PMCs (small blue circles). White circles show regions where igneous oxides were identified. (B.) PMC selection (hollow blue circles) using the FeO/SiO_2 expression from Table 3-3. This expression selected carbonate and igneous oxides minerals present in Dourbes, requiring manual deselection of oxide PIXL PMCs.

Figure 3-14: Map of High Salt (red), Alteration (yellow), and Low Salt (blue) ROIX for Dourbes (sol 257).

Figure 3-15: Stepwise list of the methods used to produce map and measure abrasion mark abundances within each mineral group.

Figure 4-1: The solar longitude ($^\circ$; Ls) and timing of the “Non-Dusty” and “Dusty” seasons (described by Haberle et al. 2017) plotted against the regular seasons of the northern and southern hemispheres. The aphelion (A) and perihelion (P) orbital positions are also plotted.

Figure 4-2: (A.) Focus merge MAHLI image (2656MH0008020011001215C00_DXXX) of the ChemCam target Rannoch Moor (sol 2656; dust coverage of 48.8%). The uneven radial clearing of dust in the top right was produced from a shockwave produced as the laser ablates the outer surface of rock (circles). White arrows point to areas where surface topography prevented dust removal. (B.) Focus merge MAHLI image (2581MH0006990010904050C00_DXXX) of the DRT target Canachair (sol 2581; dust coverage of 25.8%). The wire-bristle brushes of the DRT have

left small scratch marks in the target surface following dust removal. Most of the dust has been removed from the image center, however some remains.

Figure 4-3: Focus merge MAHLI images of As Is targets taken throughout MSL under varying lighting conditions. (A) Sgurr of Eigg target from sol 2000 under full sunlight (2000MH0001930000800300R00_DXXX; 37.9% dust coverage; Mudstone). (B) Burn O Vat target from sol 2166 under partial shadow (2166MH0001630000802862R00_DXXX; 45.0% dust coverage; Vein Rich Mudstone). (C.) Ladder Hills target from sol 2333 under full shadow (2333MH0005360000804213R00_DXXX; 48.3% dust coverage; Mudstone). (D.) Bogmill Pow target from sol 2660 under full sunlight (2660MH0001820011001299C00_DXXX; 23.8% dust coverage; Vein Rich Mudstone). (E.) Tay target from sol 2463 under full shadow (2463MH0001930000902360R00_DXXX; 41.5% dust coverage; Mudstone). (F.) Well Run target from sol 2604 under a partial shadow (2604MH0002990011000205C00_DXXX; 2.3% dust coverage; Mudstone).

Figure 4-4: Histogram of dust coverage on rock surfaces in Gale crater by target types (sol 46-3344)

Figure 4-5: Dust coverages on 'As is' horizontal rock surfaces plotted against sol #. Mars Year and the Curiosity traverse elevation are shown.

Figure 4-6: (A.) Map of *in situ* targets examined by Curiosity in Gale crater. Dust coverage (%) is indicated by color. Sols and stratigraphic members are labelled in white with the first target of each Mars new year (MY#) labelled in red. Namib and High Dune are a subsection of the larger Bagnold Dunes unit. White boxes indicate the locations of inset maps: (B.) Phase 2 of the Bagnold Dunes traverse, (C.) Vera Rubin Ridge, (D.) Sands of Forvie.

Figure 4-7: Globally averaged 9µm atmospheric/dust opacity measurements from the Mars Global Surveyor (MGS) Thermal Emission Spectrometer (TES) and the Mars Odyssey Orbiter (ODY) Thermal Emission Imaging System (THEMIS) for multiple Mars years (MY#; Haberle et al., 2017).

Figure 4-8: Focus merge MAHLI images of As Is targets displaying the low dust coverages and presence of black sand particles during Phase 2 of the Bagnold Dunes traverse. (A.) Sol 1609 –

Perry (1608MH0006800000602257R00_DXXX), (B.) Sol 1614 – Spider_Lake_APXS (1615MH0006840000602505R00_DXXX), (C.) Sol 1634 – Canada Falls 3 (1635MH0001530000602737R00_DXXX), and (D.) Sol 1640 – Junk of Pork Island (1640MH0001630000602966R00_DXXX). Targets have their dust coverage displayed at the bottom left and white ellipses indicate accumulations of fine sand-sized particles. The red ellipse highlights a region of high surface topography filled with fine sand-sized particles.

Figure 5-1: Set of drill bits stored in the Bit Carousel of Perseverance’s Sampling and Caching Subsystem. From left to right, one Regolith Bit, six Coring Bits, and two Abrading Bits (Image from Moeller et al. 2020).

Figure 5-2: SCS’s asymmetrical abrasion bit (leftmost) and the pattern produced during the abrasion process (Courtesy of Iona Tirona).

Figure 5-3: SHERLOC-WATSON image of the failed Rose River Falls abrasion target (sol 452; SIF_0452_0707077324_796FDR_N0260000SRLC02504_0000LMJ01). During the abrasion process, the target surface sunk into the surrounding regolith and was partially infilled by the regolith material (green arrow). Excess applied force during abrasion caused the target surface to crack (blue arrows) and break into smaller chunks (red arrows), preventing later proximity science with the PIXL instrument.

Figure 5-4: (A.) Mastcam-Z image of the gDRT cleared Alfalfa abrasion patch (sol 367; ZLF_0368_0699608205_270FDR_N0110108ZCAM03328_1100LMJ0) (B.) Close-up WATSON image of the Alfalfa abrasion.

Figure 5-5: Example of the WATSON images (A. and B.) and PIXLISE screen captures (C. and D.) overlay used to trace abrasion marks and map mineral boundaries. (A.) 7-cm standoff WATSON image SIF_0346_0697661611_539FDR_N0092982SRLC00758_0000LMJ01. (B.) 4 cm standoff WATSON image SI1_0347_0697764296_148FDR_N0092982SRLC00003_000095J02. (C.) PIXLISE screen capture of the Montpezat 1 PIXL scan. (D.) PIXLISE screencapture of the Montpezat 2 PIXL scan.

Figure 5-6: SHERLOC-WATSON images SIF_0161_0681241540_582FDR_N0060000SRLC08008_0000LMJ01.IMG (small) and

SI1_0160_0681181210_679FDR_N0060000SRLC00003_000095J01.IMG (large) of Guillaumes with all abrasion marks (blue) and PIXL FOV (red polygon) traced. (B.) Screen capture of mineral map created using pixlise.org where “Low-Salt” and “High-Salt” regions are coloured blue and red respectively.

Figure 5-7: PIXL mineral abundances for each abrasion target sampled during the Crater Floor and Delta Front campaigns.

Figure 5-8: (A). SHERLOC-WATSON images SIF_0185_0683368184_652FDR_N0070000SRLC00720_0000LMJ01.IMG of the Bellegarde abrasion patch with all abrasion marks (red) and PIXL FOV (black polygon). (B.) Screen capture of the mineral map created using pixlise.org where “Low-Salt” and “High-Salt” regions are coloured blue and red respectively.

Figure 5-9: (A). SHERLOC-WATSON image SI1_0257_0689775622_738FDR_N0080000SRLC00006_000095J01.IMG of the Dourbes abrasion patch. Abrasion marks are traced in pink and the PIXL FOVs are outlined in black. Mineral maps of the Dourbes 1 (B.) and Dourbes 2 (C.) are displayed at the top right. Regions with “Low Salt High,” “High Salt” and “Alteration” are coloured blue, red, and yellow respectively

Figure 5-10: (A). SHERLOC-WATSON image SIF_0292_0692874790_734FDR_N0090000SRLC01034_0000LMJ01.IMG of the Quartier abrasion patch. Abrasion marks are traced in blue and the PIXL FOVs are outlined in white. Mineral maps of Quartier 1 (B.) and Quartier 2 (C.) are displayed at the top right. Regions with “Low Salt High,” “High Salt” and “Alteration” are coloured blue, red, and yellow respectively

Figure 5-11: (A). SHERLOC-WATSON images SIF_0347_0697751287_792FDR_N0092982SRLC00603_0000LMJ01.IMG (small) and SI1_0346_0697669267_585FDR_N0092982SRLC00033_000095J01.IMG (large) of the Montpezat abrasion patch. Abrasion marks are traced in blue and the PIXL FOVs are outlined in white. The mineral maps for Montpezat is displayed at the top right (B.). Regions with “Low Salt High,” “High Salt” and “Alteration” are coloured blue, red, and yellow respectively

Figure 5-12: (A). SHERLOC-WATSON image SIF_0367_0699544322_300FDR_N0110108SRLC08029_0000LMJ01.IMG of the Alfalfa abrasion patch with all abrasion marks (red) and PIXL FOV (black polygon) traced. (B.) Screen capture of mineral map created using pixlise.org where “Low-Salt,” “High-Salt,” and “Alteration” regions are coloured blue, red, and yellow respectively.

Figure 5-13: (A). SHERLOC-WATSON images SI1_0483_0709779049_878FDR_N0261004SRLC00033_000095J01 (large) and SI1_0485_0710008591_199FDR_N0261004SRLC00009_000095J01 (small) of the Thornton Gap abrasion patch. All abrasion marks are traced in red and the PIXL FOV is outlined in black. (B.) Screen capture of mineral map created using pixlise.org where “Low-Salt,” “High-Salt,” and “Alteration” regions are coloured blue, red, and yellow respectively.

Figure 5-14: (A). SHERLOC-WATSON image SI1_0504_0711704525_972FDR_N0261222SRLC00033_000095J02 of the Berry Hollow abrasion patch. All abrasion marks are traced in red and the PIXL FOVs are outlined in black. Mineral maps of Berry Hollow 1 (B.) and Berry Hollow 2 (C.) are displayed at the top right. Regions with “Low Salt High,” “High Salt” and “Alteration” are coloured blue, red, and yellow respectively.

Figure 5-15: (A). SHERLOC-WATSON image SIF_0568_0717381433_183FDR_N0290000SRLC01031_0000LMJ01 of the Novarupta abrasion patch. Mineral maps of Novarupta 2 (B.) and Novarupta 3 (C.) are displayed at the top right. Regions with “Low Salt High,” “High Salt” and “Alteration” are coloured blue, red, and yellow respectively.

Figure 5-16: (A). SHERLOC-WATSON image SIF_0617_0721745943_003FDR_N0301172SRLC08027_0000LMJ01 of the Uganik Island abrasion patch. Mineral maps of Uganik Island 2 (B.) and Uganik Island 3 (C.) are displayed at the top right. Regions with “Low Salt High,” “High Salt” and “Alteration” are coloured blue, red, and yellow respectively.

Figure 5-17: Scatter plot comparing the total abrasion lengths within each PIXL FOV from the Shenandoah (blue), Máaz (orange) and Séítah (red) formations against their respective abundances of low salt materials.

Figure 5-18: Scatterplot comparing the Prodapt Levels used during the production of each abrasion patch. Points are colored based on formation: Máaz (Orange), Séítah (Yellow) and Shenandoah (Blue).

List of Tables

Table 2-1: Comparison of Earth and Mars orbits and surface conditions

Table 2-2: Geomorphically defined regions of Mount Sharp and their updated stratigraphic names.

Table 3-1: List of M2020 abrasion and core sample attempts and their outcomes.

Table 3-2: Chemical descriptions and example minerals for each mineral group included in this study¹.

Table 3-3: Expression values used to select and sort PMCs into mineral groups

Table 4-1. Summary of averaged dust coverages by target type in Gale Crater¹

Table 4-2. Summary of As Is dust coverages in Gale crater by Mars Year¹

Table 4-3: Count of averaged dust coverages above 60%¹

Table 5-1: Abrasion patches from each geologic formation.

Table 5-2: Chemical descriptions and example minerals for each mineral group included in this study.

Table 5-3: Expression values used to select and sort PMCs into mineral groups

Table 5-4: Abrasion mark and grain size statistics for all abrasion patches from M2020.

Table 5-5: Abrasion mark statistics clipped to PIXL FOVs in each abrasion patch.

List of Acronyms

Ai – Adobe Illustrator

ACI – Autofocus Context Imager

APXS – Alpha Particle X-Ray Spectroscopy

ChemCam – Chemistry and Camera

CSA – Canadian Space Agency

DRT – Dust Removal Tool

ESA – European Space Agency

GCM – Global Circulation Model

gDRT - Gas Dust Removal Tool

GHP – Greenheugh Pediments

GT – Glen Torridon

IR – Infrared

QGIS – Quantum Geographic Information System

LED – Light Emitting Diode

LIBS – Laser Induced Breakdown Spectroscopy

Ls – Solar Longitude

M2020 – Mars2020

MAHLI – Mars Hand Lens Imager

MER – Mars Exploration Rovers

MCC – Microcontext Camera

MFF – Medusa Fossae Formation

MGS – Mars Global Surveyor

MSL – Mars Science Laboratory

MY# - Mars Year and the associated number

NASA - National Aeronautics and Space Administration

ODY – Mars Odyssey Orbiter

P1BD – Phase 1 of Bagnold Dunes

P2BD – Phase 2 of Bagnold Dunes

PDS – Planetary Data System

PIXL - Planetary Instrument for X-ray Lithochemistry

PMC – PIXL Motor Count

PS – Planetary Science

RA – Rover Arm

RAT – Rock Abrasion Tool

RGB – Red Green Blue

RMI – Remote Micro Imager

RPM – Rotations per minute

ROI - Regions of Interest

SCS – Sampling and Caching Subsystem

SHERLOC - Scanning Habitable Environments with Raman and Luminescence for Organics and Chemicals

SOF – Sands of Forvie

TES – Thermal Emission Spectrometer

THEMIS - THERmal EMission Imaging System

VISIR – VLT Imager and Spectrometer for mid-Infrared

VRR – Vera Rubin Ridge

WATSON – Wide Angle Topographic Sensor for Operations and Engineering

XRF – X-Ray Fluorescence

Chapter 1: Overview

The National Aeronautics and Space Administration (NASA) and European Space Agency (ESA) have announced a joint Mars Sample Return mission that will collect a selected set of Mars samples for investigation in terrestrial laboratories (Muirhead et al., 2020). This forthcoming expedition will offer unparalleled opportunities to study the geology, history, and potential habitability of the Red Planet. Mars exploration not only furthers our comprehension of the origins of our solar system, and the formation of the terrestrial planets, but also seeks to answer the age-old question, does evidence of life exist beyond Earth? Through continued exploration and research of Mars, scientists hope to answer these fundamental questions, while simultaneously paving the way for future human exploration and colonization of our neighbouring planet.

Unlike Earth's atmosphere, which shields the surface from much of the radiant solar radiation, the thin Martian atmosphere allows nearly all radiant solar and cosmic radiation to reach the surface (Williams, 2021), producing a surface layer of cosmic/solar-altered material (Lal, 1991). The omnipresence of Martian dust at the surface further interferes with *in situ* chemistry quantifications (Schmidt et al., 2018), while suspended particles interfere with orbital observations (Haberle et al., 2017). Removing these materials is therefore crucial when studying the underlying geology of Mars. Instrumentation onboard the two most recent NASA Mars rover missions, Mars Science Laboratory (MSL; Grotzinger et al., 2012) and Mars2020 (M2020; Boeder & Soares, 2020), remove these materials when collecting *in situ* measurements. However, the accompanying high-resolution microscopic images from Gale crater and Jezero crater provide another perspective to surface accumulations of airfall dust and overall rock properties.

Both research chapters included in this thesis use microscopic images to study the surface of Mars. The first research chapter measured surface accumulations of airfall dust above horizontal rock surfaces in Gale crater to understand how seasonal wind patterns and other variables affect to dust accumulation. The second research chapter measured tool marks preserved in the abrasion patches from Jezero crater to understand how target mineralogy is affecting their abundances. While each chapter analyzes different features, both studies use

microscopic imaging techniques to extract information about the Martian surface. Together, they represent an important step forward in understanding the planet's surface processes and conditions.

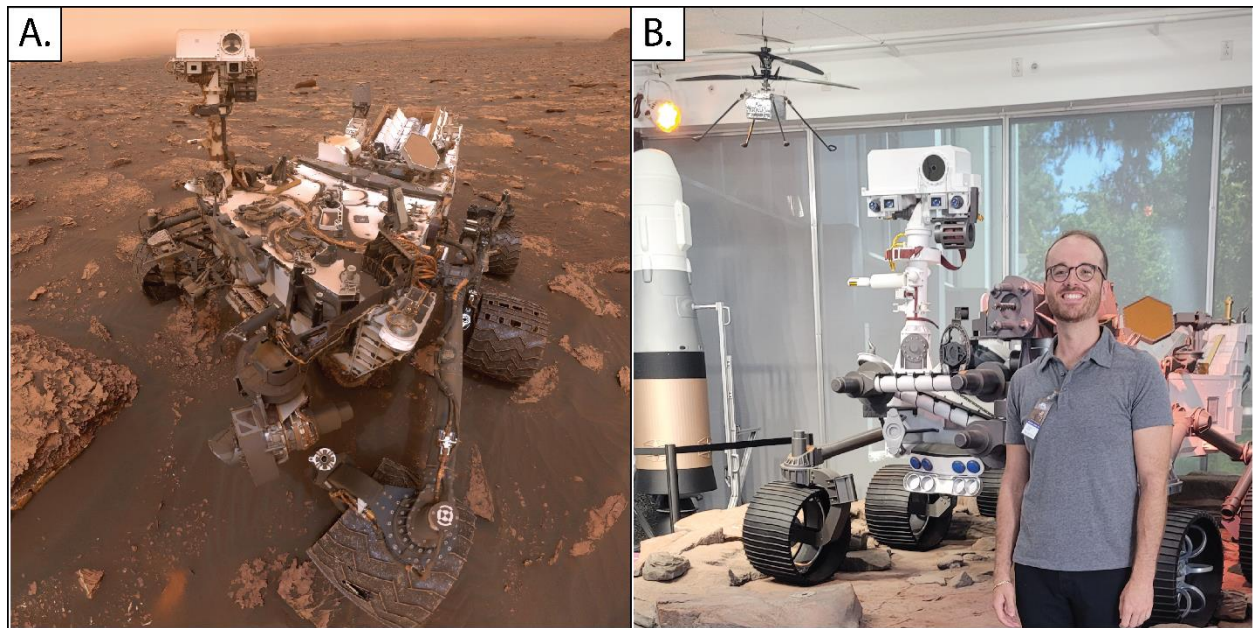


Figure 1-1: (A). MSL Curiosity rover in Gale crater, Mars (NASA/JPL-Caltech). (B) Model of the M2020 Perseverance rover and Ingenuity helicopter on display at JPL-Caltech in Pasadena, California (Author for scale, photo by Dr. Mariek Schmidt).

1.1. Surface accumulations of airfall dust in Gale crater

The accumulation of airfall dust atop solar panels lead to the recent termination of the Mars Insight Lander mission (Lorenz et al., 2020) and the earlier Mars Exploration Rovers (MER) Spirit and Opportunity missions (Vicente-Retortillo et al., 2018). These events highlight one of the many challenges future human explorations will face when living on the surface. With unknown health implications, the potential for interfering with communications during global-encompassing dust storms, and likely many more unknown dangers, a firm understanding dust mobility, suspension and seasonality is therefore imperative to our future success on Mars.

The first investigation (Chapter 4) involved measuring the areal abundance of airfall dust in Gale crater using high-resolution MAHLI images to study seasonal and spatial variations over ~6 Mars years of MSL Curiosity rover's (Figure 1-1A) geologic traverse (>25km, sol 46-3409). Our measurements are inversely correlated with orbital measurements of atmospheric dust (also

known as atmospheric opacity; Haberle et al., 2017), showing greater accumulations of dust during Southern winter that gradually decrease as Mars enters the windy Southern summer season. Dust coverages also showed decreases with elevation gain and in proximity to aeolian sand dune deposits. This work builds from the work of Schmidt et al. (2018) and provides the longest record of surface dust measurements to date.

1.2. Variable tool mark preservation in the abrasion surfaces in Jezero crater

In preparation for future Mars Sample Return and fulfillment of its mission objectives, the M2020 Perseverance rover has recently dispensed rock and regolith samples collected during its Crater Floor (sols 0-379; Williams et al, 2023; Farley et al., 2022; Liu et al., 2022), and Delta Front campaigns (sol ~415-641; Williams et al., 2023). To characterize rock outcrops and potentially leading to sampling, the Perseverance rover produces an abrasion patch and performs proximity science. Proximity science is a term that I will use throughout this thesis to describe rover instrumentation that performs close-up analysis of target surfaces. Examples of these instruments include the Scanning Habitable Environments with Raman and Luminescence for Organics and Chemicals (SHERLOC) and Planetary Instrument for X-ray Lithochemistry (PIXL; these proximity science instruments and others are described in greater detail in section 3.1.2). The abrasion process removes surface layers of alteration and weathering (up to 16 mm; Moeller et al., 2020), exposing relatively fresh rock. The resultant abrasion patch is 50 mm in diameter, to a minimal depth of 2 mm to remove sufficient coatings, with indentations and radial chisel marks that interfere with the interpretation of the target surface. Complications during the abrasion process have also prevented 4 abrasion patches from being produced.

The second investigation of this thesis (Chapter 5) uses high-resolution microscopic SHERLOC-WATSON and Micro-Context Camera (MCC) images of these abrasion patches to (1) understand how rock composition affects tool mark preservation, (2) provide another perspective for interpreting rock properties, and (3) provide observations, which may improve the adaptive drilling algorithm and reduce the number of failed abrasion patches in the future. The results from this study found target surfaces rich in primary igneous minerals (e.g.

olivine, pyroxene, feldspar, and igneous oxides), primarily materials from the crater floor, were more resistant to abrasion, required greater force for remove material, and preserved more abrasion marks. Sedimentary rocks sampled during the Delta Front campaign were made of softer sulfate- and carbonate-cemented materials (Williams et al., 2023), requiring less force to remove material, produced flatter abrasion patches, and preserved fewer abrasion marks.

1.3. Thesis Format

Chapter 2: Literature Review

Is a literature review that details fundamental knowledge to understand the two research chapters of this thesis. This information include:

- Mars geologic background
- Martian atmosphere
- Mars Seasons
- Particle Mobiliy
- Wind Generation
- Dust Composition and potential origins

Chapter 3: Methods

Provides descriptions of rover instrumentation used and mentioned in this thesis. This section also describes the methods used throughout the two research chapters.

Chapter 4: Surface dust coverages on rock targets in Gale crater Influence of seasonal wind variability, topographic control, and proximity to aeolian sand fields

This is the first research chapter of this thesis. It details the results from ~6 Mars years of dust measurements in Gale crater. This chapter is formatted as a manuscript and will be modified and submitted for publication in the peer-reviewed Journal of Geophysical Research: Planets.

Chapter 5: Quantification of tool marks in abrasion patches of Jezero crater: Comparison of mineralogy and material properties between rocks of the crater floor and delta front

This is the second research chapter of this thesis. This work measures tool marks preserved in the 10 abrasion patches successfully produced during the M2020 crater floor and delta front campaigns. This chapter is formatted as a manuscript and will be modified for publication in the peer-reviewed Journal of Geophysical Research: Planets.

Chapter 6: Thesis Conclusions

This final chapter summarizes the main findings and conclusions from these two research chapters. It also discusses their significance, implications and considerations for future work.

1.4 References

- Boeder, P. A., & Soares, C. E. (2020). Mars 2020: Mission, science objectives and build. *Systems Contamination: Prediction, Control, and Performance 2020*, 11489, 1148903. <https://doi.org/10.1117/12.2569650>
- Farley, K. A., Stack, K. M., Shuster, D. L., Horgan, B. H. N., Hurowitz, J. A., Tarnas, J. D., Simon, J. I., Sun, V. Z., Scheller, E. L., Moore, K. R., McLennan, S. M., Vasconcelos, P. M., Wiens, R. C., Treiman, A. H., Mayhew, L. E., Beyssac, O., Kizovski, T. V., Tosca, N. J., Williford, K. H., ... Zorzano, M.-P. (2022). Aqueously altered igneous rocks sampled on the floor of Jezero crater, Mars. *Science*, 377(6614), eabo2196. <https://doi.org/10.1126/science.abo2196>
- Grotzinger, J. P., Crisp, J., Vasavada, A. R., Anderson, R. C., Baker, C. J., Barry, R., Blake, D. F., Conrad, P., Edgett, K. S., Ferdowski, B., Gellert, R., Gilbert, J. B., Golombek, M., Gómez-Elvira, J., Hassler, D. M., Jandura, L., Litvak, M., Mahaffy, P., Maki, J., ... Wiens, R. C. (2012). Mars Science Laboratory Mission and Science Investigation. *Space Science Reviews*, 170(1), 5–56. <https://doi.org/10.1007/s11214-012-9892-2>
- Haberle, R. M., Clancy, R. T., Forget, F., Smith, M. D., & Zurek, R. W. (2017). *The Atmosphere and Climate of Mars*. Cambridge University Press.
- Lal, D. (1991). Cosmic ray labeling of erosion surfaces: In situ nuclide production rates and erosion models. *Earth and Planetary Science Letters*, 104(2), 424–439. [https://doi.org/10.1016/0012-821X\(91\)90220-C](https://doi.org/10.1016/0012-821X(91)90220-C)

- Liu, Y., Tice, M. M., Schmidt, M. E., Treiman, A. H., Kizovski, T. V., Hurowitz, J. A., Allwood, A. C., Henneke, J., Pedersen, D. A. K., VanBommel, S. J., Jones, M. W. M., Knight, A. L., Orenstein, B. J., Clark, B. C., Elam, W. T., Heirwegh, C. M., Barber, T., Beegle, L. W., Benzerara, K., ... Zorzano, M.-P. (2022). An olivine cumulate outcrop on the floor of Jezero crater, Mars. *Science*, 377(6614), 1513–1519. <https://doi.org/10.1126/science.abo2756>
- Lorenz, R. D., Lemmon, M. T., Maki, J., Banfield, D., Spiga, A., Charalambous, C., Barrett, E., Herman, J. A., White, B. T., Pasco, S., & Banerdt, W. B. (2020). Scientific Observations With the InSight Solar Arrays: Dust, Clouds, and Eclipses on Mars. *Earth and Space Science*, 7(5), e2019EA000992. <https://doi.org/10.1029/2019EA000992>
- Moeller, R. C., Jandura, L., Rosette, K., Robinson, M., Samuels, J., Silverman, M., Brown, K., Duffy, E., Yazzie, A., Jens, E., Brockie, I., White, L., Goreva, Y., Zorn, T., Okon, A., Lin, J., Frost, M., Collins, C., Williams, J. B., ... Biesiadecki, J. (2020). The Sampling and Caching Subsystem (SCS) for the Scientific Exploration of Jezero crater by the Mars 2020 Perseverance Rover. *Space Science Reviews*, 217(1), 5. <https://doi.org/10.1007/s11214-020-00783-7>
- Muirhead, B. K., Nicholas, A., & Umland, J. (2020). Mars Sample Return Mission Concept Status. *2020 IEEE Aerospace Conference*, 1–8. <https://doi.org/10.1109/AERO47225.2020.9172609>
- Schmidt, M. E., Perrett, G. M., Bray, S. L., Bradley, N. J., Lee, R. E., Berger, J. A., Campbell, J. L., Ly, C., Squyres, S. W., & Tesselaar, D. (2018). Dusty Rocks in Gale crater: Assessing Areal Coverage and Separating Dust and Rock Contributions in APXS Analyses. *Journal of Geophysical Research: Planets*, 123(7), 1649–1673. <https://doi.org/10.1029/2018JE005553>
- Vicente-Retortillo, Á., Martínez, G. M., Renno, N., Newman, C. E., Ordonez-Etxeberria, I., Lemmon, M. T., Richardson, M. I., Hueso, R., & Sánchez-Lavega, A. (2018). Seasonal Deposition and Lifting of Dust on Mars as Observed by the Curiosity Rover. *Scientific Reports*, 8(1), Article 1. <https://doi.org/10.1038/s41598-018-35946-8>

Williams, M. (n.d.). *How bad is the radiation on Mars?* Retrieved November 14, 2022, from <https://phys.org/news/2016-11-bad-mars.html>

Chapter 2: Literature Review

2.1 Geologic Background

The Martian surface is subdivided into three epochs: Noachian (4.5-3.7 Ga), Hesperian (3.7-3.0 Ga) and the Amazonian (~3.0 Ga - Present) (Carr & Head, 2010). Dating of the Martian surface is based on the intersection and number of super-imposed craters across the planet's surface (e.g., Carr & Head, 2010; Platz et al., 2013), rock and mineral compositions (e.g., Ehlmann & Edwards, 2014), stratigraphic relationships between rock layers and surface features (e.g., Holm-Alwmark et al., 2021), and the analysis of Martian meteorites (e.g., Anderson et al., 2020; Borg & Drake, 2005; Udry et al., 2020; Udry & Day, 2018)

The Noachian Period (~4.5-3.7 Ga), named after the heavily cratered Noachis region, experienced high rates of cratering, erosion, valley formation, formation of Tharsis and the widespread production of weathering products, such as phyllosilicates (Figure 2-1; Carr & Head, 2010). Noachian terrains have characteristic overlapping and interbedded ejecta blanket of ancient craters, mountainous rim materials, and uplifted basement rock in impact basins (Scott & Carr, 1978). Isidis Planitia and Hellas Basin are two expansive surface features of the Martian terrain that formed during the late heavy bombardment era of the Noachian (Figure 2-1). Standing 9km high, and approximately 5000 km across, Tharsis, a volcanic plateau which hosts the largest volcanoes in the solar system (e.g., Arsia Mons, Pavonis Mons, and Ascraeus Mons; Crumpler & Aubele, 1978; Figure 2A) was likely the most volcanically active region on Mars during this period (Phillips et al., 2001). The presence of phyllosilicates across the Noachian terrain (Bibring et al. 2006), geomorphic evidence of lakes and rivers (Carr, 2007; Fassett & Head, 2008), evidence of groundwater movement and surface water at Meridiani (Figure 2-1; Grotzinger et al., 2005), and chlorine enrichments in localized topographic lows suggests surface conditions were relatively warm and wet during the Noachian. Greenhouse models indicate that conditions capable of sustaining widespread precipitation on Mars, using only carbon dioxide (CO₂) and water vapour (H₂O), would be difficult (Kasting, 1991). However, the geologic record suggests that warm, wet conditions were only occasionally met during this period, and may have resulted from large impacts or volcanic activity (Segura et al., 2002).

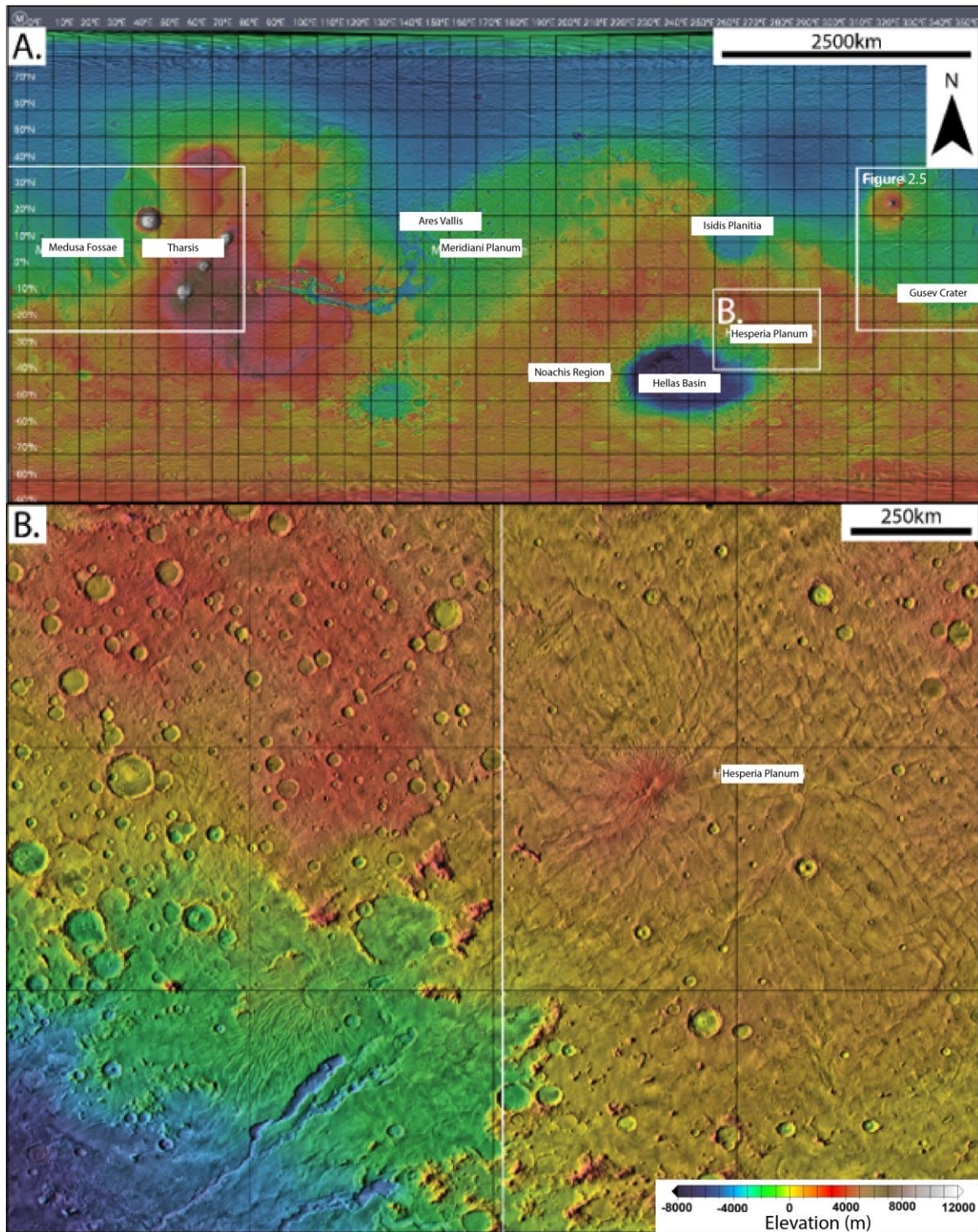


Figure 2-1: (A.) Mars Orbiter Laser Altimeter (MOLA) global elevation map of Mars with various regions of interest labeled in white. The white box around the Medusa Fossae Formation provides global context for Figure 2-5. (B.) Inset map displaying the heavily cratered Noachian terrain surrounding Hellas basin (left of white line) and the smoother, less frequently cratered volcanic Hesperian aged plains (right of white line).

Named after Hesperia Planum (Figure 2-1B), the Hesperian Period (3.7-3 Ga) is characterized by continued, and potentially episodic, volcanism which formed extensive lava plains (Watters & Maxwell, 1986), and comparatively lower rates of valley and canyon formation than the Noachian (Fassett & Head, 2007). The decline of impacts towards the end of the Noachian allowed volcanism to become the primary geologic process of Mars during Hesperian, generating plains of flood basalts and volcanic craters/calderas (Greeley & Spudis, 1981).

The Hesperian is further characterized by large outflow channels and their terminal lakes or seas (Parker et al., 1989), extremely low rates of erosion (Golombek et al., 2006), a steep decline and possible cessation of rock alteration to form phyllosilicates, and the accumulation of sulphate-rich deposits, particularly in the western hemisphere (Bibring et al., 2006). Erosion rates of the uppermost Noachian and Hesperian lava plains of Gusev crater, and Ares Vallis (the landing site of Pathfinder), were estimated to be between 0.02-0.03 nm/yr, several magnitudes less than the terrestrial erosion rates of 10^4 - 10^5 nm/yr (Golombek et al., 2006). These surface measurements, along with orbital observations, estimate erosion rates declined by 2-5 magnitudes following the Noachian and have persisted since. Some post-Noachian units, such as the Medusa Fossae Formation (MFF) and the polar layered deposit, are thought to have experienced locally elevated erosion rates (Carr & Head, 2010; Golombek et al., 2006)

Lasting from the middle of the terrestrial Archaean to the present, the Amazonian (~3.0 Ga - present) is the longest epoch in the Martian geologic record (Carr & Head, 2010). Impact cratering, tectonism, and volcanism throughout the Amazonian produced extensive geomorphological changes to the Martian terrain with low erosion and weathering rates persisting since the Hesperian (Golombek et al., 2006). Resulting from lowered rates of terrain building, surficial processes that involve ice and wind are more evident in the Amazonian, as demonstrated by the presence of dunes in almost every image of the Martian surface. The preservation of primary textures on volcanic flows and impact ejecta indicate that erosion of primary rock surfaces is minimal, and that wind activity largely involves reworking of unconsolidated fragmental materials (Carr, 2007). These fragmental materials include basaltic sands, sulfates, and carbonates that likely formed from a variety of processes (Stern et al., 2018).

These materials have accumulated and eroded over much of the planet's history through processes such as impacts, volcanism, erosion, weathering, and evaporation (Carr, 2007).

The thin contemporary Martian atmosphere allows a large portion of Sun's radiation to reach the surface (i.e., incident solar radiation, the radiant solar energy that hits the Earth's surface; Belessiotis et al., 2016). These high-energy cosmic rays induce nuclear transmutation of the incident surface, forming cosmogenic noble gases (Reedy et al., 1983). The abundance of these cosmogenic noble gases can therefore be used to date surface exposure and estimate erosion rates. With wet conditions favouring rapid erosion, the wetter surface conditions and associated thicker Martian atmosphere during the Amazonian are thought to have contributed to greater erosion rates during this period, lowering surface exposure age. The termination of fluvial activity during the Hesperian, continuing into the Amazonian, significantly lowered the erosion rates during these periods (Carr & Head, 2010; Farley et al., 2014; Golombek et al., 2006). Radiogenic K-Ar dating of a mudstone encountered along the floor of Gale crater, the landing site of the MSL Curiosity rover mission, found that the material was 4.21 ± 0.35 billion years (Farley et al., 2014). Studying the cosmogenic noble gases present, specifically ^3He , ^{21}Ne , and ^{36}Ar , the surface exposure age was found to be 78 ± 30 million years (Farley et al., 2014), and illustrates the lower erosion rates experienced during the Amazonian, and perhaps the Hesperian. With sand-sized particles traveling limited distances under contemporary atmospheric conditions (Stern et al., 2018), eroded materials in recent times are likely to be proximal to their source material.

2.2 Martian Atmosphere

Despite Mars' greater orbital distance compared to that of the Earth, both planets have similar rotation rates and orbital inclinations, producing similar diurnal and seasonal patterns. (Table 2. 1). One of the greatest differences between the two planets is their atmospheres (Figure 2-2). Earth's 1 bar atmosphere (Table 2-1), absorbs a significant portion of the Sun's radiant solar energy, shielding humans from harmful rays and decreasing our exposure to ~ 0.62 rads/yr (Williams, 2021). Greenhouse gases, such CO_2 and H_2O , trap re-radiated heat from the planet's surface, preventing it from escaping into space (Bouwman, 1990). These gases increase Earth's surface temperatures, prevent large diurnal temperature swings, and create a habitable global

climate. The Martian atmosphere is predominantly CO₂ (Figure 2-2) but is much thinner (<1% of the density of Earth's), allowing the loss of surface thermal energy at night, and results in large diurnal temperature swings (Finn et al., 1996). Due to its distance from the Sun, Mars receives less than 50% of Earth's sunlight (Solar Insolation, Table 2-1); however, the thin atmosphere permits more of the unscattered, high-energy solar radiation (8 rads/yr) to reach the planet's surface (Williams, 2021). For future human missions to Mars, the Martian climate will prove to be one of the most challenging obstacles to overcome.

Table 2-1: Comparison of Earth and Mars orbits and surface conditions

	Earth¹	Mars
Average Distance from Sun (million km)	151.5	246.3
Aphelion Distance (km)	152	249
Perihelion Distance (km)	147	207
Obliquity to Orbit (degrees)	23.4	25.2
Orbital Eccentricity	0.02	0.09
Rotation Period (hours)	24.0	24.6
Surface Pressure (bar)	1	0.01
Solar Insolation (W/m²)	1370	590

¹Information gathered by the United States Naval Observatory Nautical Almanac Office & Great Britain Nautical Almanac Office (1981).

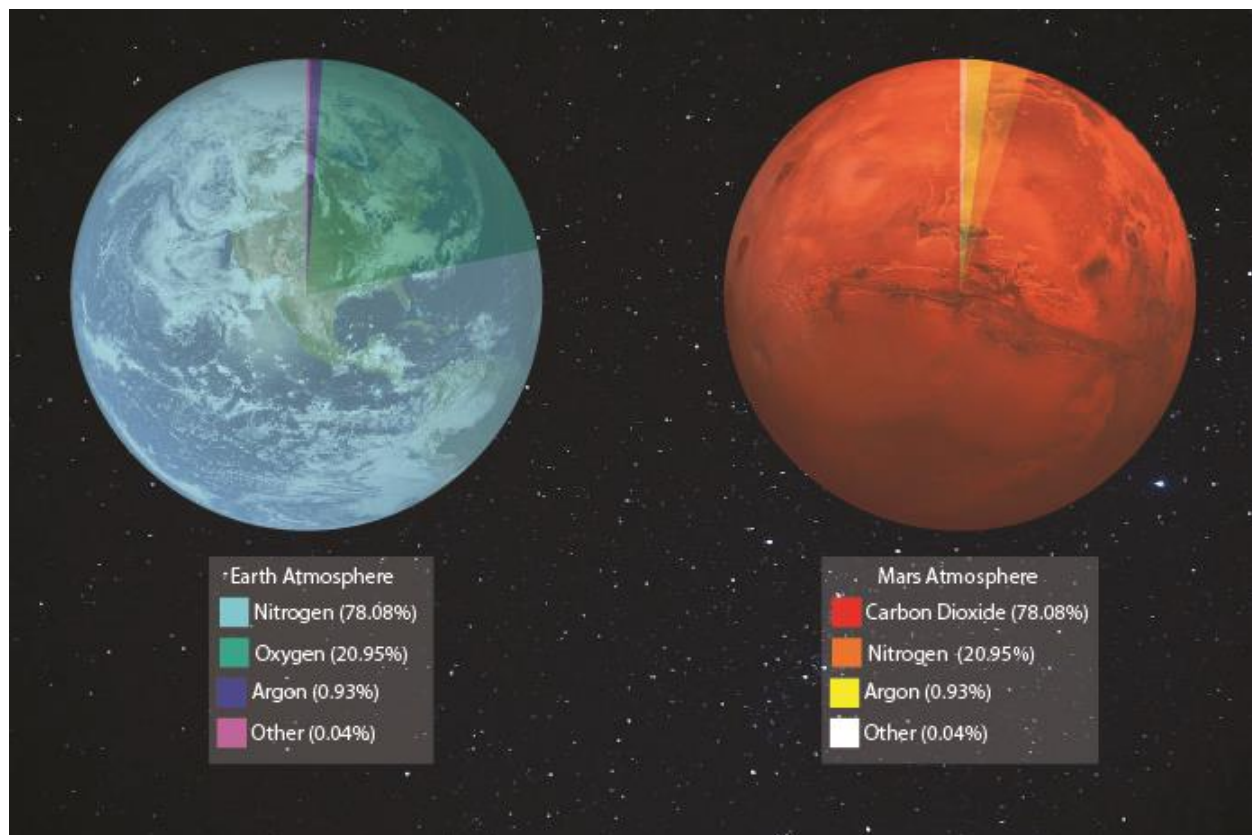


Figure 2-2; Atmospheric compositions of Earth (*Earth's atmosphere*, n.d.) and Mars (Owen et al., 1977). Planets not to scale. Atmosphere of Mars is less than 1% of Earth's. (Adapted from *Comparing the Atmospheres of Mars and Earth*, n.d.)

2.3 Mars Seasons

Mars experiences four seasons similar to Earth, however, its more elliptic orbit amplifies seasonal variations. Like Earth, the orbital obliquity of Mars causes the Southern and Northern Hemispheres to experience opposite seasons. When the planet approaches perihelion, the Southern hemisphere is tilted towards the Sun and experiences Southern Summer. When the Northern hemisphere is tilted away from the Sun, it experiences Northern Winter. The inverse relationships are true when Mars approaches aphelion. While the Martian climate can be classified into four seasons (Khavrus & Shelevytsky, 2012), it is more easily divided into two distinct intervals: the “Non-Dusty” and “Dusty” seasons (Haberle et al., 2017; J. Liu et al., 2003; Smith, 2004, 2008).

Haberle et al. (2017) detail the “Non-Dusty” (Solar Longitude, L_s , $\sim 0-135^\circ$) season of Mars spanning from the start of spring until halfway through summer in the Northern Hemisphere,

and inversely, autumn until halfway through winter in the Southern Hemisphere (Figure 2-3). Atmospheric opacity, a measure of electromagnetic transmittance through the Martian atmosphere that is increased by the presence of suspended dust, is lowest during the “Non-Dusty” season. This indicates the gravitational settling of atmospheric dust, and is responsible for the accumulation of surficial dust and its removal from the atmosphere (Vicente-Retortillo et al., 2018). Due to the planet’s very low surface pressure (Table 2-1), as the planet increases its distance from the Sun, daily surface temperatures decrease and permit atmospheric CO₂ to condense at the poles (Leovy, 2001). This annual removal of CO₂ has lowered the atmospheric pressure by as much as 20% in some years (Phillips et al., 2001; Zurek et al., 1992). Because CO₂ is a greenhouse gas, its removal from the atmosphere results in a decrease in atmospheric heat capacity and increases diurnal and seasonal temperature variations (Leovy, 2001). The diurnal surface air temperatures in Martian polar regions vary by up to 90°C (Zurek et al., 1992), whereas the extreme climate of terrestrial northeastern Siberia varies by only 50°C (Leovy, 2001) and produce strong thermal winds (Haberle et al., 1979).

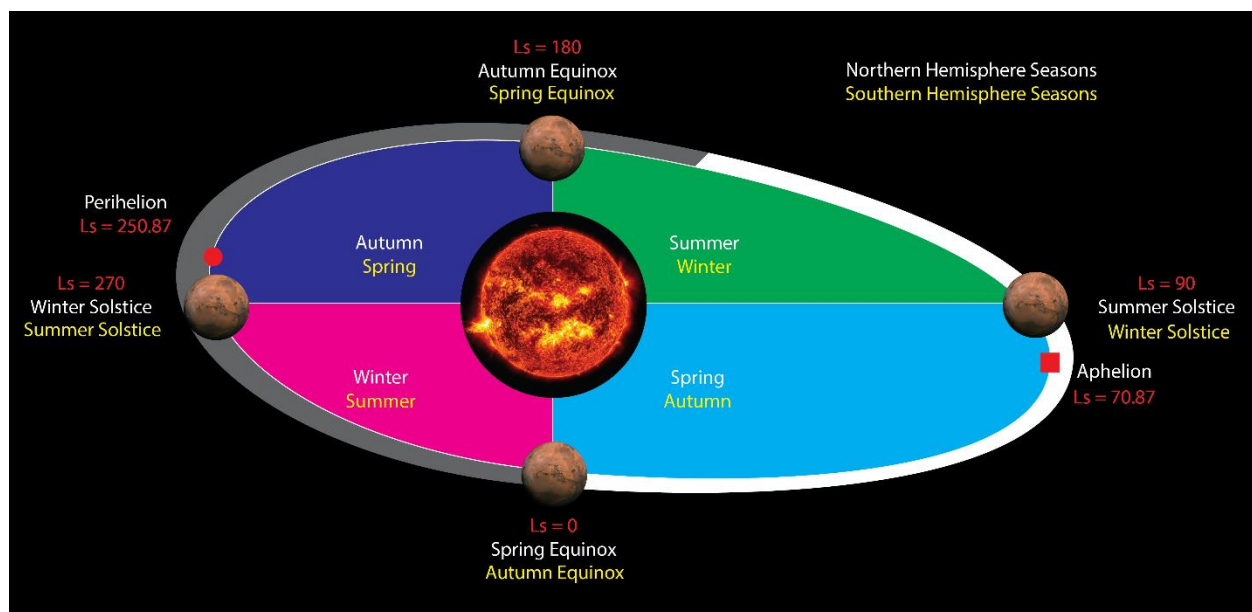


Figure 2-3: Mars' orbit around the Sun subdivided into seasonal quadrants according to equinox. The orbital eccentricity and sizes of Mars and the Sun are not to scale. The red square and circle indicate aphelion and perihelion respectively. The white halo represents the “Non-Dusty” season described by Haberle et al. (2017; Ls 0-135°). The grey halo represents the “Dusty” season (Ls 135-360°).

Spanning from the end of the “Non-Dusty” season through to the spring equinox (Ls 135-°360°), the “Dusty” season is characterized by increased atmospheric opacity (Haberle et al., 2017) and indicates dust lifting exceeds gravitational settling during this period (Vicente-Retortillo et al., 2018). Dust aerosols are suspended through a variety of mechanisms, such as: the seasonal retreat of polar ice caps, downslope windstorms and the migration of low-pressure air masses (Smith & Lemmon, 1999). Suspended dust aerosols significantly affect the thermal structure of the Martian atmosphere. By absorbing solar radiation and escaping surface thermal energy, dust particles in the atmosphere are a major drive of atmospheric circulation (Conrath, 1975; Guzewich, Wilson, et al., 2014; Haberle et al., 1982). Dust aerosols suspend through a variety of mechanisms; however, the location, spatial extent, and seasonality of these dust-lifting events vary significantly between years. Despite this variability, fluxes of dust aerosols are recorded each year, causing increased atmospheric opacity, and driving atmospheric circulation and wind generation (Haberle et al., 2017).

2.4 Particle Mobility and Wind Generation

The arid conditions of the modern-day Martian surface results in wind processes playing an important role in sediment transport. Understanding the conditions that initiate and sustain particle motion is fundamental for determining wind speed requirements of mobilization and the frequency of such events. Like Earth, Martian wind applies a shear force to the surface along the atmospheric boundary layer (Sullivan & Kok, 2017). At a given particle size, the most-exposed grains are the first to be mobilized. At relatively low wind friction speeds (also known as shear velocity, shear stress expressed in units of velocity) these grains will move sporadically but possess generally insufficient energy to dislodge and activate the remaining bed (Bagnold, 1936). The same-sized particles at higher wind friction speeds carry greater energy and will begin to saltate across the bed (Figure 2-4). The transfer of energy between stationary and saltating grains cascade and cause additional grain movement (Sullivan & Kok, 2017).

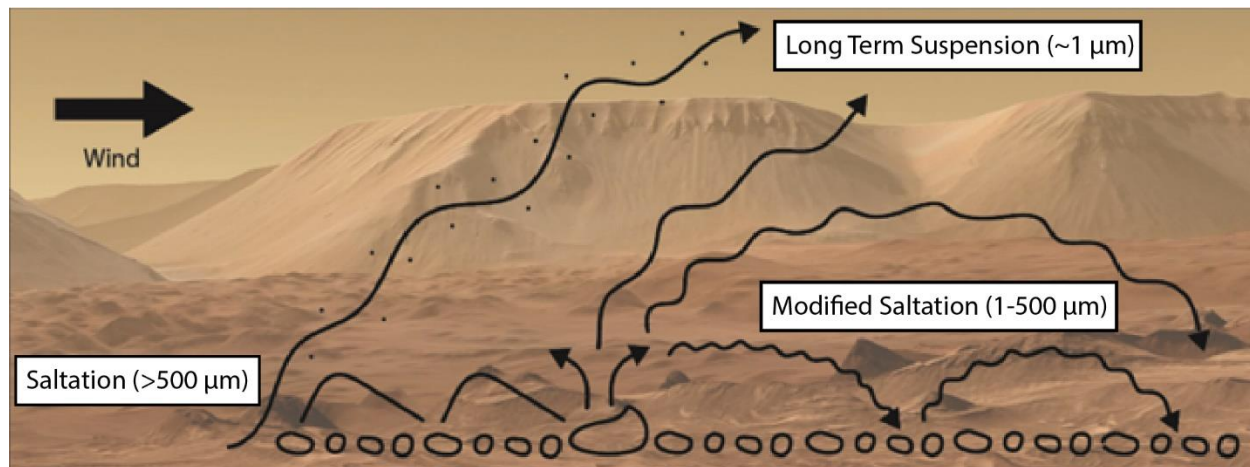


Figure 2-4: Illustration of aeolian sediment transport. Winds cause saltation of $>500\ \mu\text{m}$ grains (Baker et al., 2018). Finer grains ($\sim 1\ \mu\text{m}$) are lofted, and suspended long-term in the atmosphere (Guzewich et al., 2014). Collisions between saltating grains and larger ($1\text{--}500\ \mu\text{m}$), immobile material -aid in lofting fine particles or result in modified saltation trajectories (Adapted from Nickling & Neuman, 2009).

With an estimated exchange of approximately $2.9 \times 10^{12}\ \text{kg/yr}$ of dust between the Martian surface and atmosphere, dust activity is one of the most dynamic and prevalent geological processes of contemporary Mars, however the precise mechanisms which mobilize and suspend dust particles are not well quantified (Newman et al., 2022). Since the density of the Martian atmosphere is less than 1% that of the Earth, greater shear velocities, and greater wind velocities, are required to initiate particle movement (Greeley et al., 1980; Johnson et al., 2020). Previous studies suggest surface winds rarely exceed the threshold required to mobilize sand-sized particles, however, more recent work demonstrate how relatively short-lived, strong gusts are capable of mobilizing sand-sized particles and can trigger substantial saltation downwind (Figure 2-4; Baker et al., 2018).

On a global scale, winds capable of suspending Martian dust particles ($\sim 1.0\ \mu\text{m}$; Guzewich et al., 2014) and saltating sand-sized particles are thought to be generated from a variety of sources: thermal contrasts between the edge of retreating CO_2 polar ice caps and the adjacent uncovered ground (Burk, 1976; Haberle et al., 1979; Toigo et al., 2002), downslope windstorms (Magalhães & Young, 1995; Siili et al., 1997) and the migration of low-pressure air masses generated by differential heating (Gómez-Elvira et al., 2012; Wang et al., 2003). Once dust suspension has been initiated, further additions of dust aerosols raise the heat capacity of the

Martian atmosphere and significantly affect its thermal structure (Smith & Lemmon, 1999). As the planet approaches perihelion during Southern Summer, these conditions generate seasonally higher wind speeds and initiate the transport of larger sediments (M. M. Baker, Newman, et al., 2018; V. R. Baker, 2002; V. R. Baker et al., 2002; Newman et al., 2017; P. H. Smith & Lemmon, 1999). Orbital measurements of atmospheric conditions and *in situ* studies of sediment transport have helped refine General Circulation Models (GCM) of Mars that are frequently used in studies to understand Mars' present and past climate (Zurek et al., 1992).

2.5 Dust Composition and Origin

The first orbital images of a Martian dust storm were taken by Mariner 9 in 1971 (Leovy et al., 1973). Since then, decades of further observations have demonstrated how planet-encircling or global dust storms are a common, approximately triennial (Liu et al., 2003), Martian phenomenon that envelope the planet for weeks to months at a time. Global and smaller, regional storms suspend and mix Martian dust particles, producing a globally homogenous dust unit (Yen et al., 2005, 2013). Rover magnets aboard Pathfinder and Mars Exploration Rover (MER) were the first to capture Martian airfall dust and record *in situ* compositional measurements. The presence of magnetite (Fe_3O_4) in the dust attracted the material towards the rover magnets and revealed a basaltic composition rich in S- and Cl-, framework silicates, mostly feldspar, with minor amounts of pyroxene, and amorphous phases (Bertelsen et al., 2004; Goetz et al., 2005; Hamilton et al., 2005; Madsen et al., 2003). Berger et al. (2016) later modeled the APXS spectra composition of airfall dust that had settled on the science observation tray (O-tray) on the MSL Curiosity rover. The dust from Gale crater was enriched in S, Cl, and Fe relative to typical Martian soils. The overall S/Cl ratio (3.7 ± 0.7) was consistent with observations from Gusev crater and Meridiani Planum (Berger et al., 2016; Foley et al., 2003; Goetz et al., 2005; Yen et al., 2005) and supports the argument of global dust and soil homogenization (Yen et al., 2005, 2013).

While trillions of kilograms of airfall dust blankets the Martian terrain, to supply such an immense volume of material makes a single source highly unlikely. Millenia of dust storms and the associated homogenization of material further complicates the origin story of Martian dust. Early studies of Terrestrial loess deposits suggested glacial grinding to be the only natural process that could efficiently comminute sand-sized quartz particles into silt-sized particles (Smalley &

Krinsley, 1978). Studies since have suggested other mechanisms, such as frost shattering, fluvial breakdown, volcanism, aeolian abrasion, glacial grinding and salt weathering as potential sources of fine dust martial (Derbyshire et al., 1998; Ojha et al., 2018; Smalley & Krinsley, 1978; Whalley & McGreevy, 1983; J. Wright et al., 1998). With a rich history of volcanic activity and particularly explosive volcanism, the basaltic composition suggests that ancient ash deposits could be a significant contributor to the Martian dust reservoir (Bandfield et al., 2013; Ojha et al., 2018; Wilson & Head, 2007). The presence of olivine, a mineral highly susceptible to alteration in liquid water, in Martian dust supports the idea that fluvial activity played a minimal role in its formation (Goetz et al., 2005; Ojha et al., 2018). The relatively short, and episodic, lifetimes of Martian glaciers and fluvial features prevent significant dust production from any associated processes.

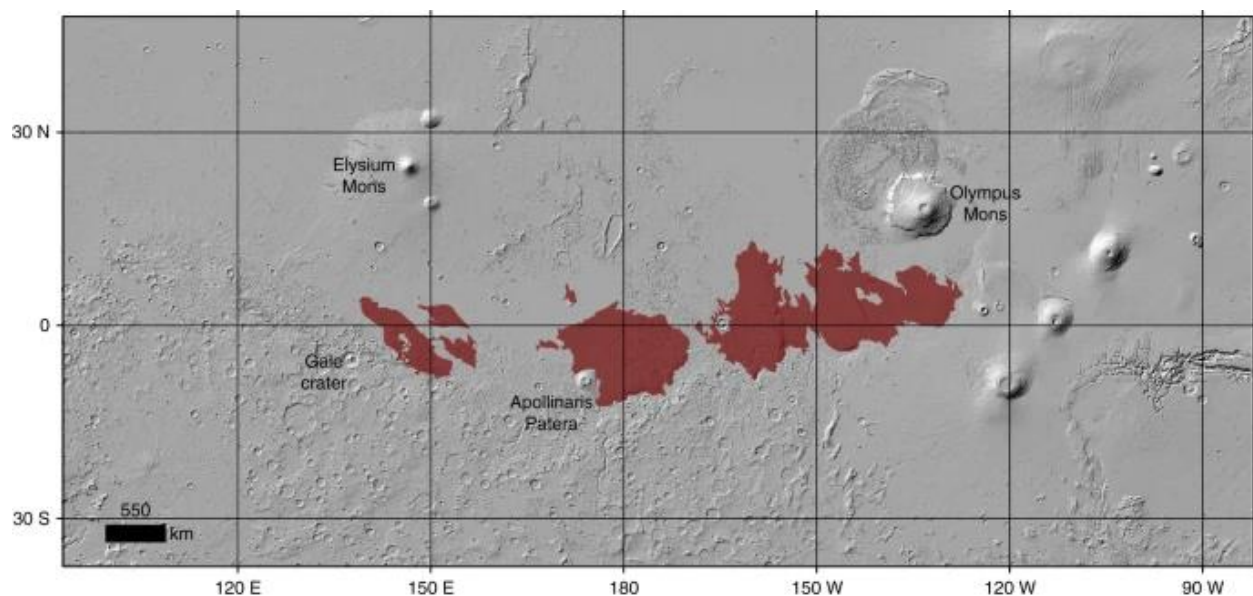


Figure 2-5: MOLA shaded relief image displaying the geographical extent of the Medusa Fossae Formation (Red; Ojha et al. 2018).

To accommodate the volume of material, potential sources of Martian dust must be expansive and have similar enrichments of S^{2-} and Cl^{-} . Ojha et al., (2018) suggested a large sedimentary unit, known as the Medusa Fossae Formation, to be a significant contributor to the Martian dust reservoir. With an age ranging between the Amazonian to the Hesperian eras (3.7-3.0 Ga; Kerber & Head, 2010), the MFF lies along the equatorial region of Mars, near the global dichotomy that separates the northern and southern highlands (Figure 2-1 and 2.5). Several depositional models have been proposed for the MFF, including glacial activity during the early

Hesperian which emplaced paleo-polar deposits with incorporated aeolian sediment (Tanaka, 2000), atmospheric deposition of aeolian sediment (Greeley & Guest, 1987; Scott & Tanaka, 1986; Tanaka, 2000), coarse-grained ignimbrite deposits from plinian-style eruptions (Malin, 1979; Scott & Tanaka, 1986), and fine-grained distal ashfall from volcanic eruptions (Ojha & Lewis, 2018). The present day MFF exceeds $2 \times 10^6 \text{ km}^2$ (Bradley et al., 2002) and hosts huge yardangs up to 10s km in scale (Ward, 1979). Being large aeolian erosional landforms, the presence of Yardangs in MFF demonstrate that this region is heavily eroded from an original area of $5 \times 10^6 \text{ km}^2$ (Bradley et al., 2002). With similar S/Cl enrichments to Martian dust determined by Berger et al. (2016) and evidence of significant erosion, the Medusa Fossae could be a major contributor to the Martian dust reservoir (Ojha et al., 2018).

2.6 Gale crater

Located between the ancient, heavily-cratered southern highlands and Elysium Planitia, Gale crater (4.49°S, 137.42°E) is an approximately 150 km diameter impact crater and comprises four main geomorphic units: a raised crater rim, a flat crater floor, a central mound (Mount Sharp) and a surrounding ejecta blanket (Figure 2-6. B and C; Schwenzer et al., 2012). Crater counting of the surrounding area and the Gale crater ejecta blanket indicate that it formed $\sim 3.6 \text{ Ga}$, during the Late Noachian (Le Deit et al., 2013; Thomson et al., 2008). In August 2012, the Curiosity rover landed in the NNW quadrangle between the central mound and crater rim (Figure 2-6c) and has been performing ground-based investigations of Gale crater for more than a decade since (Grotzinger et al., 2012; VanBommel et al., 2023).

While only some of the Gale crater stratigraphic units contain aeolian dune deposits, all have experienced erosion and are locally covered by a layer of aeolian airfall dust. That is not to say erosion has been constant across Gale crater (Schwenzer et al., 2012). Straddling the global dichotomy, the associated pre-impact topography results in Gale crater's northern rim sitting lower. Comparing the shallower slopes of the northern rim to the higher, southern rim and the preserved portions of the ejecta blanket to the south illustrates that erosion is stronger in northern Gale crater (Greeley & Guest, 1987). The central mound contains an angular unconformity that drives its sediments into an upper and lower unit (Thomson et al., 2011). Channels cut through the upper sections of the mound incise underlying sediments, and produce

depositional fans along the southern slopes of the mound (Thomson et al., 2008). These features indicate the central mound is an erosional remnant of a once larger sediment pile.

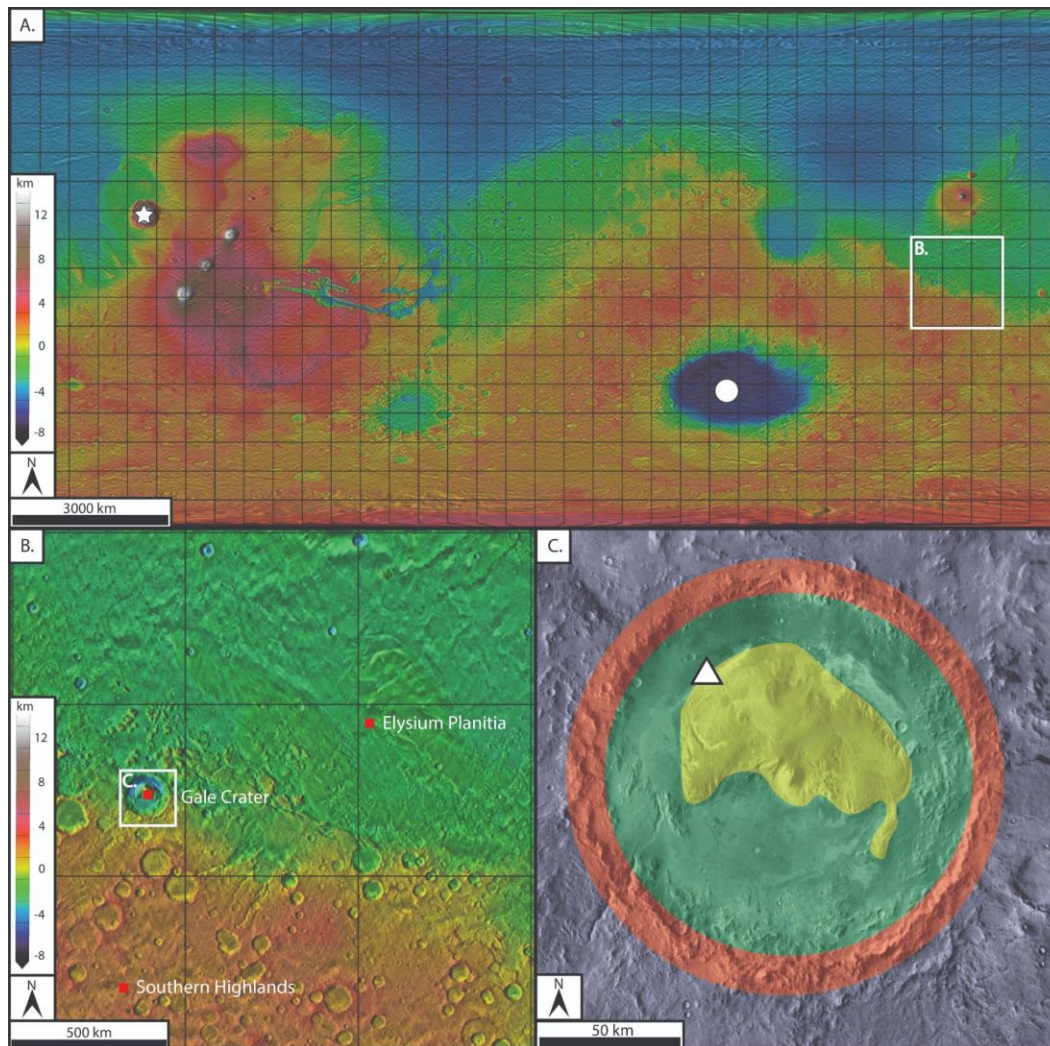


Figure 2-6: (A.) Digital elevation model (DEM) the Martian surface, displaying Olympus Mons, the highest elevation (white star), and Hellas impact basin, the lowest elevation (white circle). (B.) Mars DEM showing location of Gale crater in relation to Elysium Planitia and the heavily-cratered Southern highlands. (C.) HiRISE image of Gale crater with the four main geomorphic units: ejecta blanket (purple), crater rim (red), crater floor (green) and the central mound (yellow). The white triangle indicates the Curiosity landing site (Schwenzer et al. 2012).

The crater depth-diameter ratio is important for interpreting the formation and subsequent history of a crater; deviation from the standard depth-diameter ratio (0.06 to 0.16; (Wu et al., 2022) indicates sediment removal or deposition following impact. Similar to a medieval castle, the central mound of Gale crater is separated from the crater rim by a moat,

deeper in the north than in the south. The northern portion of the moat has been partially filled by sediments, including layered deposits beneath the central mount material, while the southern and southeastern sides of the moat have been partially infilled by massive lobes of landslide material likely sourced from the nearby crater rim (Cabrol et al., 1999; Pelkey et al., 2004). Variable depths between the northern and southern sections of the moat complicate the maximum depth of Gale crater. The highest elevation in Gale crater, the central mound, rises nearly 6 km above the crater floor and ~1 km above the 4.5 km tall southern crater rim. The floor of Gale crater is also gently dipping towards the north, an incline that is likely caused by a regional slope and contributes to the height difference between the northern and southern crater rims. Gale crater has a depth-diameter ratio of ~0.03 and is consistent with the general morphology of Martian craters (Garvin et al., 2000). Despite the northern crater rim experiencing greater erosion than its southern counterpart, the crater-depth ratio of Gale crater suggests that it has not experienced much erosion overall and that the crater floor is buried by only a small amount, <1 km, of post-cratering infill (Schwenzer et al., 2012).

2.6.1 Mount Sharp / Aeolis Mons

Rising nearly 6 km from the crater floor, Aeolis Mons (colloquially known as, and will be further referred to as, Mount Sharp; Figure 2-6c) is a central mound of sediments that displays a variety of morphologies and compositions separated by an angular unconformity (Schwenzer et al., 2012). The upper group of sediments from the central mound form rounded hill slopes with infrared (IR) reflectance spectra dominated by sulphate signatures while the lower group is strongly layered and the spectra are dominated by hydrous phyllosilicate absorption features (Milliken et al., 2010). These mineralogical differences, above and below the angular unconformity, suggest that they were formed by different processes (Milliken et al., 2010; Thomson et al., 2011).

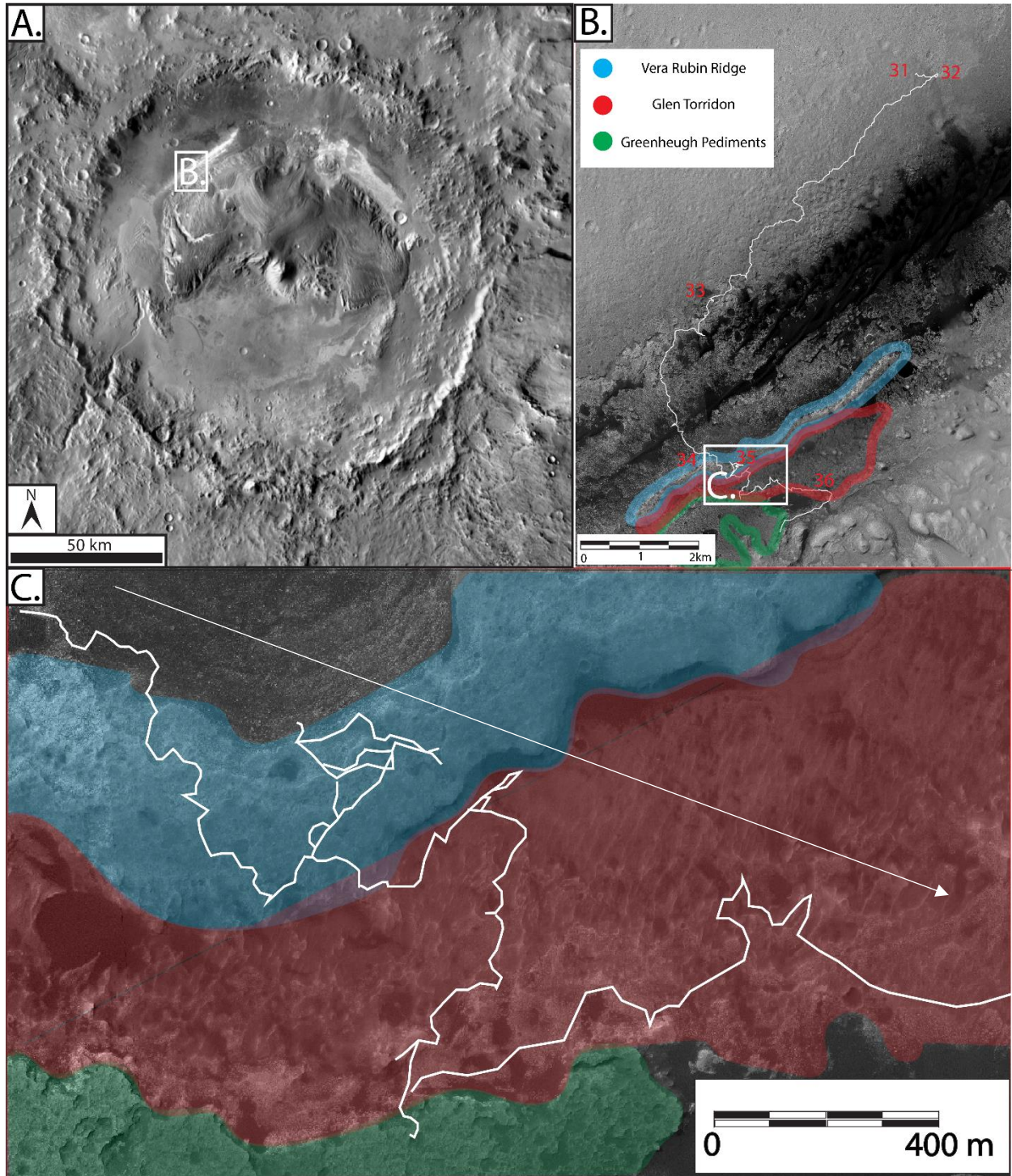


Figure 2-7: (A.) HiRISE image of Gale crater. (B.) HiRISE image of the area of operations (AO) for Mars Science Laboratory (MSL). The white line indicates the rovers traverse (sol 0 to 3344), with red numbers indicating the first sol of each Mars year. Coloured outlines indicate the surface features used to assign the Legacy names used in this study. (C.) Zoomed in view of MSL's MY34 and MY35 AO. The white arrow shows the general direction of Curiosity's travel.

Table 2-2: Geomorphically defined regions of Mount Sharp and their constituent stratigraphic units.

Geomorphically Defined Names	Associated Stratigraphic Member¹
Glen Torridon	Glasgow Knockfarril Hill Jura
Vera Rubin Ridge	Knockfarril Hill Jura Pettegrove Point

¹Stratigraphic names defined by Fedo et al. (2022) using ground based observations.

The presence of channels and delta fan deposits along the base of Mount Sharp suggest Gale crater once hosted a crater lake early in its history (Cabrol et al., 1999). These geomorphic features along with the detection of abundant phyllosilicates, a class of silicate that is strongly associated with water and formed through hydrolysis, further supports the paleo-lake hypothesis of Gale crater. Requiring water and surface conditions that allow the presence of water, these features are interpreted to be a combination of late Noachian and early Hesperian-aged material. Investigations of these units by MSL suggest the rock layers making up Mount sharp are products of fluvial (Williams et al., 2013), deltaic (Grotzinger et al., 2015), lacustrine (Edgar et al., 2020; Kah et al., 2018) and aeolian (Banham et al., 2018, 2021) processes.

Prior to MSL landing in Gale crater, orbital imagery was used to divide Mount Sharp into regions according to spectral characteristics, geomorphic features and topographic variations; Vera Rubin Ridge (VRR) Glen Torridon (GT) and the Greenheugh Pediments (GHP) are the recent names of the subdivided features of Mount Sharp (Figure 2-7). VRR is ~6.5km long, and ~200m wide, and is one of the most prominent geomorphic features of Mount Sharp (Fraeman et al., 2020). The northern slopes of VRR rise ~100m above the crater floor while a steep gradient along the southern margin forms the geomorphic boundary of GT, an approximately NE/SW-oriented trough-shaped geomorphic feature (Edgar et al., 2020; Fraeman et al., 2020). GT is characterized by a northern topographic valley, or trough, that gradually ascends to the south, eventually standing taller than VRR. A southern escarpment capped by a sandstone unit marks the southern

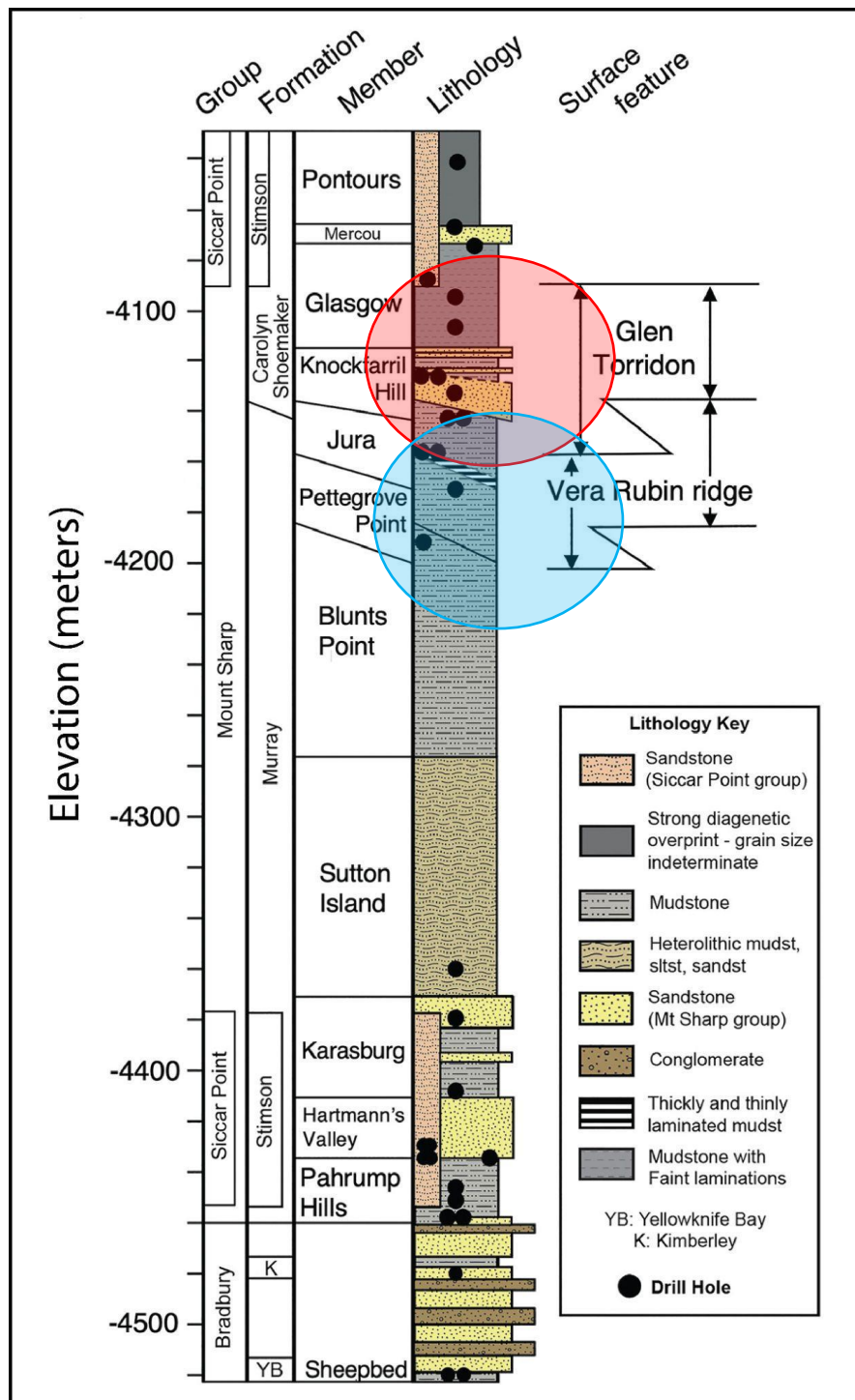


Figure 2-8: Stratigraphic column of rocks encountered by the MSL Curiosity rover in Gale crater. Inclined boundaries between members and lithologies result from elevation differences of observed contact. The geomorphically defined names for Vera Rubin Ridge (blue) and Glen Torridon (red), and their associated lithologies. (Modified from Fedo et al., 2022).

boundary between GT and GHP. Forming a near-vertical, small cliff above GT, the GHP is a sandstone-capped geomorphic feature that define this region(Fedo et al., 2022).

While the terminology of VRR, GT and GHP are used throughout the literature, Fedo et al. (2022) details how their orbital spectral characteristics and geomorphic differences do not correspond with stratigraphic boundaries. The topographically prominent VRR and the lower-lying GT region, which were previously thought to be unique, are both from the Jura member of the Murray Formation despite their geomorphic boundary (Figure 5-9). Subregions of the Glen Torridon, the fractured clay-bearing unit and the fractured intermediate unit, were previously separated by a boundary but were similarly found to occur within the same member of the Carolyn Shoemaker Formation. Chapter 4 does not focus on dust coverages based on stratigraphy, the geomorphically defined VRR, GT, and GHP names will be used for the remainder of the thesis. These names have been used extensively in published literature and their borders are more easily discerned in satellite images (Figure 2-7; see Table 2-2 for updated names).

2.7 Isidis Planitia and the Nili Fossae

Isidis Planitia, alternatively known as the Isidis basin, is a large ~1500 km wide impact feature that formed during the Middle-to-Early Noachian (~4.0 Ga; ; Mustard et al., 2007). Concentric ring features along its perimeter, formally known as the Nili Fossae, are believed to be relaxation graben structures caused by the immense weight of the Isidis mascon (geological structure that has a positive gravitational anomaly; Fassett & Head III, 2005). These features are well-exposed, largely dust free, and reveal a large portion of the Noachian crust (Brown et al., 2020). The Nili Fossae are a mineralogically rich and diverse region of Mars, hosting abundant phyllosilicates and other hybrid phases, mafic minerals and carbonates (Ehlmann & Edwards, 2014; Mandon et al., 2020). Strong orbital detections of carbonate minerals in association with olivine bearing materials suggest that the Nili Fossae region possess hydrothermally altered ultramafic rocks (Brown et al., 2010, 2020). Carbonate rocks are of particular interest when investigating sedimentary and hydrothermal Martian systems. Carbonates not only record fluid composition, pH, and temperatures of formation (Bridges et al., 2019), and also because the associated hydrothermal activity is known to provide sufficient energy for biological activity on Earth (Brown et al., 2010). Due to its diverse mineralogy and potential for preserving evidence of

biological activity, the Nili Fossae region was a strong candidate for the MSL and Mars2020 (M2020) missions.

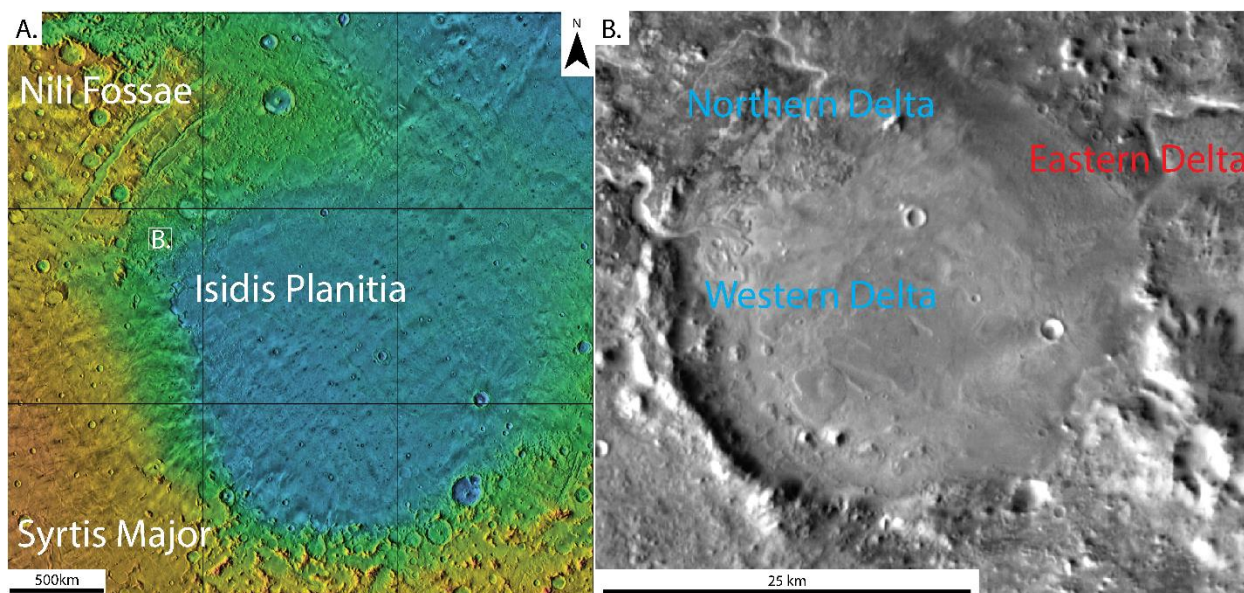


Figure 2-9: (A.) MOLA elevation map displaying the locations of the Nili Fossae, Isidis Planitia and Syrtis Major. (B.) HiRISE image of Jezero crater displaying the locations of the two inflowing (blue) deltas and single outflowing (red) channel.

2.8 Jezero crater

Located along the western flanks of Isidis Planitia (~4.0Ga; Werner, 2008) and northeast of Syrtis Major (a younger shield volcano; Mustard et al., 2007), Jezero crater was the selected landing site for the M2020 mission (Boeder & Soares, 2020). The modern day Jezero crater is ~45km diameter open basin, that one hosted a lake (Boeder & Soares, 2020). The presence of two inflowing deltas along the western and northern crater rims, and a single outflowing channel at the eastern crater rim suggests that Jezero crater was once hydrologically open (Figure 2-9; Fassett & Head III, 2005). Crater counting and following inlet valleys upstream suggests fluvial activity in Jezero crater terminated around the time of the Noachian Hesperian boundary (3.6-3.6 Ga), similar timing to the cessation of fluvial activity in other valley networks on Mars. Orbital investigations of Jezero crater's western delta found Mg-rich carbonates in association with olivine rich materials and Mg/Fe-phyllosilicates. The detection of carbonates and phyllosilicates in Jezero crater are likely hydrothermal in origin, indicating that Jezero crater once hosted water,

and perhaps microbial life. These features led to Jezero crater being selected as the landing site of the M2020 mission (Abilleira et al., 2019)

Since landing February 18th 2021 (Farley et al., 2022) Perseverance has successfully completed its first two campaigns: the Crater Floor campaign (Sun et al., 2023), and the Delta Front campaign (Williams et al. 2023). During this time, Perseverance has examined rock of the Máaz, Séítah, and Shenandoah formations (Ives et al., 2023) with its payload, and has successfully sampled and cached 1 samples for return to Earth (Williams, et al., 2023).

2.8.1 Máaz Formation

The Máaz formation was one of the first features studied by M2020 shortly after touching down at the Octavia E. Butler landing site. This unit sits at the lowest elevation along the traverse and was therefore inferred to be the oldest interval of the Máaz sequence (Farley et al., 2022). Upon arrival, Perseverance abraded the rock surface using the Sampling and Caching Subsystem's (SCS) abrasion bit (Moeller et al., 2020). The freshly exposed rock contained interlocking millimeter-sized, inter-connected light and dark grains with a pervasive yet heterogeneously distributed brown tint. While some elongated grains were visible in the abrasion patch (Guillaumes; Table 3-1), there were no discernible grain orientations. Large (~5mm) irregularly shaped voids/pits were also visible in the abrasion patches (Farley et al., 2022). Some of these voids/pits were unfilled, however others were partially/fully filled by a bright-white mineral.

Perseverance continued westward along Artuby Ridge, an ~1km long linear scarp with 2-3m tall southwesterly dipping strata, eventually crossing into the Artuby Member (Farley et al., 2022). The Artuby Member possesses distinct decimeter-thick layering with rounded protrusions, and a coarse granular texture. Layering from the Artuby Member were overlain by a resistant caprock, the Rochette Member, and can be seen extending hundreds of metres along Artuby Ridge (Figure 2-10). The Rochette Member is only ~0.5m thick with centimeter-scale layering, and periodically structureless. An abrasion patch in the Rochette Member, called Bellegarde (discussed in further detail in Chapter 5), revealed comparatively smaller crystals (~0.5mm; Farley et al., 2022) than Roubion. Similar, yet less pervasive brown material stained the crystals in

Bellgarde, but did not contain any of the voids/pits seen in Guillaumes. Rather these voids and pits were filled with a white mineral.

Multispectral Mastcam-Z observations (Bell et al., 2021), SuperCam laser-induced breakdown spectroscopy (LIBS; Wiens et al., 2020), and Planetary Instrument for X-ray Lithochemistry (PIXL; Allwood et al., 2020) x-ray fluorescence mapping found the Mááz Formation to be dominated by common primary igneous minerals (e.g. augite, plagioclase, ilmenite and ferrosilite). However, no IR spectra or LIBS compositions of olivine were detected (Farley et al., 2022). PIXL mapping indicated that the block to prismatic white grains were chemically consistent with plagioclase (Al-rich regions). The darker grain compositions were consistent with the Ca-rich pyroxene Augite (Farley et al., 2022). The brown patches and stains were mostly Fe and Si materials and overlapped with some igneous Fe silicate minerals such as Fe-bearing pyroxene and olivine. While Mastcam-Z detected iron oxides present in both abrasion patches (Guillaumes and Bellegarde), none were detected in the associated PIXL scans (Farley et al., 2022). Raman spectroscopy found that the bright-white crack/void-filling minerals were hydrous Ca sulfate and Na perchlorate (Farley et al., 2022).

Averaging the bulk compositions of Mááz abrasion patches, Farley et al. (2022) found that SO_3 and Cl^- abundances were elevated compared to typical unaltered Martian igneous rocks (Filiberto et al., 2016). By excluding the PIXL Motor Count (PMC) associated with the bright white salt-rich areas, the primary Mááz Formation compositions were basaltic, with enrichments in FeO_T and P_2O_5 compared to Earth's basalts.

2.8.2 Séítah Formation

Following the inspection of Artuby Ridge, Perseverance began investigating the second formation of the Crater Floor campaign, Séítah (Figure 2-10). Investigations of the Séítah Formation were limited to ~1 to 10m tall ridges trending northeast southwest with sand ripples, loose cracks, and boulders cover the remaining region. Observations from Farley et al. (2022) found that Séítah contained two distinct Members: (1) the strongly layered Bastide Member, and (2) the overlying Content Member.

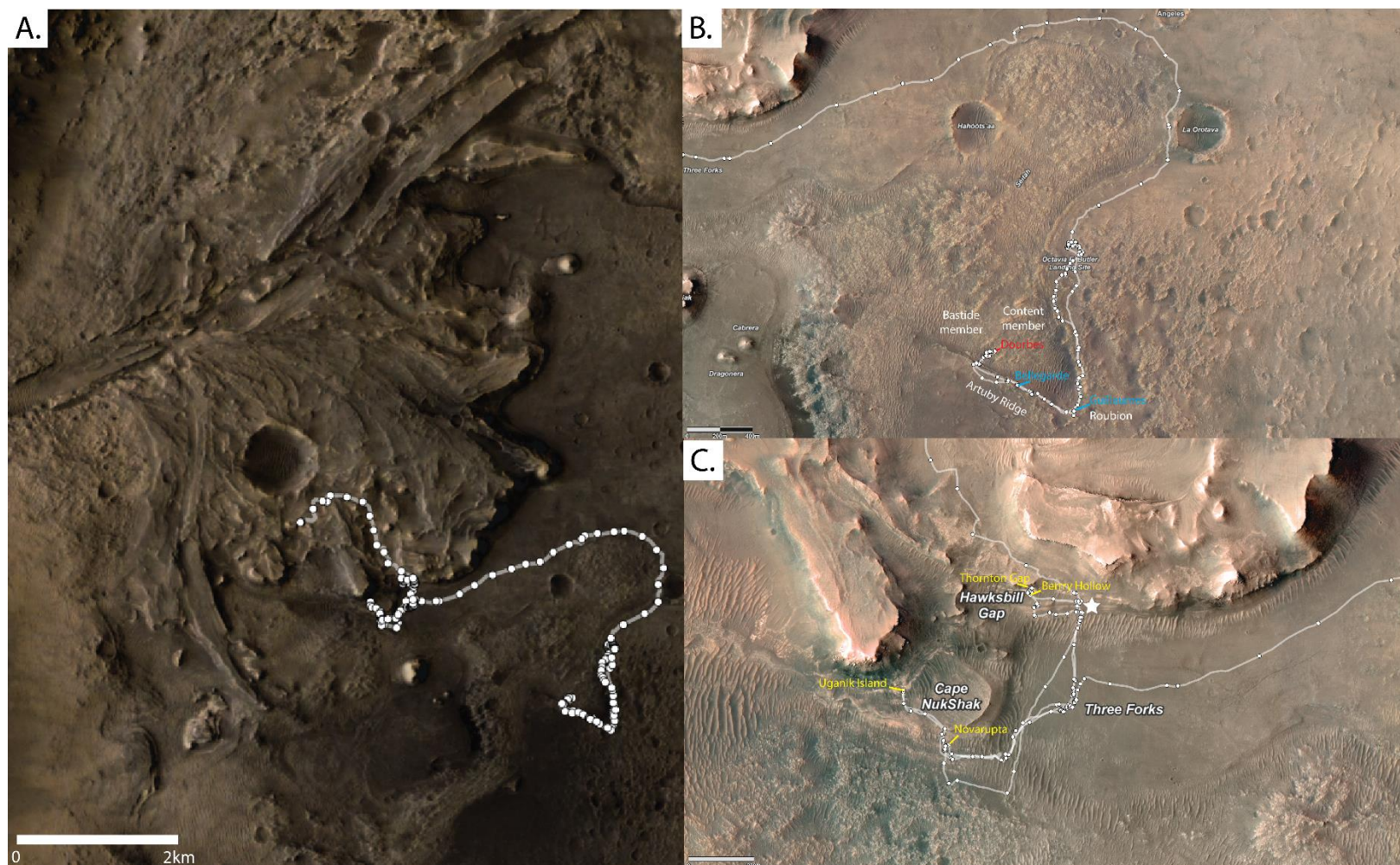


Figure 2-10: (A.) HiRISE image of Jezero crater's western delta. The white line indicates the M2020 Perseverance rover's traverse to date with white circles indicating key observation points. (B.) Inset map displaying the location of Crater Floor campaign. Members and outcrops of the Séítah (red) and Máaz (blue) formations are labeled in white. Abrasion patch names are coloured according to formation. (C.) Inset map displaying the location of outcrops investigated during the Crater Floor campaign. Abrasion target names are displayed in yellow.

Layers within the Bastide Member were predominantly 1-3cm thick, thickening upwards, and reaching up 10 to 40cm structureless layers in some areas (Tice et al., 2022). Layering from Bastide showed no indications of aeolian or fluvial transport (e.g. planar laminations or ripple/dune cross stratification); however, some layer boundaries did display centimeter scale undulations. Layers were densely packed, clast-supported, with homogenous 2 to 3 mm dark grey-green grains/crystals (Farley et al., 2022). Millimetre-sized grain distributions were consistent across multiple outcrops, with no visual grading or sorting at layer boundaries. Abrasion patch observations found these grains were mostly equant in shape (diameters are approximately equal in all directions) with some elongated grains (Farley et al., 2022). The overlying Content member is structureless, and filled with abundant millimeter-to-centimeter sized pits. Observations of Content were limited to small, localized surface exposures, making it difficult to define its origin.

Unlike the Máaz Formation, which was predominantly olivine-free, multispectral Mastcam-Z images and SuperCam IR spectra from samples of the Séítah Formation identified an abundance of olivine minerals. Further observations by LIBS found that these olivine detections were from the 2 to 3mm gray-green grains from Bastide, and had compositions approaching pure olivine (Farley et al., 2022). By averaging LIBS comp from 25 Bastide member rocks, Farley et al. (2022) found that the olivine detections from Séítah extend towards mixtures with augite and plagioclase, and showed minimal compositional overlap with the plagioclase-augite Máaz formation. Further investigating the mineralogy of Séítah, Perseverance produced two abrasion patches in two separate Bastide member outcrops (Dourbes and Quartier; Farley et al., 2022; Y. Liu et al., 2022). These abrasion are dominantly composed of olivine (65 ± 5 vol%), with less abundant augite (~13 vol%), mesostatis (~10%), and secondary materials (~12 vol%; Liu et al., 2022). Olivine and augite grains are seen throughout the Dourbes abrasion patch; however, Liu et al. (2022) observed some augite grains with identical crystal orientations surrounding a single olivine grain. This observation is characteristic of poikilitic textures; a large pyroxene oikocryst surrounds a smaller olivine chadacryst, which is characteristic of an igneous olivine cumulate, and led to Séítah's classification as an olivine cumulate.

The presence of (Fe, Mg)-carbonates, sulfates, and perchlorates in the altered regions of Dourbes indicate that secondary alteration occurred following the deposition of the olivine cumulate material (Tice et al., 2022), however the precise timing between deposition and subsequent olivine alteration, carbonation and sulfate emplacement cannot be constrained. While Mg-Ca- sulfate materials are present in both Séítah and Máaz formations, the lack of evidence for carbonate materials in Máaz suggests that the carbonation process was limited to the Séítah formation. Furthermore, if the carbonate and sulfate materials had formed from the same fluid, there should be an equivalent quantity of Fe-bearing sulfate, or other minerals (e.g. Fe-oxide) in Dourbes. The saline brine that produced the sulfate materials in Máaz and Séítah formations is likely a later fluid that is distinct from the carbonate-forming fluids (Tice et al., 2022).

2.9 Shenandoah Formation

After completing the Crater floor campaign, Perseverance raced towards Three Forks along the southern edge of Jezero crater's western delta, known as the Shenandoah formation. The traverse for the Delta Front campaign started and ended at the Cape Nukshak, and extended northeast to include the Hawksbill Gap outcrop (Figure 10C.). Proximity science and remote observations found Jezero's western delta front indicate it includes a suite of sedimentary rocks consistent with subaqueous deposition by a series of broadly unconfined density currents (Mangold et al., 2021; Williams et al., 2023). Studying the Delta Front lithofacies, Williams et al. (2023) suggest that the prevalent mode of deposition occurred via turbidite-related processes. This depositional process was described as sediment-gravity flows that are mobilized downslope, with subsequent grain deposition as flow energy decreases with distance (Williams et al. 2023).

Perseverance encountered the lowest inferred stratigraphic unit of the Shenandoah formation at its easternmost investigation of Hawksbill Gap. These lower units were very-fine-to-medium sandstones and siltstones. Spectra from both lithologies found Mg/Fe-phyllsilicates and strong crystalline hematite absorption (Dehouck et al. 2023). Traveling west and upsection, Perseverance identified two fine-to-coarse grained sandstones separated by ~3m layering of hydrated sulfate-cemented siltstones. Perseverance produced an abrasion patch, Berry Hollow (Figure 2-10C), in the hydrated sulfate-cemented siltstone unit and Thronton Gap in the overlying

fine-to-coarse grained sandstones during the investigation of Hawksbill Gap. The uppermost member of the Hawksbill Gap outcrop, location of the Thornton Gap abrasion patch, is a thick-bedded pebbly fine-to-medium sandstone with carbonate-cement.

Returning to Cape Nukshak, Perseverance identified interbedded sandstone and inferred siltstone amongst the lowest layers, overlain by ~6m of medium sandstone (Williams et al., 2023). While LIBS and VLT Imager and Spectrometer for mid-Infrared (VISIR) inspections of Cape Nukshak revealed higher concentrations of MgO overall (Beyssac et al. 2023), the upper intervals and Uganik Island abrasion patch contained sulfate-cemented siltstones and sandstones similar to those from Hawksbill Gap. These similar lithologies are thought to be lateral equivalents of the same unit (Williams et al. 2023). A unique lithology was sampled near the base of Cape Nukshak; the Amalik outcrop, source of the Novarupta abrasion patch, which produced VISIR spectral signatures consistent with Mg-rich serpentine (Hurowitz, et al., 2023).

In summary, aqueous alteration was detected in each Jezero formation. The olivine cumulate material from Séítah contained carbonates and smaller abundances of sulfate materials. The Máaz formation is an Fe-rich evolved basalt that is largely free of unaltered olivine, with no detectable carbonates, but comparatively higher sulfate abundances than the underlying Séítah formation. The lack of Fe-bearing sulfates in Séítah suggests that the fluids that produced the carbonate and sulfate materials along the crater floor were distinct from one another. *In situ* science and observations from Perseverance confirmed the orbital detections of detrital igneous materials, carbonates, Fe/Mg-phylosilicates and other hydrated minerals. The same sulfate-cemented sandstone and siltstone were detected at Hawksbill Gap and Cape Nukshak, however each outcrop was found to contain unique lithologies. The uppermost unit of Hawksbill Gap and location of the Thornton Gap abrasion was a carbonate-rich sandstone and granule conglomerate, whereas one of the lowest outcrops from Cape Nukshak contained Mg-rich serpentine. Results from the first two M2020 campaigns highlight the mineral diversity of Isidis Planitia, the surrounding region, and Jezero crater.

2.10 References

- Abilleira, F., Aaron, S., Baker, C., Burkhart, D., Kruizinga, G., Kangas, J., Jesick, M., Lange, R., McCandless, S.-E., Ryne, M., Seubert, J., Wagner, S., & Wong, M. (2019). *Mars 2020 mission design and navigation overview* [Data set]. Root. <https://dataverse.jpl.nasa.gov/dataset.xhtml?persistentId=hdl:2014/45974>
- Allwood, A. C., Wade, L. A., Foote, M. C., Elam, W. T., Hurowitz, J. A., Battel, S., Dawson, D. E., Denise, R. W., Ek, E. M., Gilbert, M. S., King, M. E., Liebe, C. C., Parker, T., Pedersen, D. A. K., Randall, D. P., Sharrow, R. F., Sondheim, M. E., Allen, G., Arnett, K., ... Zimmerman, R. (2020). PIXL: Planetary Instrument for X-Ray Lithochemistry. *Space Science Reviews*, 216(8), 134. <https://doi.org/10.1007/s11214-020-00767-7>
- Anderson, F. S., Levine, J., & Whitaker, T. (2020). Dating a Martian meteorite with 20 Myr precision using a prototype in-situ dating instrument. *Planetary and Space Science*, 191, 105007. <https://doi.org/10.1016/j.pss.2020.105007>
- Bagnold, R. A. (1936). The Movement of Desert Sand. *Proceedings of the Royal Society of London Series A*, 157, 594–620. <https://doi.org/10.1098/rspa.1936.0218>
- Baker, M. M., Newman, C. E., Lapotre, M. G. A., Sullivan, R., Bridges, N. T., & Lewis, K. W. (2018). Coarse Sediment Transport in the Modern Martian Environment. *Journal of Geophysical Research: Planets*, 123(6), 1380–1394. <https://doi.org/10.1002/2017JE005513>
- Baker, V. R. (2002). High-Energy Megafloods: Planetary Settings and Sedimentary Dynamics. In *Flood and Megaflood Processes and Deposits* (pp. 1–15). John Wiley & Sons, Ltd. <https://doi.org/10.1002/9781444304299.ch1>
- Baker, V. R., Maruyama, S., & Dohm, J. M. (2002). *A Theory for the Geological Evolution of Mars and Related Synthesis (GEOMARS)*. 1586.
- Bandfield, J. L., Edwards, C. S., Montgomery, D. R., & Brand, B. D. (2013). The dual nature of the martian crust: Young lavas and old clastic materials. *Icarus*, 222(1), 188–199. <https://doi.org/10.1016/j.icarus.2012.10.023>

- Banham, S. G., Gupta, S., Rubin, D. M., Edgett, K. S., Barnes, R., Van Beek, J., Watkins, J. A., Edgar, L. A., Fedo, C. M., Williams, R. M., Stack, K. M., Grotzinger, J. P., Lewis, K., Ewing, R. C., Day, M., & Vasavada, A. R. (2021). A Rock Record of Complex Aeolian Bedforms in a Hesperian Desert Landscape: The Stimson Formation as Exposed in the Murray Buttes, Gale crater, Mars. *Journal of Geophysical Research: Planets*, 126(4), e2020JE006554. <https://doi.org/10.1029/2020JE006554>
- Banham, S. G., Gupta, S., Rubin, D. M., Watkins, J. A., Sumner, D. Y., Edgett, K. S., Grotzinger, J. P., Lewis, K. W., Edgar, L. A., Stack-Morgan, K. M., Barnes, R., Bell III, J. F., Day, M. D., Ewing, R. C., Lapotre, M. G. A., Stein, N. T., Rivera-Hernandez, F., & Vasavada, A. R. (2018). Ancient Martian aeolian processes and palaeomorphology reconstructed from the Stimson formation on the lower slope of Aeolis Mons, Gale crater, Mars. *Sedimentology*, 65(4), 993–1042. <https://doi.org/10.1111/sed.12469>
- Belessiotis, V., Kalogirou, S., & Delyannis, E. (2016). Chapter Three—Solar Distillation—Solar Stills. In V. Belessiotis, S. Kalogirou, & E. Delyannis (Eds.), *Thermal Solar Desalination* (pp. 103–190). Academic Press. <https://doi.org/10.1016/B978-0-12-809656-7.00003-9>
- Bell, J. F., Maki, J. N., Mehall, G. L., Ravine, M. A., Caplinger, M. A., Bailey, Z. J., Brylow, S., Schaffner, J. A., Kinch, K. M., Madsen, M. B., Winhold, A., Hayes, A. G., Corlies, P., Tate, C., Barrington, M., Cisneros, E., Jensen, E., Paris, K., Crawford, K., ... Wolff, M. J. (2021). The Mars 2020 Perseverance Rover Mast Camera Zoom (Mastcam-Z) Multispectral, Stereoscopic Imaging Investigation. *Space Science Reviews*, 217(1), 24. <https://doi.org/10.1007/s11214-020-00755-x>
- Berger, J. A., Schmidt, M. E., Gellert, R., Campbell, J. L., King, P. L., Flemming, R. L., Ming, D. W., Clark, B. C., Pradler, I., VanBommel, S. J. V., Minitti, M. E., Fairén, A. G., Boyd, N. I., Thompson, L. M., Perrett, G. M., Elliott, B. E., & Desouza, E. (2016). A global Mars dust composition refined by the Alpha-Particle X-ray Spectrometer in Gale crater. *Geophysical Research Letters*, 43(1), 67–75. <https://doi.org/10.1002/2015GL066675>
- Bertelsen, P., Goetz, W., Madsen, M. B., Kinch, K. M., Hviid, S. F., Knudsen, J. M., Gunnlaugsson, H. P., Merrison, J., Nørnberg, P., Squyres, S. W., Bell, J. F., Herkenhoff, K. E., Gorevan, S.,

- Yen, A. S., Myrick, T., Klingelhöfer, G., Rieder, R., & Gellert, R. (2004). Magnetic Properties Experiments on the Mars Exploration Rover Spirit at Gusev Crater. *Science*, 305(5685), 827–829. <https://doi.org/10.1126/science.1100112>
- Bibring, J.-P., Langevin, Y., Mustard, J. F., Poulet, F., Arvidson, R., Gendrin, A., Gondet, B., Mangold, N., Pinet, P., Forget, F., Berthé, M., Bibring, J.-P., Gendrin, A., Gomez, C., Gondet, B., Jouglet, D., Poulet, F., Soufflot, A., Vincendon, M., ... Neukum, G. (2006). Global Mineralogical and Aqueous Mars History Derived from OMEGA/Mars Express Data. *Science*, 312(5772), 400–404. <https://doi.org/10.1126/science.1122659>
- Boeder, P. A., & Soares, C. E. (2020). Mars 2020: Mission, science objectives and build. *Systems Contamination: Prediction, Control, and Performance 2020*, 11489, 1148903. <https://doi.org/10.1117/12.2569650>
- Borg, L., & Drake, M. J. (2005). A review of meteorite evidence for the timing of magmatism and of surface or near-surface liquid water on Mars. *Journal of Geophysical Research: Planets*, 110(E12). <https://doi.org/10.1029/2005JE002402>
- Bouwman, A. F. (1990). *Soils and the greenhouse effect*. <https://www.osti.gov/biblio/6704123>
- Bradley, B. A., Sakimoto, S. E. H., Frey, H., & Zimbelman, J. R. (2002). Medusae Fossae Formation: New perspectives from Mars Global Surveyor. *Journal of Geophysical Research: Planets*, 107(E8), 2-1-2–17. <https://doi.org/10.1029/2001JE001537>
- Bridges, J. C., Hicks, L. J., & Treiman, A. H. (2019). Chapter 5—Carbonates on Mars. In J. Filiberto & S. P. Schwenzer (Eds.), *Volatiles in the Martian Crust* (pp. 89–118). Elsevier. <https://doi.org/10.1016/B978-0-12-804191-8.00005-2>
- Brown, A. J., Hook, S. J., Baldridge, A. M., Crowley, J. K., Bridges, N. T., Thomson, B. J., Marion, G. M., de Souza Filho, C. R., & Bishop, J. L. (2010). Hydrothermal formation of Clay-Carbonate alteration assemblages in the Nili Fossae region of Mars. *Earth and Planetary Science Letters*, 297(1), 174–182. <https://doi.org/10.1016/j.epsl.2010.06.018>

- Brown, A. J., Viviano, C. E., & Goudge, T. A. (2020). Olivine-Carbonate Mineralogy of the Jezero crater Region. *Journal of Geophysical Research: Planets*, 125(3), e2019JE006011. <https://doi.org/10.1029/2019JE006011>
- Burk, S. D. (1976). Diurnal Winds Near the Martian Polar Caps. *Journal of the Atmospheric Sciences*, 33(6), 923–939. [https://doi.org/10.1175/1520-0469\(1976\)033<0923:DWNTMP>2.0.CO;2](https://doi.org/10.1175/1520-0469(1976)033<0923:DWNTMP>2.0.CO;2)
- Cabrol, N. A., Grin, E. A., Newsom, H. E., Landheim, R., & McKay, C. P. (1999). Hydrogeologic Evolution of Gale crater and Its Relevance to the Exobiological Exploration of Mars. *Icarus*, 139(2), 235–245. <https://doi.org/10.1006/icar.1999.6099>
- Carr, M. H. (2007). *The Surface of Mars*. Cambridge University Press.
- Carr, M. H., & Head, J. W. (2010). Geologic history of Mars. *Earth and Planetary Science Letters*, 294(3), 185–203. <https://doi.org/10.1016/j.epsl.2009.06.042>
- Comparing the atmospheres of Mars and Earth.* (n.d.). https://www.esa.int/ESA_Multimedia/Images/2018/04/Comparing_the_atmospheres_of_Mars_and_Earth#.Y3O9FQ6U5a0.link
- Conrath, B. J. (1975). Thermal structure of the Martian atmosphere during the dissipation of the dust storm of 1971. *Icarus*, 24(1), 36–46. [https://doi.org/10.1016/0019-1035\(75\)90156-6](https://doi.org/10.1016/0019-1035(75)90156-6)
- Crumpler, L. S., & Aubele, J. C. (1978). Structural evolution of Arsia Mons, Pavonis Mons, and Ascreus Mons: Tharsis region of Mars. *Icarus*, 34(3), 496–511. [https://doi.org/10.1016/0019-1035\(78\)90041-6](https://doi.org/10.1016/0019-1035(78)90041-6)
- Deit, L. L., Hauber, E., Fueten, F., Pondrelli, M., Rossi, A. P., & Jaumann, R. (2013). Sequence of infilling events in Gale crater, Mars: Results from morphology, stratigraphy, and mineralogy. *Journal of Geophysical Research: Planets*, 118(12), 2439–2473. <https://doi.org/10.1002/2012JE004322>
- Derbyshire, E., Meng, X., & Kemp, R. (1998). Provenance, transport and characteristics of modern aeolian dust in western Gansu Province, China, and interpretation of the Quaternary loess

record. *Journal of Arid Environments* - *J ARID ENVIRON*, 39, 497–516.
<https://doi.org/10.1006/jare.1997.0369>

Earth's atmosphere. (n.d.).
https://www.cs.mcgill.ca/~rwest/wikispeedia/wpcd/wp/e/Earth%2527s_atmosphere.htm

Edgar, L. A., Fedo, C. M., Gupta, S., Banham, S. G., Fraeman, A. A., Grotzinger, J. P., Stack, K. M., Stein, N. T., Bennett, K. A., Rivera-Hernández, F., Sun, V. Z., Edgett, K. S., Rubin, D. M., House, C., & Beek, J. V. (2020). A Lacustrine Paleoenvironment Recorded at Vera RubinRidge, Gale crater: Overview of the Sedimentology and Stratigraphy Observed by the Mars ScienceLaboratory Curiosity Rover. *Journal of Geophysical Research: Planets*, 125(3), e2019JE006307. <https://doi.org/10.1029/2019JE006307>

Ehlmann, B. L., & Edwards, C. S. (2014). Mineralogy of the Martian Surface. *Annual Review of Earth and Planetary Sciences*, 42(1), 291–315. <https://doi.org/10.1146/annurev-earth-060313-055024>

Farley, K. A., Malespin, C., Mahaffy, P., Grotzinger, J. P., Vasconcelos, P. M., Milliken, R. E., Malin, M., Edgett, K. S., Pavlov, A. A., Hurowitz, J. A., Grant, J. A., Miller, H. B., Arvidson, R., Beegle, L., Calef, F., Conrad, P. G., Dietrich, W. E., Eigenbrode, J., Gellert, R., ... Moores, J. E. (2014). In Situ Radiometric and Exposure Age Dating of the Martian Surface. *Science*, 343(6169), 1247166. <https://doi.org/10.1126/science.1247166>

Farley, K. A., Stack, K. M., Shuster, D. L., Horgan, B. H. N., Hurowitz, J. A., Tarnas, J. D., Simon, J. I., Sun, V. Z., Scheller, E. L., Moore, K. R., McLennan, S. M., Vasconcelos, P. M., Wiens, R. C., Treiman, A. H., Mayhew, L. E., Beyssac, O., Kizovski, T. V., Tosca, N. J., Williford, K. H., ... Zorzano, M.-P. (2022). Aqueously altered igneous rocks sampled on the floor of Jezero crater, Mars. *Science*, 377(6614), eabo2196. <https://doi.org/10.1126/science.abo2196>

Fassett, C. I., & Head III, J. W. (2005). Fluvial sedimentary deposits on Mars: Ancient deltas in a crater lake in the Nili Fossae region. *Geophysical Research Letters*, 32(14). <https://doi.org/10.1029/2005GL023456>

- Fassett, C. I., & Head, J. W. (2007). Valley formation on martian volcanoes in the Hesperian: Evidence for melting of summit snowpack, caldera lake formation, drainage and erosion on Ceraunius Tholus. *Icarus*, 189(1), 118–135. <https://doi.org/10.1016/j.icarus.2006.12.021>
- Fassett, C. I., & Head, J. W. (2008). Valley network-fed, open-basin lakes on Mars: Distribution and implications for Noachian surface and subsurface hydrology. *Icarus*, 198(1), 37–56. <https://doi.org/10.1016/j.icarus.2008.06.016>
- Fedo, C. M., Bryk, A. B., Edgar, L. A., Bennett, K. A., Fox, V. K., Dietrich, W. E., Banham, S. G., Gupta, S., Stack, K. M., Williams, R. M. E., Grotzinger, J. P., Stein, N. T., Rubin, D. M., Caravaca, G., Arvidson, R. E., Hughes, M. N., Fraeman, A. A., Vasavada, A. R., Schieber, J., & Sutter, B. (2022). Geology and Stratigraphic Correlation of the Murray and Carolyn Shoemaker Formations Across the Glen Torridon Region, Gale crater, Mars. *Journal of Geophysical Research: Planets*, 127(9), e2022JE007408. <https://doi.org/10.1029/2022JE007408>
- Filiberto, J., Baratoux, D., Beaty, D., Breuer, D., Farcy, B. J., Grott, M., Jones, J. H., Kiefer, W. S., Mane, P., McCubbin, F. M., & Schwenzer, S. P. (2016). A review of volatiles in the Martian interior. *Meteoritics & Planetary Science*, 51(11), 1935–1958. <https://doi.org/10.1111/maps.12680>
- Finn, J. E., McKay, C. P., & Sridhar, K. R. (1996). Martian Atmosphere Utilization by Temperature-Swing Adsorption. *SAE Transactions*, 105, 1063–1067.
- Foley, C. N., Economou, T., & Clayton, R. N. (2003). Final chemical results from the Mars Pathfinder alpha proton X-ray spectrometer. *Journal of Geophysical Research: Planets*, 108(E12). <https://doi.org/10.1029/2002JE002019>
- Fraeman, A. A., Edgar, L. A., Rampe, E. B., Thompson, L. M., Frydenvang, J., Fedo, C. M., Catalano, J. G., Dietrich, W. E., Gabriel, T. S. J., Vasavada, A. R., Grotzinger, J. P., L’Haridon, J., Mangold, N., Sun, V. Z., House, C. H., Bryk, A. B., Hardgrove, C., Czarnecki, S., Stack, K. M., ... Wong, G. M. (2020). Evidence for a Diagenetic Origin of Vera Rubin Ridge, Gale crater,

- Mars: Summary and Synthesis of Curiosity's Exploration Campaign. *Journal of Geophysical Research: Planets*, 125(12), e2020JE006527. <https://doi.org/10.1029/2020JE006527>
- Garvin, J. B., Sakimoto, S. E. H., Frawley, J. J., & Schnetzler, C. (2000). North Polar Region Craterforms on Mars: Geometric Characteristics from the Mars Orbiter Laser Altimeter. *Icarus*, 144(2), 329–352. <https://doi.org/10.1006/icar.1999.6298>
- Goetz, W., Bertelsen, P., Binau, C. S., Gunnlaugsson, H. P., Hviid, S. F., Kinch, K. M., Madsen, D. E., Madsen, M. B., Olsen, M., Gellert, R., Klingelhöfer, G., Ming, D. W., Morris, R. V., Rieder, R., Rodionov, D. S., de Souza, P. A., Schröder, C., Squyres, S. W., Wdowiak, T., & Yen, A. (2005). Indication of drier periods on Mars from the chemistry and mineralogy of atmospheric dust. *Nature*, 436(7047), Article 7047. <https://doi.org/10.1038/nature03807>
- Golombek, M. P., Grant, J. A., Crumpler, L. S., Greeley, R., Arvidson, R. E., Bell III, J. F., Weitz, C. M., Sullivan, R., Christensen, P. R., Soderblom, L. A., & Squyres, S. W. (2006). Erosion rates at the Mars Exploration Rover landing sites and long-term climate change on Mars. *Journal of Geophysical Research: Planets*, 111(E12). <https://doi.org/10.1029/2006JE002754>
- Gómez-Elvira, J., Armiens, C., Castañer, L., Domínguez, M., Genzer, M., Gómez, F., Haberle, R., Harri, A.-M., Jiménez, V., Kahanpää, H., Kowalski, L., Lepinette, A., Martín, J., Martínez-Frías, J., McEwan, I., Mora, L., Moreno, J., Navarro, S., de Pablo, M. A., ... Martín-Torres, J. (2012). REMS: The Environmental Sensor Suite for the Mars Science Laboratory Rover. *Space Science Reviews*, 170(1), 583–640. <https://doi.org/10.1007/s11214-012-9921-1>
- Greeley, R., & Guest, J. E. (1987). Geologic map of the eastern equatorial region of Mars. In *IMAP* (No. 1802-B). U.S. Geological Survey. <https://doi.org/10.3133/i1802B>
- Greeley, R., Leach, R., White, B., Iversen, J., & Pollack, J. (1980). Threshold windspeeds for sand on Mars: Wind tunnel simulations. *Geophysical Research Letters*, 7(2), 121–124. <https://doi.org/10.1029/GL007i002p00121>
- Grotzinger, J. P., Arvidson, R. E., Bell, J. F., Calvin, W., Clark, B. C., Fike, D. A., Golombek, M., Greeley, R., Haldemann, A., Herkenhoff, K. E., Jolliff, B. L., Knoll, A. H., Malin, M.,

- McLennan, S. M., Parker, T., Soderblom, L., Sohl-Dickstein, J. N., Squyres, S. W., Tosca, N. J., & Watters, W. A. (2005). Stratigraphy and sedimentology of a dry to wet eolian depositional system, Burns formation, Meridiani Planum, Mars. *Earth and Planetary Science Letters*, 240(1), 11–72. <https://doi.org/10.1016/j.epsl.2005.09.039>
- Grotzinger, J. P., Crisp, J., Vasavada, A. R., Anderson, R. C., Baker, C. J., Barry, R., Blake, D. F., Conrad, P., Edgett, K. S., Ferdowski, B., Gellert, R., Gilbert, J. B., Golombek, M., Gómez-Elvira, J., Hassler, D. M., Jandura, L., Litvak, M., Mahaffy, P., Maki, J., ... Wiens, R. C. (2012). Mars Science Laboratory Mission and Science Investigation. *Space Science Reviews*, 170(1), 5–56. <https://doi.org/10.1007/s11214-012-9892-2>
- Grotzinger, J. P., Gupta, S., Malin, M. C., Rubin, D. M., Schieber, J., Siebach, K., Sumner, D. Y., Stack, K. M., Vasavada, A. R., Arvidson, R. E., Calef, F., Edgar, L., Fischer, W. F., Grant, J. A., Griffes, J., Kah, L. C., Lamb, M. P., Lewis, K. W., Mangold, N., ... Wilson, S. A. (2015). Deposition, exhumation, and paleoclimate of an ancient lake deposit, Gale crater, Mars. *Science*, 350(6257), aac7575. <https://doi.org/10.1126/science.aac7575>
- Guzewich, S. D., Smith, M. D., & Wolff, M. J. (2014). The vertical distribution of Martian aerosol particle size. *Journal of Geophysical Research: Planets*, 119(12), 2694–2708. <https://doi.org/10.1002/2014JE004704>
- Guzewich, S. D., Wilson, R. J., McConnochie, T. H., Toigo, A. D., Banfield, D. J., & Smith, M. D. (2014). Thermal tides during the 2001 Martian global-scale dust storm. *Journal of Geophysical Research: Planets*, 119(3), 506–519. <https://doi.org/10.1002/2013JE004502>
- Haberle, R. M., Clancy, R. T., Forget, F., Smith, M. D., & Zurek, R. W. (2017). *The Atmosphere and Climate of Mars*. Cambridge University Press.
- Haberle, R. M., Leovy, C. B., & Pollack, J. B. (1979). A numerical model of the Martian polar cap winds. *Icarus*, 39(2), 151–183. [https://doi.org/10.1016/0019-1035\(79\)90161-1](https://doi.org/10.1016/0019-1035(79)90161-1)
- Haberle, R. M., Leovy, C. B., & Pollack, J. B. (1982). Some effects of global dust storms on the atmospheric circulation of Mars. *Icarus*, 50(2), 322–367. [https://doi.org/10.1016/0019-1035\(82\)90129-4](https://doi.org/10.1016/0019-1035(82)90129-4)

- Hamilton, V. E., McSween Jr., H. Y., & Hapke, B. (2005). Mineralogy of Martian atmospheric dust inferred from thermal infrared spectra of aerosols. *Journal of Geophysical Research: Planets*, 110(E12). <https://doi.org/10.1029/2005JE002501>
- Holm-Alwmark, S., Kinch, K. M., Hansen, M. D., Shahrzad, S., Svennevig, K., Abbey, W. J., Anderson, R. B., Calef III, F. J., Gupta, S., Hauber, E., Horgan, B. H. N., Kah, L. C., Knade, J., Miklusick, N. B., Stack, K. M., Sun, V. Z., Tarnas, J. D., & Quantin-Nataf, C. (2021). Stratigraphic Relationships in Jezero crater, Mars: Constraints on the Timing of Fluvial-Lacustrine Activity From Orbital Observations. *Journal of Geophysical Research: Planets*, 126(7), e2021JE006840. <https://doi.org/10.1029/2021JE006840>
- Hurotz, J., Tice, M. M., Allwood, A. C., Cable, M., Bosak, T., Broz, T., . . . Yanchilina, A. (2023). The petrogenetic history of the Jezero crater delta from from microscopical observations by the Mars2020 PIXL instrument. *54th Lunar and Planetary Science Conference 2023 (LPI Contrib. No. 2806)*. The Woodlands, Texas.
- Ives, L. R. W., Stack-Morgan, K. M., Gupta, S., Caravaca, G., Russell, P., Shuster, D. L., Williams, A. J., Holm-Alwmark, S., Barnes, R., Bell, J. F., Beyssac, O., Brown, A., Flannery, D., Frydenvang, J., Grotzinger, J., Lamb, M. P., Horgan, B., Hurowitz, J. A., Kalucha, H., ... Annex, A. M. (2023, July 2). *Physical Sedimentology and Stratigraphy of the lower Western Fan (Shenandoah formation) Jezero crater, Mars*: International Conference on Fluvial Sedimentology 2023. <https://hal.science/hal-04052730>
- Johnson, W., Withrow-Maser, S., Young, L., Malpica, C., Koning, W. J. F., Kuang, W., Fehler, M., Tuano, A., Chan, A., Datta, A., Chi, C., Lumba, R., Escobar, D., Balaram, J., Tzanetos, T., & Grip, H. F. (2020). *Mars Science Helicopter Conceptual Design* (ARC-E-DAA-TN78199). <https://ntrs.nasa.gov/citations/20200002139>
- Kah, L. C., Stack, K. M., Eigenbrode, J. L., Yingst, R. A., & Edgett, K. S. (2018). Syndepositional precipitation of calcium sulfate in Gale crater, Mars. *Terra Nova*, 30(6), 431–439. <https://doi.org/10.1111/ter.12359>

- Kasting, J. F. (1991). CO₂ condensation and the climate of early Mars. *Icarus*, 94(1), 1–13. [https://doi.org/10.1016/0019-1035\(91\)90137-I](https://doi.org/10.1016/0019-1035(91)90137-I)
- Kerber, L., & Head, J. W. (2010). The age of the Medusae Fossae Formation: Evidence of Hesperian emplacement from crater morphology, stratigraphy, and ancient lava contacts. *Icarus*, 206(2), 669–684. <https://doi.org/10.1016/j.icarus.2009.10.001>
- Khavrus, V., & Shelevytsky, I. (2012). Geometry and the physics of seasons. *Physics Education*, 47(6), 680. <https://doi.org/10.1088/0031-9120/47/6/680>
- Leovy, C. (2001). Weather and climate on Mars. *Nature*, 412(6843), Article 6843. <https://doi.org/10.1038/35084192>
- Leovy, C. E., Zurek, R. W., & Pollack, J. B. (1973). Mechanisms for Mars Dust Storms. *Journal of the Atmospheric Sciences*, 30(5), 749–762. [https://doi.org/10.1175/1520-0469\(1973\)030<0749:MFMDS>2.0.CO;2](https://doi.org/10.1175/1520-0469(1973)030<0749:MFMDS>2.0.CO;2)
- Liu, J., Richardson, M. I., & Wilson, R. J. (2003). An assessment of the global, seasonal, and interannual spacecraft record of Martian climate in the thermal infrared. *Journal of Geophysical Research: Planets*, 108(E8). <https://doi.org/10.1029/2002JE001921>
- Liu, Y., Tice, M. M., Schmidt, M. E., Treiman, A. H., Kizovski, T. V., Hurowitz, J. A., Allwood, A. C., Henneke, J., Pedersen, D. A. K., VanBommel, S. J., Jones, M. W. M., Knight, A. L., Orenstein, B. J., Clark, B. C., Elam, W. T., Heirwegh, C. M., Barber, T., Beegle, L. W., Benzerara, K., ... Zorzano, M.-P. (2022). An olivine cumulate outcrop on the floor of Jezero crater, Mars. *Science*, 377(6614), 1513–1519. <https://doi.org/10.1126/science.abo2756>
- Madsen, M. B., Bertelsen, P., Goetz, W., Binau, C. S., Olsen, M., Folkmann, F., Gunnlaugsson, H. P., Kinch, K. M., Knudsen, J. M., Merrison, J., Nørnberg, P., Squyres, S. W., Yen, A. S., Rademacher, J. D., Gorevan, S., Myrick, T., & Bartlett, P. (2003). Magnetic Properties Experiments on the Mars Exploration Rover mission. *Journal of Geophysical Research: Planets*, 108(E12). <https://doi.org/10.1029/2002JE002029>

- Magalhães, J. A., & Young, R. E. (1995). Downslope Windstorms in the Lee of Ridges on Mars. *Icarus*, 113(2), 277–294. <https://doi.org/10.1006/icar.1995.1124>
- Malin, M. C. (1979). *Mars: Evidence of indurated deposits of fine materials*. 2072, 54.
- Mandon, L., Quantin-Nataf, C., Thollot, P., Mangold, N., Lozac'h, L., Dromart, G., Beck, P., Dehouck, E., Breton, S., Millot, C., & Volat, M. (2020). Refining the age, emplacement and alteration scenarios of the olivine-rich unit in the Nili Fossae region, Mars. *Icarus*, 336, 113436. <https://doi.org/10.1016/j.icarus.2019.113436>
- Mangold, N., Gupta, S., Gasnault, O., Dromart, G., Tarnas, J. D., Sholes, S. F., Horgan, B., Quantin-Nataf, C., Brown, A. J., Le Mouélic, S., Yingst, R. A., Bell, J. F., Beyssac, O., Bosak, T., Calef, F., Ehlmann, B. L., Farley, K. A., Grotzinger, J. P., Hickman-Lewis, K., ... Williford, K. H. (2021). Perseverance rover reveals an ancient delta-lake system and flood deposits at Jezero crater, Mars. *Science*, 374(6568), 711–717. <https://doi.org/10.1126/science.abl4051>
- Milliken, R. E., Grotzinger, J. P., & Thomson, B. J. (2010). Paleoclimate of Mars as captured by the stratigraphic record in Gale crater. *Geophysical Research Letters*, 37(4). <https://doi.org/10.1029/2009GL041870>
- Moeller, R. C., Jandura, L., Rosette, K., Robinson, M., Samuels, J., Silverman, M., Brown, K., Duffy, E., Yazzie, A., Jens, E., Brockie, I., White, L., Goreva, Y., Zorn, T., Okon, A., Lin, J., Frost, M., Collins, C., Williams, J. B., ... Biesiadecki, J. (2020). The Sampling and Caching Subsystem (SCS) for the Scientific Exploration of Jezero crater by the Mars 2020 Perseverance Rover. *Space Science Reviews*, 217(1), 5. <https://doi.org/10.1007/s11214-020-00783-7>
- Mustard, J. F., Poulet, F., Head, J. W., Mangold, N., Bibring, J.-P., Pelkey, S. M., Fassett, C. I., Langevin, Y., & Neukum, G. (2007). Mineralogy of the Nili Fossae region with OMEGA/Mars Express data: 1. Ancient impact melt in the Isidis Basin and implications for the transition from the Noachian to Hesperian. *Journal of Geophysical Research: Planets*, 112(E8). <https://doi.org/10.1029/2006JE002834>

- Newman, C. E., Gómez-Elvira, J., Marin, M., Navarro, S., Torres, J., Richardson, M. I., Battalio, J. M., Guzewich, S. D., Sullivan, R., Torre, M. de la, Vasavada, A. R., & Bridges, N. T. (2017). Winds measured by the Rover Environmental Monitoring Station (REMS) during the Mars Science Laboratory (MSL) rover's Bagnold Dunes Campaign and comparison with numerical modeling using MarsWRF. *Icarus*, 291, 203–231. <https://doi.org/10.1016/j.icarus.2016.12.016>
- Newman, C. E., Hueso, R., Lemmon, M. T., Munguira, A., Vicente-Retortillo, Á., Apestigue, V., Martínez, G. M., Toledo, D., Sullivan, R., Herkenhoff, K. E., de la Torre Juárez, M., Richardson, M. I., Stott, A. E., Murdoch, N., Sanchez-Lavega, A., Wolff, M. J., Arruego, I., Sebastián, E., Navarro, S., ... Guzewich, S. D. (2022). The dynamic atmospheric and aeolian environment of Jezero crater, Mars. *Science Advances*, 8(21). <https://doi.org/10.1126/sciadv.abn3783>
- Nickling, W. G., & Neuman, C. M. (n.d.). Aeolian Sediment Transport. In *Geomorphology of Desert Environments*. https://doi.org/10.1007/978-1-4020-5719-9_17
- Ojha, L., & Lewis, K. (2018). The Density of the Medusae Fossae Formation: Implications for its Composition, Origin, and Importance in Martian History. *Journal of Geophysical Research: Planets*, 123(6), 1368–1379. <https://doi.org/10.1029/2018JE005565>
- Ojha, L., Lewis, K., Karunatillake, S., & Schmidt, M. (2018). The Medusae Fossae Formation as the single largest source of dust on Mars. *Nature Communications*, 9(1), Article 1. <https://doi.org/10.1038/s41467-018-05291-5>
- Owen, T., Biemann, K., Rushneck, D. R., Biller, J. E., Howarth, D. W., & Lafleur, A. L. (1977). The composition of the atmosphere at the surface of Mars. *Journal of Geophysical Research (1896-1977)*, 82(28), 4635–4639. <https://doi.org/10.1029/JS082i028p04635>
- Parker, T. J., Stephen Saunders, R., & Schneeberger, D. M. (1989). Transitional morphology in West Deuteronilus Mensae, Mars: Implications for modification of the lowland/upland boundary. *Icarus*, 82(1), 111–145. [https://doi.org/10.1016/0019-1035\(89\)90027-4](https://doi.org/10.1016/0019-1035(89)90027-4)

- Pelkey, S. M., Jakosky, B. M., & Christensen, P. R. (2004). Surficial properties in Gale crater, Mars, from Mars Odyssey THEMIS data. *Icarus*, 167(2), 244–270. <https://doi.org/10.1016/j.icarus.2003.09.013>
- Phillips, R. J., Zuber, M. T., Solomon, S. C., Golombek, M. P., Jakosky, B. M., Banerdt, W. B., Smith, D. E., Williams, R. M. E., Hynek, B. M., Aharonson, O., & Hauck II, S. A. (2001). Ancient Geodynamics and Global-Scale Hydrology on Mars. *Science*, 291(5513), 2587–2591. <https://doi.org/10.1126/science.1058701>
- Platz, T., Michael, G., Tanaka, K. L., Skinner, J. A., & Fortezzo, C. M. (2013). Crater-based dating of geological units on Mars: Methods and application for the new global geological map. *Icarus*, 225(1), 806–827. <https://doi.org/10.1016/j.icarus.2013.04.021>
- Reedy, R. C., Arnold, J. R., & Lal, D. (1983). Cosmic-Ray Record in Solar System Matter. *Annual Review of Nuclear and Particle Science*, 33(1), 505–538. <https://doi.org/10.1146/annurev.ns.33.120183.002445>
- Schwenzer, S. P., Abramov, O., Allen, C. C., Bridges, J. C., Clifford, S. M., Filiberto, J., Kring, D. A., Lasue, J., McGovern, P. J., Newsom, H. E., Treiman, A. H., Vaniman, D. T., Wiens, R. C., & Wittmann, A. (2012). Gale crater: Formation and post-impact hydrous environments. *Planetary and Space Science*, 70(1), 84–95. <https://doi.org/10.1016/j.pss.2012.05.014>
- Scott, D. H., & Tanaka, K. L. (1986). Geologic map of the western equatorial region of Mars. *IMAP*, Article 1802-A. <https://doi.org/10.3133/i1802A>
- Segura, T. L., Toon, O. B., Colaprete, A., & Zahnle, K. (2002). Environmental Effects of Large Impacts on Mars. *Science*, 298(5600), 1977–1980. <https://doi.org/10.1126/science.1073586>
- Siili, T., Haberle, R. M., & Murphy, J. R. (1997). Sensitivity of Martian Southern polar cap edge winds and surface stresses to dust optical thickness and to the large-scale sublimation flow. *Advances in Space Research*, 19(8), 1241–1244. [https://doi.org/10.1016/S0273-1177\(97\)00276-7](https://doi.org/10.1016/S0273-1177(97)00276-7)

- Smalley, I. J., & Krinsley, D. H. (1978). Loess deposits associated with deserts. *CATENA*, 5(1), 53–66. [https://doi.org/10.1016/S0341-8162\(78\)80006-X](https://doi.org/10.1016/S0341-8162(78)80006-X)
- Smith, M. D. (2004). Interannual variability in TES atmospheric observations of Mars during 1999–2003. *Icarus*, 167(1), 148–165. <https://doi.org/10.1016/j.icarus.2003.09.010>
- Smith, M. D. (2008). Spacecraft Observations of the Martian Atmosphere *. *Annual Review of Earth and Planetary Sciences*, 36, 191–219. <https://doi.org/10.1146/annurev.earth.36.031207.124334>
- Smith, P. H., & Lemmon, M. (1999). Opacity of the Martian atmosphere measured by the Imager for Mars Pathfinder. *Journal of Geophysical Research: Planets*, 104(E4), 8975–8985. <https://doi.org/10.1029/1998JE900017>
- Stern, J. C., Sutter, B., Archer, P. D., Eigenbrode, J. L., McAdam, A. C., Franz, H. B., Knudson, C., Ming, D. W., Wong, G., Freissinet, C., Malespin, C. A., Navarro-Gonzalez, R., Szopa, C., & Mahaffy, P. R. (2018). Major Volatiles Evolved From Eolian Materials in Gale crater. *Geophysical Research Letters*, 45(19), 10,240–10,248. <https://doi.org/10.1029/2018GL079059>
- Sullivan, R., & Kok, J. F. (2017). Aeolian saltation on Mars at low wind speeds. *Journal of Geophysical Research: Planets*, 122(10), 2111–2143. <https://doi.org/10.1002/2017JE005275>
- Sun, V. Z., Hand, K. P., Stack, K. M., Farley, K. A., Milkovich, S., Kronyak, R., Simon, J. I., Hickman-Lewis, K., Shuster, D., J F Bell, I. I. I., Gupta, S., Herd, C. D. K., Maurice, S., Paar, G., & Wiens, R. C. (n.d.). *Exploring the Jezero crater Floor: Overview of Results from the Mars 2020 Perseverance Rover's First Science Campaign*. 53rd Lunar and Planetary Science Conference, The Woodlands, TX. Retrieved March 28, 2023, from <https://ntrs.nasa.gov/citations/20220000501>
- Tanaka, K. L. (2000). Dust and Ice Deposition in the Martian Geologic Record. *Icarus*, 144(2), 254–266. <https://doi.org/10.1006/icar.1999.6297>

- Thomson, B. J., Bridges, N. T., Milliken, R., Baldrige, A., Hook, S. J., Crowley, J. K., Marion, G. M., de Souza Filho, C. R., Brown, A. J., & Weitz, C. M. (2011). Constraints on the origin and evolution of the layered mound in Gale crater, Mars using Mars Reconnaissance Orbiter data. *Icarus*, 214(2), 413–432. <https://doi.org/10.1016/j.icarus.2011.05.002>
- Thomson, B. J., Bridges, N. T., Milliken, R. E., Bell, J. F., Calvin, W. M., & Weitz, C. M. (2008). *New Constraints on the Origin and Evolution of the Layered Deposits in Gale crater, Mars*. 1456.
- Thomson, B. J., Bridges, N. T., Milliken, R., Hook, S., Baldrige, A., Crowley, J., & Marion, G. (2008). *Signs of aqueous activity in Gale crater, Mars as viewed by Mars Reconnaissance Orbiter. 2008*, P41B-1365.
- Tice, M. M., Hurowitz, J. A., Allwood, A. C., Jones, M. W. M., Orenstein, B. J., Davidoff, S., Wright, A. P., Pedersen, D. A. K., Henneke, J., Tosca, N. J., Moore, K. R., Clark, B. C., McLennan, S. M., Flannery, D. T., Steele, A., Brown, A. J., Zorzano, M.-P., Hickman-Lewis, K., Liu, Y., ... THE PIXL TEAM. (2022). Alteration history of Séítah formation rocks inferred by PIXL x-ray fluorescence, x-ray diffraction, and multispectral imaging on Mars. *Science Advances*, 8(47), eabp9084. <https://doi.org/10.1126/sciadv.abp9084>
- Toigo, A. D., Richardson, M. I., Wilson, R. J., Wang, H., & Ingersoll, A. P. (2002). A first look at dust lifting and dust storms near the south pole of Mars with a mesoscale model. *Journal of Geophysical Research: Planets*, 107(E7), 4-1-4–13. <https://doi.org/10.1029/2001JE001592>
- Udry, A., & Day, J. M. D. (2018). 1.34 billion-year-old magmatism on Mars evaluated from the co-genetic nakhlite and chassignite meteorites. *Geochimica et Cosmochimica Acta*, 238, 292–315. <https://doi.org/10.1016/j.gca.2018.07.006>
- Udry, A., Howarth, G. H., Herd, C. D. K., Day, J. M. D., Lapen, T. J., & Filiberto, J. (2020). What Martian Meteorites Reveal About the Interior and Surface of Mars. *Journal of Geophysical Research: Planets*, 125(12), e2020JE006523. <https://doi.org/10.1029/2020JE006523>
- VanBommel, S. J., Berger, J. A., Gellert, R., O’Connell-Cooper, C. D., McCraig, M. A., Thompson, L. M., Fedo, C. M., Des Marais, D. J., Fey, D. M., Yen, A. S., Clark, B. C., Treiman, A. H., & Boyd,

- N. I. (2023). Elemental composition of manganese- and phosphorus-rich nodules in the Knockfarril Hill member, Gale crater, Mars. *Icarus*, 392, 115372. <https://doi.org/10.1016/j.icarus.2022.115372>
- Vicente-Retortillo, Á., Martínez, G. M., Renno, N., Newman, C. E., Ordonez-Etxeberria, I., Lemmon, M. T., Richardson, M. I., Hueso, R., & Sánchez-Lavega, A. (2018). Seasonal Deposition and Lifting of Dust on Mars as Observed by the Curiosity Rover. *Scientific Reports*, 8(1), Article 1. <https://doi.org/10.1038/s41598-018-35946-8>
- Wang, H., Richardson, M. I., Wilson, R. J., Ingersoll, A. P., Toigo, A. D., & Zurek, R. W. (2003). Cyclones, tides, and the origin of a cross-equatorial dust storm on Mars. *Geophysical Research Letters*, 30(9). <https://doi.org/10.1029/2002GL016828>
- Ward, A. W. (1979). Yardangs on Mars: Evidence of recent wind erosion. *Journal of Geophysical Research: Solid Earth*, 84(B14), 8147–8166. <https://doi.org/10.1029/JB084iB14p08147>
- Watters, T. R., & Maxwell, T. A. (1986). Orientation, relative age, and extent of the Tharsis Plateau Ridge System. *Journal of Geophysical Research: Solid Earth*, 91(B8), 8113–8125. <https://doi.org/10.1029/JB091iB08p08113>
- Werner, S. C. (2008). The early martian evolution—Constraints from basin formation ages. *Icarus*, 195(1), 45–60. <https://doi.org/10.1016/j.icarus.2007.12.008>
- Whalley, W. B., & McGreevy, J. P. (1983). Weathering. *Progress in Physical Geography: Earth and Environment*, 7(4), 559–586. <https://doi.org/10.1177/030913338300700404>
- Wiens, R. C., Maurice, S., Robinson, S. H., Nelson, A. E., Cais, P., Bernardi, P., Newell, R. T., Clegg, S., Sharma, S. K., Storms, S., Deming, J., Beckman, D., Ollila, A. M., Gasnault, O., Anderson, R. B., André, Y., Michael Angel, S., Arana, G., Auden, E., ... Willis, P. (2020). The SuperCam Instrument Suite on the NASA Mars 2020 Rover: Body Unit and Combined System Tests. *Space Science Reviews*, 217(1), 4. <https://doi.org/10.1007/s11214-020-00777-5>
- Williams, M., & Today, U. (n.d.). *How bad is the radiation on Mars?* Retrieved November 14, 2022, from <https://phys.org/news/2016-11-bad-mars.html>

- Williams, R. M. E., Grotzinger, J. P., Dietrich, W. E., Gupta, S., Sumner, D. Y., Wiens, R. C., Mangold, N., Malin, M. C., Edgett, K. S., Maurice, S., Forni, O., Gasnault, O., Ollila, A., Newsom, H. E., Dromart, G., Palucis, M. C., Yingst, R. A., Anderson, R. B., Herkenhoff, K. E., ... Moores, J. E. (2013). Martian Fluvial Conglomerates at Gale crater. *Science*, 340(6136), 1068–1072. <https://doi.org/10.1126/science.1237317>
- Williams, A., Russell, P. S., Sun, V., Shuster, D., Stack, K. M., Farley, K., . . . Wadhwa, M. (2023). Exploring the Joezero delta front: Overview of results from the Mars 2020 Perseverance rover's second science campaign. *54th Lunar and Planetary Science Conference 2023*.
- Wilson, L., & Head, J. W. (2007). Explosive volcanic eruptions on Mars: Tephra and accretionary lapilli formation, dispersal and recognition in the geologic record. *Journal of Volcanology and Geothermal Research*, 163(1), 83–97. <https://doi.org/10.1016/j.jvolgeores.2007.03.007>
- Wright, J., Smith, B., & Whalley, B. (1998). Mechanisms of loess-sized quartz silt production and their relative effectiveness: Laboratory simulations. *Geomorphology*, 23(1), 15–34. [https://doi.org/10.1016/S0169-555X\(97\)00084-6](https://doi.org/10.1016/S0169-555X(97)00084-6)
- Wu, B., Wang, Y., Werner, S. C., Prieur, N. C., & Xiao, Z. (2022). A Global Analysis of Crater Depth/Diameter Ratios on the Moon. *Geophysical Research Letters*, 49(20), e2022GL100886. <https://doi.org/10.1029/2022GL100886>
- Yen, A. S., Gellert, R., Clark, B. C., Ming, D. W., King, P. L., Schmidt, M. E., Leshin, L., Morris, R. V., Squyres, S. W., & Campbell, J. L. (2013, January 1). *Evidence for a Global Martian Soil Composition Extends to Gale crater*. Lunar and Planetary Science Conference, The Woodlands, TX. <https://ntrs.nasa.gov/citations/20130009717>
- Yen, A. S., Gellert, R., Schröder, C., Morris, R. V., Bell, J. F., Knudson, A. T., Clark, B. C., Ming, D. W., Crisp, J. A., Arvidson, R. E., Blaney, D., Brückner, J., Christensen, P. R., DesMarais, D. J., de Souza, P. A., Economou, T. E., Ghosh, A., Hahn, B. C., Herkenhoff, K. E., ... Zipfel, J. (2005). An integrated view of the chemistry and mineralogy of martian soils. *Nature*, 436(7047), Article 7047. <https://doi.org/10.1038/nature03637>

Zurek, R. W., Barnes, J. R., Haberle, R. M., Pollack, J. B., Tillman, J. E., & Leovy, C. B. (1992). Dynamics of the atmosphere of Mars. In *Mars* (pp. 835–933). <https://ui.adsabs.harvard.edu/abs/1992mars.book..835Z>

Chapter 3: Methods

This chapter describes the methods used to (1) quantify airfall dust coverage on horizontal rock surfaces in Gale crater (see Chapter 4; Schmidt et al., 2018), and (2) measure the abundance and lengths of abrasion marks preserved in the abrasion targets from Jezero crater (see Chapter 5). Both studies use high-resolution images captured from microscopy cameras aboard the Mars Science Laboratory (MSL) and Mars 2020 (M2020) mission payloads, along with image editing and enhancing programs (e.g., Adobe Photoshop, Illustrator and ImageJ) to investigate the Martian surface.

3.1 Rover Instrumentation

The Curiosity (MSL) and Perseverance (M2020) rovers are equipped with similar instrumentation suites to study the surface of Mars. Both the MSL and M2020 missions were tasked with exploring the habitability of Mars, while also documenting the ancient environments preserved in the stratigraphic rock records of Gale crater and Jezero crater (Farley et al., 2020; Grotzinger et al., 2012). The M2020 mission was assigned the additional task of preparing, documenting, and caching a set of samples to be returned to Earth in a later mission (Farley et al., 2020).

3.1.1 Curiosity Rover MSL

The primary objective of the MSL mission was to deploy a mobile science laboratory to the surface of Mars (Grotzinger et al., 2012). “Once deployed, the rover would assess the biological potential of Gale crater, characterize the geology of the landing region, investigate planetary processes that may have influenced habitability, and to characterize the spectrum of radiation experienced at the planet’s surface (Grotzinger et al., 2012).” The mission was designed to have a minimum lifetime of one Mars year (~23 months), and recently celebrated its ten-year anniversary on the Martian surface. The subsections that follow describe the instrumentation aboard Curiosity that were used, or referenced, in Chapter 4.

Mars Hand Lens Imager

The Mars Hand Lens Imager (MAHLI; Figure 3-1) is a 2-megapixel color camera, with a focusable macro lens, aboard the Curiosity rover as part of the MSL instrument suite. MAHLI is

comprised of three main components: a camera mounted on the end of Curiosity's Robotic Arm (RA), an electronics and data storage assembly inside the hull of the rover and a calibration target mounted on the RA. At a minimum working distance of $\sim 2.1\text{cm}$, image products have $14\mu\text{m}$ pixel scales, and can resolve very coarse silt grains (Edgett et al., 2012).

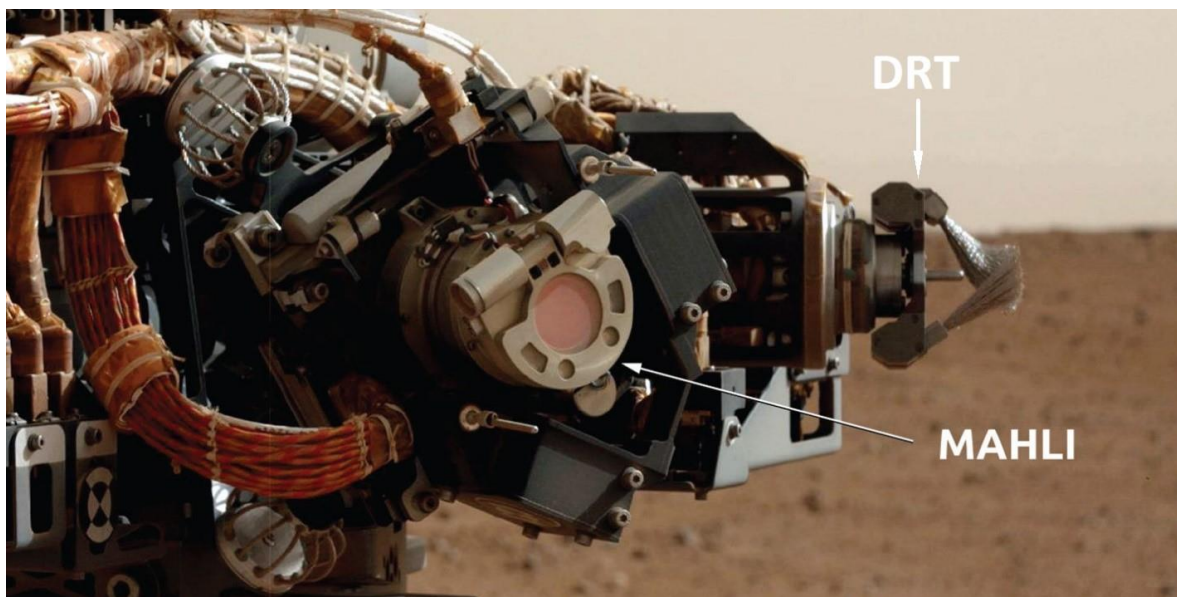


Figure 3-1: Mastcam image of Curiosity's rover arm showing the location of MAHLI and the DRT (image courtesy of NASA JPL/Caltech).

The primary objective of MAHLI is to investigate the stratigraphy, texture, structure, mineralogy, and morphology of geologic units in Gale crater (Edgett et al., 2012). Since landing August 6th 2012, MAHLI has provided unprecedented microscopic imagery of the Martian surface and has given critical insight to airfall dust deposits, their accumulation and mobility at the surface-level. Individual dust particles are unresolvable by MAHLI as they are only a few micrometres in diameter (Guzewich et al., 2014; Lemmon et al., 2004; Wolff et al., 2006; Wolff & Clancy, 2003), however MAHLI can easily resolve larger dust clumps ($>14\mu\text{m}$, the finest MAHLI pixel scale) that form from dust's natural stickiness (Schmidt et al., 2018). To be resolvable in MAHLI images, these dust clumps must be at least ~ 3 pixels in size, resolving down to coarse silt sized particles that form from dust's natural stickiness (Schmidt et al., 2018).

The MAHLI instrument captures images from three standardized working distances (~ 2 , ~ 5 and $\sim 25\text{cm}$; Edgett et al., 2015) and merges them using onboard software to create the highest

resolution image known as the “focus merge image.” With the purpose of quantifying the abundance of airfall dust covering horizontal rock surfaces in Gale crater, chapter 4 solely uses the highest resolution focus merge image captured by the MAHLI instrument.

ChemCam

The Chemistry and Camera (ChemCam) seen in Figure 3-2, is an instrument suite containing the LIBS and the Remote Micro-Imager (RMI). The mast unit houses the laser, RMI, telescope and the associated electronics, while the hull contains the de-multiplexer, three spectrometers, the thermoelectric cooler, electronics, data processing unit and the low-voltage power supply (Wiens et al., 2012).

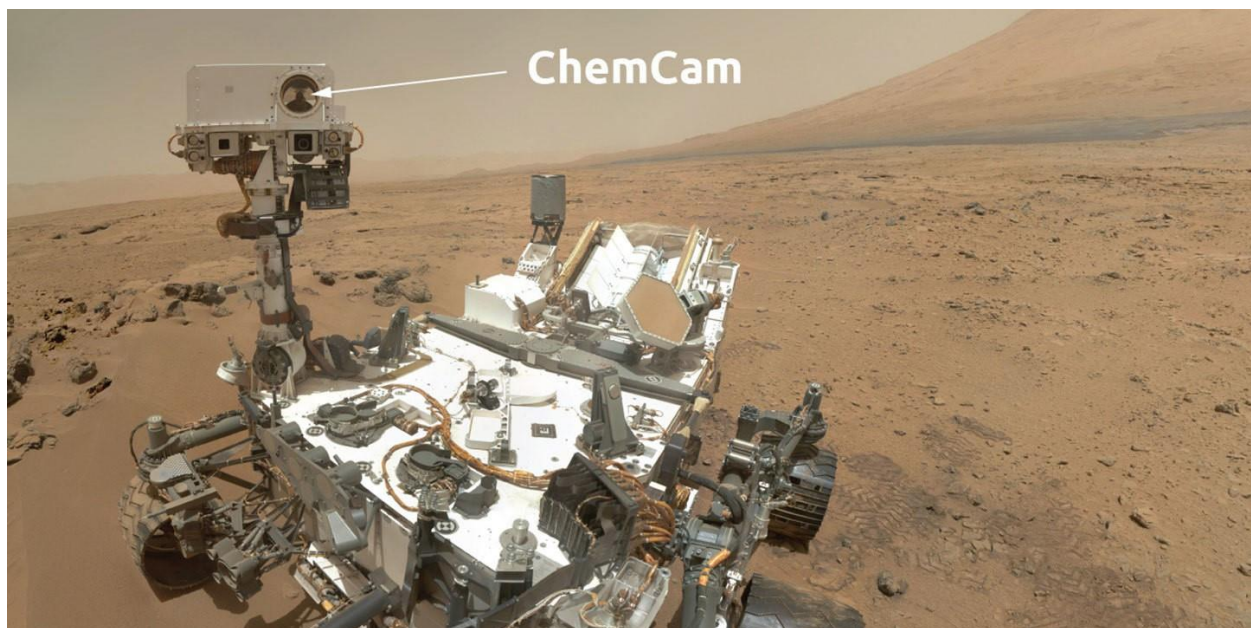


Figure 3-2: MAHLI image of Curiosity taken from the extended rover arm. White arrow displays the location of the ChemCam aboard the mast unit (NASA JPL/Caltech).

The primary objective of ChemCam is to obtain major element compositions for rocks and soils; however, another feature of LIBS is the ability to remove surface coatings of dust from the target surface (Wiens et al., 2012). When used, ChemCam fires the laser in a series of pulses incident on the target surface, ablating/vaporising the outer layer of rock. As the laser strikes the surface, a small shockwave is produced as atoms hit by the incident laser become excited and are converted in plasma, emitting light. The onboard spectrometer is used to measure this emitted light and capture major element abundances from the target surface, however the first

few laser shots are ignored as they may capture compositional data for the mobilized dust (Wiens et al., 2012).

Dust Removal Tool

Attached to the RA of Curiosity, the Dust Removal Tool (DRT), seen in Figure 3-1, hosts two rotating stainless-steel wire-bristle brushes designed to clear rocky surfaces of dust and other loose material. The overall design of the DRT resembles the brush on the Rock Abrasion Tool (RAT): a powerful rock hammer and brush combo aboard the historical Mars Exploration Rovers (MER) Spirit and Opportunity (Gorevan et al., 2003). A metal rod of fixed length centered between the DRT's brushes, visible in Figure 3-1 above, ensures proper standoff height (the height of the camera above the target surface) from the target surface when lowering the rover arm. The DRT has been used intermittently throughout MSL (Vasavada et al., 2014). Engineering anomalies and other complications have infrequently inhibited use of the DRT (Berger et al., 2020).

3.1.2 Perseverance Rover

The success of Curiosity led the Mars2020 Perseverance rover to follow a similar design but was equipped with a more sophisticated and updated instrument suite (Farley et al., 2020). The Mars2020 mission was tasked with (1) exploring Jezero crater, (2) collecting rock and regolith samples to be returned to Earth in the near future, and (3) perform technology demonstrations to prepare for continued Mars exploration (Farley et al., 2020). The following subsections will describe the instrumentation used and discussed in Chapter 5.

SHERLOC (WATSON)

The Scanning Habitable Environments with Raman and Luminescence for Organics and Chemicals (SHERLOC) is a suite of instruments attached to the RA of Perseverance. The deep-ultraviolet native fluorescence and resonance Raman spectrometer, Autofocus Context Imager (ACI), Wide Angle Topographic Sensor for Operations and eNginEering (WATSON) camera, along with the remaining Perseverance payload, provide sub-millimeter scale, spatially resolved detections and characterizations of organic matter and minerals on the Martian surface (Bhartia et al., 2021).

The high spatial resolution of the ACI (10.1 $\mu\text{m}/\text{pixel}$) is used to focus the Raman spectrometer on the target while also documenting surface textures and structures of the observed rock and regolith. The resolution power of the ACI is higher than that of the MAHLI camera (14 μm), allowing finer materials to be resolved, but it only produces grayscale images over a 500-600nm bandpass (Fries et al., 2022). Distinguishing red-brown dust particles from other surface features is nearly impossible in greyscale images.

The WATSON camera is capable of capturing red-green-blue (RGB) images of the Martian surface from a range of working distances, providing greater geological context at a range of spatial scales (Bhartia et al., 2021). Unfortunately, WATSON is not co-boresighted with the spectrometer/ACI, requiring the rover arm to move for WATSON to view the same target. At this time, a standardized method for co-registering these data products does not exist and analysts must manually overlay WATSON and ACI images when using both image types (Bhartia et al., 2021)

Planetary Instrument for X-Ray Lithochemistry

Attached to the Perseverance rover's RA, the Planetary Instrument for X-Ray Lithochemistry (PIXL; Figure 3-3) is a microfocus X-ray fluorescence instrument. PIXL, and the associated multispectral micro-context camera (MCC), record sub-millimeter scale geochemistry and surface textures by focusing an X-ray beam on a small point ($\sim 150 \mu\text{m}$ diameter), and measuring the induced X-ray fluorescence (XRF) of the incident surface (Allwood et al., 2020). Interactions between minerals and the incident x-ray beam amplify or remove unique diffraction peaks allowing mineral identities, sizes, and crystallographic orientations to be constrained. The unique configuration of PIXL includes a dual detector system, which captures the x-ray spectra at two orientations to the target surface. By comparing spectral signals between these detectors Tice et al. (2023) have developed expressions which remove diffraction issues resulting from surface roughness and diffraction effects and produce the most accurate chemical quantifications of the target surface. Sensitive enough to capture major and minor rock-forming elements, PIXL can also detect trace elements after a single 10 second observation (Allwood et al., 2020). PIXL scans can be performed as 1 to 3 lines up 36 mm in length, as rectangular grids up to 4 x 12 mm^2 , and as square grids up to 22 x 22 mm^2 (Tice, et al., 2023). Square PIXL scans

from the crater floor and delta front campaigns were limited to smaller grid sizes of $\sim 7 \times 7 \text{ mm}^2$ or smaller. PIXL scan points, measurements, and the co-registered MCC images are viewable in the data-viewing software PIXLISE (Ye et al., 2021). Here the spatial distribution and abundances of elements can be accurately compared with physical textures and internal structures of the target surface (Allwood et al., 2020; Ye et al., 2021). The square and rectangular XRF maps with densely packed PIXL points were preferred in chapter 5 as they provided the highest spatial resolution to the geochemical data, and allowed mineral boundaries to be defined with greater accuracy, see section 3.3.2.

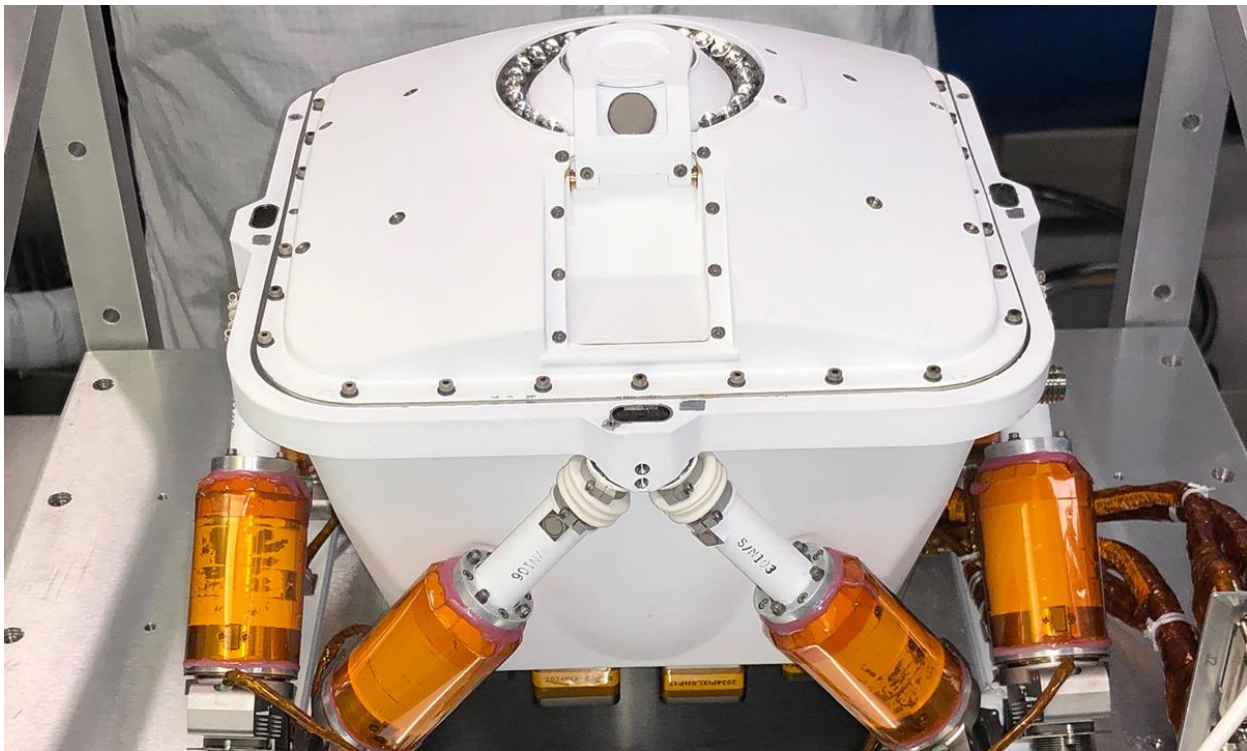


Figure 3-3: PIXL sensor before attaching it to the RA of the Perseverance Rover at NASA's jet Propulsion Laboratory in Pasadena California (NASA JPL/Caltech).

Sampling and Caching Subsystem

To extract core samples, abrade rock/regolith surfaces, and to search for biosignatures of past life, the Perseverance rover's Sampling and Caching System (SCS; Figure 3-4) comes equipped with coring bits, 2 abrasion bits and a single regolith bit. When coring at approximately 200 rpm, the RA exerts an additional downward force of 300 N between the stabilizer mechanism and the target surface. This added force prevents the coring bit from walking or jumping during

first contact with the target surface (Moeller et al., 2020). To prevent potential damage and calibration issues of other the proximity science instruments (e.g., SHERLOC and PIXL) attached to the RA, these tools are vibrationally isolated from the corer's rotary percussive drilling loads (Moeller et al., 2020).

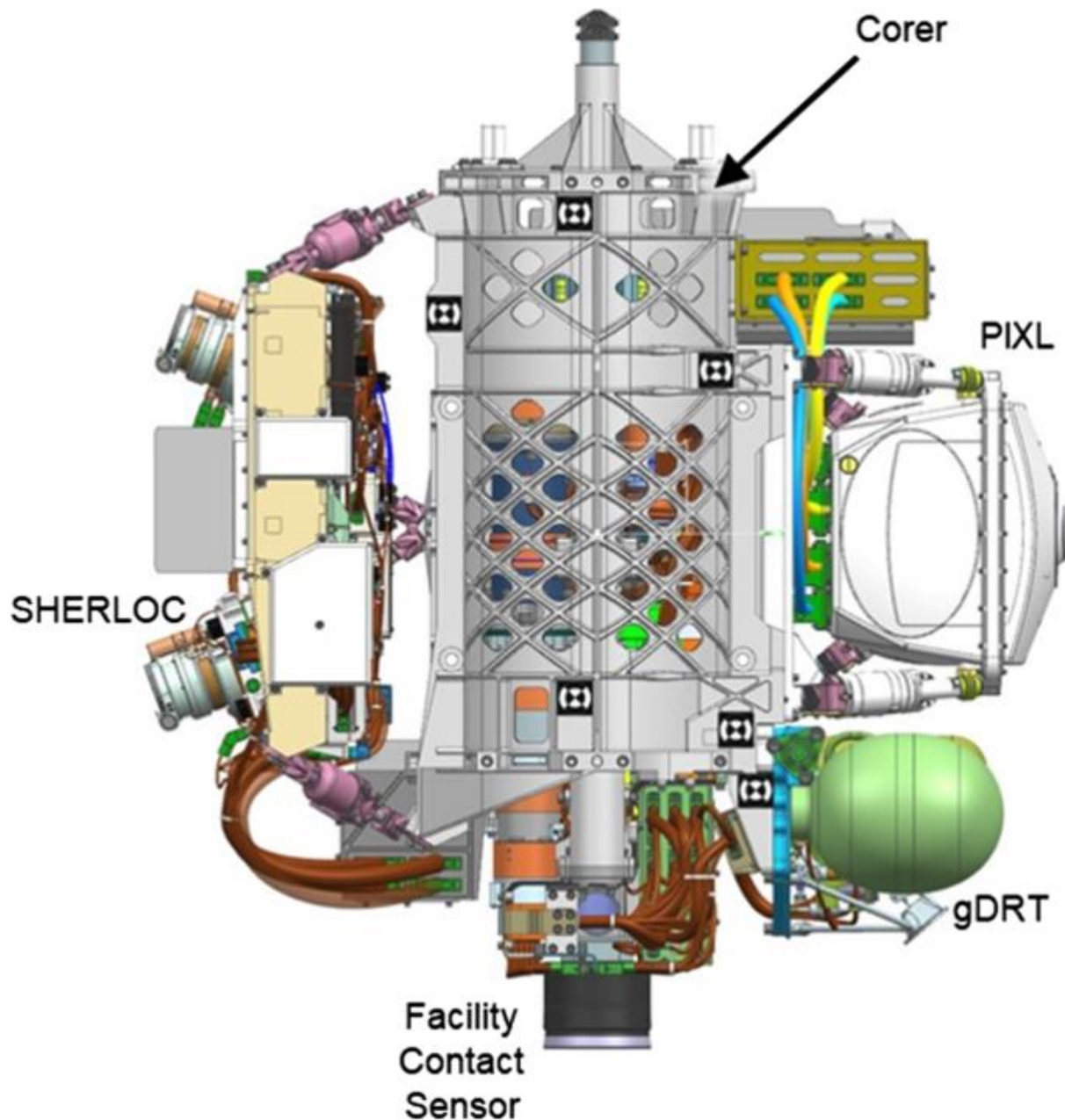


Figure 3-4: Configuration schematic of the SCS turret highlighting other instruments installed on the RA. Labelled are the SHERLOC-WATSON camera, Cored, PIXL, gDRT and the Facility Contact Sensor (Moeller et al., 2020).

Abrading follows a similar process to drilling, however, the rotation rate is decreased to 37 rpm to accommodate the larger surface area of the Abrading Bit face (50 mm diameter; Moeller et al., 2020). The abrasion bits themselves are designed with three parallel lines of teeth, each with differing lengths, and are arranged asymmetrically (Figure 3-5). As the drill spins and impacts the rock, a pattern of crisscrossed marks are etched into the target surface, gradually chipping away material with subsequent impacts. The nominal abrasion depth needs to exceed 2 mm across the entire abrasion patch to remove sufficient dust and surface coatings of altered material. A burst of nitrogen gas from the Gas Dust Removal Tool (gDRT) removes abrasion fines from the target surface, revealing the underlying surface for analysis by the SHERLOC and PIXL instruments.

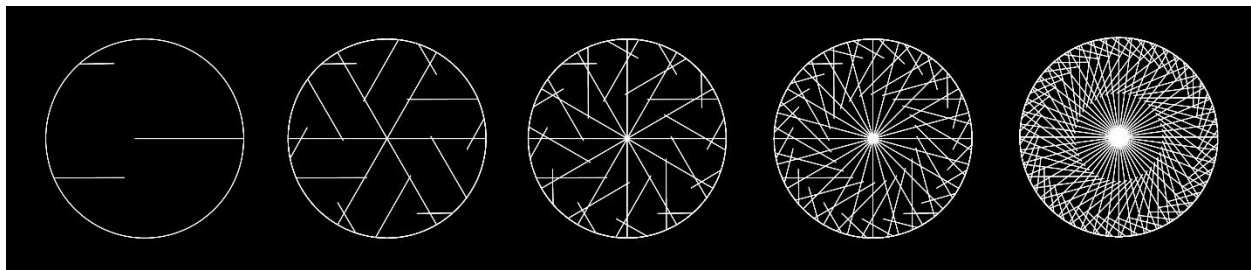


Figure 3-5: Rotary-Percussive Drill bit (left) and the radial chisel mark pattern (Courtesy NASA/JPL-Caltech).

Gas Dust Removal Tool

The previous MER and MSL missions used mechanical approaches, in the form of rotary abrasion/brush-based methods, to remove dust but failed to remove a sufficient amount of material required for effective PIXL and SHERLOC investigations (Moeller et al., 2020). The Gas Dust Removal Tool (gDRT), was selected as the dust removal instrument included in the M2020 mission payload. The gDRT (Figure 3-4) is a cold nitrogen gas system that performs the necessary removal of dust via pressured flow pulses. The gDRT is nominally used to remove dust from abrasion patches and to expose underlying rock surfaces (Jens et al., 2018). In the 50mm diameter abrasion patches, which have a maximum depth of 16mm, tests of the gDRT proved that it was more effective than a mechanical brush due to the size, depth and edge wall effects of the abrasion. Requiring 3-4 puffs at different angles to remove sufficient dust from typical

abrasion patches, the Perseverance rover was loaded with a limited supply of ~888 nominal puffs (Jens et al., 2018).

3.2 Surface Dust Coverages in Gale crater

This section summarizes the methods to quantify dust coverages on rock surfaces imaged by MAHLI in Gale crater. A more detailed description of these methodologies is provided by Schmidt et al. (2018). Chapter 4 builds from the results of Schmidt et al. (2018; sols 46-1511), which includes work from Rebekka Lee, Samantha Bay, and Nicholas Bradley. The subsequent dataset, ranging from sol 1511-3409, was collected by myself and Izzy Marincic.

Informally known as the “Dusty Planet,” an uneven layer of dust blankets the Martian surface. Atmospheric models have determined individual dust particle sizes to be ~1.0 in diameter (Guzewich et al., 2014; Wolff et al., 2006; Wolff & Clancy, 2003), however the inherent stickiness of Martian dust, caused by an array of Van der Waals adhesive forces (Landis, 1997), produces irregularly shaped dust aggregates. These aggregates bury the terrain beneath a variably thick and distributed layer of dust. With a maximum resolving power of 14 μm per pixel, MAHLI is unable to resolve individual dust particles but the larger dust aggregates are observable. Individual dust particles, too fine to be resolved in MAHLI images, are potentially missed in the methods described in Schmidt et al. (2018).

In the previous work by Schmidt et al. (2018), dust particles were identified in all surface targets, including those where a dust removal method was performed (e.g., ChemCam and DRT). Dust removal is most effective on flat, homogeneous rock surfaces, and less efficient for targets with variable surface topography. While chapter 4 does not use APXS data, dust contributes significant amounts of SO_3 , Cl and other light elements, such as Na and Ca, to APXS quantifications and distracts from the true geochemistry of the target rock (Schmidt et al., 2018).

3.2.1 Image Acquisition and Selection

To measure the abundance of airfall dust covering horizontal rock surfaces in Gale crater, the publicly released highest-resolution focus merge image for each Alpha Particle X-Ray Spectrometer (APXS) rock target was collected the NASA Science Mars Exploration Multimedia Raw Images website (<https://mars.nasa.gov/msl/multimedia/raw-images/>). All APXS targets are

georeferenced and co-registered with MAHLI images, however not all MAHLI images are paired with APXS results. While this study does not focus on APXS results, it exclusively uses MAHLI images that are co-registered with APXS targets.

APXS results are collected from a 1.7 cm diameter FOV of the target surface. The dust coverage measurements from chapter 4 and Schmidt et al. (2018) are collected from the same 1.7 cm FOV at the centre of each MAHLI image. This allows the dust coverage and its associated geochemistry to be assessed in the APXS data. The range and scale for each image were determined using the focus motor count associated with each image (K. Edgett et al., 2015; Yingst et al., 2016). While the APXS results align with the centre of their associated MAHLI images, offsets up to 15 mm have been documented between data products (Schmidt et al., 2018). Focusing on the centre of MAHLI image also decreases vignetting effects towards the edges.

3.2.2 Target Selection and Assigning Target Type

Targets were categorized into three target types (As Is, ChemCam and DRT) based on the dust removal method applied prior to MAHLI image acquisition. The 'As Is' target type describes an untouched, natural rock surface. Since they are undisturbed accumulations of airfall dust, As Is targets provide the best context for interpreting temporal and spatial trends in airfall dust throughout the MSL mission. Use of the ChemCam and LIBS produces a characteristic scorch mark and radial clearing of dust resulting from the shockwave produced by the laser striking the target surface. Finally, application of the Dust Removal Tool (DRT) exposes the underlying rock surface by clearing up to 2mm of surface debris, and may produce radial scratch-like abrasion where the wire-bristles scraped the underlying rock surface, particularly for softer lithologies, including mudstones.

3.2.3 Dust Measuring Methods

Chapter 4 included used three image manipulation or alteration methods to quantify airfall dust abundances. Method 1 changes MAHLI images to greyscale, then measures the light and dark dust particles using a threshold selection tool in ImageJ. Changing a MAHLI image to greyscale would often amplify vignetting effects, leading to inaccurate dust measurements towards the image's periphery (Figure 3-6C). Since our dust measurements are focused on the

center of each, these vignetting effects were often negligible, however targets with partial shadows or variable surface topographies complicated Method 1's measurements. Method 2 uses an online photo-editing website to enhance MAHLI images, brightening shaded regions, and emphasize colour contrasts between dust and the underlying surface. Editing the MAHLI images before selecting dust particles also reduces vignetting effects. Method 2 would then select dust particles in the edited RGB image using a threshold tool in ImageJ. Method 3 uses the same edited image from Method 2, but involves image alteration using the photo-editing software Adobe Photoshop. Here the user manually selects dust pixels and their associated RGB colour saturation, changing them to an unnatural colour, often green. In a similar method, the underlying rock surface and non-dust particles were changed to a black. The final image was therefore a binary-coloured image of user-defined pixels identified to be dust particles and natural rock surface. These pixels were then measured using the same procedure as Method 1. Each method is discussed in slightly greater detail below, however full descriptions can be found in Schmidt et al. (2018).

Method 1

The first dust measurement measures dust abundance in greyscale MAHLI images. For method 1, unedited high-resolution focus merge images (Figure 3-6A) are opened in ImageJ, a Java-based image processing program that displays edits, processes and saves 8-, 16-integer and 32-bit floating images (Collings 2007). ImageJ's ability to process and measure features from 24-bit images (standard color images) and 8-bit (greyscale images) allows dust coverage of varying colour types to be measured. In addition, ImageJ allows measurements of areal coverage and provides pixel value statistics using defined selections and intensity thresholds (Schneider et al., 2012). Images were changed to 8-bit greyscale and the Sharpen Tool was used to enhance the contrast between adjacent light and dark pixels, accentuating the edges of dust particles. Dust pixels are selected with greater accuracy once the sharpening effect is applied. Light and dark dust pixels are then selected using the Threshold Tool, and the resulting areal coverages is measured using the Analyze Particles operation (measures the number of selected pixels against the total pixel count; Figure 3-6 B and C; Schmidt et al. 2018). These measurements are then combined to get a total dust coverage measurement for Method 1 (Schmidt et al., 2018).

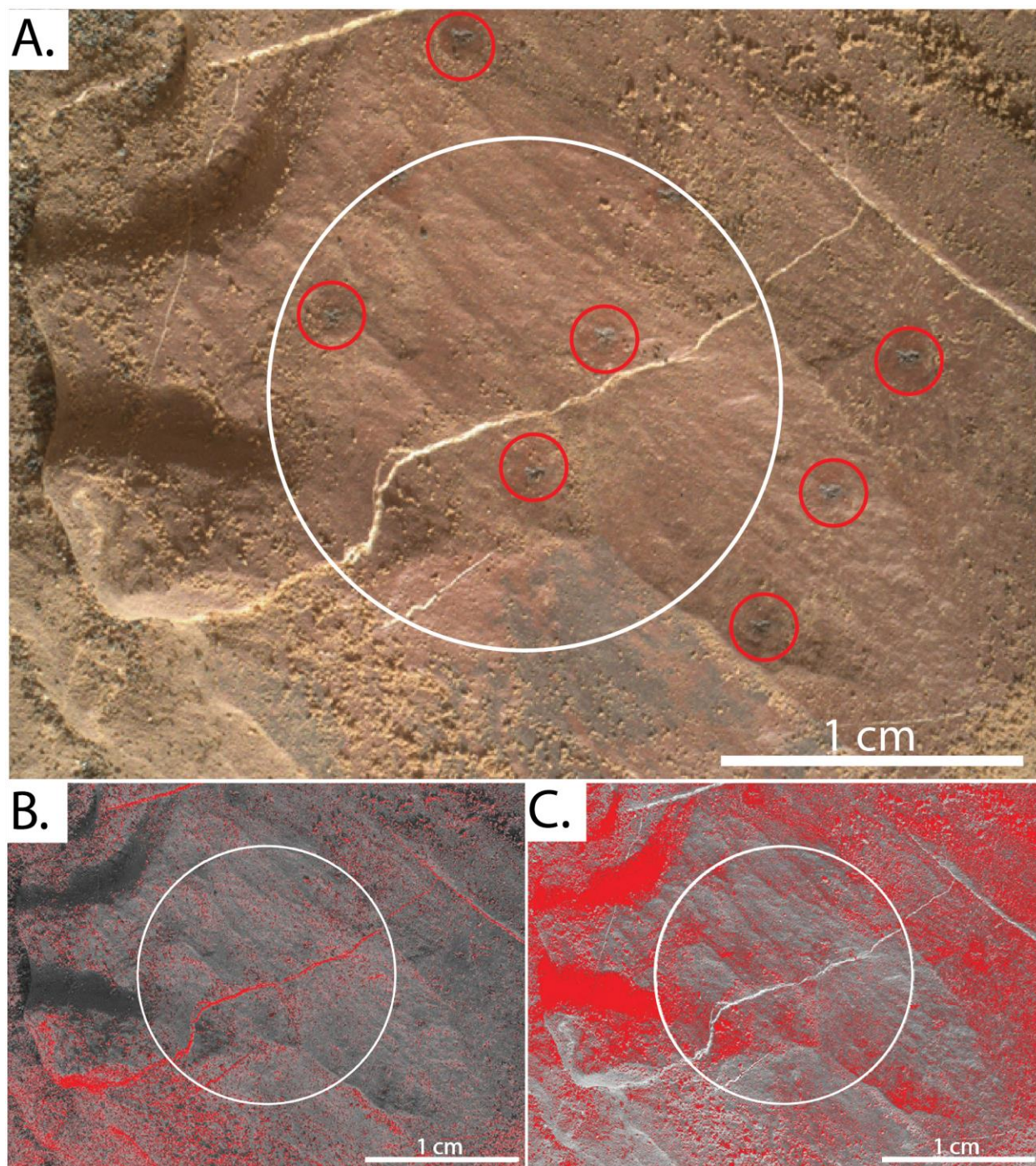


Figure 3-6: (A.) Highest resolution original focus merge image for ChemCam target Babbit (Sol 2029 Babbit; 2029MH0001930000801501R00_DXXX) with a standoff height of 1.8 cm. Red ellipses show locations of some ChemCam LIBS burn marks. (B.) Image from Panel A. changed to 8-bit greyscale. The light-coloured dust pixels were selected using Method 1 (red). The selected pixels measured to be 7.61% within the 17mm APXS FOV (white circle). (C.) The dark-coloured pixels were selected using Method 1 (red). The selected pixels measured to be 20.8% for the APXS FOV. The combined Method 1 dust coverage is 28.41%).

Method 2

The second dust measuring method enhances the MAHLI image from Method 1 (Figure 3-6A) and measures dust abundance in RGB. Method 2 edits the MAHLI image using BeFunky.com, a free online photo editing website, to brighten shaded regions, increase the color contrast between dust grains and the underlying rock surface, sharpen edges between features, and apply a filter that enhances the red saturation of dust particles and the blue of the underlying rock surface (Figure 3-7B). The Beautify tool is used to warm images, creating a greater contrast between red-coloured pixels and brightening features covered by shadows. The BeFunky.com website is useful when analyzing images that are partially or completely shaded by Curiosity'. Unlike the Sharpen tool from ImageJ, which applies a standardized sharpening to the entire image, the Sharpen tool on BeFunky.com applies a user-defined degree of sharpening. The Cross-Process filter applies a blue hue to the image while also applying an adjustable contrast filter. Contrast is another useful alteration that enhances colours and clarifies the image, separating surface features from overlying debris (sand grains, dust particles, cracks etc.). Satisfied with the image enhancement (Figure 3-7B.), the images are then opened in ImageJ to measure dust coverages. Unlike Method 1, Method 2 does not change the image to greyscale, rather the Color Threshold tool is used to select dust pixels according to their saturation and brightness. The Analyze Particles operation is then used to measure the percentage of selected dust pixels to the total number of pixels in the image (Figure 3-7C; Schmidt et al. 2018).

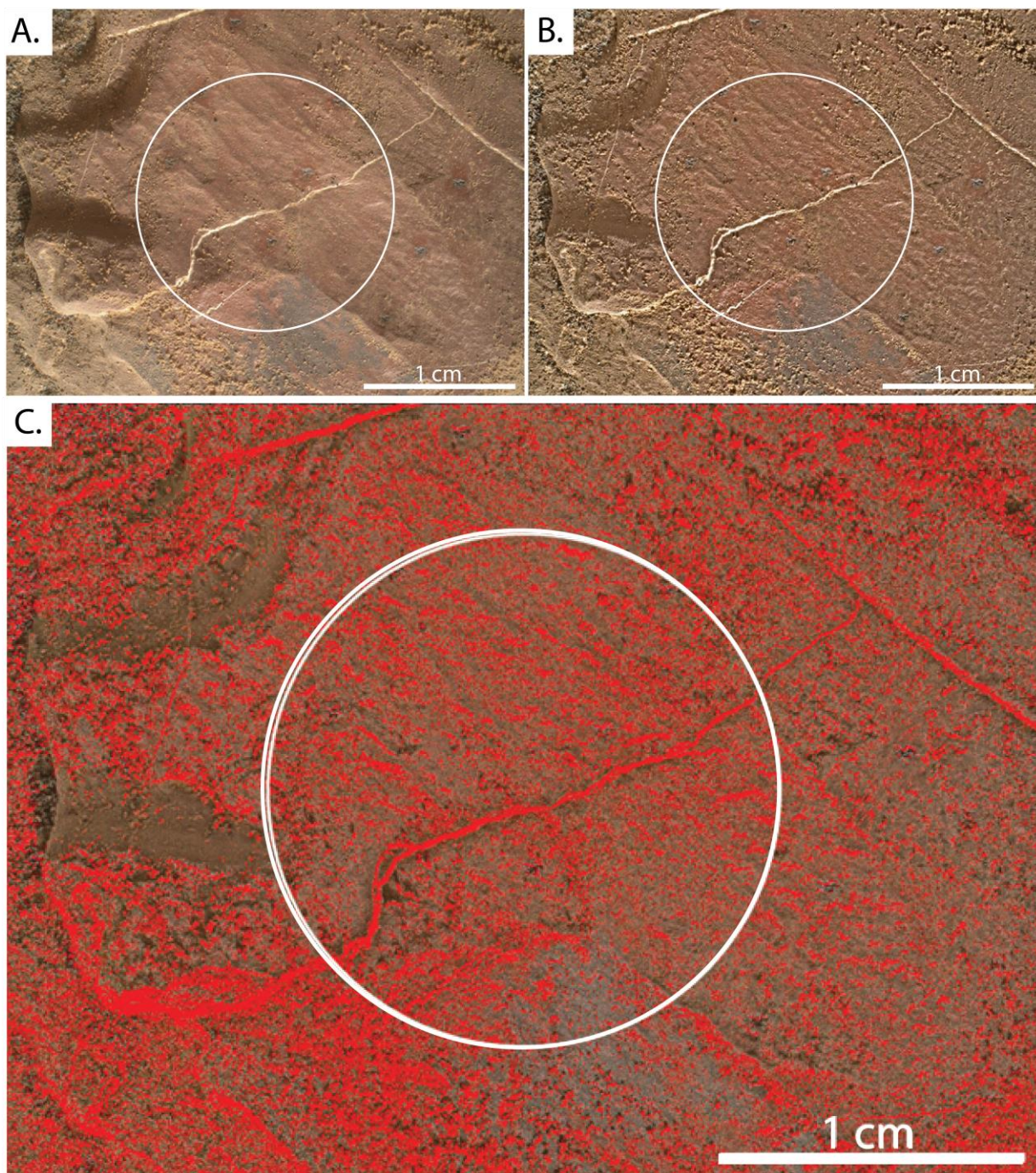


Figure 3-7: (A.) Highest resolution original focus merge image for ChemCam target Babbit (Sol 2029 Babbit; 2029MH0001930000801501R00_DXXX) with a standoff height of 1.8 cm. (B.) BeFunky.com edited image (edited from A.) Edges of dust particles are more pronounced following image editing. (C.) Figure 3-10: Dust pixel selection (29.843%) using Image J and following Method 2. Dust particles cover 25.6%% of the 17mm APXS FOV (white circle).

Method 3

The third method is the most hands-on approach to measuring dust abundance as the analyst manually separates dust pixels from the underlying surface. Further image processing in Adobe Photoshop is performed in Method 3, using the same BeFunky.com image from Method 2. Adobe Photoshop is a powerful raster-graphics editor that allows easy image manipulation. While there are numerous uses of Photoshop, the Replace Colour Tool was the main operation used in this study. This tool allows the user to select a pixel from the loaded image, and all other pixels that are associated with the same 24-bit colour value and edit its colour. A user-defined buffer can be applied to expand the selected pixels and grab other similarly coloured pixels from the total image. Pixels of dust are manually selected, and changed to a lime-green colour, as it is an unnatural colour for the Martian surface and does not appear in any images prior to editing. The underlying rock surface is changed to black (Figure 3-8B). The resulting binary image is then exported and opened in ImageJ where it is converted into 8-bit greyscale and sharpened (similar to Method 1). The light coloured pixels, which were previously lime-green and represented dust pixels, are then selected using the Threshold Tool and the Analyze Particles function is used to measure the selected pixels (Figure 3-8C).

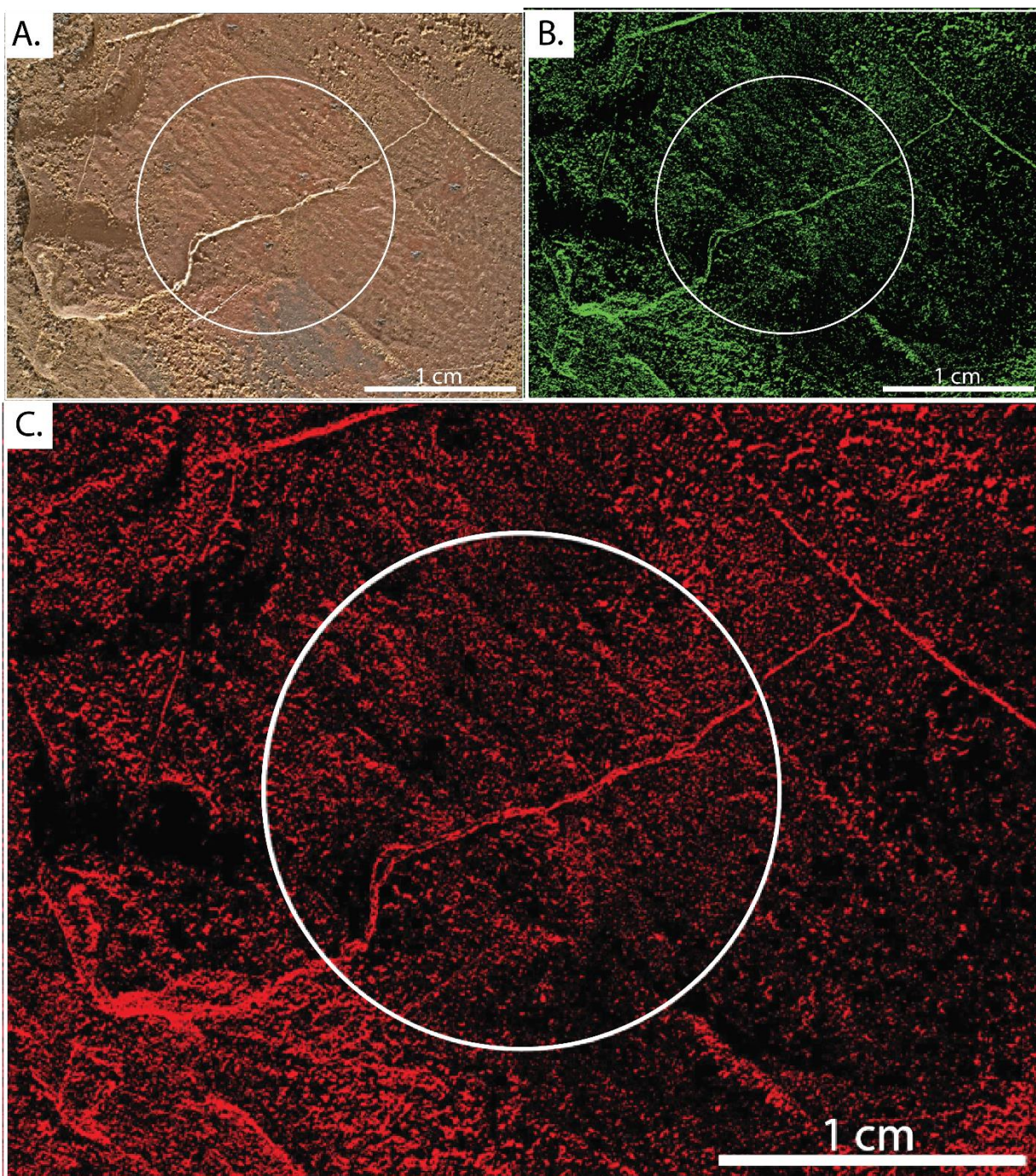


Figure 3-8: BeFunky.com editing of the highest resolution original focus merge image for ChemCam target Babbit (Sol 2029 Babbit; 2029MH0001930000801501R00_DXXX) with a standoff height of 1.8 cm. (B.) Binary colour image created in Adobe Photoshop using Method 3. The dust pixels identified in the edited BeFuky.com image have been changed to lime green while the underlying rock surface is changed to black. (C.) Selection of all dusty particles (38.1% areal dust coverage) using ImageJ and following Method 3. Dust particles cover 28.4% of the 17mm APXS FOV (white circle).

3.2.4 Final Dust Abundance in APXS FOV

To represent the APXS field, a scaled 17mm diameter circle is placed at the centre of each method, and the Analyze Particles operation is used again to determine the percent areal coverage of dust within the FOV (Schmidt et al., 2018). Because MAHLI images are taken at different standoff heights (the height of the camera above the target surface), the number of pixels needed to measure a 17mm diameter circle varies between targets.

3.2.5 Mapping and Classifying Dust Data

To map the distribution of dust coverages along the MSL rover traverse, each rock target was plotted using the associated georeferenced data (elevation, northing, easting and solar longitude) that is made publicly available on the Curiosity (MSL) Analysts Notebook (<https://an.rsl.wustl.edu/msl/mslbrowser>). Targets were further sorted by season using solar longitude. Mapping was performed in the free and open-source software Quantum Geographic Information Systems (QGIS; version 3.14 <https://www.qgis.org/>).

3.2.6 Sources of Error

Each dust measurement varied by <5% and were averaged to get a final dust coverage measurement. Method 3 was treated as the most accurate dust measuring method as the entire dust selection was determined by analyst. The threshold tool that was used in Methods 1 and 2 to select pixels fits all pixel colour values onto a distribution to be selected, producing inherent overlap between some dust pixels and the underlying rock surface. Despite this, Method 2 and 3 measurements rarely varied by more than 5%, and was often caused by an over selection of pixels in Method 2 by the threshold tool. It was more common for Method 1 to exceed this 5% due to vignetting effects. In such cases, these values were still recorded, however the averaged dust measurement were limited to Methods 2 and 3.

3.3 Abrasion Mark Mapping in Jezero crater

This section summarizes the methods used to measure abrasion marks and mineral abundances across the 10 abraded rock targets examined by M2020.

The M2020 mission has recently completed its first two campaigns, the Crater Floor (sol ~0-379; Williams et al., 2023) and Delta Front campaigns (sol ~415-641; Williams et al., 2023). During such time Perseverance has extracted 18 core samples, and successfully produced 10 abrasion patches. Unfortunately, complications during coring and abrasion have prevented 2 cores and 5 abrasion patches from being successful (see Table 3-1; Figure 3-9). While an array of variables may have prevented core extraction and abrasion patch productions, this study focuses on the abrasion marks preserved in the rock surface following successful abrasion to understand the effect that rock type and secondary alteration has on the abrasion process.

3.3.1 Image Acquisition and Selection

This study requires geochemical data to understand the effect secondary alteration has on the abrasion process. Therefore, only the abrasion patches analyzed by PIXL were analyzed. To accurately trace all abrasion marks and later overlay each PIXL scan, the highest resolution SHERLOC-WATSON images were selected for each abrasion patch. A combination of high standoff images where the entire abrasion patch was visible and close-up images of key features or sections were used for sections with finer abrasion marks. For some samples (e.g., Uganik Island, sol 614; Figure 3-10) with small or few abrasion marks on a fine-grained and/or lightly coloured substrate, abrasion mark identification was difficult. For these targets, grayscale ACI images were more useful for distinguishing abrasion marks.

Table 3-1: List of M2020 abrasion and core sample attempts and their outcomes.

Campaign	Abrasion			Core Sample		
	Sol	Name	Outcome	Sol	Name	Outcome
Crater Floor	160	Guillaumes	Success	168	Roubion	Failed
	186	Bellegarde	Success	190	Montdenier	Success
				196	Montagnac	Success
	206	Garde	Success			
	251	Pont du Loup	Failed			
	253	Dourbes	Success	262	Salette	Success
				271	Coulettes	Success
	288	Soberro	Failed			
	292	Quartier	Success			
				306	Pauls	Dumped
				337	Malay	Success
	346	Montpezat	Success			
	367	Alfalfa	Success			
				374	Atsah	Success
Delta Front	452	Rose River Falls	Failed			
	471	Elkwallow Flats	Failed			
	482	Thronton Gap	Success	490	Swift Run	Success
				495	Skyland	Success
				499	Witness Tube	Success
	504	Berry Hollow	Success	509	Hazeltop	Success
				516	Bearwallow	Success
	562	Chiniak	Success			
	568	Novarupta	Success			
				580	Magiek	Success
	593	Topographers Peak	Failed			
	612	Uganik Island	Success			
				635	Atmo Mountain	Success
				639	Crosswind Lake	Success

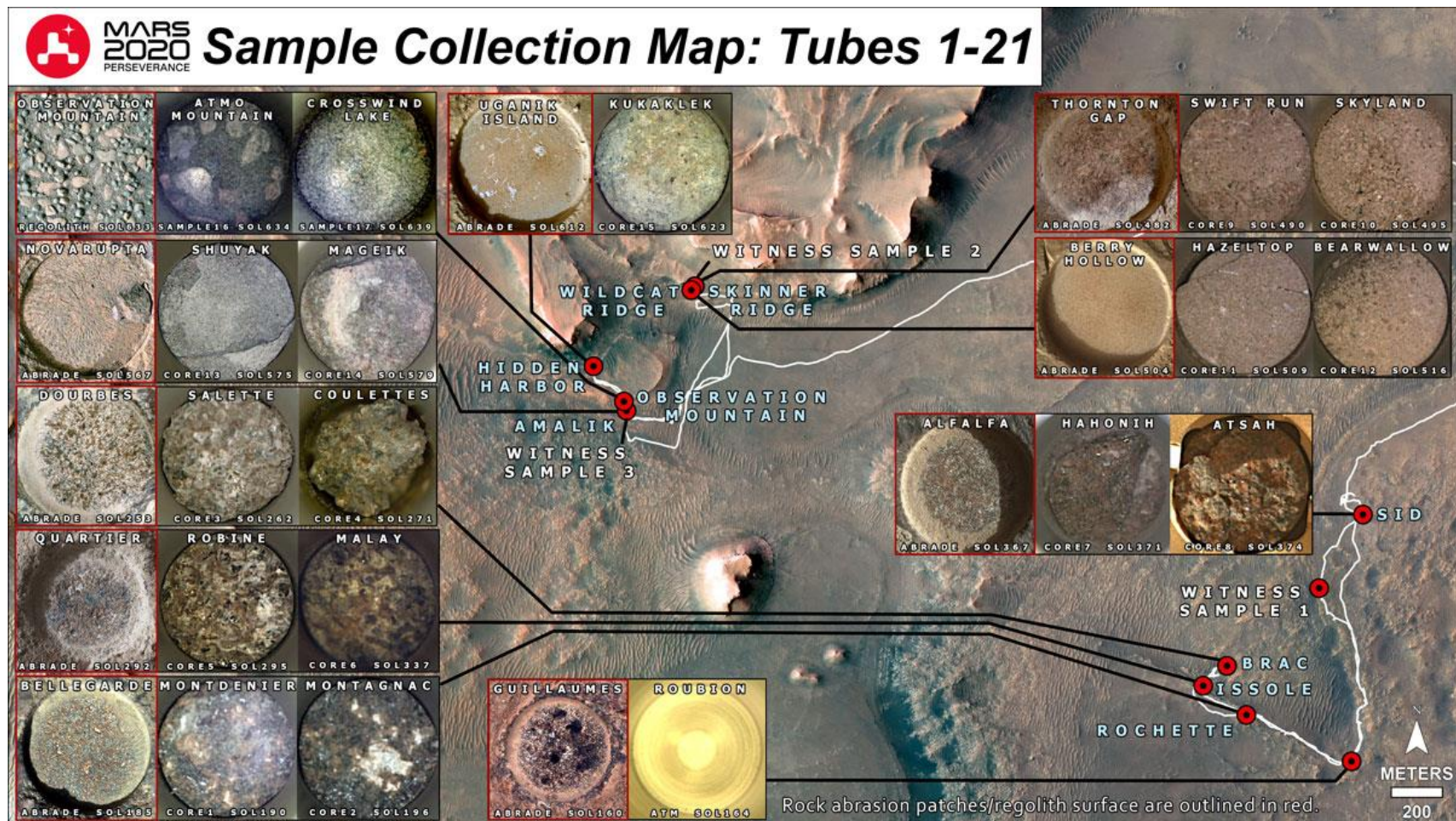


Figure 3-9: Graphic map showing the locations (red dots) where Perseverance collected and sealed 18 sample tubes to be returned to Earth. Red squares show the abrasion patch associated with each core sample (images to the right of each abrasion), excluding Montpezat (sol 346) and the Observation Mountain regolith samples (sol ~630; NASA JPL/Caltech).



Figure 3-10: SHERLOC-WATSON image (SIF_0617_0721745943_003FDR_N0301172SRLC08027_0000LMJ01) of the Uganik Island (sol 614) abrasion patch where abrasion marks are barely visible.

3.3.2 Mineral Mapping

The PIXLISE software produces element maps for each PIXL scan (Ye et al., 2021). PIXLISE displays the co-registered PIXL scans and MCC images where chemical abundances of each PIXL spot (called PIXL PMC or PMC) are plotted above an MCC image of the abraded surface (see Figure 3-11). For this study PIXL map scans with densely packed PMCs were required to define mineral boundaries. Of the three PIXL scan types, only the densely PMC-populated rectangular (4x12 mm²) and square (up to 22x22 mm², but commonly 5x5 mm² to 7x7 mm²) scans were used. PIXL line scans were excluded since PMCs are too dispersed, possibly missing some minerals and/or preventing accurate mineral grain boundaries and rock textures from being defined (Figure 3-12).

Igneous rocks were examined by the Perseverance rover during the Crater Floor campaign. Subsequent interactions with aqueous solutions have modified the mineralogy, composition and texture of these primary igneous materials. Products of these secondary mineral assemblages include carbonate materials in the Séítah formation, iron oxides and the deposition of sulfate and perchlorate salts (Farley et al., 2022). Proximity science throughout the Delta Front campaign and remote observations revealed a suite of sedimentary rocks that are consistent with subaqueous deposition, likely via a turbidite-related process (Williams et al., 2023; Sun et al., 2023). Sedimentary materials from the lower delta front were a combination of sulfate- and carbonate-cemented siltstones and mudstones with detrital igneous grains (Williams et al., 2023). To separate each PIXL scan into the original unaltered materials and secondary altered materials, three mineral groups were selected in each abrasion patch: (1) Low-Salt, (2) High-Salt and (3) Alteration (see Table 3-2 for descriptions of each mineral group).

Minerals were classified based on age, starting with the youngest materials. Sulfates and other salts (High-salt mineral group) are secondary minerals which fill pore spaces, voids, and cracks in their host rock (Farley et al., 2022) and are likely the youngest mineral present. These were the first materials selected in each abrasion patch. Since each abrasion target possesses a unique mineralogy and composition, each target required unique expressions to select the desired minerals. These expressions select PIXL PMCs based on chemical abundances (see Table 3-3), which are then classified into Regions of Interest (ROI) and prevents their section in

subsequent expressions. Carbonates and perchlorates (included in the alteration mineral group) were selected using FeO/SiO_2 and SO_3/Cl abundances, however these criteria will also select igneous oxides, such as magnetite (Fe_3O_4) and ilmenite (FeTiO_3). To ensure their proper classification, a $\text{FeO-TiO}_2\text{-Cr}_2\text{O}_3$ RGB colour mixed image was used (see Figure 3-13). PMCs that incorrectly selected igneous oxides were manually deselected, while the remaining PMCs were classified into the Alteration ROI. The remaining low-salt PMCs were selected and classified into the Low-Salt ROI. The final mineral ROIs were then exported from PIXLISE as a .jpeg (Figure 3-14).

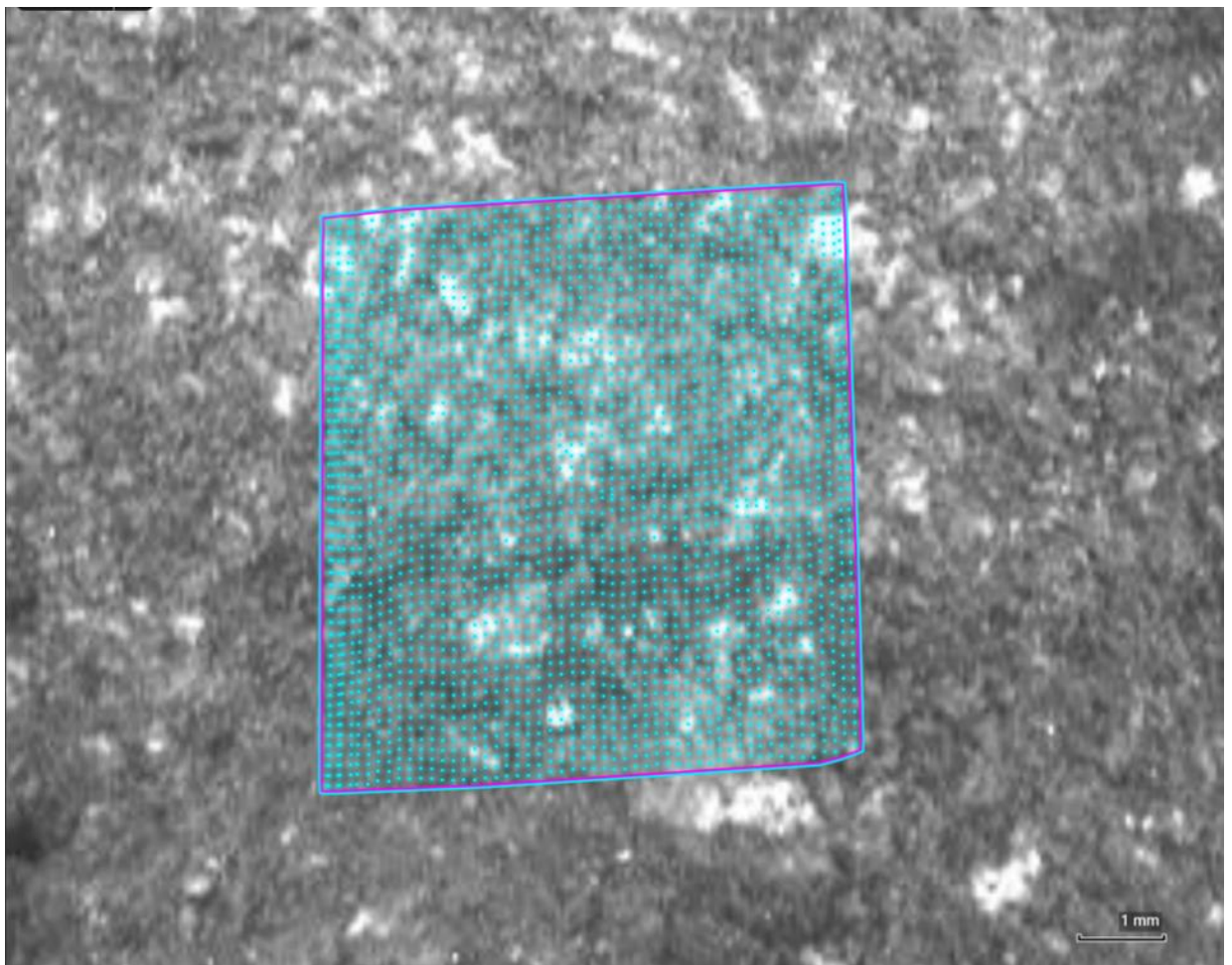


Figure 3-11: Guillaume (sol 167) abrasion target with co-registered PIXL scan. Each blue point represents a $\sim 120\ \mu\text{m}$ PMC and the pink-blue line encloses the map area (Background MCC image: PCW_0167_0681701844_000RCM_N00600000631116810003075J05)

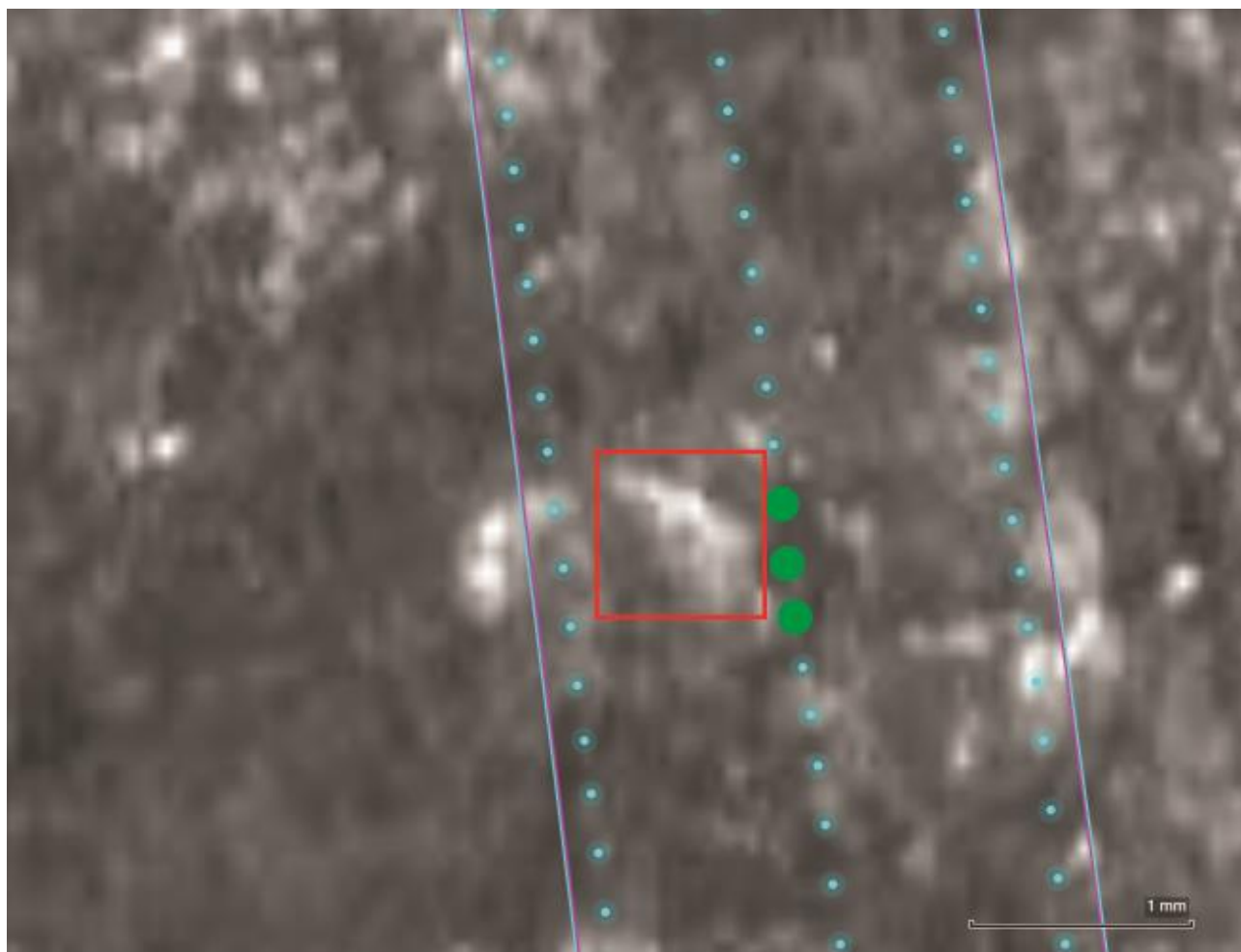


Figure 3-12: Montpezat (Sol 347) abrasion and associated PIXL 3-line scan. Each blue point represents an $\sim 120\ \mu\text{m}$ PIXL PMC. The red square surrounds a lightly coloured mineral that PMCs 201, 202 and 203 (green circles) likely missed due to the distance between lines (Background MCC image: PCW_0347_0697754573_000RCM_N00929821225528370003075J01.png). A secondary square PIXL scan was used to measure mineral abundance to compare with preserved abrasion marks.

Table 3-2: Chemical descriptions and example minerals for each mineral group included in this study¹.

Mineral Groups	General Description
Low Salt	<p>SiO₂-rich, SO₃ and Cl poor. Primary igneous material.</p> <p>This mineral group includes:</p> <ul style="list-style-type: none"> • Olivine e.g., (Mg, Fe)₂SiO₄ • Pyroxene e.g.,. Augite ((Ca,Na)(Mg,Fe,Al)(Si,Al)₂O₆) • Aluminosilicate e.g., Sanidine/Orthoclase/Microcline (KAlSi₃O₈) • Oxides e.g., Magnetite (Fe₃O₄) and Ilmenite (FeTiO₃) • Phosphates e.g., Apatite (Ca₅(PO₄)₃F)
High Salt	<p>SiO₂-poor, SO₃ and Cl rich. Secondary salt-rich materials.</p> <p>This mineral group includes:</p> <ul style="list-style-type: none"> • Halite e.g., (NaCl) • Anhydrite e.g., (CaSO₄) • Magnesium Sulfate e.g., (MgSO₄) • Perchlorate e.g., (NaClO₂)
Alteration	<p>Fe-rich, SiO₂-poor and/or SO₃ and Cl-rich secondary alteration material.</p> <p>This mineral group includes:</p> <ul style="list-style-type: none"> • Magnesite e.g., MgCO₃ • More Ferroan Carbonates e.g., (Mg,Fe)CO₃

¹(Schmidt et al., in prep.)

Table 3-3: Expression values used to select and sort PMCs into mineral groups

Campaign	Sol	Name	Rock Type	Expression Values
Crater Floor	167	Guillaumes ¹	Igneous	Low Salt: <2 wt% SO ₃ , <4 wt % Cl High Salt: >2 wt% SO ₃ , >4 wt% Cl
	187	Bellegarde ¹	Igneous	Low Salt: <4.85% SO ₃ , <3 wt% Cl High Salt: >4.85% SO ₃ , >3 wt% Cl
	257	Dourbes ¹	Igneous	Low Salt: <10 wt% SO ₃ Alteration: >35 wt% FeO, <30 wt% SiO ₂ High Salt: >10 wt% SO ₃
	294	Quartier ¹	Igneous	Low Salt: <7.5 wt% SO ₃ Alteration: >35 wt% FeO, <30% SiO ₂ High Salt: >7.5 wt% SO ₃
	364	Montpezat ¹	Igneous	Low Salt: <1.5 wt% SO ₃ , <1.5 wt% Cl Alteration: >1.5 wt% SO ₃ , >1.5 wt% Cl High Salt: > 1.5 wt% SO ₃
	367	Alfalfa ¹	Igneous	Low Salt: <2% SO ₃ , <4% Cl Alteration: >4 wt% Cl, <2 wt% SO ₃ High Salt: >2 wt% SO ₃
Delta Front	484	Thornton Gap	Sedimentary	Low Salt: <10 wt% SO ₃ , <10 wt% Cl Alteration: >20 wt% FeO, <20 wt% SiO ₂ High Salt: >10 wt% SO ₃ , >10 wt% Cl
	505	Berry Hollow	Sedimentary	Low Salt: <15 wt% SO ₃ Medium Salt: 25 > x > 15 wt% SO ₃ High Salt: >25 wt% SO ₃
	570	Novarupta	Sedimentary	Low Salt: <5% wt% SO ₃ Alteration: <25 wt% SiO ₂ High Salt: >5% wt% SO ₃
	617	Uganik Island	Sedimentary	Low Salt: <15 wt% SO ₃ Medium Salt: 35 > x > 15 wt% SO ₃ High Salt: >35 wt% SO ₃

¹Expression values given by Schmidt et al. (in prep)

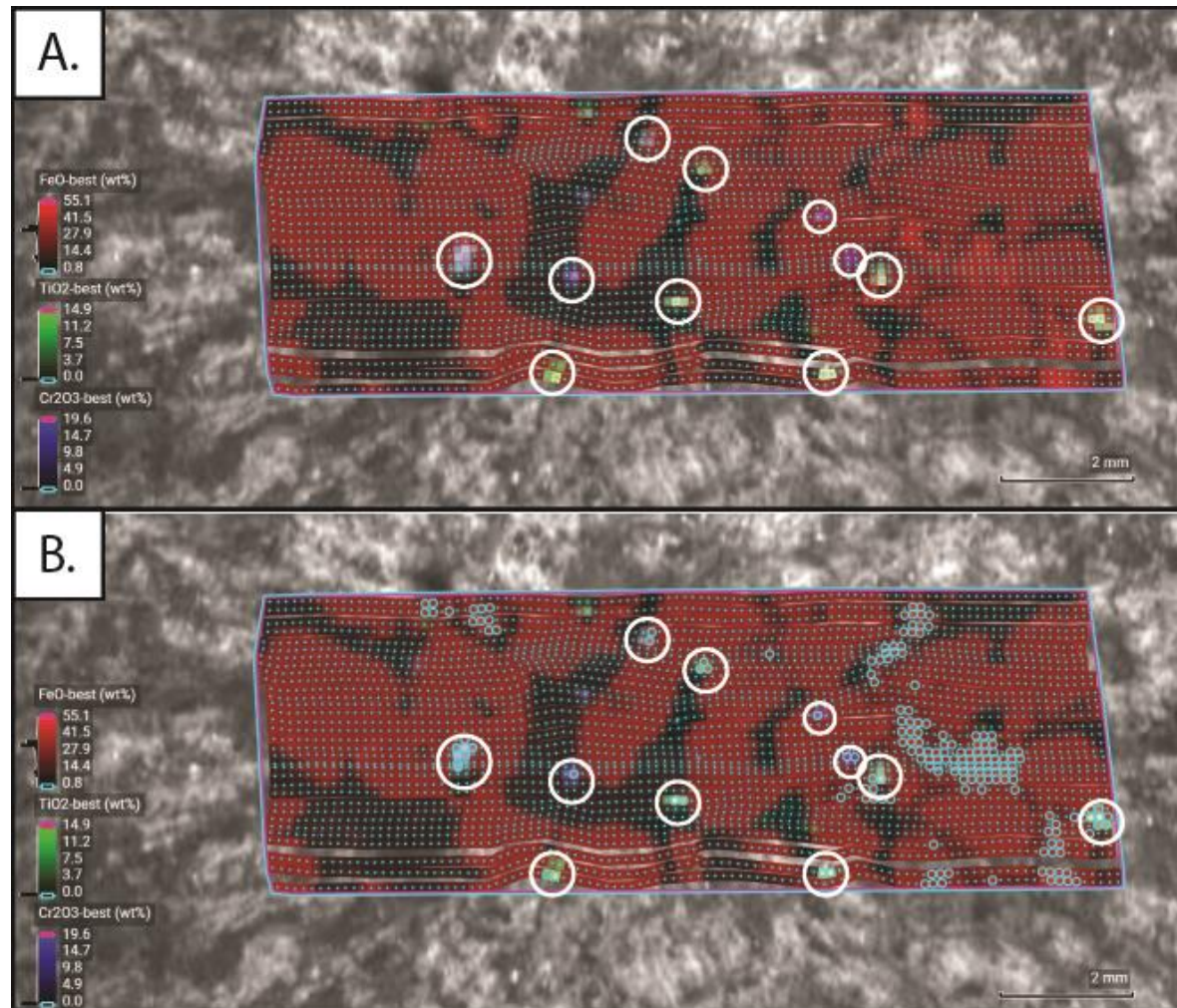


Figure 3-13: Dourbes (Sol 257) abrasion patch and the co-registered PIXL scan and MCC image (PCW_0257_0689790669_000RCM_N00800000890639430006075J01). A FeO-TiO₂-Cr₂O₃ RGB colour mixed image overlays the MCC image. (A.) Shows all the PIXL PMCs (small blue circles). White circles show regions where igneous oxides were identified. (B.) PMC selection (hollow blue circles) using the FeO/SiO₂ expression from Table 3-3. This expression selected carbonate and igneous oxides minerals present in Dourbes, requiring manual deselection of oxide PIXL PMCs.

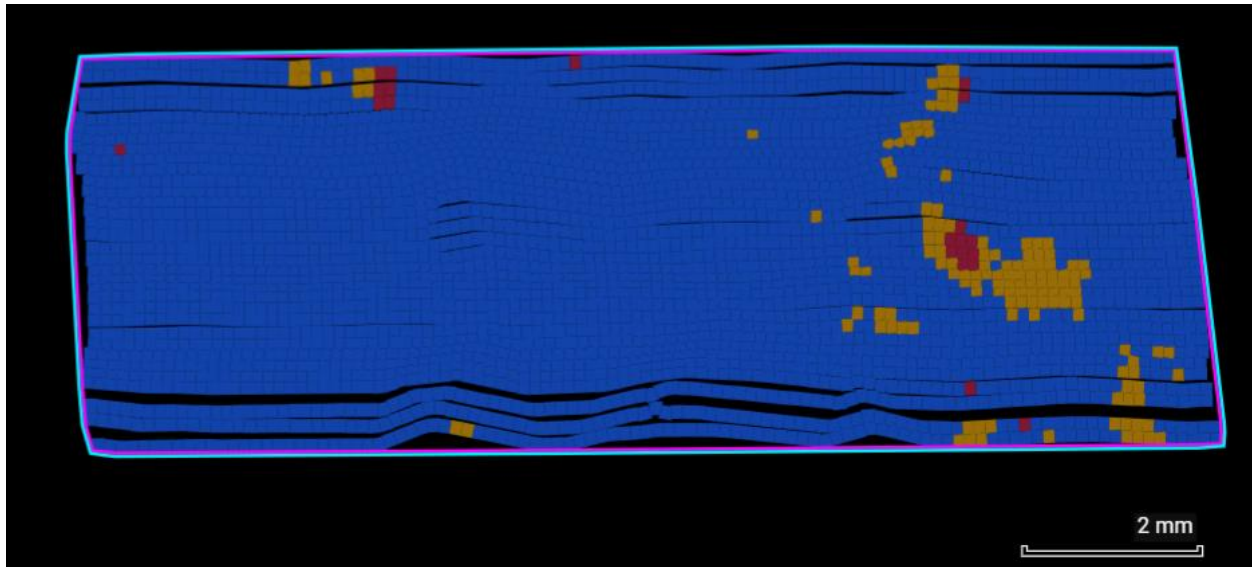


Figure 3-14: Map of High Salt (red), Alteration (yellow), and Low Salt (blue) ROIX for Dourbes (sol 257).

3.3.3 Measuring Abrasions

Adobe Illustrator (AI) and QGIS are the two software used to map and measure abrasion marks within each abrasion patch. AI is a versatile vector-based, image editing, and artwork software capable of exporting file formats usable in QGIS. QGIS (v3.28.2 Firenze) is a free, open-source software for creating, editing and analyzing geospatial information.

Abrasion Mark Tracing

The highest-resolution SHERLOC-WATSTON images were opened and overlaid in AI. Each abrasion mark was manually traced using the *Pen Tool*, which creates a vector-line (also known as a path). This tool was also used to trace the scale bar, whose length would later be used to normalize all other abrasion lengths. Each continuous linear etch mark preserved in the target surface was considered an abrasion mark. This definition would also include features such as mineral cleavages and fractures. While they are not ‘abrasion marks,’ mineral cleavage and fractures are linear rock features that form in response to stresses, in this case, those produced during abrasion. They were therefore considered as ‘abrasion marks’ in this study. Satisfied with the abrasion traces, the ungrouped paths were transferred to a new document absent of any background images and exported as an AutoDesk RealDWG(.dxf) file.

Vectorizing ROIs

To quantify abrasion mark lengths and abundance within each mineral group, the PIXLISE ROIs (Figure 3-14) needed to be vectorized. Screen captures from PIXLISE were opened in AI and positioned above the high-resolution SHERLOC-WATSON images from Section 3.4.1. The *Image Trace* tool in AI was used to separate each ROI into individual paths. The *Image Trace* tool classifies the selected image into a user-defined number of colour classes; more classes preserve the resolution and the boundaries between shapes, however fewer classes forces AI to merge edges of similar coloured pixels together, and distorts ROIs when converted in vectorized shapes. To avoid distortion and to preserve ROI shapes, more user-defined classes were assigned. The *Image Trace* product creates a thin, darker coloured border around each PIXL PMC that needs to be preserved. Deleting this border would form hundreds of disconnected shapes that would create hundreds of smaller paths if used as the abrasion mark clipping mask. To avoid this problem, the borders were changed to the same colour as the ROI, grouped together and changed into a *Compound Path*. Combining the borders and PMCs as a *Compound Path* is essential. Skipping this step keeps each PIXL PMC as an individual paths, and the problem would persist. Three compound paths, one for each mineral type (Low Salt, High Salt, and Alteration), were generated for each PIXL scan and were exported as an AutoDesk RealIDWG (.dxf) file. Exporting them as the same file type as the abrasion trace preserves their position relative to the abrasion trace.

Clipping Abrasion Marks to ROI and Measurements

The AutoDesk Real DWG (.dxf) files for the abrasion marks and mineral ROIs were opened in QGIS as vector layers and projected to the EPSG:357 WGS 84: Pseudo Mercator coordinate system. Projecting these layers allowed them to be measured in QGIS. The *Field Calculator* was used to measure the length of each abrasion mark using the \$length function. These values were then exported to Microsoft Excel, and their values were normalized the known length of the scale bar.

The \$area function from the *Field Calculator* was then used on the compound paths from Section 3.4.2 and the PIXL FOV to measure their respective areas. These values were then divided by PIXL FOV's area to calculate how much of its area is occupied by each mineral type. The

percent areal abundance of Low Salt, High Salt and Alteration mineral types were then subtracted from the PIXL FOV's area to find the area of missing data. This missing PIXL data can be caused by diffraction scattering due to surface roughness and thermal drift of the RA during the PIXL scan.

The abrasion marks were then clipped to mineral type *Compound Paths* to measure the abrasion mark abundance within each mineral type. These abrasion lengths were then measured using the *\$length* function in the *Field Calculator*. Similar to before, these values were then exported to Microsoft Excel, and their values were normalized to the known length of the scale bar.

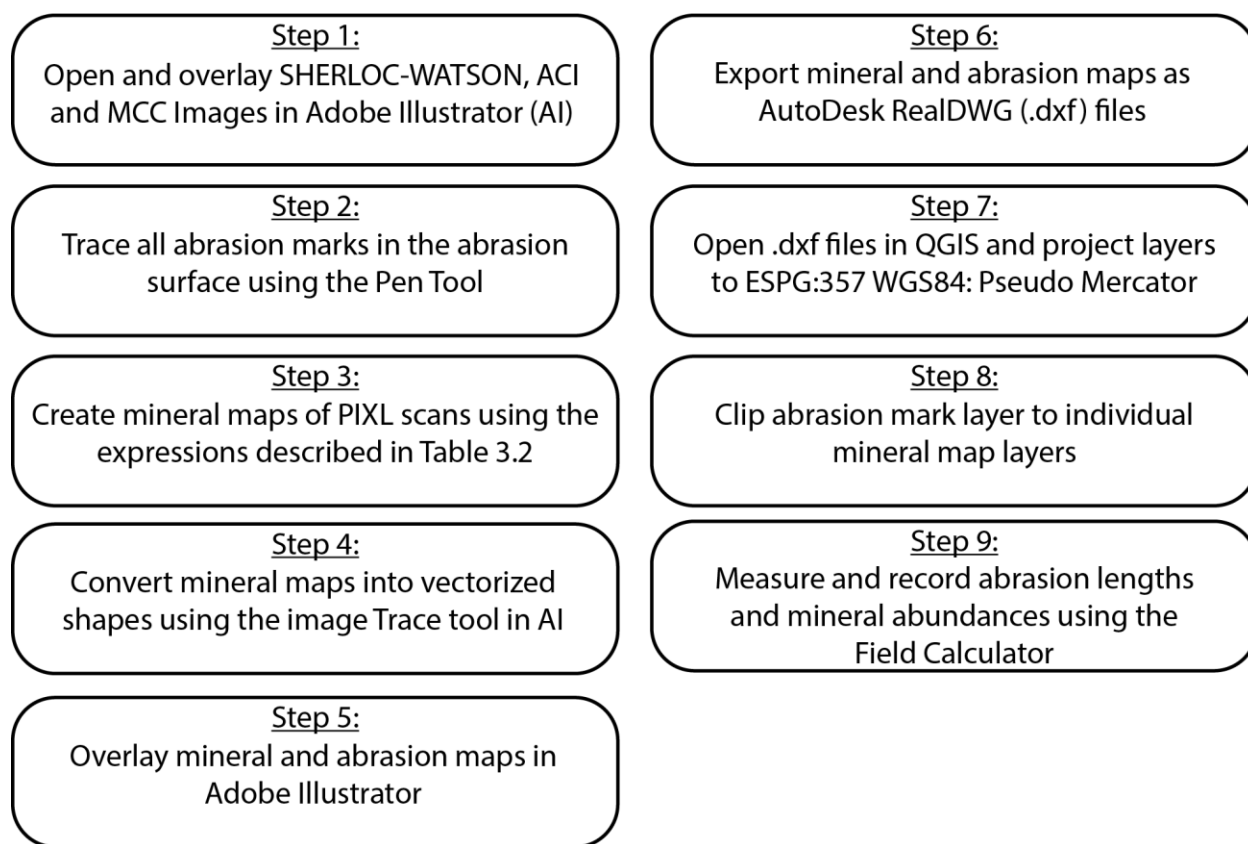


Figure 3-15: Stepwise list of the methods used to produce map and measure abrasion mark abundances within each mineral group.

3.5 References

- Allwood, A. C., Wade, L. A., Foote, M. C., Elam, W. T., Hurowitz, J. A., Battel, S., Dawson, D. E., Denise, R. W., Ek, E. M., Gilbert, M. S., King, M. E., Liebe, C. C., Parker, T., Pedersen, D. A. K., Randall, D. P., Sharrow, R. F., Sondheim, M. E., Allen, G., Arnett, K., ... Zimmerman, R. (2020). PIXL: Planetary Instrument for X-Ray Lithochemistry. *Space Science Reviews*, 216(8), 134. <https://doi.org/10.1007/s11214-020-00767-7>
- Berger, J. A., Gellert, R., Boyd, N. I., King, P. L., McCraig, M. A., O'Connell-Cooper, C. D., Schmidt, M. E., Spray, J. G., Thompson, L. M., VanBommel, S. J. V., & Yen, A. S. (2020). Elemental Composition and Chemical Evolution of Geologic Materials in Gale crater, Mars: APXS Results From Bradbury Landing to the Vera Rubin Ridge. *Journal of Geophysical Research: Planets*, 125(12), e2020JE006536. <https://doi.org/10.1029/2020JE006536>
- Bhartia, R., Beegle, L. W., DeFlores, L., Abbey, W., Razzell Hollis, J., Uckert, K., Monacelli, B., Edgett, K. S., Kennedy, M. R., Sylvia, M., Aldrich, D., Anderson, M., Asher, S. A., Bailey, Z., Boyd, K., Burton, A. S., Caffrey, M., Calaway, M. J., Calvet, R., ... Zan, J. (2021). Perseverance's Scanning Habitable Environments with Raman and Luminescence for Organics and Chemicals (SHERLOC) Investigation. *Space Science Reviews*, 217(4), 58. <https://doi.org/10.1007/s11214-021-00812-z>
- Edgett, K., Caplinger, M., Maki, J., Ravine, M., Ghaemi, F., McNair, S., Herkenhoff, K., Duston, B., Willson, R., Yingst, R., Kennedy, M., Minitti, M., Sengstacken, A., Supulver, K., Lipkaman, L., Krezoski, G., Henderson, M., Jones, T., Nixon, B., & Kirk, R. (2015). *Curiosity's robotic arm-mounted Mars Hand Lens Imager (MAHLI): Characterization and calibration status*. <https://doi.org/10.13140/RG.2.1.3798.5447>
- Edgett, K. S., Yingst, R. A., Ravine, M. A., Caplinger, M. A., Maki, J. N., Ghaemi, F. T., Schaffner, J. A., Bell, J. F., Edwards, L. J., Herkenhoff, K. E., Heydari, E., Kah, L. C., Lemmon, M. T., Minitti, M. E., Olson, T. S., Parker, T. J., Rowland, S. K., Schieber, J., Sullivan, R. J., ... Goetz,

- W. (2012). Curiosity's Mars Hand Lens Imager (MAHLI) Investigation. *Space Science Reviews*, 170(1), 259–317. <https://doi.org/10.1007/s11214-012-9910-4>
- Farley, K. A., Stack, K. M., Shuster, D. L., Horgan, B. H. N., Hurowitz, J. A., Tarnas, J. D., Simon, J. I., Sun, V. Z., Scheller, E. L., Moore, K. R., McLennan, S. M., Vasconcelos, P. M., Wiens, R. C., Treiman, A. H., Mayhew, L. E., Beyssac, O., Kizovski, T. V., Tosca, N. J., Williford, K. H., ... Zorzano, M.-P. (2022). Aqueously altered igneous rocks sampled on the floor of Jezero crater, Mars. *Science*, 377(6614), eabo2196. <https://doi.org/10.1126/science.abo2196>
- Farley, K. A., Williford, K. H., Stack, K. M., Bhartia, R., Chen, A., de la Torre, M., Hand, K., Goreva, Y., Herd, C. D. K., Hueso, R., Liu, Y., Maki, J. N., Martinez, G., Moeller, R. C., Nelessen, A., Newman, C. E., Nunes, D., Ponce, A., Spanovich, N., ... Wiens, R. C. (2020). Mars 2020 Mission Overview. *Space Science Reviews*, 216(8), 142. <https://doi.org/10.1007/s11214-020-00762-y>
- Gorevan, S. P., Myrick, T., Davis, K., Chau, J. J., Bartlett, P., Mukherjee, S., Anderson, R., Squyres, S. W., Arvidson, R. E., Madsen, M. B., Bertelsen, P., Goetz, W., Binau, C. S., & Richter, L. (2003). Rock Abrasion Tool: Mars Exploration Rover mission. *Journal of Geophysical Research: Planets*, 108(E12). <https://doi.org/10.1029/2003JE002061>
- Grotzinger, J. P., Crisp, J., Vasavada, A. R., Anderson, R. C., Baker, C. J., Barry, R., Blake, D. F., Conrad, P., Edgett, K. S., Ferdowski, B., Gellert, R., Gilbert, J. B., Golombek, M., Gómez-Elvira, J., Hassler, D. M., Jandura, L., Litvak, M., Mahaffy, P., Maki, J., ... Wiens, R. C. (2012). Mars Science Laboratory Mission and Science Investigation. *Space Science Reviews*, 170(1), 5–56. <https://doi.org/10.1007/s11214-012-9892-2>
- Jens, E., Nakazono, B., Brockie, I., Vaughan, D., & Klatte, M. (2018). Design, development and qualification of a gas-based dust removal tool for mars exploration missions. *2018 IEEE Aerospace Conference*, 1–8. <https://doi.org/10.1109/AERO.2018.8396448>
- Landis, G. A. (1997). Mars dust removal technology. *IECEC-97 Proceedings of the Thirty-Second Intersociety Energy Conversion Engineering Conference (Cat. No.97CH6203)*, 1, 764–767 vol.1. <https://doi.org/10.1109/IECEC.1997.659288>

- Lemmon, M. T., Wolff, M. J., Smith, M. D., Clancy, R. T., Banfield, D., Landis, G. A., Ghosh, A., Smith, P. H., Spanovich, N., Whitney, B., Whelley, P., Greeley, R., Thompson, S., Bell, J. F., & Squyres, S. W. (2004). Atmospheric Imaging Results from the Mars Exploration Rovers: Spirit and Opportunity. *Science*, 306(5702), 1753–1756. <https://doi.org/10.1126/science.1104474>
- Moeller, R. C., Jandura, L., Rosette, K., Robinson, M., Samuels, J., Silverman, M., Brown, K., Duffy, E., Yazzie, A., Jens, E., Brockie, I., White, L., Goreva, Y., Zorn, T., Okon, A., Lin, J., Frost, M., Collins, C., Williams, J. B., ... Biesiadecki, J. (2020). The Sampling and Caching Subsystem (SCS) for the Scientific Exploration of Jezero crater by the Mars 2020 Perseverance Rover. *Space Science Reviews*, 217(1), 5. <https://doi.org/10.1007/s11214-020-00783-7>
- Schmidt, M. E., Perrett, G. M., Bray, S. L., Bradley, N. J., Lee, R. E., Berger, J. A., Campbell, J. L., Ly, C., Squyres, S. W., & Tesselaar, D. (2018). Dusty Rocks in Gale crater: Assessing Areal Coverage and Separating Dust and Rock Contributions in APXS Analyses. *Journal of Geophysical Research: Planets*, 123(7), 1649–1673. <https://doi.org/10.1029/2018JE005553>
- Tice, M. M., O'Neil, L. P., Clark, B. C., Ganly, B. P., Jones, M. W., Orenstein, B. J., . . . Hurowitz, J. A. (2023). PIXL on Perseverance as a Complete X-Ray Spectroscopic Instrument: ANalyzing X-Ray Fluorescence, Scattering, and Diffraction of Martian Rocks. *54th Lunar and Planetary Science Conference 2023*, (p. 2). The Woodlands, Texas. Retrieved from <chrome-extension://efaidnbmnnnibpcajpcglclefindmkaj/https://www.hou.usra.edu/meetings/lpsc2023/pdf/2659.pdf>
- Vasavada, A. R., Grotzinger, J. P., Arvidson, R. E., Calef, F. J., Crisp, J. A., Gupta, S., Hurowitz, J., Mangold, N., Maurice, S., Schmidt, M. E., Wiens, R. C., Williams, R. M. E., & Yingst, R. A. (2014). Overview of the Mars Science Laboratory mission: Bradbury Landing to Yellowknife Bay and beyond. *Journal of Geophysical Research: Planets*, 119(6), 1134–1161. <https://doi.org/10.1002/2014JE004622>

- Wiens, R. C., Maurice, S., Barraclough, B., Saccoccio, M., Barkley, W. C., Bell, J. F., Bender, S., Bernardin, J., Blaney, D., Blank, J., Bouyé, M., Bridges, N., Bultman, N., Caïs, P., Clanton, R. C., Clark, B., Clegg, S., Cousin, A., Cremers, D., ... Wong-Swanson, B. (2012). The ChemCam Instrument Suite on the Mars Science Laboratory (MSL) Rover: Body Unit and Combined System Tests. *Space Science Reviews*, 170(1–4), 167–227. <https://doi.org/10.1007/s11214-012-9902-4>
- Williams, A., Russell, P. S., Sun, V., Shuster, D., Stack, K. M., Farley, K., . . . Wadhwa, M. (2023). Exploring the Joezero delta front: Overview of results from the Mars 2020 Perseverance rover's second science campaign. *54th Lunar and Planetary Science Conference 2023*.
- Wolff, M. J., & Clancy, R. T. (2003). Constraints on the size of Martian aerosols from Thermal Emission Spectrometer observations. *Journal of Geophysical Research: Planets*, 108(E9). <https://doi.org/10.1029/2003JE002057>
- Wolff, M. J., Smith, M. D., Clancy, R. T., Spanovich, N., Whitney, B. A., Lemmon, M. T., Bandfield, J. L., Banfield, D., Ghosh, A., Landis, G., Christensen, P. R., Bell, J. F., & Squyres, S. W. (2006). Constraints on dust aerosols from the Mars Exploration Rovers using MGS overflights and Mini-TES. *Journal of Geophysical Research: Planets*, 111(E12). <https://doi.org/10.1029/2006JE002786>
- Ye, C., Hermann, L., Yildirim, N., Bhat, S., Moritz, D., & Davidoff, S. (2021). *PIXLISE-C: Exploring The Data Analysis Needs of NASA Scientists for Mineral Identification* (arXiv:2103.16060). arXiv. <https://doi.org/10.48550/arXiv.2103.16060>
- Yingst, R. A., Edgett, K. S., Kennedy, M. R., Krezoski, G. M., McBride, M. J., Minitti, M. E., Ravine, M. A., & Williams, R. M. E. (2016). MAHLI on Mars: Lessons learned operating a geoscience camera on a landed payload robotic arm. *Geoscientific Instrumentation, Methods and Data Systems*, 5(1), 205–217. <https://doi.org/10.5194/gi-5-205-2016>

Chapter 4: Surface dust coverages on rock targets in Gale crater: Influence of seasonal wind variability, elevation and proximity to aeolian sand fields.

Henley T.L.J., Schmidt M.E., Bray S.L., Bradley N.J., Lee R.E., Marincic I.K., Turner K.W.

4.1 Abstract:

Dust particles mobilized during regional, and global dust storms, increase atmospheric opacity, inhibiting orbital observations of the Martian surface. Despite the prevalence of dust and sand particles, the precise mechanisms facilitating their movement and suspension are not well understood. Regional and seasonal winds mix and mobilize these suspended particles, producing a homogenized dust composition that blankets the Martian terrain beneath a thin variegated layer. Using Mars Hand Lens Imager (MAHLI) images and methods described by Schmidt et al. (2018), we estimated 6 Mars Years (MY) of dust coverages across 697 rock targets imaged along the Mars Science Laboratory (MSL) *Curiosity* rover's geologic traverse (Sols 0-3409) and evaluated potential geospatial and seasonal (Ls) correlations. Selected targets include undisturbed deposits of airfall dust, referred to in this study as "As Is" targets, and surfaces that have been partially cleared using *Curiosity*'s Chemistry and Camera (ChemCam; a laser-induced breakdown spectrometer) and stainless-steel wire-bristle Dust Removal Tool (DRT). Partially cleared surfaces by the ChemCam ($n = 77$), and DRT ($n = 221$), have dust coverages ranging from 1.2% to 64.1% and 1.2% to 60.4% respectively. The highest dust coverages for each Mars year were recorded before reaching aphelion (Ls 70°), with dust accumulations gradually decreasing towards southern summer (Ls 270°-360°). The highest dust coverage (76.6%) was found for rock targets at the top of Vera Rubin Ridge at the start of MY34, before the MY34 global dust storm. Subsequent New Years maximum's have decreased by approximately 15% annually (MY35 60.7%, and MY36 45.7%), suggesting that dust is less abundant at higher elevations, or that the atmospheric dust load has increased since the MY34 dust storm. Two regions of low dust coverage (<20%) were found in close proximity to aeolian sand dune deposits, that likely result from saltating sand particles striking and lofting dust particles. This study provides the first long-term *in situ* surface measurements of Martian dust, furthering our understanding and providing another perspective to active sediment transport across the surface of Mars. The ascent of Vera

Rubin Ridge recorded the highest dust maximum, 76.8%, at the start of MY34. New Year maxima in subsequent years have decreased by ~15% annually (MY35 60.7%, and MY36 45.7%), indicating that dust particles are less abundant at higher elevations. Two sequences of low dust coverage targets (<20%) were recorded during MSL in proximity to aeolian sand dune deposits, thought to be caused by additional dust removal by saltating sand particles. With previous studies relying on orbital observations to understand dust mobility, this study provides *in situ* surface measurements of Martian dust, furthering our understanding and providing another perspective to active sediment transport across the surface of Mars.

4.2 Introduction:

The Martian surface is covered by a thin, variable layer of fine-grained dust that is periodically mobilized by regional and less frequent planet-encircling, global dust storms before re-settling at the surface. Dust particles on the surface and suspended in Martian atmosphere require careful consideration when interpreting orbital and *in situ* results, as it may contribute up to 10% uncertainty in chemical quantifications (Czarnecki et al., 2022; Schmidt et al., 2018). Dust mobility at the surface and in the thin Martian atmosphere require consideration when interpreting orbital and *in situ* results. Dust also affects hardware, including solar panels, where dust build up has led or contributed to mission end for all solar-powered spacecraft (e.g., Pathfinder/Sojourner; Landis, 1996; Crisp et al., 2004; Phoenix et al., 2009; Stella et al., 2009; Mars Exploration Rovers Spirit and Opportunity; J. A. Crisp et al., 2003; InSight, Lorenz et al., 2020). For the nuclear-powered Mars Science Laboratory (MSL) in Gale crater, accumulations of air fall dust on rover hardware have been found to vary over time (Yingst et al., 2020). Dust also affects the interpretation of textural information in microscopic images captured by the Mars Hand Lens Imager (MAHLI; Edgett et al., 2012; Greeley et al., 2006), as well as elemental compositions determined by the Alpha Particle X-Ray Spectrometer (APXS; Schmidt et al., 2018).

With an estimated exchange of 2.9×10^{12} kg/yr of dust between the Mars surface and atmosphere (Pollack et al., 1979), dust aerosols are always present in the Martian atmosphere (Smith et al., 2000). Dust aerosols significantly affect the present-day Mars surface and atmospheric temperatures by absorbing and scattering radiant energy at the visible and infrared wavelengths (Pollack et al., 1977, 1979). Seasonal fluxes of dust aerosols and increasing solar

insolation as Mars approaches perihelion (Solar longitude (Ls) $\sim 251^\circ$; Baker et al., 2018; Newman et al., 2002a, 2002b; Smith et al., 2000) has led the Martian year to be divided into two distinct intervals: the “Dusty” and “Non-Dusty” seasons (Haberle et al., 2017; J. Liu et al., 2003; Smith, 2004, 2008). The “Non-Dusty” season (Ls 0-135°) spans from the start of spring until halfway through summer in Northern Hemisphere, and inversely, autumn until halfway through winter in the Southern Hemisphere (Haberle et al., 2017; Figure 4-1). During this period, the gravitational settling of dust decreases atmospheric opacity and increases surface deposits of airfall dust as dust is removed from the atmosphere (Vicente-Retortillo et al., 2018). The remaining time period (Ls 135-360°), termed the “Dusty” season, is characterized by increased atmospheric opacity (Haberle et al., 2017) and indicates dust lifting exceeds gravitational settling during this period (Vicente-Retortillo et al., 2018).

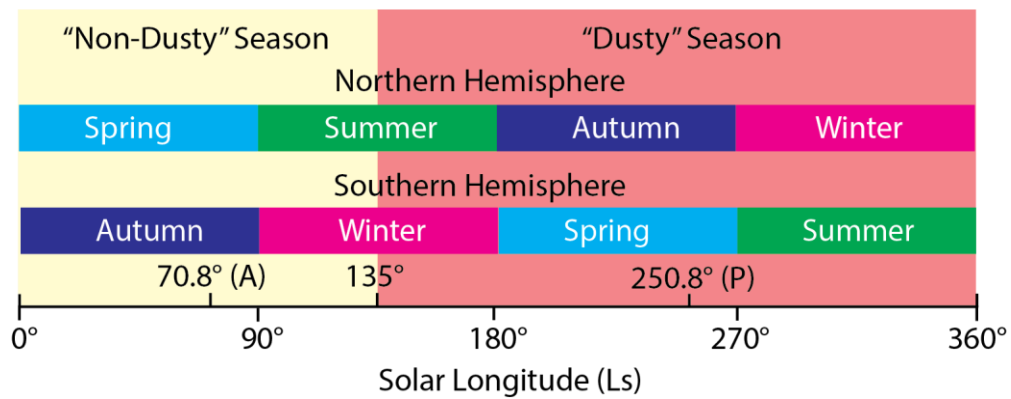


Figure 4-1: The solar longitude ($^\circ$; Ls) and timing of the “Non-Dusty” and “Dusty” seasons (described by Haberle et al. 2017) plotted against the regular seasons of the northern and southern hemispheres. The aphelion (A) and perihelion (P) orbital positions are also plotted.

The first observation of Mars dust storms described yellow clouds on the surface of Mars by French amateur astronomer Honore Flaugergue, dates back to the early 1800s. The precise mechanisms to loft dust and suspend it in the Martian atmosphere are not well quantified. (Newman et al., 2002a, 2002b). Particle mobility is initiated as wind speeds overcome the force of gravity and static friction, moving a particle from rest into motion, termed *static* threshold (Bagnold, 1941; Greeley, 2002). The thin Martian atmosphere hinders aeolian sediment transport, requiring significantly higher wind speeds to initiate particle movement. Using the minimum wind speeds needed to mobilize particles on Earth (Sagan & Pollack, 2020), laboratory

simulations of the Martian environment found that the lowest friction velocities were able to mobilize particles 80-100 μm in diameter were most easily mobilized (Greeley, 2002). To overcome the gravitational force of larger grains, and the interparticle surface and electrochemical forces (i.e., cohesion) of smaller particles, greater friction velocities are required (Fletcher, 1976). While previous studies suggest surface winds would rarely exceed the threshold value required to mobilize sand-sized particles (Pollack et al., 1977, 1979; P. H. Smith et al., 1997), ground-based observations of active ripple migration (M. M. Baker, Lapotre, et al., 2018), variable atmospheric opacities (Korablev et al., 2005), and observed regional and global dust storms demonstrate that this is not the case. Further complicating the dust conundrum, dust aerosols suspended in the lower atmosphere ($\sim 10\text{-}40$ km altitude) are ~ 1.0 μm (Guzewich et al., 2014), a measurement corroborated by studies that span multiple missions (Clancy et al., 1995; Pollack et al., 1995; Toon et al., 1977; Wolff et al., 2006; Wolff & Clancy, 2003). The inherent stickiness of dust means that these clay-sized dust particles require wind speeds which exceed the static threshold of coarse sand to be suspended (Greeley, 2002).

Despite dust being recognized as an important feature on Mars since Viking (Pollack et al., 1979), its origin(s) remain enigmatic. *In situ* observations of Martian dust by the MSL APXS found that it is enriched in S and Cl, at a constant S/Cl of 3.7 ± 0.7 with an otherwise basaltic composition similar to average Mars crust (Berger et al., 2016; Taylor & McLennan, 2009; VanBommel et al., 2016). Contrary to terrestrial dust, which have a quartz-rich granitic lithology, Martian dust is rich in feldspar with minor amounts of olivine, pyroxene, amorphous phases and magnetite (Hamilton et al., 2005; Madsen et al., 2009; Ruff, 2004). Since global and smaller, regional storms suspend and mix dust particles in the Martian atmosphere, these events have produced a globally homogeneous dust unit (Yen et al., 2005, 2013). However the abundance of Martian dust suggests that a single source is highly unlikely. Martian dust likely derives from a variety of sources, similar to those on Earth: glacial grinding, frost shattering, fluvial comminution, volcanism, aeolian abrasion, and salt weathering (Derbyshire et al., 1998; Whalley & McGreevy, 1983; Wright et al., 1998; Wright, 2001). The abundance of volcanoes at the Martian surface, with indicators of explosive volcanism, and a basaltic composition that is similar to the Martian crust, ancient ash deposits may be a significant contributor to the Martian dust

reservoir (Bandfield et al., 2013; Wilson & Head, 2007). In particular, the yardang fields of the Medusa Fossae Formation and the surrounding area have the highest enrichments of S and Cl across the Martian surface, and share a similar S/Cl ratio to Martian dust, making them another likely source of Martian dust (Ojha et al., 2018; Ojha & Lewis, 2018).

Orbital observations have been used to quantify and record dust activity across Mars (e.g., Wu et al., 2022; Newman et al., 2022; Douté et al., 2014). Only recently have in situ studies sought to quantify dust abundance and activity across the Martian surface. Martian dust devils, vortices formed in unstable atmospheric conditions and heating on and near planetary surfaces (Balme et al., 2003), have been observed at the landing sites of the Mars Pathfinder (MPF; e.g., Metzinger et al., 1999; Smith & Lemmon, 1999), Spirit (e.g., Greeley et al., 2006) and Phoenix Mars (e.g., Ellehoy et al., 2010). These events are most common mid-day during the “Dusty” southern spring and summer seasons, suspending dust particles and leaving low-albedo streaks in their path (Greeley et al., 2010). Individual dust devils persist for only brief periods, approximately 3 minutes (Greeley et al., 2010), limiting their contributions of dust to global atmospheric dust content.

By quantifying the abundance of dust on horizontal rock surfaces in Gale crater over >25km (sols 46-3409 or 6 Mars Years,) we investigate how changes in seasonal atmospheric conditions, elevation, and eolian activity affect dust abundance at the Mars surface. This study focusses on microscopic MAHLI images of rock targets examined by the APXS, expanding upon and using the methods developed by Schmidt et al. (2018). BeFunky.com, a free online photo editing website, was used to brighten shaded regions, increase the color contrast between dust grains and the underlying rock surface, sharpen edges between features, and apply a filter that enhances the red saturation of dust particles and the blue of the underlying rock surface. Adobe Photoshop was the final image editing software used in this study. Photoshop allows the user to manually edit images and features for pixel-based images, raster graphics and vector graphics.

4.3 Methods

This section includes a condensed explanation of the methods used in Chapter 4. This information is described in greater detail in Section 3.2.

To understand the distribution of Martian airfall dust, we use high-resolution microscopic images taken by the MSL MAHLI instrument, a 2-megapixel color camera with a focusable macro lens attached to the end of the Curiosity rover's arm (Edgett et al., 2012). The best pixel scale for MAHLI is 14 μm x 14 μm , giving image products a best resolution of 28-42 μm . Individual dust particles (~ 1.0 μm) are smaller than MAHLI pixel scale, however the inherent stickiness of dust causes it to form scattered, approximately coarse silt-size (31-63 μm ; Wentworth, 1922) clumps that are resolvable in image products. We use the highest-resolution, lowest standoff focus merge images, which are a stack of images acquired from multiple focus positions from a single standoff height, that are merged together using software onboard the rover or on Earth. The image products are available on the Planetary Data System (PDS) image node (<http://pds-geosciences.wustl.edu/missions/msl/>). Range and scale are found using the focus motor count associated with each image (K. Edgett et al., 2015; Yingst et al., 2016).

Schmidt et al. (2018) developed three methods for determining dust coverage on rock surfaces, making use of the narrow color range of Mars dust (Bell III et al., 2000) and texture to differentiate it from underlying surfaces. Lighting conditions (full sunlight, partial and full shadow, and white light (LED) illumination during nighttime observation) vary between samples. Detailed instructions for the three methods used in this study are detailed in Schmidt et al. (2018); only brief descriptions are below. For each of these methods the dust coverages were recorded within a 1.7mm diameter circle at the center of each MAHLI image to represent the APXS FOV. This was done to correlate our dust measurements with chemical datasets, and to reduce vignetting effects towards the edges of MAHLI images. Dust measurements typically varied by less than 5% but could exceed 10% due to poor lighting conditions (time of day and shadows from the rover's instrumentation). Method 1 changes images to 8-bit greyscale, decreasing the visibility of dust grains in shaded regions, and generated comparatively lower dust abundances to the other methods. In these instances, Method 1 was still performed and would result in larger variations between dust measurements, or it was omitted if lighting conditions were too poor. The final dust measurement is the averaged dust coverages between the three methods, and would be reduced to methods 2 and 3 when lighting conditions prevented an accurate Method 1 measurement. This study also gathered the following information for each

APXS target: sol, target name, rock type, target type, lighting conditions, target orientation, solar longitude (Ls), elevation, northing, easting, MAHLI image number, pixel scale, focus motor count (FMC), and standoff.

This work used ImageJ, a Java-based image-processing program, to display, edit, process and save 8-, 16-bit integer and 32-bit floating images (Collings 2007). ImageJ's ability to process and measure features from 24-bit images (standard color images) and 8-bit (greyscale images) allows dust coverage of varying colour types to be measured. ImageJ was of particular use in this study as the program allows for the measurements of areal coverage and provides pixel value statistics using defined selections and intensity thresholds (Schneider et al. 2012).

4.3.1 Method 1

For Method 1, unedited high-resolution focus merge images are opened in ImageJ and converted to 8-bit greyscale. The Sharpen tool enhances the contrast between adjacent light and dark pixels, accentuating dust particles edges. This sharpening results in greater accuracy when selecting dusty pixels from the underlying rock surface. Light and dark dust pixels are then selected using the Threshold Tool and the resulting areal coverages is measured using the Analyze Particles operation (measures the number of selected pixels against the total pixel count; Schmidt et al. 2018). The combined pixel selection within the 17 mm APXS FOV is the final dust coverage measurement for Method 1 (Schmidt et al., 2018).

4.3.2 Method 2

Method 2 begins with MAHLI image enhancement on BeFunky.com to brighten shaded regions, increase the color contrast between dust grains and the underlying rock surface, sharpen edges between features and apply a filter that enhances the reds in dust and makes the bedrock blue. The Beautify tool on BeFunky.com is used to warm images, creating greater contrast between red-coloured pixels and brightening features that are covered by shadows. The BeFunky.com website is particularly useful when analyzing images that are partially or completely shaded and is especially useful when Curiosity's shadow fills the center of the image. Unlike the Sharpen tool from ImageJ, which applies a standardized sharpening to the entire image, the Sharpen tool on BeFunky.com applies a user-defined degree of sharpening. The Cross-

Process filter applies a blue hue to the image while also applying an adjustable contrast filter. Contrast is useful as it is a second process that enhances colours and clarifies the image, separating surface features from overlying debris (sand grains, dust particles, cracks, etc.). Once satisfied with the image enhancement from BeFunky.com, the images are then opened in ImageJ to measure the abundance of airfall dust. The Color Threshold tool has two adjustable bars, saturation and brightness, that are used to select the darkest and lightest areas of dust. The Analyze Particles operation is then used to measure the percentage of selected dust pixels to the total number of pixels in the image (Schmidt et al. 2018).

4.3.3 Method 3

For Method 3, the edited BeFunky.com MAHLI image is opened in Adobe Photoshop for pixel colour altering. Adobe Photoshop is a powerful raster-graphics editor that allows for easy image manipulation. While the uses of Photoshop are widespread, the Replace Colour Tool was the main operation used in this study. This tool allows the user to select a pixel from the loaded image, and all other pixels that are associated with the same 24-bit colour value and edit its colour. A user-defined buffer can be applied to expand the selected pixels and grab other similarly coloured pixels from the total image. Pixels of dust are selected with this tool and changed to a lime-green colour, as it is an unnatural colour for the Martian surface and does not appear in any images prior to editing, while the underlying rock surface is changed to black. The resulting binary image is then exported and opened in ImageJ where it is converted into 8-bit greyscale and sharpened (similar to Method 1). The light coloured pixels, which were previously lime-green and represented dust pixels, are then selected using the Threshold Tool and the Analyze Particles function is used to measure the selected pixels.

4.3.4 Target Type

Targets were categorized into three target types (ChemCam, DRT, and As Is) according to the method of dust removal used prior to MAHLI image acquisition. To remove dust from rock surfaces in Gale crater prior to APXS and rock textural analysis by MAHLI, the MSL mission relies on the Dust Removal Tool (DRT) and to a lesser extent, the Chemistry and Camera (ChemCam). Located at the end of the Rover Arm, the DRT hosts two rotating stainless-steel-wire-bristle brushes that clear rock surfaces of dust and other loose material (Grotzinger et al.,

2012). In practice, the DRT removes much, but not all of the dust. The hard bristles of the DRT also scratch softer rock surfaces (including mudstones), obscuring finer textures, and mixing powdered rock with the dust fines (Schmidt et al., 2018). The ChemCam laser can also clear some dust from rock surfaces. As a series of laser pulses incident on the target surface, the outer layer of rock is ablated/vaporized. Upon the laser striking the surface, small shockwaves mobilize and remove thin surface coverings of dust. The shockwave mobilizes particles away from the target area, and deposits them nearby as an elevated ring of dust material. The ChemCam is particularly useful for targets that cannot be brushed (e.g. due to surface topography) but dust removal may be uneven and localized (Schmidt et al., 2018; Wiens et al., 2012). Because this study was interested in understanding the spatial and temporal fluctuations of Martian dust, it relied on targets with undisturbed accumulations of air fall dust (“As Is” targets).

4.4 Results

To understand the distribution of Martian air fall dust on the Mars surface, dust coverages on 690 horizontal rock targets were determined (Table 4-1). Over half of the targets were undisturbed, ‘As Is’ surfaces, and yielded the highest average (32.9%) and widest range of dust coverages (0.4% to 76.6%). Targets treated by the ChemCam laser and DRT have lower median dust coverage (35.10% and 22.1%, respectively). of dust removal by DRT Frequency and ChemCam has varied along the rover’s traverse, with engineering constraints preventing use of the DRT during much of the early part of the mission (Vasavada et al., 2014). Use of the ChemCam laser to remove dust from APXS rock targets became more frequent after MY33 (Gasnault, et al., 2023). After treatment by either method, a significant amount of dust may remain, particularly when the rock surface contains topographic irregularities, such as diagenetic veins or nodules (Figure 4-2). Rock targets best suited for dust removal are well indurated with smooth, flat surfaces (Schmidt et al., 2018).

Table 4-1. Summary of averaged dust coverages by target type in Gale Crater¹

Target Type	n ²	Minimum (%)	Median (%)	Maximum (%)	Average (%)
As Is	399	0.4	30.5	76.6	32.2
ChemCam	77	9.8	35.10	60.7	35.4
DRT	221	2.3	22.1	50.6	23.2

¹Total sol range: 46-3409; ²n = 697 total targets

Dust on rock surfaces is variable, and all target types range to relatively low dust coverages (Figure 4). Dust coverages counts are relatively consistent up to 50% (Figure 4-3), however a group of As Is targets with <10% (n=53) is associated with two stretches of the rover's traverse through regions with active eolian dunes: Phase 2 of the Bagnold Dunes traverse (MY33, sols 1601-1653; Johnson et al., 2018) and in proximity to the Sands of Forvie (MY36, sols 3028-3344; Sullivan et al., 2022). A decrease of median dust coverages in MY33 and MY36 is likely a result of the rover traverse passing near eolian dune fields during those Mars Years (Table 4-2). Over time, we observe a gradual decrease in maximum dust coverages as Curiosity has climbed in elevation. Excluding the partial recording of MY31, maximum and median dust coverages were highest in MY34 (Table 4-2). Both maximum and median dust coverages decreased in MY35 and again in MY36 as Curiosity traversed Glen Torridon (GT).

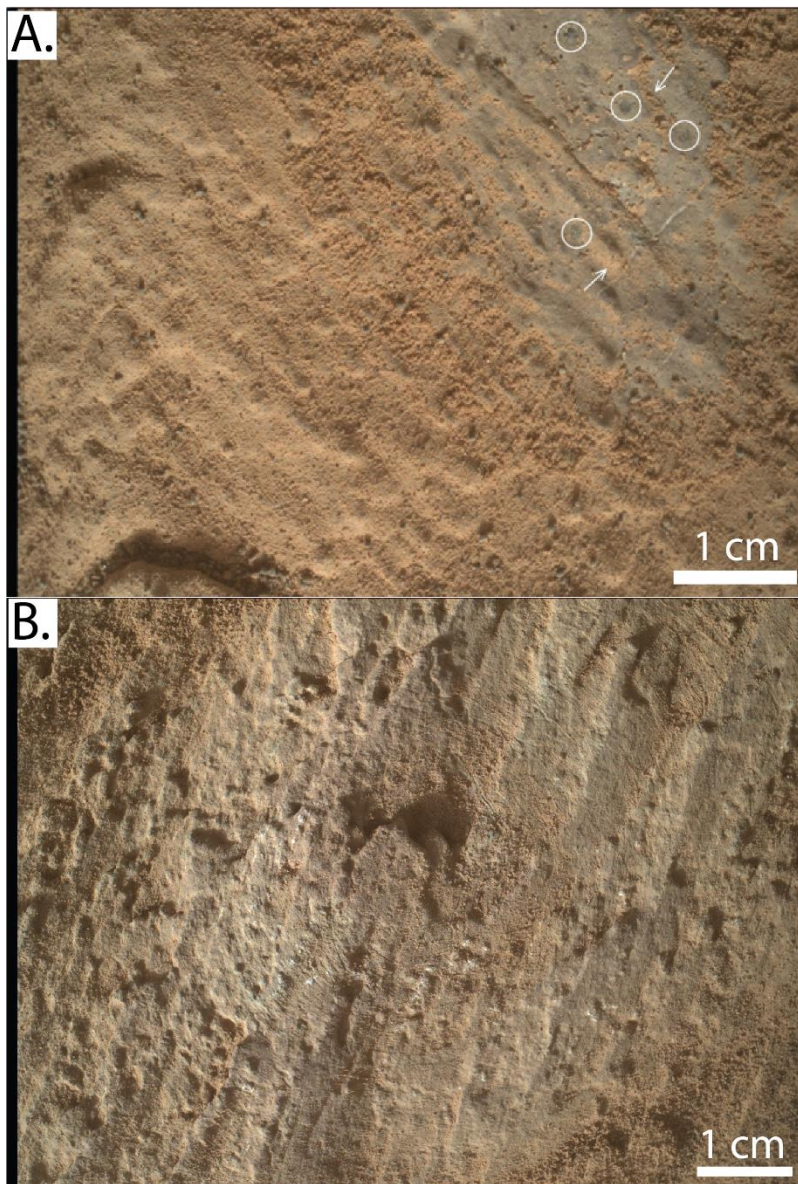


Figure 4-2: (A.) Focus merge MAHLI image (2656MH0008020011001215C00_DXXX) of the ChemCam target Rannoch Moor (sol 2656; dust coverage of 48.8%). The uneven radial clearing of dust in the top right was produced from a shockwave produced as the laser ablates the outer surface of rock (circles). White arrows point to areas where surface topography prevented dust removal. (B.) Focus merge MAHLI image (2581MH0006990010904050C00_DXXX) of the DRT target Canachair (sol 2581; dust coverage of 25.8%). The wire-bristle brushes of the DRT have left small scratch marks in the target surface following dust removal. Most of the dust has been removed from the image center, however some remains.

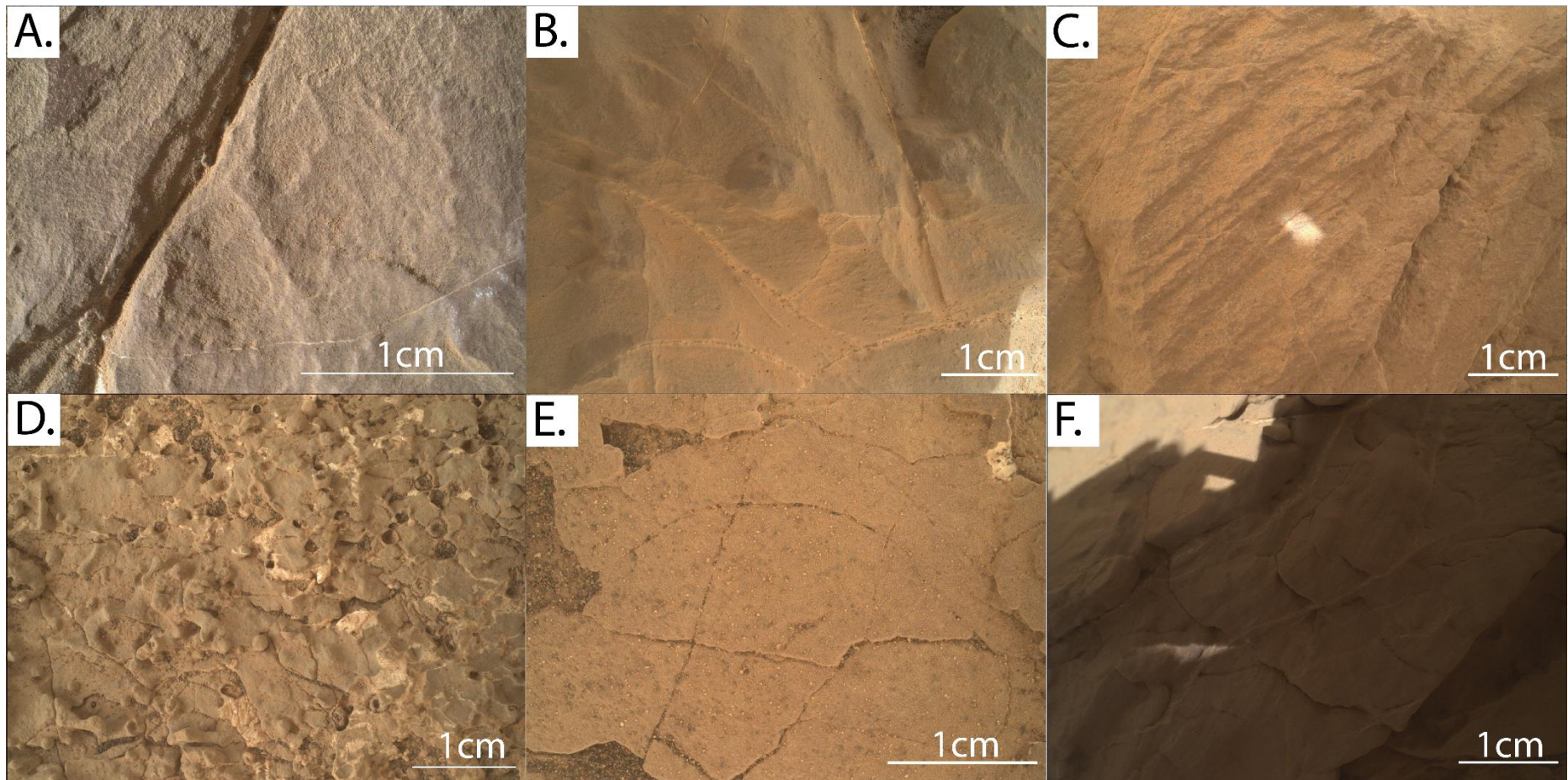


Figure 4-3: Focus merge MAHLI images of As Is targets taken throughout MSL under varying lighting conditions. (A) Sgurr of Eigg target from sol 2000 under full sunlight (2000MH0001930000800300R00_DXXX; 37.9% dust coverage; Mudstone). (B) Burn O Vat target from sol 2166 under partial shadow (2166MH0001630000802862R00_DXXX; 45.0% dust coverage; Vein Rich Mudstone). (C.) Ladder Hills target from sol 2333 under full shadow (2333MH0005360000804213R00_DXXX; 48.3% dust coverage; Mudstone). (D.) Bogmill Pow target from sol 2660 under full sunlight (2660MH0001820011001299C00_DXXX; 23.8% dust coverage; Vein Rich Mudstone). (E.) Tay target from sol 2463 under full shadow (2463MH0001930000902360R00_DXXX; 41.5% dust coverage; Mudstone). (F.) Well Run target from sol 2604 under a partial shadow (2604MH0002990011000205C00_DXXX; 2.3% dust coverage; Mudstone).

Table 4-2. Summary of As Is dust coverages in Gale crater by Mars Year¹

Mars Year	n	Minimum (%)	Median (%)	Maximum (%)	Average (%)
31 ²	28	22.0	51.7	76.6	53.8
32	57	7.1	44.5	70.3	42.0
33	79	0.4	15.9	61.6	20.9
34	94	5.3	40.3	76.0	41.6
35	81	2.3	31.4	60.7	31.6
36 ³	60	3.1	15.2	45.7	17.8

¹sol 47-3409; ²incomplete Mars year (Ls ~176-360°); ³incomplete Mars year (Ls 0-153.8°)

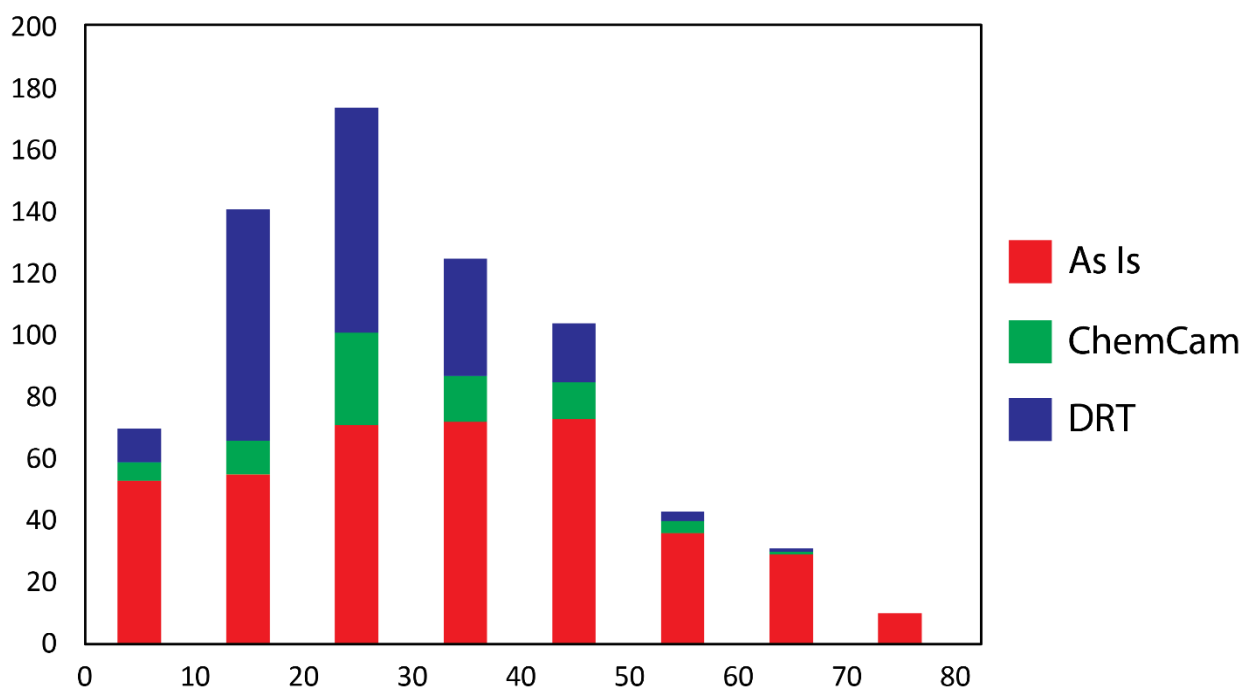


Figure 4-4: Histogram of dust coverage on rock surfaces in Gale crater by target types (sol 46-3344).

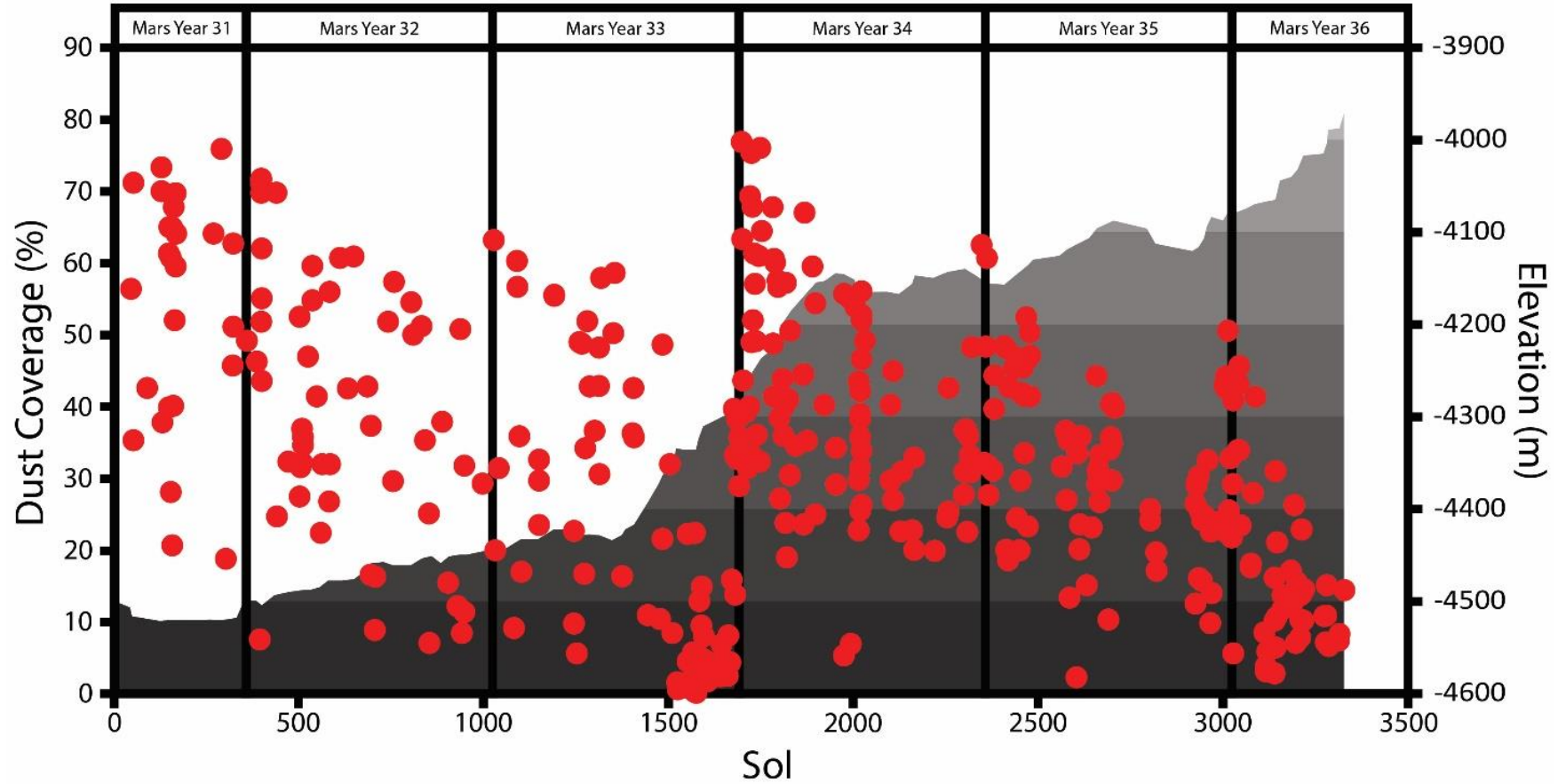


Figure 4-5: Dust coverages on 'As is' horizontal rock surfaces plotted against sol #. Mars Year and the Curiosity traverse elevation are shown.

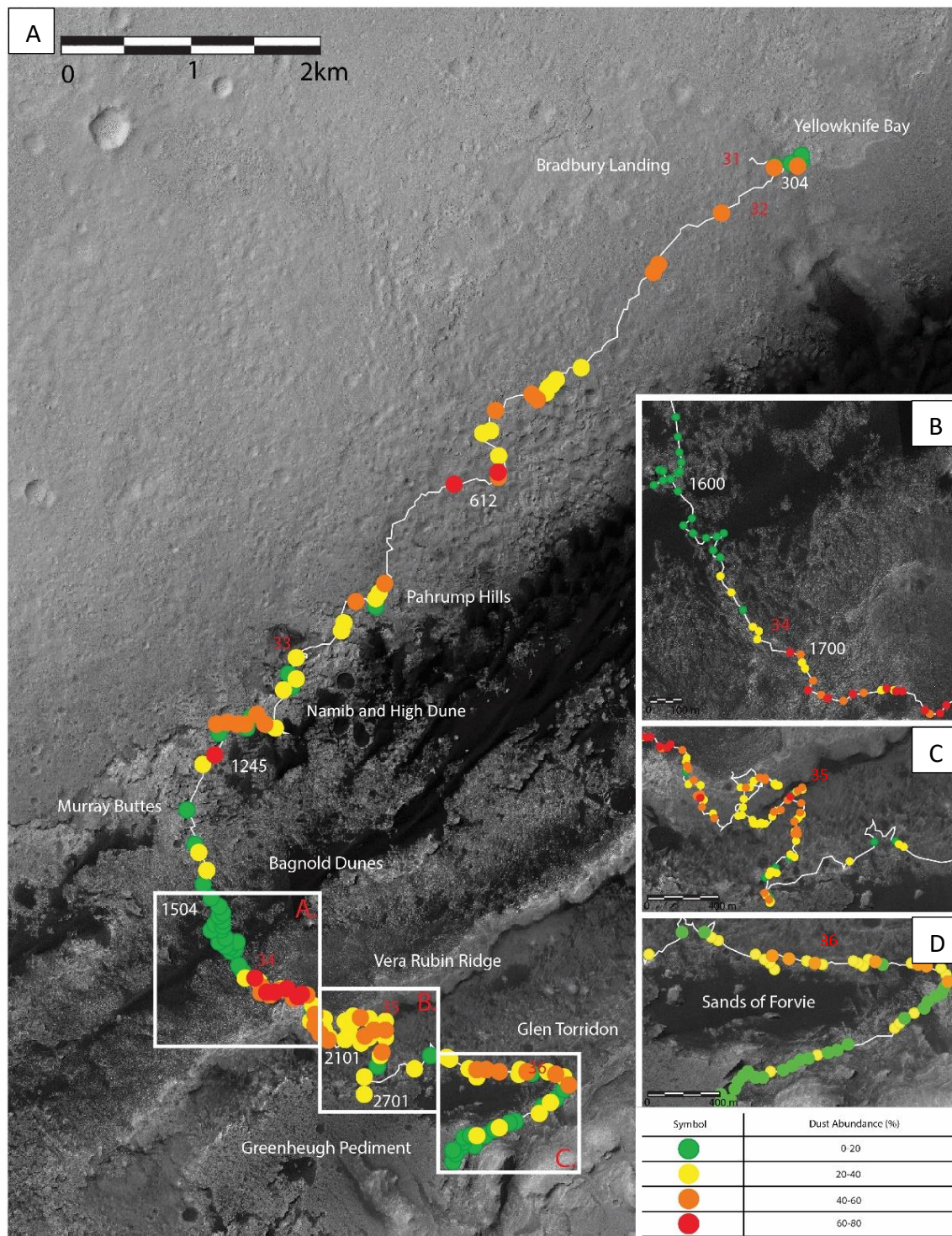


Figure 4-6: (A.) Map of *in situ* targets examined by Curiosity in Gale crater. Dust coverage (%) is indicated by color. Sols and stratigraphic members are labelled in white with the first target of each Mars new year (MY#) labelled in red. Namib and High Dune are a subsection of the larger Bagnold Dunes unit. White boxes indicate the locations of inset maps: (B.) Phase 2 of the Bagnold Dunes traverse, (C.) Vera Rubin Ridge, (D.) Sands of Forvie.

4.4.1 Annual Dust Descriptions

MSL began its investigation of Gale crater mid-MY31 (Ls $\sim 176^\circ$). Shortly after touching down at Bradbury Landing, Curiosity captured its first MAHLI image of a dusty rock target JM2_Alternate_APXS (sol 47). Targets from Bradbury Landing and Yellowknife Bay demonstrated that dust coverages varied in Gale crater (14.6% to 76.6%; Figure 4-5); where dust coverages from adjacent targets, separated by only a few metres (e.g. Persillon (sol 154) and Nastapoka (sol 158)) varied by more than 40%. The partial recording of MY31 limits any seasonal patterns from being observed, however the highest dust coverage (76.6% from Costello, sol 129) was recorded near the end of the year.

Entering MY32 (sol 360) and traveling SW along the Bagnold Dunes (Figure 4-6) , Curiosity continued to observe targets with elevated dust coverages. The highest dust coverage of MY32 (70.3% at Pine Plains, sol 442) and four other targets with more than 65% dust coverage (sols 399-442) were recorded before Mars reached aphelion (Ls 70° or sol 470; Figure 4-5). Following aphelion, maximum dust coverages began to decrease as the year progressed (Figure 4-5 and 4.6). Values dropped below 50% as Curiosity explored Pahrump hills during the windier, southern summer season (Ls 270° - 360° ; Figure 4-1). Unlike MY31, maximum dust coverages persisted at lower values for the remainder of the year and did not exceed 50.8% coverage (Live Oak Canyon, sol 937).

Transitioning into MY33, MAHLI images showed that dust coverages had slightly increased, reaching its annual maximum of 66.3% (Big Arm Night, sol 1028; Table 4-2) before reaching aphelion. Elevated dust coverages persisted for Phase 1 of the Bagnold Dunes traverse (P1BD) as Curiosity examined the barchan dunes of Namib and High Dunes, a small section of the expansive Bagnold Dunes unit (Figure 4-6A; Bridges & Ehlmann, 2018), and traveled SW towards Murray Buttes. Turning SE and traveling perpendicular to Bagnold Dunes, maximum dust coverages gradually decreased to values less than 48.4% (Serowe, sol 1484) as Mars approached southern summer. In the 100 sols (sols 1500-1600) leading up to Phase 2 of the Bagnold Dunes traverse (P1BB; sols 1601-1659), maximum dust coverages decreased dramatically to $<20\%$. These values decreased below 10% during P2BD, persisting until Curiosity reached the base of Vera Rubin Ridge (VRR; Figure 4-6B). Our recordings of extremely low dust coverages during P2BD

align with windiest Mars season and when impact ripple migration was resolvable (Baker et al., 2018).

After leaving Bagnold Dunes, the Curiosity rover continued its SE traverse toward and ascending CRR. As Mars entered MY34, maximum dust coverages increased significantly to 76.0% (Tupper Ledge, sol 1748), representing the highest dust coverage found by this study (Table 4-2; Figure 4-5). Transitioning into northern autumn (Ls 180°; southern spring), dust storms began to form in the northern hemisphere and continued to expand, covering much of the northern hemisphere and tropics (Guzewich et al., 2019; Malin et al., 2018f, 2018g, 2018c). By Ls ~188°, substantial dust activity had occurred independently in the southern hemisphere, along with storms forming along the receding southern seasonal CO₂ polar ice cap (Guzewich et al., 2019; Malin et al., 2018c, 2018d). By Ls ~193°, the storm was termed global as individual events merged, and continued to grow with sporadic dust lifting for the next two weeks (Guzewich et al., 2019; Malin et al., 2018a, 2018d). The storm began to decay near Ls 205°, with dust returning to climatologically typical levels for southern summer (Guzewich et al., 2019; Malin et al., 2018a, 2018e, 2018b). Excluding Volksrust (sol 1869; Ls 88.9°; dust coverage of 67.0%) and Ardmillan (sol 2361; Ls 329°; dust coverage of 60.7%), all dust coverages >60% were recorded along VRR before Mars had reached perihelion (Ls 70°; Figure 4-1; Figure 4-5; Figure 4-6C). Upon reaching the summit of VRR, maximum dust coverages decreased at a faster rate than previous Mars years along the crater floor (Figure 4-5 and 4.6). Aside from the 5.3% and 7.0% dust coverages of Benbeccula (sol 1975) and Stirling Castle (sol 1993), minimum dust coverages increased above 20% as MSL climbed VRR and persisted into Glen Torridon (GT) for the remainder of MY34.

Maximum dust coverages increased again at the beginning MY35 to 52.4% (Paible, sol 2468; Ls 39°), however this seasonal increase was less >20% than MY34 despite the MY34 dust storm. Two high dust coverage targets, Fife (53.0%; Ls 304°) and Ardmillan (60.1%; Ls 329°), were recorded near the end of MY35 and may represent the settling of dust following the MY35 dust storm. As Curiosity continued its exploration of GT and examined the northern margin of the Greenheugh Pediment, maximum dust coverages decreased steadily to 40.0% (Brantome) on sol 3027 (Ls 328°; Figure 4-5). The elevated minimum dust coverages from MY34 began to decrease

back to crater floor levels (<10%) as Curiosity approached the Sands of Forvie (SOF; Figure 4-5B and C).

At the MY36 New Year, maximum dust coverages increased again, reaching 41%, Gout Rossignol (sol 3088; Ls 4.6°; Table 4-2). As Curiosity turned to the SW and traverse the southern margin of the SOF (Figure 4-6C), a second series of low dust coverage targets was encountered. This second series did not exceed 31% dust coverage, and ranged as low as 4.29% (Cladech, sol 3139; Ls 9.5°). This length of the traverse was at a similar distance to an aeolian dune deposit as P2BD, however at different times of the year. In this instance, Curiosity travelled along the SOF during southern autumn into winter. The increase in elevation along the southern edge of the SOF was paired with further decreases to surface dust coverages.

4.5 Discussion

Dust abundances on the surface of rocks were highly variable in Gale crater. In some instances, targets separated by only a few metres had dust coverages vary by up to 65%. These differences were often caused by variable surface topographies between targets; for example, protrusions and indentations in the target surface shield dust particles from winds, allowing them to persist on the surface for longer periods of time, leading to increase our dust coverages measurements. Examples of these features include: cracks, eroded diagenetic veins, nodules, and bedding. Nevertheless, dust coverages are normally distributed (Figure 4-4). Corresponding dust coverage determinations with geospatial and temporal information revealed seasonal trends, similar to those observed in past studies of Mars atmospheric dust. In addition, trends with elevation and proximity to sand dunes were observed.

4.5.1 Seasonal Variations

Previous studies have documented greater dust activity during the latter half of the Mars year (Ls 180°; e.g., e.g., Conrath, 1975; Douté, 2014; Haberle et al., 2017; Newman et al., 2019; Sagan et al., 1972, 1973; Sagan & Pollack, 2020). During this period, atmospheric circulation and seasonal winds are strongest. As expected, our measurements of dust coverages are inversely correlated with overall dust suspension indicated by ground-based (e.g., Guzewich et al., 2019; Lemmon et al., 2015, 2019) and orbital measurements of atmospheric opacity, a measure of

electromagnetic transmittance through the Mars atmosphere (Haberle et al., 2017). Furthermore, our results corroborate the MY31-34 MSL Mastcam optical depth measurements reported by Lemmon et al. (2018), suggesting a consistent assessment of dust content in Gale crater. The congruence of these results validate and strengthen the reliability of both datasets.

Atmospheric opacities are lowest during Southern Autumn and the beginning of Winter (Ls 0-135°; Figure 4-1), when seasonal winds are lowest and allow dust particles to fall out of suspension. This seasonal deposition of airfall dust corresponds with the observed increase of maximum dust coverages at the start of each Mars New Year (Figure 4-5). During the “dusty” southern spring and summer seasons (Ls 135-360°), stronger wind speeds suspend dust particles in the atmosphere, contributing to and driving further atmospheric circulation. During such time, maximum dust coverages are gradually decreasing, reaching their lowest annual abundances near perihelion (Ls 251°). The temporal correlations between our dust measurements and earlier recordings of atmospheric opacity exemplify the effect seasonal winds have on dust activity.

Our results generally agree with global average dust (or atmospheric) opacities (Haberle et al., 2017), demonstrating similar periods of dust suspension and deposition. However *in situ* measurements demonstrate annual, steady decrease in dust coverage over MY32 to 36. Local dust suspension is therefore likely gradual during periods when globally averaged atmospheric opacities indicate minimal dust activity (Figure 4-5 and 4.8; Haberle et al., 2017) and not limited to the “dusty” season. Dust particles are locally/regionally active before changes are seen in global average atmospheric opacities. Since maximum dust coverages gradually decrease following each New Year, our results suggest localized gusts and/or winds are sufficiently strong to mobilize dust clumps during the Non-Dusty season.

Dust devils have been observed in Gale crater throughout the MSL campaign (e.g., Steakley & Murphy, 2016), and may have contributed to some of the low dust coverages recorded in this study. These short-lived convective vortexes are known to suspend and saltate dust particles in their paths, producing streaks of cleared surfaces with lower albedos (Greeley et al., 2006). While short-lived dust devils may explain some low dust coverage measurements, these events are mostly limited to the southern spring and summer seasons (Greeley et al., 2010).

These stochastic events therefore do not explain the gradual decrease of dust coverages seen in each Mars year, but may contribute at times.

Dust activity earlier in the Mars Year is not unique to Gale crater. Calvin et al. (2015) measured the seasonal retreat of polar ice deposits across three Mars years (MY29-31), and observed two separate dust lifting events beginning near Ls 25° and persisting until Ls 35°, likely caused by katabatic winds that formed as cold dense parcels of wind descended from higher elevations along the polar cap. While this study does not estimate a particle size for the suspended dust, it demonstrates that locally/regionally-generated winds mobilize dust particles elsewhere on Mars. These small regional dust events are not uncommon, however they are less efficient at increasing the overall atmospheric dust load during southern autumn and winter (Cantor et al., 2001; Kahre et al., 2006).

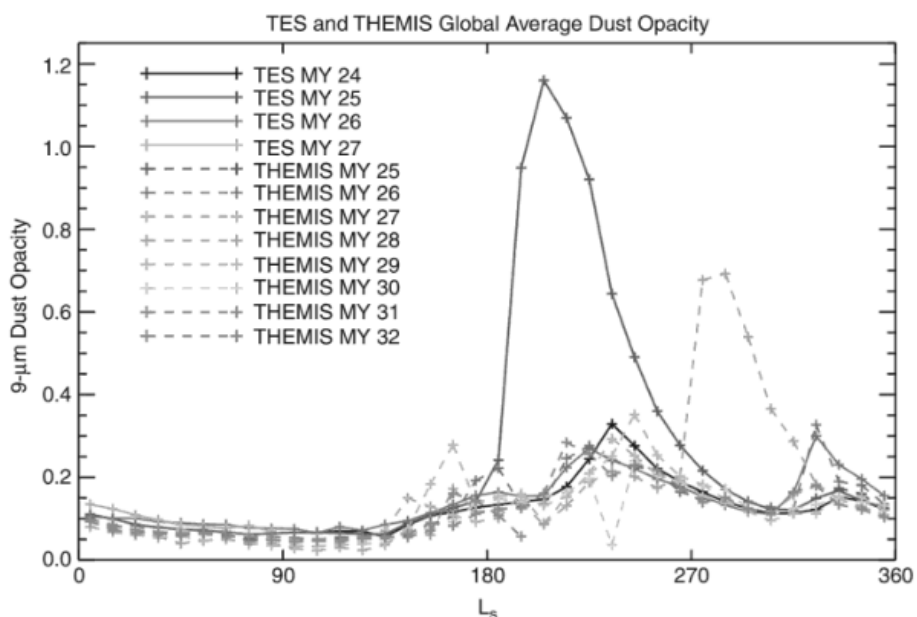


Figure 4-7: Globally averaged 9 μ m atmospheric/dust opacity measurements from the Mars Global Surveyor (MGS) Thermal Emission Spectrometer (TES) and the Mars Odyssey Orbiter (ODY) Thermal Emission Imaging System (THEMIS) for multiple Mars years (MY#; Haberle et al., 2017).

While Calvin et al. (2015) do not estimate the grain size of their observed dust particles, their results and those presented here demonstrate how aeolian activity near aphelion produce sufficient wind speeds to mobilize dust particles. However, globally averaged atmospheric

opacity measurements (Figure 4-7) detect only minor increases in the atmospheric dust load (atmospheric dust particles diameter, $\sim 1.0\ \mu\text{m}$; Guzewich et al. 2014). Where is this mobilized dust going? It is important to note that our measurements quantify the surface coverages of dust clumps that are fine sand-sized ($125\text{-}250\ \mu\text{m}$; e.g. Bridges et al., 2017; Greeley et al., 1980) and not individual dust particles. Additionally, these larger dust clumps require lower wind velocities to mobilize. Unfortunately, wind speeds in Gale crater are not well constrained as Curiosity's Remote Environmental Monitoring System suffered damage during landing (Gómez-Elvira et al., 2014). As a result, wind speeds could not be combined with our observed dust mobility.

4.5.2. Proximity to Aeolian Dune Deposits

The first series of low dust coverages ($<10\%$) recorded during Phase 2 of the Bagnold Dunes traverse (sol 1601-1659, southern summer; Figure 4-6B) revealed an important relationship between airfall dust deposits and their proximity to aeolian sand dune deposits. As Curiosity traveled SW, parallel to Bagnold Dunes and the prevailing wind directions in Gale crater (NE to SW; Bridges et al., 2017; Silvestro et al., 2013, 2016), dust coverages in MY32 and the first half of MY33 showed no abnormalities. It wasn't until Curiosity turned SE (near the Pahrump Hills label in Figure 4-4A), perpendicular to Bagnold Dunes and prevailing wind directions, maximum dust coverages decreased significantly and is consistent with localized dust removal and suspension.

Active impact ripple migration, ripples that form through grain splash when the sand bed is impacted by saltating grains (Lapotre & Rampe, 2018), was also observed during P2BD traverse (Baker et al., 2018) and indicates wind speeds capable of initiating saltation and transport of sand-sized particles. The ~ 100 times less dense atmosphere (Figure 2-2) and $\sim 1/3$ gravitational mean of Mars require wind speeds ~ 7 times greater than those requires to initiate sediment transport on Earth. However once these conditions are met, the thin Martian atmosphere applies minimal drag during suspension, maximizing the magnitude of energy transferred during collision, lowering the impact threshold, and facilitates further saltation downwind (Claudin & Andreotti, 2006; Kok, 2010a, 2010b; Kok et al., 2012; Kok & Renno, 2009).

Active ripple migration (Baker et al. 2018) implies active saltation in Bagnold Dunes during phase 2 of the campaign, where grains collided with stationary particles, causing saltation of sand-sized particles and lofting of dust-sized grains. Dusty rock surfaces in the path of these saltating grains would be cleared of any surface debris, and best explains our recording of localized low dust coverages. Like other regions, small surface features (e.g., cracks, eroded diagenetic veins, etc.) would shield dust from seasonal winds, allowing it to persist on the surface. However the characteristic black sand of Bagnold Dunes occupied these surface features in most MAHLI images from P2BD campaign (Figure 4-8). While these features are not unique to the Bagnold Dunes region, the presence of black sand suggests earlier deposits of dust had been ejected and replaced by saltating sand grains. In particular, the red ellipse in Figure 4-8B shows a small surface feature which may have previously shielded dust clumps. This area is now relatively dust free and is currently filled with sand particles; the same saltating particles that likely impacted and ejected the dusty material.

Low dust coverages were also observed along the SoF and support the interpretation that saltating sand grains at aeolian sand dunes remove and suspend dust. Prevailing winds blow SW in Gale crater, which is consistent with low dust coverage rock surfaces downwind of SOF having been caused by saltating sand grains. Surfaces along the upwind northern edge of the SoF would be unaffected by saltating sand grains during the windy season and were covered by a ‘normal’ layer of dust (Dust coverage range: 3.1% to 50.6%, Median: 24.5%; sols 2945 to 3139). As Curiosity’s traverse turned SW along the southern, downwind edge of the SoF, observed dust coverages reach comparable lows to those seen at P2BD (Dust coverage range: 5.4% to 31.0%, Median: 14.53%; sols 3142 to 3409).

The timing with response to Mars seasons is also relevant to the dust coverage variations observed at the SoF. At the MY36 New Year, Curiosity traversed the northern edge of the SoF and the seasons increase in maximum dust coverage was observed (Maximum of 45.7%, sol 3044 – Pazayac; Ls 10°; Figure 4-5 and 4.6D). Maximum dust coverages on rock surfaces decreased as the year progressed, and as Curiosity traveled along the southern, downwind margin of the SoF. Previous observations of aeolian dune deposits at this time of the year, P1BD traverse, found that sand particles were immobile (M. M. Baker, Lapotre, et al., 2018; N. T. Bridges & Ehlmann, 2018).

While the maximum dust coverages south of the SoF seasonally decreased, since sand particles were likely immobile at this time, these abnormally low dust coverages suggest that sand particles not only contribute to dust removal during southern spring and summer, but may also prevent dust from accumulating as it settles out of suspension towards the Mars New Year.

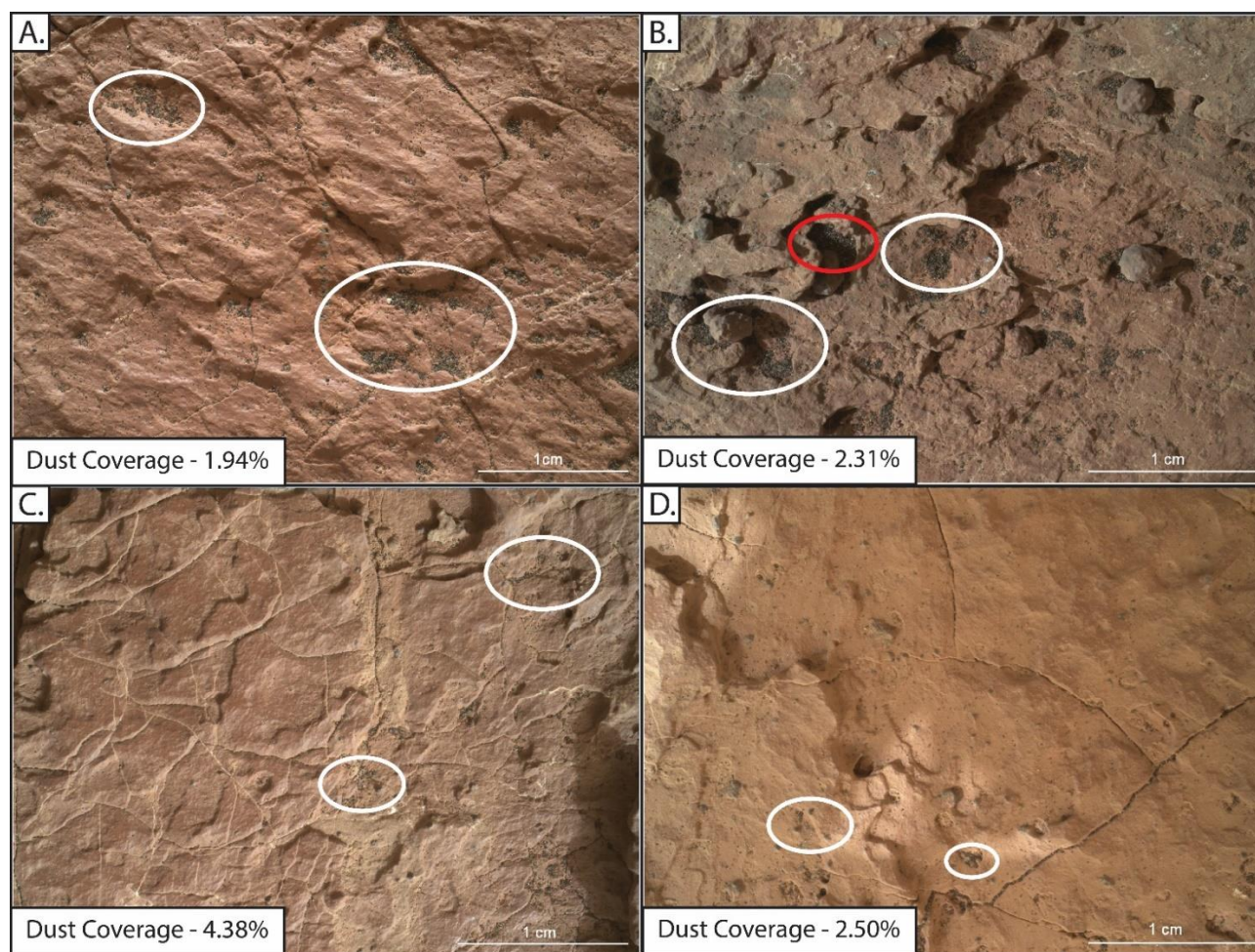


Figure 4-8: Focus merge MAHLI images of As Is targets displaying the low dust coverages and presence of black sand particles during Phase 2 of the Bagnold Dunes traverse. (A.) Sol 1609 – Perry (1608MH0006800000602257R00_DXXX), (B.) Sol 1614 – Spider_Lake_APXS (1615MH0006840000602505R00_DXXX), (C.) Sol 1634 – Canada Falls 3 (1635MH0001530000602737R00_DXXX), and (D.) Sol 1640 – Junk of Pork Island (1640MH0001630000602966R00_DXXX). Targets have their dust coverage displayed at the bottom left and white ellipses indicate accumulations of fine sand-sized particles. The red ellipse highlights a region of high surface topography filled with fine sand-sized particles.

4.5.3. Elevation Change

From landing to its gradual climb of Mount Sharp (+530 m, sols 46-3409), annual dust maximums have decreased (Table 4-2; excluding MY34). Below VRR (MY31-33), dust coverages would frequently exceed 60% (n=26), however these values are increasingly rare following the ascent of VRR (MY34-36; n=13). The only targets above VRR with >60% dust coverage were recorded around the MY34 (before the MY34 global dust storm) and MY35 New Year. The ascent along the southern edge of the SoF further demonstrates the effect of elevation on dust coverages. Not only did MY36 record the lowest New Years spike of maximum dust coverages, but the subsequent rate of dust removal was also hastened by the further increase in elevation as Curiosity continued its ascent of Mount Sharp. Our results are consistent with dust becoming less abundant at higher elevations in Gale crater, or perhaps that surface dust deposits have decreased since the MY34 global dust storm. This observation is consistent with elevation playing a role in diminishing dust coverages at higher altitudes.

Table 4-3: Count of averaged dust coverages above 60%¹

Mars Year	n	n > 60% Dust Coverage	Percent > 60% Dust Coverage
31 ²	28	11	39%
32	57	14	25%
33	79	1	1%
34	94	12	13%
35	81	1	1%
36 ³	60	0	0%

¹sol 47-3409; ²incomplete Mars year (Ls ~176-360°); ³incomplete Mars year (Ls 0-153.8°)

Since decreasing maximum dust coverages are influenced by increasing seasonal wind speeds, the rate at which these values decrease can be used to interpret seasonal wind generation. Upon reaching VRR's summit, MY34-36 maximum dust coverages are seen decreasing at greater rates than those along the crater floor (MY31-33), suggesting wind speeds are greater at higher elevations in Gale crater. Sullivan et al. (2022) attributed sand transport in GT (resolvable in Mastcam images using change detection) to seasonally enhanced winds in combination with local katabatic winds descending the slopes of Mount Sharp. Katabatic winds

are produced by the gravitational pull of dense parcels of air from higher elevations, gaining speed as they descend. In their study, it was unclear whether sediment transport in GTY was the product of these wind components occurring simultaneously, or serially; however their field evidence support the argument for greater wind speeds at higher elevations in Gale crater, and supports our observations. Dust particles mobilized by katabatic winds would be removed at higher elevations, consistent with our recordings of lower dust coverages in VRR and GT, and moved to lower elevations along Mount Sharp.

4.6 Conclusion

Dust coverages atop 697 horizontal rock surfaces were measured across six Mars (4 full, and 2 partial annual recordings) using high-resolution MAHLI images throughout MSL's traverse of Gale crater. Measurements of undisturbed airfall dust accumulations, referred to as As Is targets in this study, followed seasonal patterns consistent with previous studies (e.g., Haberle et al., 2017; Guzewich et al., 2019; Vincente-Retorillo et al., 2018). Our measurements of dust mirror atmospheric opacities; dust coverages are highest during the "Non-Dusty" season ($L_s \sim 0-135^\circ$) and lowest during the "Dusty" season ($L_s \sim 135-360^\circ$). Contrary to the globally averaged atmospheric opacities that imply little to no dust activity during the "Non-Dusty" season, maximum dust coverages in Gale crater gradually decrease throughout the year suggesting dust activity is not limited to the "Dusty" season. Dust on rock surfaces is apparently less abundant at higher elevations in Gale crater, and may be indicative of stronger winds at higher elevations along Mt. Sharp. Decreased dust coverages during Phase 1 of the Bagnold Dunes traverse and along the southern edge of the Sands of Forvie suggest that surfaces in proximity to aeolian sand dune deposits may accumulate less dust due to saltating sand grains impacting and ejecting dust particles.

With dust being ubiquitous, but seasonally variable, our observations can be used to improve other studies that use orbital data and *in situ* measurements to study the Martian surface. With Schmidt et al. (2018) discussing how very fine dust particles may be contributing to ~10% uncertainty in APXS quantifications, our observations may be used to improve datasets that seek to correct for dust chemistry. Using our observations, Czarnecki et al. (2022) found that dust coverage did not affect the bulk hydration measurements from orbital CRISM 3 μm band depth.

However, other studies should assess the effects of surface dust cover on orbital datasets (e.g. HiRISE and CRISM), especially those that are interested in studying surfaces that overlap with Berger et al. (2016)'s dust composition quantifications.

The methods that were developed by Schmidt et al. (2018) and used throughout this study can be applied other rover missions, such as M2020, EXOMars and Tianwen1, to measure dust abundances in other regions. This study has demonstrated the highly variable nature of dust within Gale crater, however observations from other latitudes and regions would help to further constrain surface dust activity in preparation for future human missions. Further observations of Martian dust seasonality and assessments of its seasonal deposition atop rover hardware (e.g. Yingst et al., 2020) will help to improve future solar panel design, and hopefully prolong active rover missions.

4.7 Acknowledgements

I wish to express my sincerest gratitude to my supervisor and Canadian Space Agency MSL Participating Scientist Dr. Mariek Schmidt, for her unwavering support throughout this research. I would also to thank our incredible research assistant Izzy Marincic, and those that preceded her, for their incredible efforts and contributions to the dust data set.

4.8 References

- Bagnold, R. A. (1941). The physics of blown sand and desert dunes. Chapman & Hall.
- Baker, M. M., Lapotre, M. G. A., Minitti, M. E., Newman, C. E., Sullivan, R., Weitz, C. M., Rubin, D. M., Vasavada, A. R., Bridges, N. T., & Lewis, K. W. (2018). The Bagnold Dunes in Southern Summer: Active Sediment Transport on Mars Observed by the Curiosity Rover. *Geophysical Research Letters*, 45(17), 8853–8863. <https://doi.org/10.1029/2018GL079040>
- Baker, M. M., Newman, C. E., Lapotre, M. G. A., Sullivan, R., Bridges, N. T., & Lewis, K. W. (2018). Coarse Sediment Transport in the Modern Martian Environment. *Journal of Geophysical Research: Planets*, 123(6), 1380–1394. <https://doi.org/10.1002/2017JE005513>
- Bandfield, J. L., Edwards, C. S., Montgomery, D. R., & Brand, B. D. (2013). The dual nature of the martian crust: Young lavas and old clastic materials. *Icarus*, 222(1), 188–199. <https://doi.org/10.1016/j.icarus.2012.10.023>
- Bell III, J. F., McSween Jr., H. Y., Crisp, J. A., Morris, R. V., Murchie, S. L., Bridges, N. T., Johnson, J. R., Britt, D. T., Golombek, M. P., Moore, H. J., Ghosh, A., Bishop, J. L., Anderson, R. C., Brückner, J., Economou, T., Greenwood, J. P., Gunnlaugsson, H. P., Hargraves, R. M., Hviid, S., ... Soderblom, L. (2000). Mineralogic and compositional properties of Martian soil and dust: Results from Mars Pathfinder. *Journal of Geophysical Research: Planets*, 105(E1), 1721–1755. <https://doi.org/10.1029/1999JE001060>
- Berger, J. A., Schmidt, M. E., Gellert, R., Campbell, J. L., King, P. L., Flemming, R. L., Ming, D. W., Clark, B. C., Pradler, I., VanBommel, S. J. V., Minitti, M. E., Fairén, A. G., Boyd, N. I., Thompson, L. M., Perrett, G. M., Elliott, B. E., & Desouza, E. (2016). A global Mars dust composition refined by the Alpha-Particle X-ray Spectrometer in Gale crater. *Geophysical Research Letters*, 43(1), 67–75. <https://doi.org/10.1002/2015GL066675>
- Bridges, N. T., & Ehlmann, B. L. (2018). The Mars Science Laboratory (MSL) Bagnold Dunes Campaign, Phase I: Overview and introduction to the special issue. *Journal of Geophysical Research: Planets*, 123(1), 3–19. <https://doi.org/10.1002/2017JE005401>

- Bridges, N. T., Sullivan, R., Newman, C. E., Navarro, S., van Beek, J., Ewing, R. C., Ayoub, F., Silvestro, S., Gasnault, O., Le Mouélic, S., Lapotre, M. G. A., & Rapin, W. (2017). Martian aeolian activity at the Bagnold Dunes, Gale crater: The view from the surface and orbit. *Journal of Geophysical Research: Planets*, 122(10), 2077–2110. <https://doi.org/10.1002/2017JE005263>
- Campbell, J. L., Perrett, G. M., Gellert, R., Andrushenko, S. M., Boyd, N. I., Maxwell, J. A., King, P. L., & Schofield, C. D. M. (2012). Calibration of the Mars Science Laboratory Alpha Particle X-ray Spectrometer. *Space Science Reviews*, 170(1), 319–340. <https://doi.org/10.1007/s11214-012-9873-5>
- Clancy, R. T., Lee, S. W., Gladstone, G. R., McMillan, W. W., & Rousch, T. (1995). A new model for Mars atmospheric dust based upon analysis of ultraviolet through infrared observations from Mariner 9, Viking, and Phobos. *Journal of Geophysical Research: Planets*, 100(E3), 5251–5263. <https://doi.org/10.1029/94JE01885>
- Conrath, B. J. (1975). Thermal structure of the Martian atmosphere during the dissipation of the dust storm of 1971. *Icarus*, 24(1), 36–46. [https://doi.org/10.1016/0019-1035\(75\)90156-6](https://doi.org/10.1016/0019-1035(75)90156-6)
- Coyne, J., Jackson, W., & Lewicki, C. (n.d.). Phoenix Electrical Power Subsystem—Power at the Martian Pole. In 7th International Energy Conversion Engineering Conference. American Institute of Aeronautics and Astronautics. <https://doi.org/10.2514/6.2009-4518>
- Crisp, D., Pathare, A., & Ewell, R. C. (2004). The performance of gallium arsenide/germanium solar cells at the Martian surface. *Acta Astronautica*, 54(2), 83–101. [https://doi.org/10.1016/S0094-5765\(02\)00287-4](https://doi.org/10.1016/S0094-5765(02)00287-4)
- Derbyshire, E., Meng, X., & Kemp, R. (1998). Provenance, transport and characteristics of modern aeolian dust in western Gansu Province, China, and interpretation of the Quaternary loess record. *Journal of Arid Environments - J ARID ENVIRON*, 39, 497–516. <https://doi.org/10.1006/jare.1997.0369>

- Douté, S. (2014). Monitoring atmospheric dust spring activity at high southern latitudes on Mars using OMEGA. *Planetary and Space Science*, 96, 1–21. <https://doi.org/10.1016/j.pss.2013.12.017>
- Edgett, K., Caplinger, M., Maki, J., Ravine, M., Ghaemi, F., McNair, S., Herkenhoff, K., Duston, B., Willson, R., Yingst, R., Kennedy, M., Minitti, M., Sengstacken, A., Supulver, K., Lipkaman, L., Krezoski, G., Henderson, M., Jones, T., Nixon, B., & Kirk, R. (2015). Curiosity's robotic arm-mounted Mars Hand Lens Imager (MAHLI): Characterization and calibration status. <https://doi.org/10.13140/RG.2.1.3798.5447>
- Edgett, K. S., Yingst, R. A., Ravine, M. A., Caplinger, M. A., Maki, J. N., Ghaemi, F. T., Schaffner, J. A., Bell, J. F., Edwards, L. J., Herkenhoff, K. E., Heydari, E., Kah, L. C., Lemmon, M. T., Minitti, M. E., Olson, T. S., Parker, T. J., Rowland, S. K., Schieber, J., Sullivan, R. J., ... Goetz, W. (2012). Curiosity's Mars Hand Lens Imager (MAHLI) Investigation. *Space Science Reviews*, 170(1), 259–317. <https://doi.org/10.1007/s11214-012-9910-4>
- FLETCHER, B. (1976). THE INCIPIENT MOTION OF GRANULAR MATERIALS. THE INCIPIENT MOTION OF GRANULAR MATERIALS.
- Gellert, R., Rieder, R., Brückner, J., Clark, B. C., Dreibus, G., Klingelhöfer, G., Lugmair, G., Ming, D. W., Wänke, H., Yen, A., Zipfel, J., & Squyres, S. W. (2006). Alpha Particle X-Ray Spectrometer (APXS): Results from Gusev crater and calibration report. *Journal of Geophysical Research: Planets*, 111(E2). <https://doi.org/10.1029/2005JE002555>
- Greeley, R. (2002). Saltation impact as a means for raising dust on Mars. *Planetary and Space Science*, 50(2), 151–155. [https://doi.org/10.1016/S0032-0633\(01\)00127-1](https://doi.org/10.1016/S0032-0633(01)00127-1)
- Grotzinger, J. P., Crisp, J., Vasavada, A. R., Anderson, R. C., Baker, C. J., Barry, R., Blake, D. F., Conrad, P., Edgett, K. S., Ferdowski, B., Gellert, R., Gilbert, J. B., Golombek, M., Gómez-Elvira, J., Hassler, D. M., Jandura, L., Litvak, M., Mahaffy, P., Maki, J., ... Wiens, R. C. (2012). Mars Science Laboratory Mission and Science Investigation. *Space Science Reviews*, 170(1), 5–56. <https://doi.org/10.1007/s11214-012-9892-2>

- Guzewich, S. D., Smith, M. D., & Wolff, M. J. (2014). The vertical distribution of Martian aerosol particle size. *Journal of Geophysical Research: Planets*, 119(12), 2694–2708. <https://doi.org/10.1002/2014JE004704>
- Haberle, R. M., Clancy, R. T., Forget, F., Smith, M. D., & Zurek, R. W. (2017). *The Atmosphere and Climate of Mars*. Cambridge University Press.
- Hamilton, V. E., McSween Jr., H. Y., & Hapke, B. (2005). Mineralogy of Martian atmospheric dust inferred from thermal infrared spectra of aerosols. *Journal of Geophysical Research: Planets*, 110(E12). <https://doi.org/10.1029/2005JE002501>
- Johnson, J. R., Bell III, J. F., Bender, S., Cloutis, E., Ehlmann, B., Fraeman, A., Gasnault, O., Maurice, S., Pinet, P., Thompson, L., Wellington, D., & Wiens, R. C. (2018). Bagnold Dunes Campaign Phase 2: Visible/Near-Infrared Reflectance Spectroscopy of Longitudinal Ripple Sands. *Geophysical Research Letters*, 45(18), 9480–9487. <https://doi.org/10.1029/2018GL079025>
- Korablev, O., Moroz, V. I., Petrova, E. V., & Rodin, A. V. (2005). Optical properties of dust and the opacity of the Martian atmosphere. *Advances in Space Research*, 35(1), 21–30. <https://doi.org/10.1016/j.asr.2003.04.061>
- Landis, G. A. (1996). Dust obscuration of Mars solar arrays. *Acta Astronautica*, 38(11), 885–891. [https://doi.org/10.1016/S0094-5765\(96\)00088-4](https://doi.org/10.1016/S0094-5765(96)00088-4)
- Liu, J., Richardson, M. I., & Wilson, R. J. (2003). An assessment of the global, seasonal, and interannual spacecraft record of Martian climate in the thermal infrared. *Journal of Geophysical Research: Planets*, 108(E8). <https://doi.org/10.1029/2002JE001921>
- Lorenz, R. D., Lemmon, M. T., Maki, J., Banfield, D., Spiga, A., Charalambous, C., Barrett, E., Herman, J. A., White, B. T., Pasco, S., & Banerdt, W. B. (2020). Scientific Observations With the InSight Solar Arrays: Dust, Clouds, and Eclipses on Mars. *Earth and Space Science*, 7(5), e2019EA000992. <https://doi.org/10.1029/2019EA000992>
- Madsen, M. B., Goetz, W., Bertelsen, P., Binau, C. S., Folkmann, F., Gunnlaugsson, H. P., í Hjðllum, J., Hviid, S. F., Jensen, J., Kinch, K. M., Leer, K., Madsen, D. E., Merrison, J., Olsen, M.,

- Arneson, H. M., Bell III, J. F., Gellert, R., Herkenhoff, K. E., Johnson, J. R., ... Yen, A. S. (2009). Overview of the magnetic properties experiments on the Mars Exploration Rovers. *Journal of Geophysical Research: Planets*, 114(E6). <https://doi.org/10.1029/2008JE003098>
- Newman, C. E., Kahanpää, H., Richardson, M. I., Martínez, G. M., Vicente-Retortillo, A., & Lemmon, M. T. (2019). MarsWRF Convective Vortex and Dust Devil Predictions for Gale crater Over 3 Mars Years and Comparison With MSL-REMS Observations. *Journal of Geophysical Research: Planets*, 124(12), 3442–3468. <https://doi.org/10.1029/2019JE006082>
- Newman, C. E., Lewis, S. R., Read, P. L., & Forget, F. (2002a). Modeling the Martian dust cycle, 1. Representations of dust transport processes. *Journal of Geophysical Research: Planets*, 107(E12), 6-1-6–18. <https://doi.org/10.1029/2002JE001910>
- Newman, C. E., Lewis, S. R., Read, P. L., & Forget, F. (2002b). Modeling the Martian dust cycle 2. Multiannual radiatively active dust transport simulations. *Journal of Geophysical Research: Planets*, 107(E12), 7-1-7–15. <https://doi.org/10.1029/2002JE001920>
- Ojha, L., & Lewis, K. (2018). The Density of the Medusae Fossae Formation: Implications for its Composition, Origin, and Importance in Martian History. *Journal of Geophysical Research: Planets*, 123(6), 1368–1379. <https://doi.org/10.1029/2018JE005565>
- Ojha, L., Lewis, K., Karunatilake, S., & Schmidt, M. (2018). The Medusae Fossae Formation as the single largest source of dust on Mars. *Nature Communications*, 9(1), Article 1. <https://doi.org/10.1038/s41467-018-05291-5>
- Pollack, J. B., Colburn, D., Kahn, R., Hunter, J., Van Camp, W., Carlston, C. E., & Wolf, M. R. (1977). Properties of aerosols in the Martian atmosphere, as inferred from Viking Lander imaging data. *Journal of Geophysical Research (1896-1977)*, 82(28), 4479–4496. <https://doi.org/10.1029/JS082i028p04479>
- Pollack, J. B., Colburn, D. S., Flasar, F. M., Kahn, R., Carlston, C. E., & Pidek, D. (1979). Properties and effects of dust particles suspended in the Martian atmosphere. *Journal of*

- Geophysical Research: Solid Earth, 84(B6), 2929–2945.
<https://doi.org/10.1029/JB084iB06p02929>
- Pollack, J. B., Ockert-Bell, M. E., & Shepard, M. K. (1995). Viking Lander image analysis of Martian atmospheric dust. *Journal of Geophysical Research: Planets*, 100(E3), 5235–5250.
<https://doi.org/10.1029/94JE02640>
- Ruff, S. W. (2004). Spectral evidence for zeolite in the dust on Mars. *Icarus*, 168(1), 131–143.
<https://doi.org/10.1016/j.icarus.2003.11.003>
- Sagan, C., & Pollack, J. B. (2020). Windblown Dust on Mars. <https://doi.org/10.1038/223791a0>
- Sagan, C., Veverka, J., Fox, P., Dubisch, R., French, R., Gierasch, P., Quam, L., Lederberg, J., Levinthal, E., Tucker, R., Eross, B., & Pollack, J. B. (1973). Variable features on Mars, 2, Mariner 9 global results. *Journal of Geophysical Research (1896-1977)*, 78(20), 4163–4196. <https://doi.org/10.1029/JB078i020p04163>
- Sagan, C., Veverka, J., Fox, P., Dubisch, R., Lederberg, J., Levinthal, E., Quam, L., Tucker, R., Pollack, J. B., & Smith, B. A. (1972). Variable features on Mars: Preliminary mariner 9 television results. *Icarus*, 17(2), 346–372. [https://doi.org/10.1016/0019-1035\(72\)90005-X](https://doi.org/10.1016/0019-1035(72)90005-X)
- Schmidt, M. E., Perrett, G. M., Bray, S. L., Bradley, N. J., Lee, R. E., Berger, J. A., Campbell, J. L., Ly, C., Squyres, S. W., & Tesselaar, D. (2018). Dusty Rocks in Gale crater: Assessing Areal Coverage and Separating Dust and Rock Contributions in APXS Analyses. *Journal of Geophysical Research: Planets*, 123(7), 1649–1673.
<https://doi.org/10.1029/2018JE005553>
- Silvestro, S., Vaz, D. A., Ewing, R. C., Rossi, A. P., Fenton, L. K., Michaels, T. I., Flahaut, J., & Geissler, P. E. (2013). Pervasive aeolian activity along rover Curiosity's traverse in Gale crater, Mars. *Geology*, 41(4), 483–486. <https://doi.org/10.1130/G34162.1>
- Silvestro, S., Vaz, D. A., Yizhaq, H., & Esposito, F. (2016). Dune-like dynamic of Martian Aeolian large ripples. *Geophysical Research Letters*, 43(16), 8384–8389.
<https://doi.org/10.1002/2016GL070014>

- Smith, M. D. (2004). Interannual variability in TES atmospheric observations of Mars during 1999–2003. *Icarus*, 167(1), 148–165. <https://doi.org/10.1016/j.icarus.2003.09.010>
- Smith, M. D. (2008). Spacecraft Observations of the Martian Atmosphere *. *Annual Review of Earth and Planetary Sciences*, 36, 191–219. <https://doi.org/10.1146/annurev.earth.36.031207.124334>
- Smith, M. D., Pearl, J. C., Conrath, B. J., & Christensen, P. R. (2000). Mars Global Surveyor Thermal Emission Spectrometer (TES) observations of dust opacity during aerobraking and science phasing. *Journal of Geophysical Research: Planets*, 105(E4), 9539–9552. <https://doi.org/10.1029/1999JE001097>
- Smith, P. H., Bell, J. F., Bridges, N. T., Britt, D. T., Gaddis, L., Greeley, R., Keller, H. U., Herkenhoff, K. E., Jaumann, R., Johnson, J. R., Kirk, R. L., Lemmon, M., Maki, J. N., Malin, M. C., Murchie, S. L., Oberst, J., Parker, T. J., Reid, R. J., Sablotny, R., ... Wegryn, E. (1997). Results from the Mars Pathfinder Camera. *Science*, 278(5344), 1758–1765. <https://doi.org/10.1126/science.278.5344.1758>
- Stella, P. M., Chin, K., Wood, E., Herman, J., & Ewell, R. (2009). Managing PV power on Mars—MER Rovers. 2009 34th IEEE Photovoltaic Specialists Conference (PVSC), 001073–001078. <https://doi.org/10.1109/PVSC.2009.5411206>
- Sullivan, R., Baker, M., Newman, C., Turner, M., Schieber, J., Weitz, C., Hallet, B., Ellison, D., & Minitti, M. (2022). The Aeolian Environment in Glen Torridon, Gale crater, Mars. *Journal of Geophysical Research: Planets*, 127(8), e2021JE007174. <https://doi.org/10.1029/2021JE007174>
- Taylor, S. R., & McLennan, S. (2009). *Planetary Crusts: Their Composition, Origin and Evolution*. Cambridge University Press.
- Toon, O. B., Pollack, J. B., & Sagan, C. (1977). Physical properties of the particles composing the Martian dust storm of 1971–1972. *Icarus*, 30(4), 663–696. [https://doi.org/10.1016/0019-1035\(77\)90088-4](https://doi.org/10.1016/0019-1035(77)90088-4)

- VanBommel, S. J., Gellert, R., Berger, J. A., Campbell, J. L., Thompson, L. M., Edgett, K. S., McBride, M. J., Minitti, M. E., Pradler, I., & Boyd, N. I. (2016). Deconvolution of distinct lithology chemistry through oversampling with the Mars Science Laboratory Alpha Particle X-Ray Spectrometer. *X-Ray Spectrometry*, 45(3), 155–161. <https://doi.org/10.1002/xrs.2681>
- Vicente-Retortillo, Á., Martínez, G. M., Renno, N., Newman, C. E., Ordonez-Etxeberria, I., Lemmon M. T., Richardson, M. I., Hueso, R., & Sánchez-Lavega, A. (2018). Seasonal Deposition and Lifting of Dust on Mars as Observed by the Curiosity Rover. *Scientific Reports*, 8(1), Article 1. <https://doi.org/10.1038/s41598-018-35946-8>
- Whalley, W. B., & McGreevy, J. P. (1983). Weathering. *Progress in Physical Geography: Earth and Environment*, 7(4), 559–586. <https://doi.org/10.1177/030913338300700404>
- Wiens, R. C., Maurice, S., Barraclough, B., Saccoccio, M., Barkley, W. C., Bell, J. F., Bender, S., Bernardin, J., Blaney, D., Blank, J., Bouyé, M., Bridges, N., Bultman, N., Caïs, P., Clanton, R. C., Clark, B., Clegg, S., Cousin, A., Cremers, D., ... Wong-Swanson, B. (2012). The ChemCam Instrument Suite on the Mars Science Laboratory (MSL) Rover: Body Unit and Combined System Tests. *Space Science Reviews*, 170(1–4), 167–227. <https://doi.org/10.1007/s11214-012-9902-4>
- Wilson, L., & Head, J. W. (2007). Explosive volcanic eruptions on Mars: Tephra and accretionary lapilli formation, dispersal and recognition in the geologic record. *Journal of Volcanology and Geothermal Research*, 163(1), 83–97. <https://doi.org/10.1016/j.jvolgeores.2007.03.007>
- Wolff, M. J., & Clancy, R. T. (2003). Constraints on the size of Martian aerosols from Thermal Emission Spectrometer observations. *Journal of Geophysical Research: Planets*, 108(E9). <https://doi.org/10.1029/2003JE002057>
- Wolff, M. J., Smith, M. D., Clancy, R. T., Spanovich, N., Whitney, B. A., Lemmon, M. T., Bandfield, J. L., Banfield, D., Ghosh, A., Landis, G., Christensen, P. R., Bell, J. F., & Squyres, S. W. (2006). Constraints on dust aerosols from the Mars Exploration Rovers using MGS overflights and Mini-TES. *Journal of Geophysical Research: Planets*, 111(E12). <https://doi.org/10.1029/2006JE002786>

- Wright, J. S. (2001). "Desert" loess versus "glacial" loess: Quartz silt formation, source areas and sediment pathways in the formation of loess deposits. *Geomorphology*, 36(3), 231–256. [https://doi.org/10.1016/S0169-555X\(00\)00060-X](https://doi.org/10.1016/S0169-555X(00)00060-X)
- Wright, J., Smith, B., & Whalley, B. (1998). Mechanisms of loess-sized quartz silt production and their relative effectiveness: Laboratory simulations. *Geomorphology*, 23(1), 15–34. [https://doi.org/10.1016/S0169-555X\(97\)00084-6](https://doi.org/10.1016/S0169-555X(97)00084-6)
- Yen, A. S., Gellert, R., Clark, B. C., Ming, D. W., King, P. L., Schmidt, M. E., Leshin, L., Morris, R. V., Squyres, S. W., & Campbell, J. L. (2013, January 1). Evidence for a Global Martian Soil Composition Extends to Gale crater. Lunar and Planetary Science Conference, The Woodlands, TX. <https://ntrs.nasa.gov/citations/20130009717>
- Yen, A. S., Gellert, R., Schröder, C., Morris, R. V., Bell, J. F., Knudson, A. T., Clark, B. C., Ming, D. W., Crisp, J. A., Arvidson, R. E., Blaney, D., Brückner, J., Christensen, P. R., DesMarais, D. J., de Souza, P. A., Economou, T. E., Ghosh, A., Hahn, B. C., Herkenhoff, K. E., ... Zipfel, J. (2005). An integrated view of the chemistry and mineralogy of martian soils. *Nature*, 436(7047), Article 7047. <https://doi.org/10.1038/nature03637>
- Yingst, R. A., Edgett, K. S., Kennedy, M. R., Krezoski, G. M., McBride, M. J., Minitti, M. E., Ravine, M. A., & Williams, R. M. E. (2016). MAHLI on Mars: Lessons learned operating a geoscience camera on a landed payload robotic arm. *Geoscientific Instrumentation, Methods and Data Systems*, 5(1), 205–217. <https://doi.org/10.5194/gi-5-205-2016>

Chapter 5: Quantification of tool marks in abrasion patches of Jezero crater: Comparison of mineralogy and material properties between rocks of the crater floor and delta front.

Henley T.L.J., Schmidt M.E., Kizovski T.V., Labrie J., Tice M., Hurowitz J., Flannery D., Klevang D.A., Tirona I., Allwood A., Cable M., Schumacher J., O'Neil L.P.

5.1 Abstract

The Sampling and Caching Subsystem's (SCS) abrasion bit is an essential tool for the M2020 Perseverance mission for removing the weathered exterior of outcrops in order to examine the rock beneath. The abrasion process creates a 50 mm diameter, or 19.6 cm² patch that is 2-16 mm in depth depending on the topography of the unabraded surface. Etches produced from the abrasion process (abrasion marks) were noted to be variably preserved across 10 abrasion patches produced by Perseverance during the Jezero crater Floor (sols 0-379) and Delta Front (sols 415-641) campaigns. Here, we assess whether abrasion mark variability can be related to the material properties and mineralogy of target outcrops – 10 of which have been sampled for eventual return to Earth. To understand their variability, this work relates tool mark abundance (quantified using WATSON images) to mineralogy (using chemical data from the Planetary Instrument for X-ray Lithochemistry; PIXL instrument) to determine how and where these abrasion marks are preserved. Our results show that higher counts of abrasion marks (n=367-1136) were preserved in igneous crater floor targets compared to those targets from the delta front (n=153-422). This is likely due to the smaller grains sizes and higher abundances of softer minerals (e.g., sulfate, carbonate, etc.) in the sedimentary rocks of the delta. Due to excessive cracking, subsidence into the surrounding regolith, and surface topography which impeded bit progressions, high-resolution analysis by proximity instruments was unsuccessful for four of the 14 abrasion patches. The results from this study can be used to assess the abrasion method and drilling algorithm, inform future abrasion bit design, and may also help to prevent failed abrasion attempts in the future.

5.2 Introduction

Modern Mars is cold, dry, and possesses a thin atmosphere that cannot support any known terrestrial life (Rummel et al., 2014; Soffen, 1976). However, the dearth of plate tectonics and surface erosion throughout the Amazonian have allowed surface geomorphology such as ancient riverbeds, deltas and paleolakes, to be remarkably preserved (Carr, 2007, 2012; Fassett & Head, 2008). These features paint a vivid picture of a vastly different, and potentially habitable, ancient Mars. Of particular interest is Jezero crater, the landing site and current area of operations for the M2020 Perseverance rover mission. With two inflowing deltas and one outflowing channel, Jezero crater once contained a paleolake and is considered to be hydrologically open. Located within the mineral-rich Isidis Planitia and Nili Fossae region, the sediments within these relaxation graben features contain valuable information about the geological, environmental and potentially biological history of Mars (Brown et al., 2010, 2020; Goudge et al., 2018; Mustard et al., 2007, 2007, 2009; Phillips et al., 2001). Touching down in Jezero crater February 18th 2021, the objective of the M2020 mission is the search for signs of ancient life on Mars, while also identifying, preparing, documenting, and caching a suite of samples to be returned to Earth in the near future (Farley et al., 2020).

The Perseverance rover's Sampling and Caching Subsystem (SCS; Moeller et al., 2020), which includes the Robotic Arm (RA), the Turret and Coring Drill (Corer), and the Adaptive Caching Assembly (ACA), is used to remove surface coatings of dust, atmospheric and cosmic alteration, and to prepare return samples. To collect samples and to perform proximity science, the Corer is equipped with 3 types of drill bits: Regolith, Coring, and Abrasion (Figure 5-1). The Regolith bit is used to collect regolith samples, however it does not preserve stratigraphy (Moeller et al., 2020). The Coring Bits are designed to sample solid rocks such that stratigraphy is persevered. The Abrading Bits are designed with three asymmetrical teeth of differing lengths (Figure 5-2, leftmost) to remove the surface layers of weathered materials, and to provide topographically smooth surfaces suitable for further investigation by proximity science instruments. These proximity science instruments include the Scanning Habitable Environments with Raman and Luminescence for Organics and Chemicals (SHERLOC; Bhartia et al., 2021), the Wide Angle Topographic Sensor for Operations and eNginneering (WATSON) camera, PIXL

(Allwood et al., 2020), and all of their associated subsystems (e.g., Micro Context Camera and Autofocus Context Imager; MCC and ACI).



Figure 5-1: Set of drill bits stored in the Bit Carousel of Perseverance's Sampling and Caching Subsystem. From left to right, one Regolith Bit, six Coring Bits, and two Abrading Bits (Image from Moeller et al. 2020).

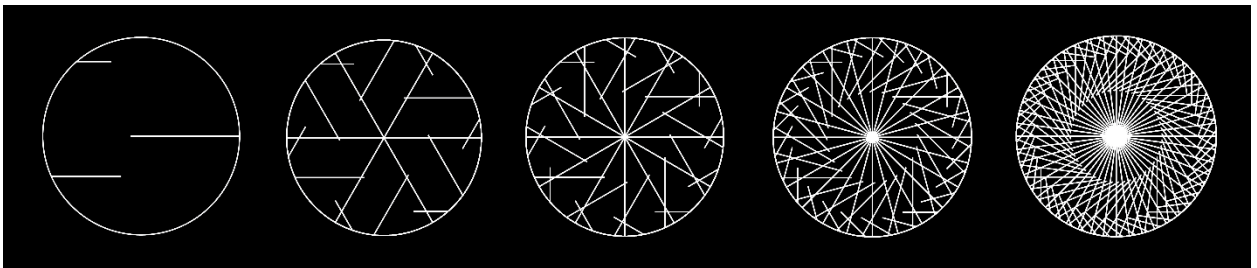


Figure 5-2: SCS's asymmetrical abrasion bit (leftmost) and the pattern produced during the abrasion process (Courtesy of Iona Tirona).

5.2.1 Rock Abrasion

Prior to abrasion, the WATSON camera is used to ensure the selected bit is properly secured in the drill chock and to capture images of the target surface prior to abrasion (with a resolution of $13.4 \mu\text{m}/\text{pixel}$; Bhartia et al., 2021). To produce an abrasion patch, the Perseverance rover lowers its RA towards the target surface and rests the SCS upon two stabilizers. During abrasion the SCS uses a proprioceptive-adaptive, or “prodapt,” algorithm to adjust the rate of penetration by varying the weight on the bit, percussion frequency, and spindle rate (or rotations per minute, RPM). If the controller notices that it is penetrating slowly (harder

surface), the algorithm will increase the prodapt level (to values between 11-20, but ranges from 0-20) and corresponding drilling parameters. For softer materials that are easier to abrade, the SCS uses a lower prodapt level (3-10) to limit the rate of penetration (Verma, et al., 2023). An initial user-defined, or “seeded,” prodapt level can be assigned prior to abrasion to prevent failed abrasion patch production; since the failed Rose River Falls abrasion patch (Figure 5-3), the M2020 team has seeded prodapt levels to prevent softer materials from fracturing during abrasion (Verma, et al., 2023).

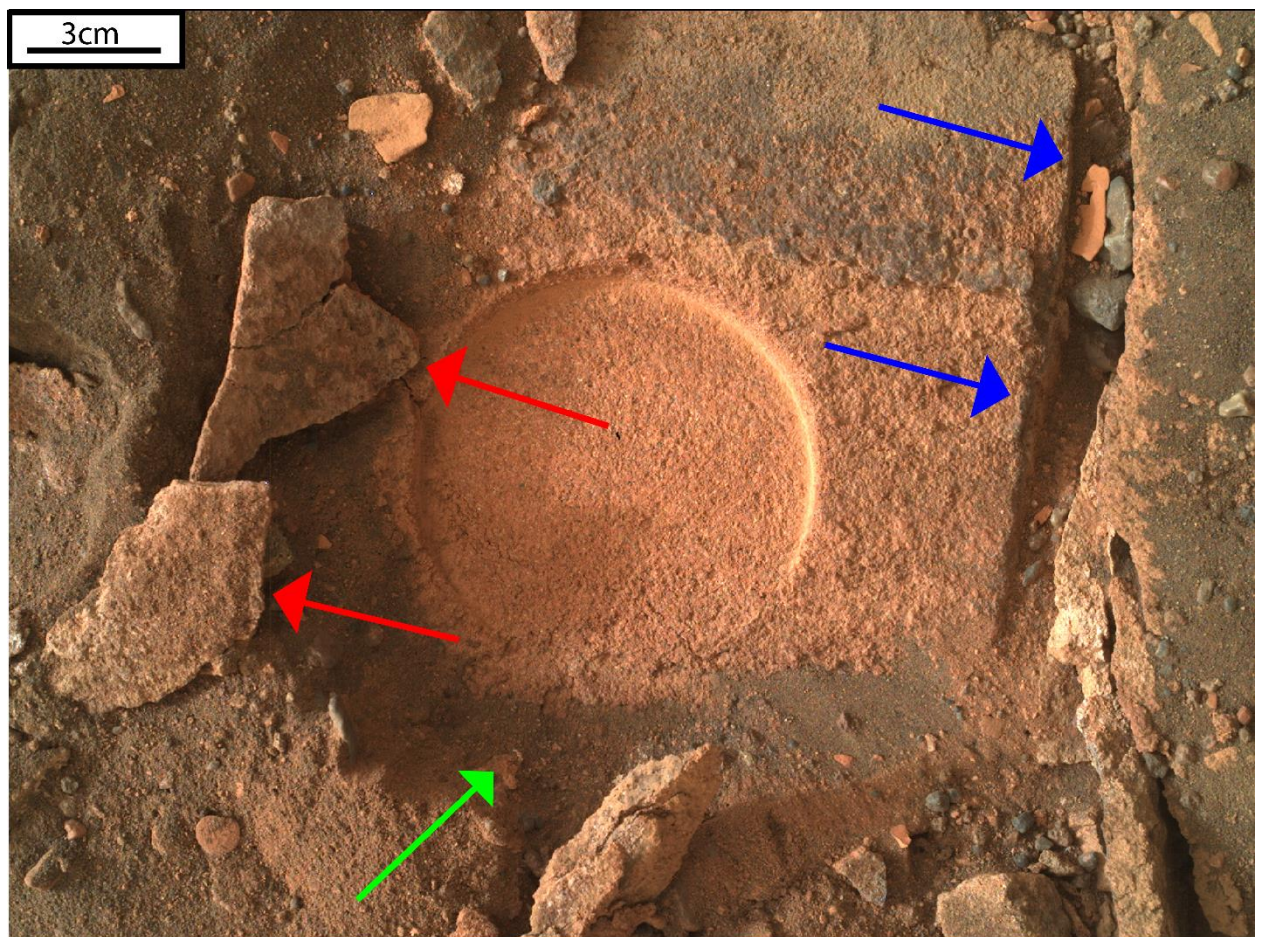


Figure 5-3: SHERLOC-WATSON image of the failed Rose River Falls abrasion target (sol 452; SIF_0452_0707077324_796FDR_N0260000SRLC02504_0000LMJ01). During the abrasion process, the target surface sunk into the surrounding regolith and was partially infilled by the regolith material (green arrow). Excess applied force during abrasion caused the target surface to crack (blue arrows) and break into smaller chunks (red arrows), preventing later proximity science with the PIXL instrument.

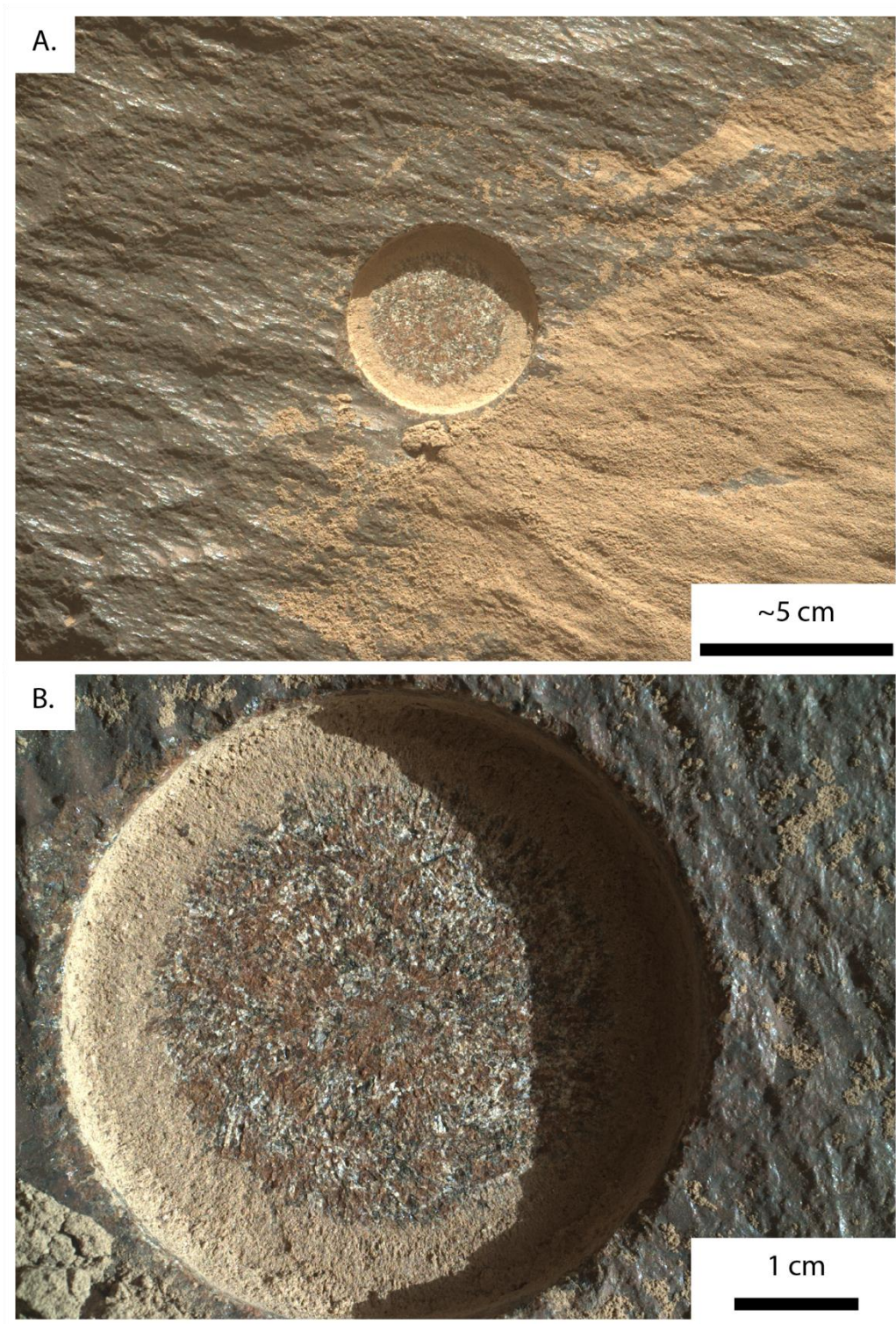


Figure 5-4: (A.) Mastcam-Z image of the gDRT cleared Alfalfa abrasion patch (sol 367; ZLF_0368_0699608205_270FDR_N0110108ZCAM03328_1100LMJ0) (B.) Close-up WATSON image of the Alfalfa abrasion.

During abrasion, the transfer of energy between the abrasion bit and the target surface creates indentations, which may appear as scratches or grooves in the rock's surface. We hereafter refer to these linear features visible in WATSON images of abrasion patches as abrasion marks. The bit teeth produce a unique pattern of linear abrasion marks and fractures in the target surface (Figure 5-2). As the Corer rotates, subsequent impacts produce additional abrasion marks and fractures. These features gradually connect to loosen material and are later removed using blasts of compressed nitrogen from the gas Dust Removal Tool (gDRT). With a successful abrasion (Figure 5-4), the final product is an approximately 5 mm diameter abrasion patch, that is 2-16 mm deep depending on surface topography (Moeller et al., 2020). In this study we quantify abrasion marks, and include all linear marks preserved in the abraded surface (scratches, grooves, cleavage and surface fractures), excluding linear grain boundaries.

5.2.2 Rover Traverse and M2020 Campaigns

To date, the M2020 has completed the Crater Floor (sols 0-379; Sun et al., 2022; submitted to JGR planets) and Lower Delta Front campaigns (sols 367-422; Williams et al., 2023), with Perseverance successfully producing 10 abrasion patches and filling 15 sample tubes (Verma, et al., 2023). During the Crater Floor campaign (Sun et al. 2023) Perseverance successfully produced four abrasion patches in the Máaz formation and 3 abrasion patches in the Séítah formation (Table 1). M2020's payload of geochemical instruments found the Máaz formation to be a FeO-rich basaltic lava full of common primary igneous minerals, including augite, plagioclase, Fe-Ti oxides, however no IR spectra or LIBS compositions of olivine were detected (Farley et al., 2020). In general, PIXL mapping found the blocky to prismatic white grains in Máaz were consistent with plagioclase while the darker grains were consistently augite, a Ca-rich pyroxene. Brown patches and stains in the Máaz abrasion patches were mostly Fe and Si materials, with overlapping compositions of some igneous Fe silicate minerals such as the Fe-bearing orthopyroxene and perhaps olivine; however, Mastcam-Z detected the presence of iron oxides in the abrasion patches of Guillaume and Bellegarde. Raman spectroscopy of the irregularly shaped voids and pits in Máaz abrasion targets were filled with secondary Ca sulfate and Na perchlorate minerals (Farley et al., 2020).

Unlike Máaz, Mastcam-Z multispectral images and SuperCam IR spectra from the Séítah formation revealed an abundance of olivine minerals, with some carbonate materials and lower abundances of sulfate. Investigation by SuperCam LIBS revealed compositions approaching pure olivine and detections that extend towards mixtures with augite and plagioclase. While both Máaz and Séítah contain plagioclase and augite minerals, Farley et al. (2022) found minimal compositional overlap between the formations. The poikilitic texture observed by Liu et al. (2022) is characteristic of an igneous olivine cumulate, and inevitably led to the classification of Séítah as an olivine cumulate. While Mg-Ca sulfate materials were detected in both crater floor units, the lack of carbonate materials in Máaz suggests the carbonation process was limited to the Séítah formation, and the saline brine that produced the sulfate materials was distinct from the carbonate-forming fluids (Tice, et al., 2023).

Table 5-1: Abrasion patches from each geologic formation.

Máaz	Séítah	Shenandoah (Delta Front)
Sol 167 – Guillaumes	Sol 206 - Garde	Sol 484 – Thornton Gap
Sol 187 – Bellegarde	Sol 257 – Dourbes	Sol 505 – Berry Hollow
Sol 364 – Montpezat	Sol 294 - Quartier	Sol 570 – Novarupta
Sol 367 - Alfalfa		Sol 614 – Uganik Island

The Delta Front campaign (sol 367-422; Williams et al., 2023), which explored the southern edge of Jezero crater’s western delta (Shenandoah formation), produced two abrasion patches in the Cape Nukshak region, and two in the Hawksbill Gap region. Proximity science and remote observations revealed a suite of sedimentary rocks consistent with subaqueous deposition, likely via turbidite-related processes (Williams et al., 2023; Sun et al., 2023). Materials from the lower delta front were a combination of sulfate- and carbonate-cemented siltstones and mudstones. While the Hawksbill Gap and Cape Nukshak regions are separated by approximately 300m, similar layers of sulfate-cemented sandstone and siltstones were identified and are thought to be lateral equivalents.

Unfortunately, complications during abrasion have prevented 4 patches from being successful (Point du Loup, Soberro, Rose River Falls, and Elkwallow Gap; Figure 5-3). These complications include: loss of stabilizer contact during abrasion, higher surface topographies that impede bit progression, cracking of the target surface, and poor rock structure overall. This study quantifies tool mark abundance and length in successful abrasion patches. These results are then compared with generalized mineral maps (separated into low salt, high salt, and alteration mineral groups) determined using PIXL quantifications. The goals of this study are to (1) understand how rock composition affects tool mark preservation; (2) provide another perspective for interpreting rock properties; and (3) provide observations, that may improve the adaptive drilling algorithm and reduce the number of failed abrasion patches in the future.

5.3 Methods

This section will briefly explain the rover instrumentation, steps used to trace abrasion marks, create PIXL mineral maps, and measure the abundance and lengths of abrasion marks within each mineral group. Some sections are copies of information in Section 3.3. For full descriptions of the rover instrumentation and methods used in Chapter 5, please see sections 3.1.2 and 3.3 respectively.

5.3.1 Rover Instrumentation

The M2020 Perseverance rover is equipped with a wide array of sophisticated instruments that will allow it to complete its mission objectives on Mars. While the rover boasts a diverse range of scientific tools, this section will concentration on the instruments used in our methods. The selected instruments allowed sub-millimeter sized abrasion marks to be resolved, measured, and compared with geochemical quantifications of the target surfaces.

Planetary Instrument for X-Ray Lithochemistry

Attached to the Perseverance rover's RA, the Planetary Instrument for X-Ray Lithochemistry (PIXL; Figure 3-3) is a microfocus X-ray fluorescence instrument. PIXL, and the associated multispectral micro-context camera (MCC), record sub-millimeter scale geochemistry and surface textures by focusing an X-ray beam on a small point, ~150 μm , and measuring the induced X-ray fluorescence (XRF) of the incident surface (Allwood et al., 2020). Interactions

between minerals and the incident x-ray beam amplify or remove unique diffraction peaks allowing mineral identities, sizes, and crystallographic orientations to be constrained. The unique configuration of PIXL includes a dual detector system (detectors A and B), which captures the x-ray spectra at two orientations to the target surface. By comparing spectral signals between these detectors Tice et al. (2023) have developed expressions which remove diffraction issues resulting from surface roughness and diffraction effects and produce the most accurate chemical quantifications of the target surface. Sensitive enough to capture major and minor rock-forming elements, PIXL can also detect trace elements after a single 10 second observation (Allwood et al., 2020). PIXL scans can be performed as 1 to 3 lines up 36 mm in length, as rectangular grids up to 4 x 12 mm², and as square grids up to 22 x 22 mm² (Tice, et al., 2023). Square PIXL scans from the crater floor and delta front campaigns were limited to smaller grid sizes of ~7x7 mm² or smaller. PIXL scan points, measurements, and the co-registered MCC images are viewable in the data-viewing software PIXLISE (Ye et al., 2021). Here the spatial distribution and abundances of elements can be accurately compared with physical textures and internal structures of the target surface (Allwood et al., 2020; Ye et al., 2021). The square and rectangular XRF maps with densely packed PIXL points were preferred as they provided the highest spatial resolution to the geochemical data, and allowed mineral boundaries to be defined with greater accuracy, see section 3.3.2.

Sampling and Caching Subsystem

The design of the Sampling and Caching System (SCS; Figure 3-4) allows M2020 to abrade rock surfaces, extract regolith and core samples, and to search for biosignatures of past life. When coring or abrading (200 rpm), the RA exerts an additional downward force of 300N between the stabilizer mechanism and the target surface. This added force prevents the selected bit from walking or jumping during first contact with the target surface (Moeller et al., 2020). Abrading follows a similar process to drilling, however the rotation rate is decreased to accommodate the larger surface area of the Abrading Bit (50mm diameter; Moeller et al., 2020). As the drill spins and impacts the rock, a unique pattern of crisscrossed marks (Figure 5-2) are etched into the target surface, gradually chipping away material with subsequent impacts.

Gas Dust Removal Tool

Following abrasion, fines are removed using puffs of cold nitrogen gas from the gas Dust Removal Tool (gDRT). In the 50 mm diameter abrasion patches, which have a maximum depth of 16 mm, tests of the gDRT proved to be more effective at removing material than a mechanical brush due to the size, depth and edge wall effects of the abrasion. With a limited supply of ~888 nominal puffs, the gDRT is primarily used to remove abrasion fines but it can also be used as a dust removal instrument for the M2020 mission (Jens et al., 2018).

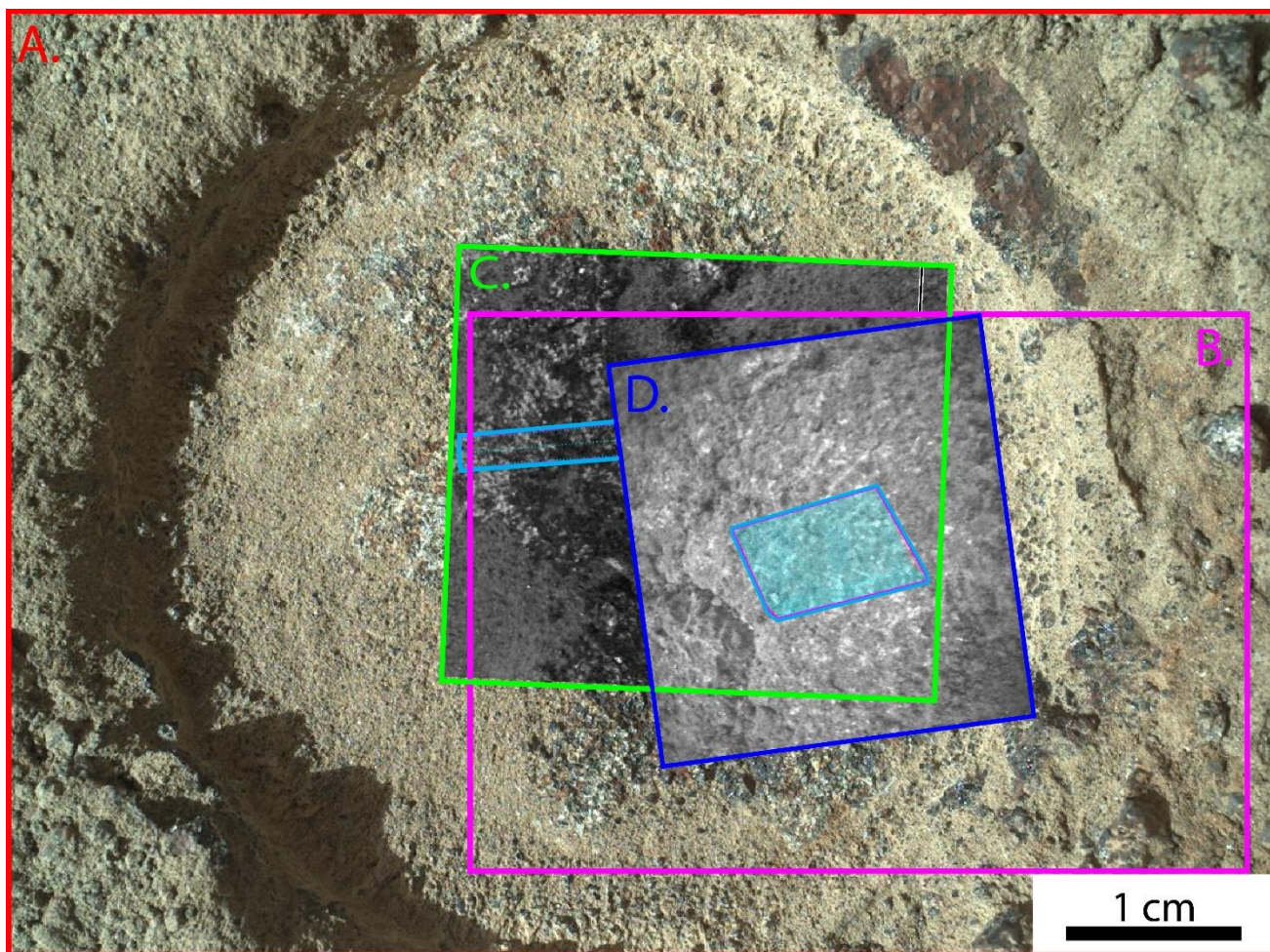
SHERLOC-WATSON

The Scanning Habitable Environments with Raman and Luminescence for Organics and Chemicals (SHERLOC) is a suite of instruments attached to the RA of Perseverance. The deep-ultraviolet native fluorescence and resonance Raman spectrometer, Autofocus Context Imager (ACI), Wide Angle Topographic Sensor for Operations and eNginEering (WATSON) camera, along with the remaining Perseverance payload, provide sub-millimeter scale, spatially resolved detections and characterizations of organic matter and minerals on the Martian surface (Bhartia et al., 2021)

The WATSON camera is capable of capturing red-green-blue (RGB) images of the Martian surface from a range of working distances, providing greater geological context at a range of spatial scales (Bhartia et al., 2021). Colour contrasts between abrasion marks and the underlying target surface were more apparent in the RGB WATSON images than the greyscale ACI images. However the ACI is higher resolution (10.1 $\mu\text{m}/\text{pixel}$ Bhartia et al., 2021) and co-boresighted with the spectrometer, making it the most accurate image product to compare with geochemical quantifications. Therefore the RGB WATSON images were used to trace abrasion marks across the entire abrasion patch, whereas ACI images were used to trace abrasion marks within the PIXL FOV.

5.3.2 Abrasion Mark Mapping

Adobe Illustrator (AI) and Quantum Geographic Information Systems (QGIS) were two software used to map and measure abrasion marks within each abrasion patch. AI is a versatile vector-based, image editing, and artwork software capable of exporting file formats usable in



QGIS. QGIS (v3.28.2 Firenze) is a free, open-source software for creating, editing, and analysing geospatial information.

Figure 5-5: Example of the WATSON images (A. and B.) and PIXLISE screen captures (C. and D.) overlay used to trace abrasion marks and map mineral boundaries. (A.) 7-cm standoff WATSON image SIF_0346_0697661611_539FDR_N0092982SRLC00758_0000LMJ01. (B.) 4 cm standoff WATSON image SI1_0347_0697764296_148FDR_N0092982SRLC00003_000095J02. (C.) PIXLISE screen capture of the Montpezat 1 PIXL scan. (D.) PIXLISE screencapture of the Montpezat 2 PIXL scan.

The highest-resolution SHERLOC-WATSON and ACI images were first opened and overlaid in AI (Figure 5-5). Each abrasion mark was then manually traced using the *Pen Tool*, which creates a vector-line (also known as a path) to a user-defined length. This tool was used to trace the scale bar, whose length would later be used to normalize all other abrasion lengths. Each continuous etch mark preserved in the target surface was considered an abrasion mark. This definition also includes features such as mineral cleavages and fractures, which are linear rock features that form in response to stresses and may be produced during abrasion. They were therefore considered as “abrasion marks” in this study. Satisfied with the abrasion traces, the ungrouped paths were then transferred to a new document absent of any background images, and exported as an AutoDesk RealDWG (.dxf) file.

5.3.3 Mineral Mapping

The PIXLISE software produces element maps for each PIXL Scan (Ye et al., 2021). PIXLISE displays the co-registered PIXL scans and MCC images where chemical abundances of each PIXL spot (called PIXL PMC or PMC) are plotted above an MCC image of the abraded surface (see Figure 3-11). For this study PIXL map scans with densely packed PMCs were required to define mineral boundaries. Of the three PIXL scan types, only the densely PMC-populated rectangular (4x12 mm²) and square (up to 22x22 mm², but commonly 5x5 mm² to 7x7 mm²) scans were used. PIXL line scans were excluded since PMCs are too dispersed, possibly missing some minerals and/or preventing accurate mineral grain boundaries and rock textures from being defined (Figure 3-12).

Igneous rocks were examined by the Perseverance rover during the Crater Floor campaign. Interactions with aqueous solutions have modified the mineralogy, composition and texture of these primary igneous materials. These secondary mineral assemblages include carbonate materials in the Séítah formation, iron oxides and the deposition of sulfate and perchlorate salts (Farley et al., 2022). Proximity science throughout the Delta Front campaign and remote observations revealed a suite of sedimentary rocks that are consistent with subaqueous deposition, likely via a turbidite-related process (Williams et al., 2023; Sun et al., 2023). Sedimentary materials from the lower delta front were a combination of sulfate- and carbonate-cemented siltstones and mudstones with detrital igneous grains (Williams et al., 2023). To

separate each PIXL scan into the original unaltered materials and secondary altered materials, three mineral groups were selected in each abrasion patch: (1) Low-Salt, (2) High-Salt and (3) Alteration (see Table 5-2 for descriptions of each mineral group).

Table 5-2: Chemical descriptions and example minerals for each mineral group included in this study.

Mineral Groups	General Description
Low Salt	<p>SiO₂-rich, SO₃ and Cl poor. Primary igneous material.</p> <p>This mineral group includes:</p> <ul style="list-style-type: none"> • Olivine e.g., (Mg, Fe)₂SiO₄ • Pyroxene e.g., Augite ((Ca,Na)(Mg,Fe,Al)(Si,Al)₂O₆) • Aluminosilicate e.g., Sanidine/Orthoclase/Microcline (KAlSi₃O₈) • Oxides e.g., Magnetite (Fe₃O₄) and Ilmenite (FeTiO₃) • Phosphates e.g., Apatite (Ca₅(PO₄)₃F)
High Salt	<p>SiO₂-poor, SO₃ and Cl poor. Secondary salt-rich materials.</p> <p>This mineral group includes:</p> <ul style="list-style-type: none"> • Halite e.g., (NaCl) • Anhydrite e.g., (CaSO₄) • Magnesium Sulfate e.g., (MgSO₄) • Perchlorate e.g., (NaClO₂)
Alteration	<p>Fe-rich, SiO₂-poor and/or SO₃ and Cl-rich secondary alteration material.</p> <p>This mineral group includes:</p> <ul style="list-style-type: none"> • Magnesite e.g., MgCO₃ • More Ferroan Carbonates e.g., (Mg,Fe)CO₃

Minerals were classified based on age, starting with the youngest materials. Sulfates and other salts (High-salt mineral group) are secondary minerals which fill pore spaces, voids, and cracks in their host rock (Farley et al., 2022) and are likely the youngest minerals present. These were the first materials selected in each abrasion patch. Since each abrasion target possesses a unique mineralogy and composition, each target required unique expressions to select the desired minerals. These expressions select PIXL PMCs based on chemical abundances (see Table

5-3), which are then classified into Regions of Interest (ROI) and prevents their selection in subsequent expressions. Carbonates and perchlorates (included in the alteration mineral group) were selected using FeO/SiO_2 and SO_3/Cl abundances, however these criteria will also select igneous oxides, such as magnetite (Fe_3O_4) and ilmenite (FeTiO_3). To ensure their proper classification, a $\text{FeO-TiO}_2\text{-Cr}_2\text{O}_3$ RGB colour mixed image was used (see Figure 3-13). PMCs that incorrectly selected igneous oxides were manually deselected, while the remaining PMCs were classified into the Alteration ROI. The remaining low-salt PMCs were selected and classified into the Low-Salt ROI. The final mineral ROIs were then exported from PIXLISE as a .jpeg (Figure 3-14).

5.3.4. Vectorizing ROIs

To quantify abrasion mark lengths and abundance within each mineral group, the PIXLISE ROIs (Figure 3-14) needed to be vectorized. Screen captures from PIXLISE were opened in AI and positioned above the high-resolution SHERLOC-WATSON images. The *Image Trace* tool in AI was used to separate each ROI into individual paths. The *Image Trace* tool classifies the selected image into a user-defined number of colour classes; more classes preserve the resolution and the boundaries between shapes, however fewer classes forces AI to merge edges of similar coloured pixels together, and distorts ROIs when converted in vectorized shapes. To avoid distortion and to preserve ROI shapes, more user-defined classes were assigned. The *Image Trace* product creates a thin, darker coloured border around each PIXL PMC that needs to be preserved. Deleting this border would form hundreds of disconnected shapes that would create hundreds of smaller paths if used as the abrasion mark clipping mask. To avoid this problem, the borders were changed to the same colour as the ROI, grouped together and changed into a *Compound Path*. Combining the borders and PMCs as a *Compound Path* is essential. Skipping this step keeps each PIXL PMC as an individual paths, and the problem would persist. Three compound paths, one for each mineral type (Low Salt, High Salt, and Alteration), were generated for each PIXL scan and were exported as an AutoDesk RealDWG (.dxf) file. Exporting them as the same file type as the abrasion trace preserves their position relative to the abrasion trace.

5.3.5 Clipping Abrasion Marks to ROI and Measurements

The AutoDesk Real DWG (.dxf) files for the abrasion marks and mineral ROIs were opened in QGIS as vector layers and projected to the ESPG:357 WGS 84: Pseudo Mercator coordinate system. Projecting these layers allowed them to be measured in QGIS. The *Field Calculator* was used to measure the length of each abrasion mark using the \$length function. These values were then exported to Microsoft Excel, and their values were then normalized to the known length of the scale bar.

The \$area function from the *Field Calculator* was then used on the compound paths and the PIXL FOV to measure their respective areas. These values were then divided by PIXL FOV's area to calculate how much of its area is occupied by each mineral type. The percent areal abundance of Low Salt, High Salt and Alteration mineral types were then subtracted from the PIXL FOV's area to find the area of missing data. This missing PIXL data can be caused by diffraction scattering due to surface roughness and thermal drift of the RA during the PIXL scan. The abrasion marks were then clipped to mineral type *Compound Paths* to measure the abrasion mark abundance within each mineral type. These abrasion lengths were then measured using the \$length function in the *Field Calculator*. Similar to before, these values were then exported to Microsoft excel, and their values were normalized to the known length of the scale bar.

Table 5-3: Expression values used to select and sort PMCs into mineral groups

Campaign	Sol	Name	Rock Type	Expression Values
Crater Floor	167	Guillaumes ¹	Igneous	Low Salt: <2 wt% SO ₃ , <4 wt % Cl High Salt:>2 wt% SO ₃ , >4 wt% Cl
	187	Bellegarde ¹	Igneous	Low Salt: <4.85% SO ₃ , <3 wt% Cl High Salt: >4.85% SO ₃ , >3 wt% Cl
	257	Dourbes ¹	Igneous	Low Salt: <10 wt% SO ₃ Alteration: >35 wt% FeO, <30 wt% SiO ₂ High Salt: >10 wt% SO ₃
	294	Quartier ¹	Igneous	Low Salt: <7.5 wt% SO ₃ Alteration: >35 wt% FeO, <30% SiO ₂ High Salt: >7.5 wt% SO ₃
	364	Montpezat ¹	Igneous	Low Salt: <1.5 wt% SO ₃ , <1.5 wt% Cl Alteration: >1.5 wt% SO ₃ , >1.5 wt% Cl High Salt: > 1.5 wt% SO ₃
	367	Alfalfa ¹	Igneous	Low Salt: <2% SO ₃ , <4% Cl Alteration: >4 wt% Cl, <2 wt% SO ₃ High Salt: >2 wt% SO ₃
Delta Front	484	Thornton Gap	Sedimentary	Low Salt: <10 wt% SO ₃ , <10 wt% Cl Alteration: >20 wt% FeO, <20 wt% SiO ₂ High Salt: >10 wt% SO ₃ , >10 wt% Cl
	505	Berry Hollow	Sedimentary	Low Salt: <15 wt% SO ₃ Medium Salt: 25> x >15 wt% SO ₃ High Salt: >25 wt% SO ₃
	570	Novarupta	Sedimentary	Low Salt: <5% wt% SO ₃ Alteration: <25 wt% SiO ₂ High Salt: >5% wt% SO ₃
	617	Uganik Island	Sedimentary	Low Salt: <15 wt% SO ₃ Medium Salt: 35 > x > 15 wt% SO ₃ High Salt: >35 wt% SO ₃

¹Expression values given by Schmidt et al. (in prep)

5.4 Results

Initial observations found that abrasion marks were variably preserved across the 10 abrasion patches included in this study. Before abrasion marks were mapped and measured, each abrasion patch was first assessed based on lithology, the quality of the abrasion, the amount of abrasion fines remaining and overall appearance.

Guillaumes – Sol 176

Guillaumes (Figure 5-6) was the first abrasion patch produced and analyzed by the PIXL instrument on the M2020 mission. The freshly exposed rock contained interlocking millimeter-sized (0.1-3.8 mm; Table 5-4), inter-connected light and dark grains with pervasive brown surface stains. Some of the grains appeared to be elongated, however no discernible grain orientation was determined (Farley et al., 2022). Large irregularly shaped voids/pits, up to 5mm in diameter, were also visible throughout the abrasion patch. Some of these voids/pits were unfilled, however others were partially or fully infilled by a bright-white mineral. The abraded surface was very jagged, requiring a prodapt level of 11 (moderately hard surface), and was covered in hundreds (n=937; Table 5-4) of small abrasion marks (see minimum, median and maximum abrasion lengths in Table 5-4). The PIXL instrument detected abundant primary igneous and salty minerals (Figure 5-6 and 5.7).

Bellegarde – Sol 187

The second abrasion patch, Bellegarde (Figure 5-8), was created in the *Rochette* caprock member of the Máaz formation and contained similar mineralogy with higher abundances of primary igneous minerals, and fewer high salt regions (Figure 5-7). The surface of Bellegarde was filled with light and dark grains, similar to Guillaumes, however the grain sizes were slightly smaller, ranging from 0.1 to 2.6 mm (Table 5-4), and were covered in less brown material. Unlike Guillaumes, Bellegarde was free of any voids/pits as these features had been filled by white minerals (secondary sulfate minerals). The abrasion surface was noticeably smoother than Guillaumes, requiring a prodapt level of 15.3 (Table 5-4), and persevered similar a higher count of similar sized abrasion marks (n=1136; Table 5-4). The higher prodapt level indicates that the surface of Bellegarde was harder than Guillaumes.

Dourbes – Sol 257

Transitioning into the Séítah formation, Perseverance studied the *Rochette* caprock member and produced the abrasion patch (Figure 5-9). Dourbes was also the first abrasion patch in M2020 to host multiple PIXL scans. The Dourbes abrasion patch is noticeably lighter colored than previous abrasion patches with abundant light brown, brown and grey-green mineral grains. While mineral grains are similar to those from the relatively olivine-free Mááz targets, ranging from 0.1 to 3.2 mm (Table 5-4), olivine and augite grains were identified throughout the Dourbes abrasion patch (Liu et al., 2022). Additionally, Liu et al. (2022) have identified augite crystals with identical crystal orientations surrounding a single olivine grain. This feature is characteristic of poikilitic textures and is indicative of an igneous origin. Alteration and high salt abundances were nearly identical between the two PIXL scans (approximately 4% for both; Figure 5-7), but were predominantly primary igneous minerals. The abrasion surface was smooth, similar to Bellegarde, required a prodapt level of 16, and persevered a similar abrasion mark count to Guillaumes (n=973; Table 5-4).

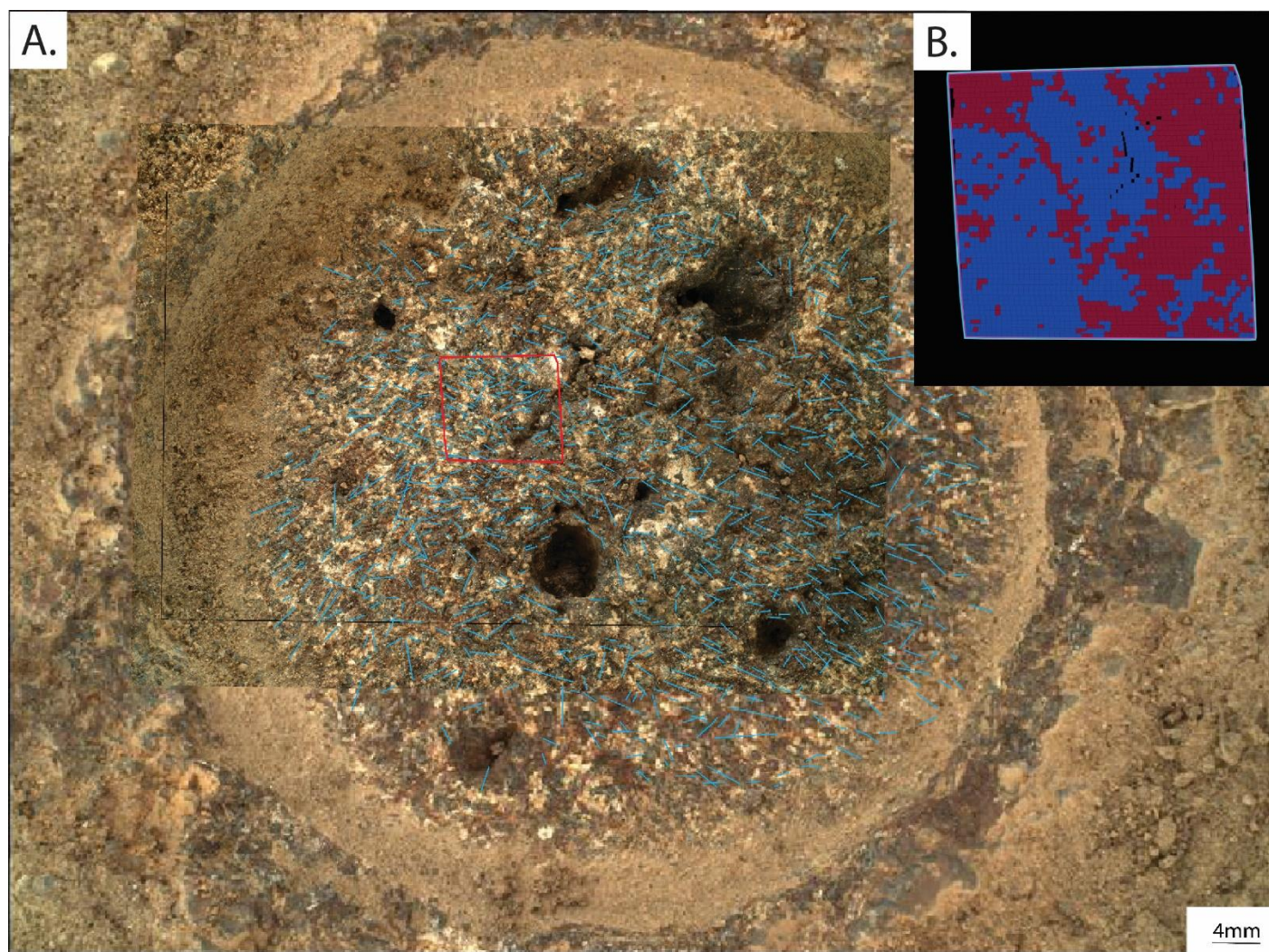


Figure 5-6: SHERLOC-WATSON images SIF_0161_0681241540_582FDR_N0060000SRLC08008_0000LMJ01.IMG (small) and SI1_0160_0681181210_679FDR_N0060000SRLC00003_000095J01.IMG (large) of Guillaumes with all abrasion marks (blue) and PIXL FOV (red polygon) traced. (B.) Screen capture of mineral map created using pixlise.org where “Low-Salt” and “High-Salt” regions are coloured blue and red respectively.

Table 5-4: Abrasion mark and grain size statistics for all abrasion patches from M2020.

Geologic Formation	Sol	Target Name	Total Abrasion Count	Total Abrasion Length (mm)	Median Abrasion Length (mm)	Maximum Abrasion Length (mm)	Minimum Abrasion Length (mm)	Maximum Grain Size (mm)	Minimum Grain Size (mm)	Average Prodapt Level
Máaz	167	Guillaumes	937	915.83	0.85	6.29	0.18	3.84	0.12	11
	187	Bellegarde	1136	1048.98	0.79	4.53	0.17	2.65	0.12	15.3
	364	Montpezat	434	477.21	0.92	5.72	0.22	0.51	0.04	12
	367	Alfalfa	357	653.13	1.62	6.60	0.23	2.35	0.03	18
Séítah	257	Dourbes 1	973	865.68	0.85	6.29	0.18	3.17	0.09	16
	270	Dourbes 2	973	865.68	0.85	6.29	0.18	3.17	0.09	16
	294	Quartier 1	367	390.74	0.94	4.08	0.19	4.23	0.09	7
	301	Quartier 2	367	390.74	0.94	4.08	0.19	4.23	0.09	7
Shenandoah	484	Thornton Gap	374	592.42	1.35	5.71	0.35	2.84	N/A	7
	505	Berry Hollow 1	295	480.36	1.34	11.68	0.33	0.59	N/A	4
	507	Berry Hollow 2	295	480.36	1.34	11.68	0.33	0.59	N/A	4
	570	Novarupta 2	422	960.64	1.78	9.08	0.43	0.57	N/A	12
	573	Novarupta 3	422	960.64	1.78	9.08	0.43	0.57	N/A	12
	614	Uganik Island 2	153	128.38	0.78	2.14	0.27	5.03	N/A	3
	617	Uganik Island 3	153	128.38	0.78	2.14	0.27	5.03	N/A	3

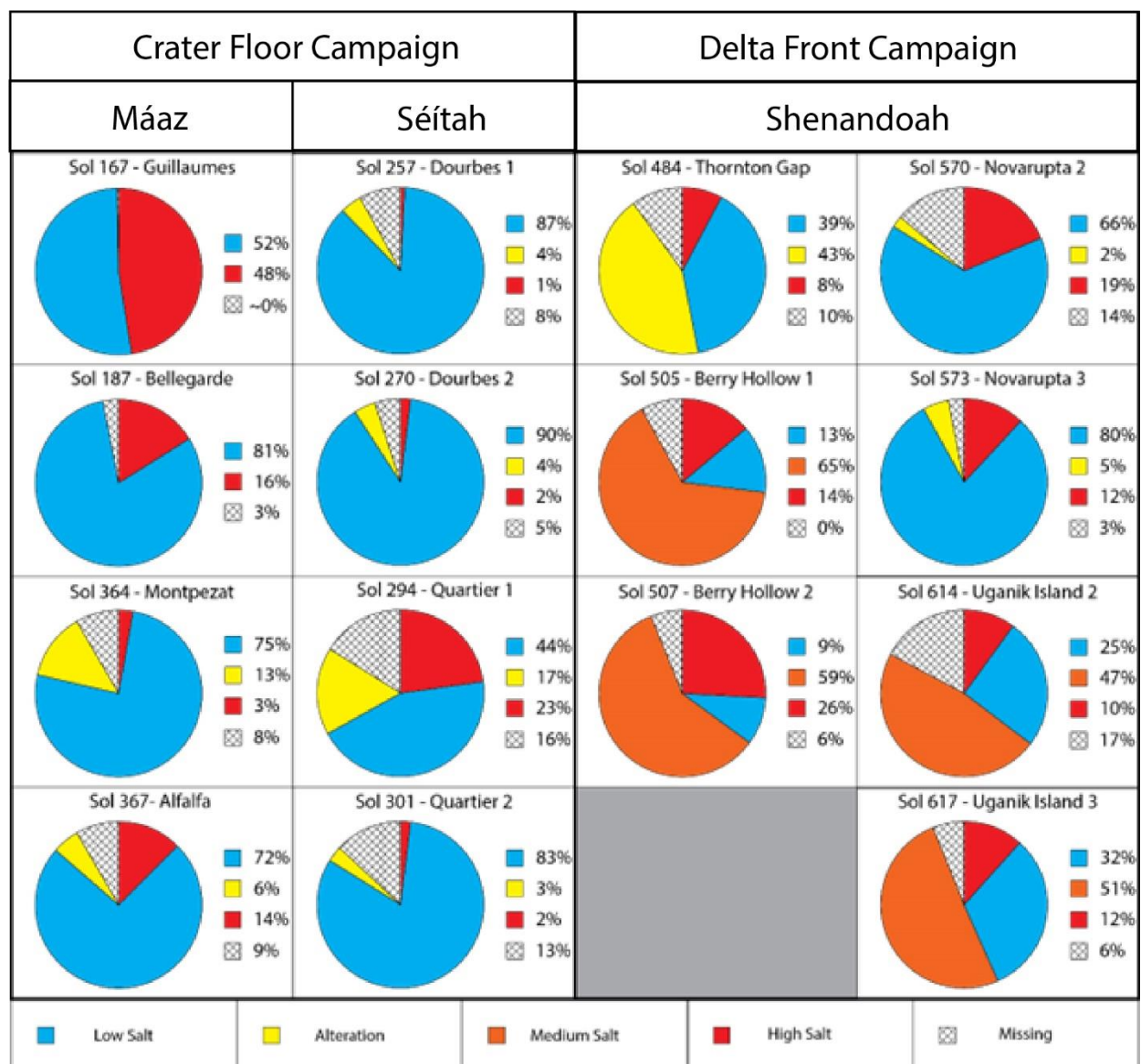


Figure 5-7: PIXL mineral abundances for each abrasion target sampled during the Crater Floor and Delta Front campaigns.

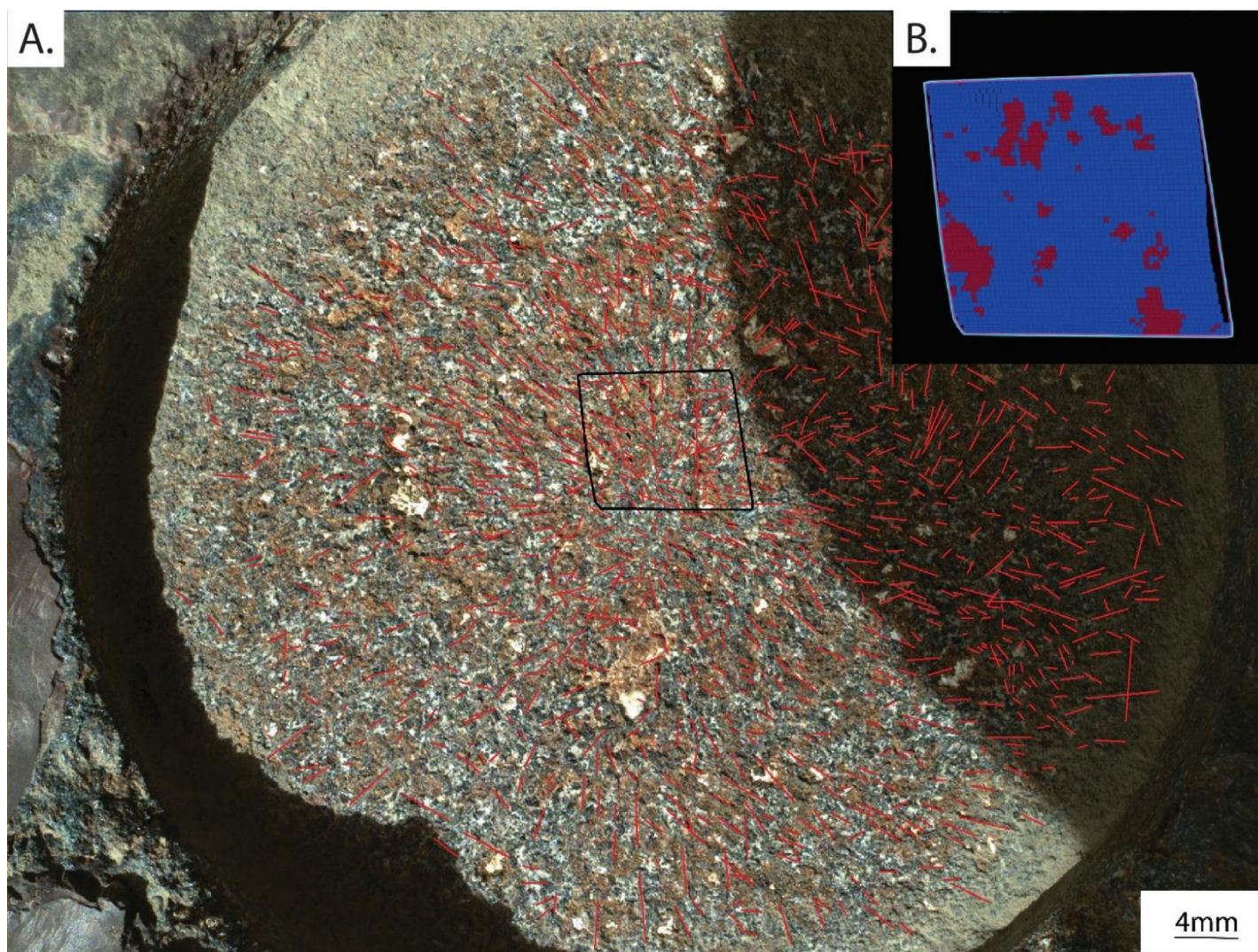


Figure 5-8: (A). SHERLOC-WATSON images SIF_0185_0683368184_652FDR_N0070000SRLC00720_0000LMJ01.IMG of the Bellegarde abrasion patch with all abrasion marks (red) and PIXL FOV (black polygon). (B.) Screen capture of the mineral map created using pixlise.org where “Low-Salt” and “High-Salt” regions are coloured blue and red respectively.

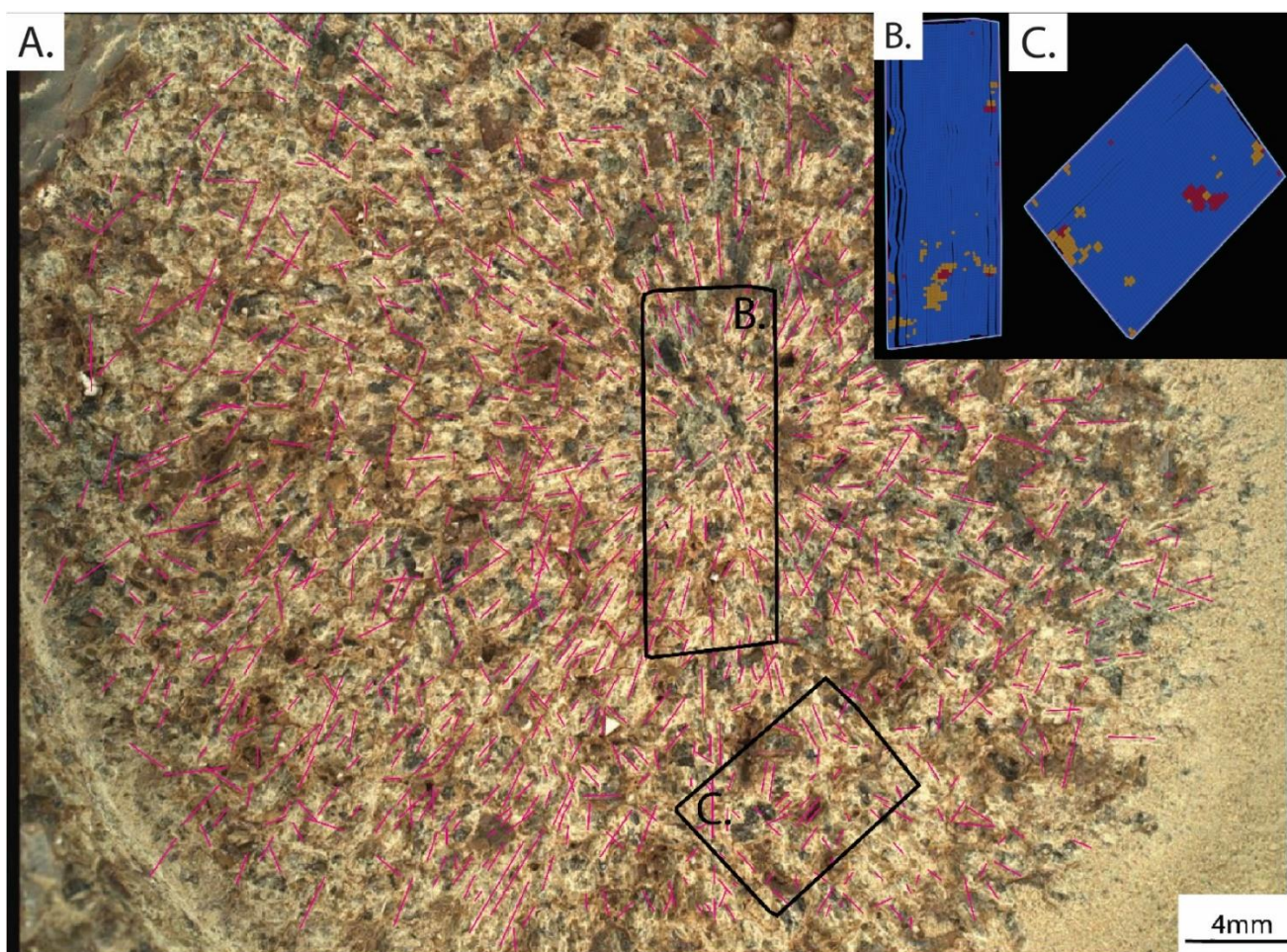


Figure 5-9: (A). SHERLOC-WATSON image SI1_0257_0689775622_738FDR_N0080000SRLC00006_000095J01.IMG of the Dourbes abrasion patch. Abrasion marks are traced in pink and the PIXL FOVs are outlined in black. Mineral maps of the Dourbes 1 (B.) and Dourbes 2 (C.) are displayed at the top right. Regions with “Low Salt High,” “High Salt” and “Alteration” are coloured blue, red, and yellow respectively

Quartier – Sol 294

Continuing its investigation of the Séítah formation, the M2020 mission abraded the *Issole* outcrop to produce the Quartier abrasion patch (Figure 5-10; Hernandez-Montenegro et al., 2023). Unlike previous abrasions, a layer of abrasion fines covered the perimeter of Quartier and limited observations to the exposed regions of the abrasion. The exposed surface was slightly darker and more jagged than Dourbes but was still lighter in color compared to the earlier Mááz targets. Mineral grains were similar in size to Dourbes (Table 5-4), however larger white minerals were visible in Quartier, particularly in the first PIXL scan (Figure 5.10B). This first PIXL scan was focused on an area with a large sulfate grain, informally known as the ‘polar bear’ grain, and contained 23.4% high salt, 16.8% alteration, and 43.6% primary igneous minerals (Figure 5-7). The second PIXL scan of Quartier (Figure 5.10C) had a composition comparable to Dourbes with predominantly primary igneous minerals (82.6%), and mineral alteration and high salt materials (2.8% and 1.8% respectively; Table 5-4). While Quartier’s overall abrasion mark count (n=367; Table 5-4) was below half of those recorded in Dourbes, the layer of abrasion fines likely cover an unknown amount of abrasion marks and lowered the overall abrasion mark measurements.

Montpezat – Sol 364

Returning to further investigate the Mááz formation, Perseverance produced the Quartier abrasion patch in the Rimplas outcrop of the Artuby member of the Mááz formation (Figure 5-11). The abraded surface was uneven (Prodapt level of 12; Table 5-4), similar to Guillaumes, however a large portion of the abrasion patch was buried beneath a layer of abrasion fines. These abrasion fines may be filling small voids and pits in abrasion surface, similar to those from Guillaumes, however these features are otherwise unresolvable in WATSON imagery. The exposed surface contains predominantly dark blue-grey and white grains, ranging from 0.05 to 0.5 mm, and 434 abrasion marks (Table 5-4). Like Quartier, abrasion mark measurements were limited to exposed surfaces and are likely under representative of their true measurements. Given the density of the abrasion marks within the exposed surface, the overall abrasion count of Montpezat would have likely resembled those from Bellegarde and Guillaumes if the entire abrasion patch was cleared of fines. Montpezat was predominantly primary igneous minerals (75.4%), with fewer alteration (13.3%) and high salt materials (3.5%).

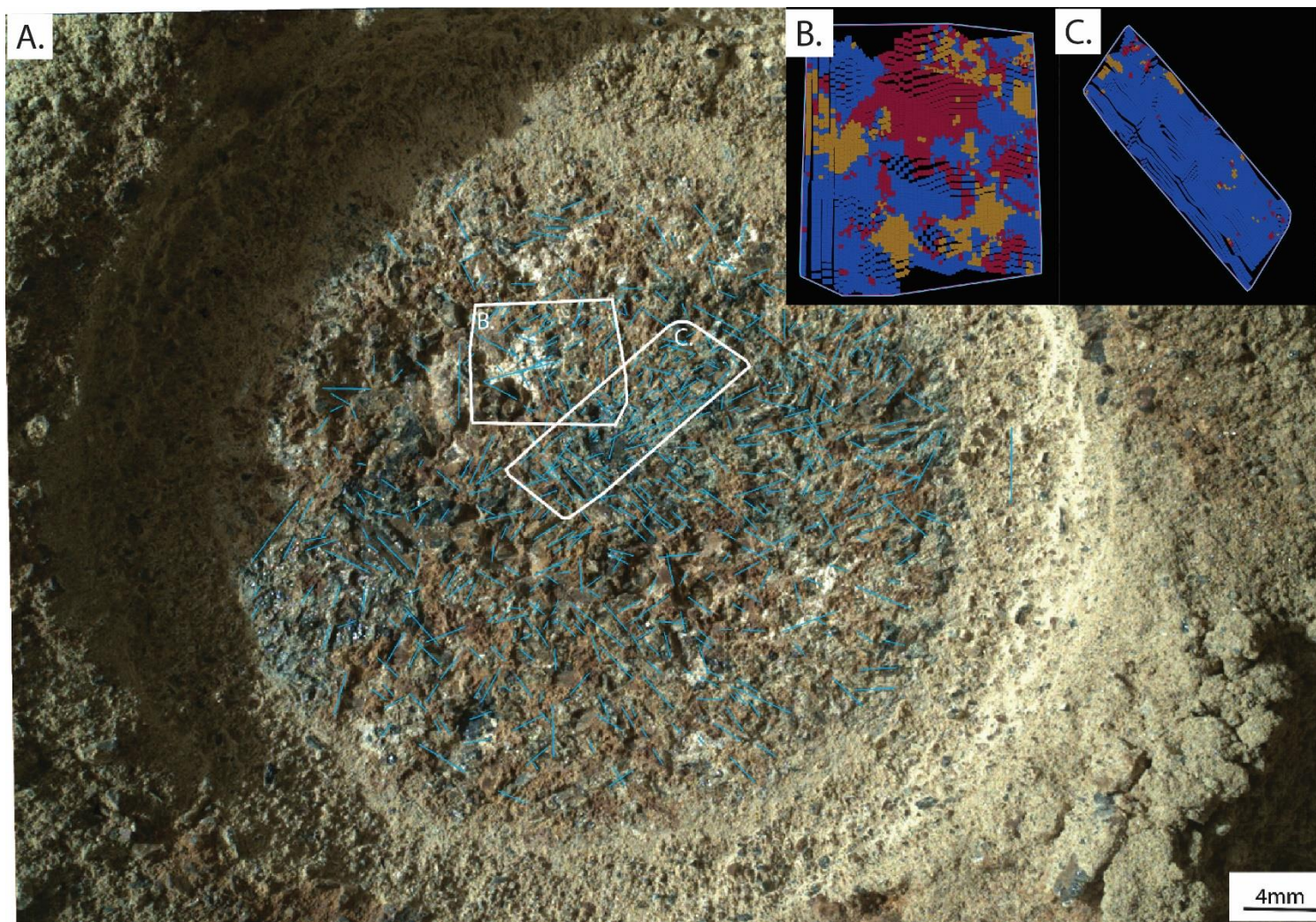


Figure 5-10: (A). SHERLOC-WATSON image SIF_0292_0692874790_734FDR_N0090000SRLC01034_0000LMJ01.IMG of the Quartier abrasion patch. Abrasion marks are traced in blue and the PIXL FOVs are outlined in white. Mineral maps of Quartier 1 (B.) and Quartier 2 (C.) are displayed at the top right. Regions with “Low Salt High,” “High Salt” and “Alteration” are coloured blue, red, and yellow respectively

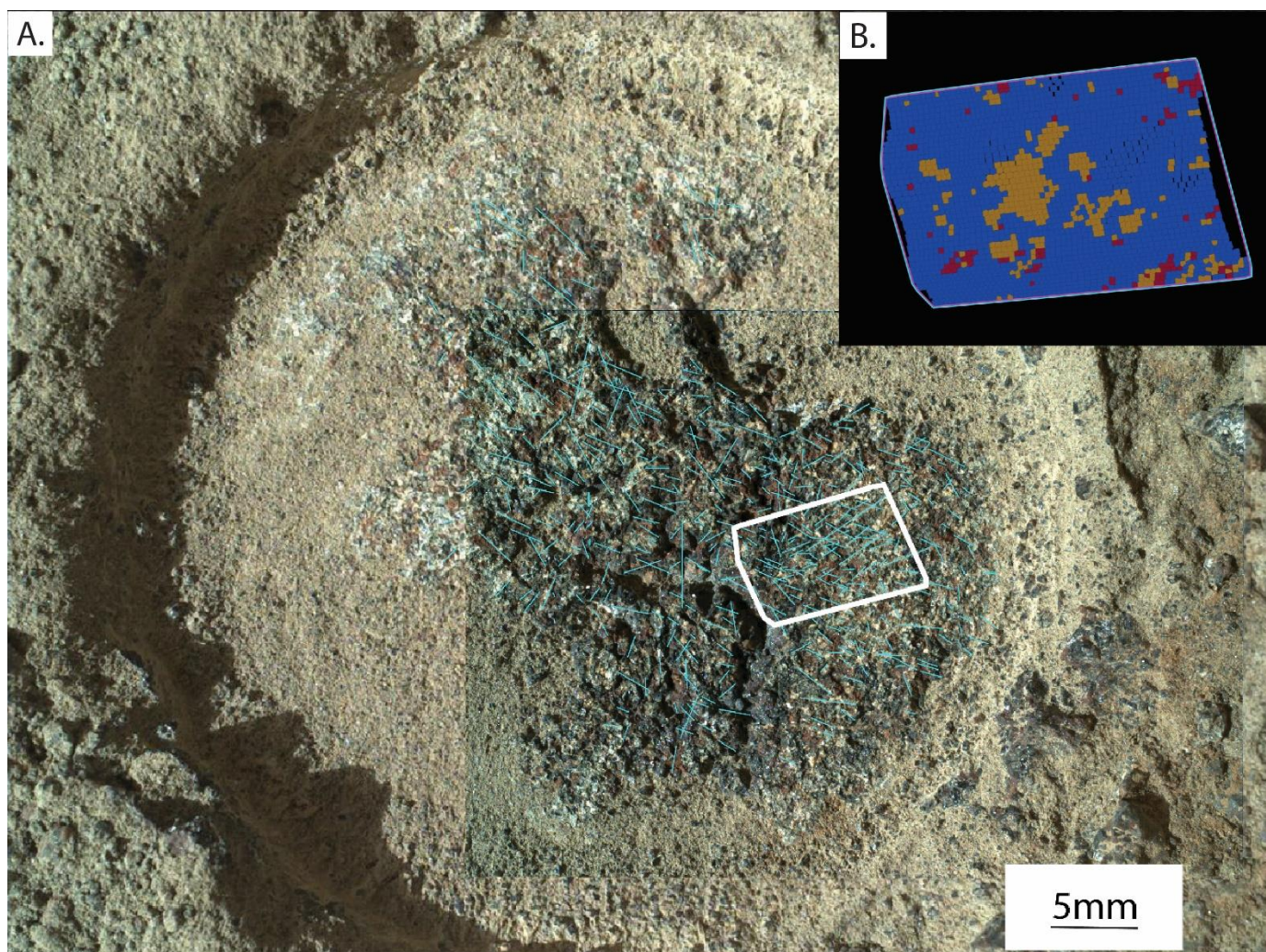


Figure 5-11: (A). SHERLOC-WATSON images SIF_0347_0697751287_792FDR_N0092982SRLC00603_0000LMJ01.IMG (small) and SI1_0346_0697669267_585FDR_N0092982SRLC00033_000095J01.IMG (large) of the Montpezat abrasion patch. Abrasion marks are traced in blue and the PIXL FOVs are outlined in white. The mineral maps for Montpezat is displayed at the top right (B.). Regions with “Low Salt High,” “High Salt” and “Alteration” are coloured blue, red, and yellow respectively

Alfalfa – Sol 369

Alfalfa (Figure 5-12), located on the Sid boulder of the Ch'al member, was the final abrasion patch produced in the Máaz formation during the Crater Floor campaign. The abrasion surface was noticeably flatter than previous targets and used the highest prodapt level (18; Table 5-4) of any target included in this study. The surface was filled with white, brown and black minerals that ranged from 0.05 to 2.4 mm in diameter (Table 5-4). PIXL scans found Alfalfa contained similar primary igneous mineral abundances to Montpezat (72%; Figure 5-7), however the high salt (14%) and alteration (6%) mineral abundances had flipped. Abrasion marks were considerably longer in Alfalfa compared to other Máaz targets, reaching up to 6.6 mm (Table 5-4), but recorded the lowest total abrasion mark count (n=357; Table 5-4) amongst the Crater Floor targets.

Thornton Gap – Sol 484

Transitioning into the Delta Front campaign, M2020 began its investigation of the Shenandoah formation. Thornton Gap (Figure 5-13), an abrasion patch from the Lower Rockytop member of Hawksbill Gap, was the first abrasion target on a sedimentary lithology. This fine-to-coarse grained sandstone. The abraded surface was smoother than any igneous target sampled during the previous Crater Floor campaign and required a prodapt level of 7. Thornton Gap contained the highest abundance of alteration materials (43.4%; Figure 5-7) and was the first target where the alteration materials exceeded both primary igneous (38.6%) and salty (7.5%) mineral abundances. Dark sub-angular granule-sized grains (Table 5-4) were easily discerned from the lighter-toned carbonate matrix. Unfortunately, the minimum grain size of Thornton Gap and other delta front targets were not resolvable in WATSON images, preventing their measurement (Table 5-4). Abrasion marks were similar in size to those in the flat Alfalfa abrasion patch (Table 5-4) and were preserved at similar abundances as well

Berry Hollow – Sol 505

Shortly after, Perseverance abraded the underlying hydrated sulfate-cemented siltstones of the Hogwallow Flats member of the Hawksbill Gap outcrop. The abraded surface was very flat, preserving the longest abrasion mark recorded in this study and a total abrasion count of n=295 (Table 5-4). Due to its cement, the Berry Hollow 1 and 2 PIXL scans were enriched in salty

materials, and could be divided into medium (65% and 58.6%, respectively) and high salt materials (13.8% and 9.1%, respectively; Figure 5-7). For comparison, if the “high salt” expression for Guillaumes was applied to the Berry Hollow scans, every PIXL PMC would be selected. The Berry Hollow 1 and 2 PIXL scans contained the lowest proportions of primary igneous minerals (13.8% and 9.1%, respectively), with no detections of alterations materials.

Novarupta – Sol 570

Following its investigation of Hawksbill Gap, Perseverance returned south to the Cape Nukshak outcrop and abraded its lowest exposed rock surface, *Enchanted Lake*. The abrasion patch, Novarupta (Figure 5-14), best preserved the expected abrasion bit pattern (Figure 5-2), with several long, continuous abrasion marks radiating from its center. Similar to Thornton Gap, the abraded surface was very flat, however mineral grains were smaller overall in Novarupta (Maximum Grain Size of 0.6mm; Table 5-4). The Novarupta 2 and 3 PIXL scans contained the highest abundance of primary igneous minerals (65.7% and 80.1%, respectively; Figure 5-7) in the Shenandoah formation, and smaller proportions of high salt and alteration materials. Despite being sedimentary, the overall composition of Novarupta resembles those from the igneous Máaz and Séítah formations, and required a similar prodapt level of 12 during abrasion (Table 5-4). With the highest abrasion mark count amongst the Shenandoah formation, Novarupta also preserved the longest total abrasion length (960.6 mm; Table 5-4).

Uganik Island – Sol 614

The final abrasion patch included in this study was produced in the Hidden Harbour member of the Yori Pass (the later equivalent of Hogwallow Flats (Figure). Similar to Berry Hollow, this material was made of hydrated sulfate-cemented siltstones, and produced a smooth abrasion surface. Abrasion marks in Uganik Island were quite small (Median abrasion length of 0.8 mm; Table 5-4), sporadic, and returned the lower total abrasion length and count for the entire M2020 mission thus far. While the fine silt, or smaller groundmass was not resolvable in SHERLOC-WATSON images, Uganik Island contained the largest individual abrasion mark (5.0 mm; Table 5-4) throughout the M2020 mission to date. The PIXL scans for Uganik Island contained similar sulfate enrichments as Berry Hollow (Figure 5-7), with a lower abundance of primary igneous minerals and not detections of alteration materials.

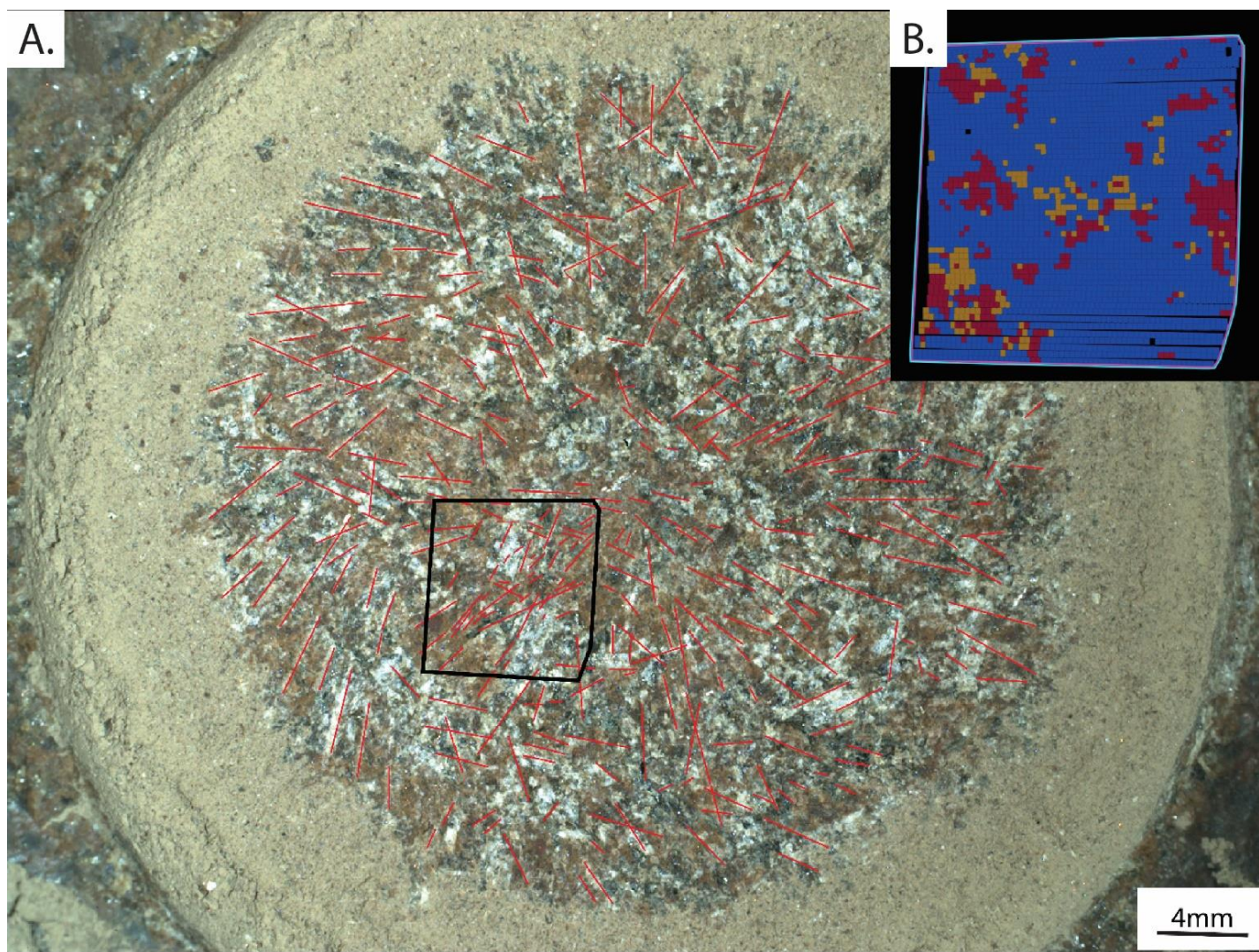


Figure 5-12: (A). SHERLOC-WATSON image SIF_0367_0699544322_300FDR_N0110108SRCLC08029_0000LMJ01.IMG of the Alfalfa abrasion patch with all abrasion marks (red) and PIXL FOV (black polygon) traced. (B.) Screen capture of mineral map created using pixlise.org where “Low-Salt,” “High-Salt,” and “Alteration” regions are coloured blue, red, and yellow respectively.

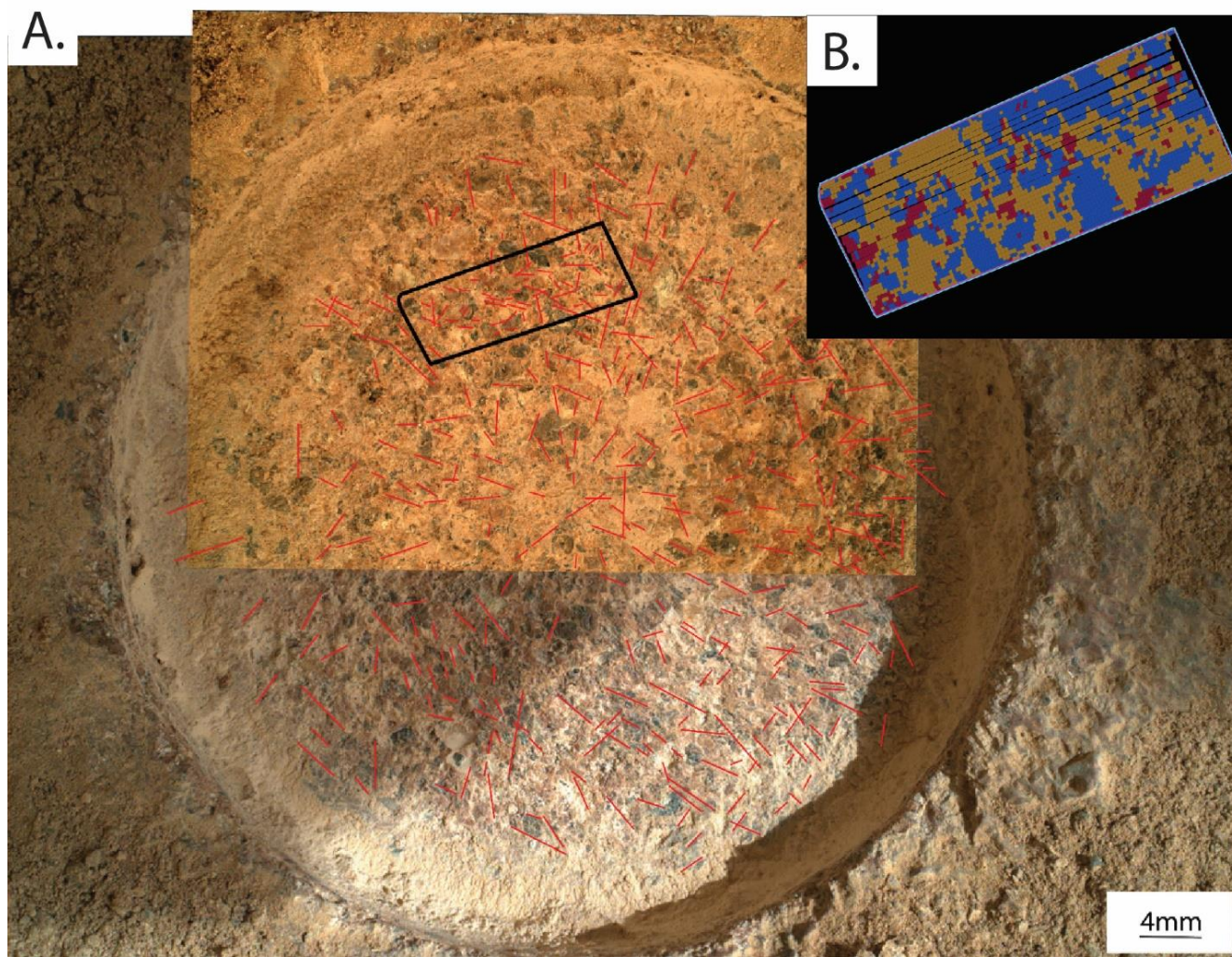


Figure 5-13: (A). SHERLOC-WATSON images SI1_0483_0709779049_878FDR_N0261004SRLC00033_000095J01 (large) and SI1_0485_0710008591_199FDR_N0261004SRLC00009_000095J01 (small) of the Thornton Gap abrasion patch. All abrasion marks are traced in red and the PIXL FOV is outlined in black. (B.) Screen capture of mineral map created using pixlise.org where “Low-Salt,” “High-Salt,” and “Alteration” regions are coloured blue, red, and yellow respectively.

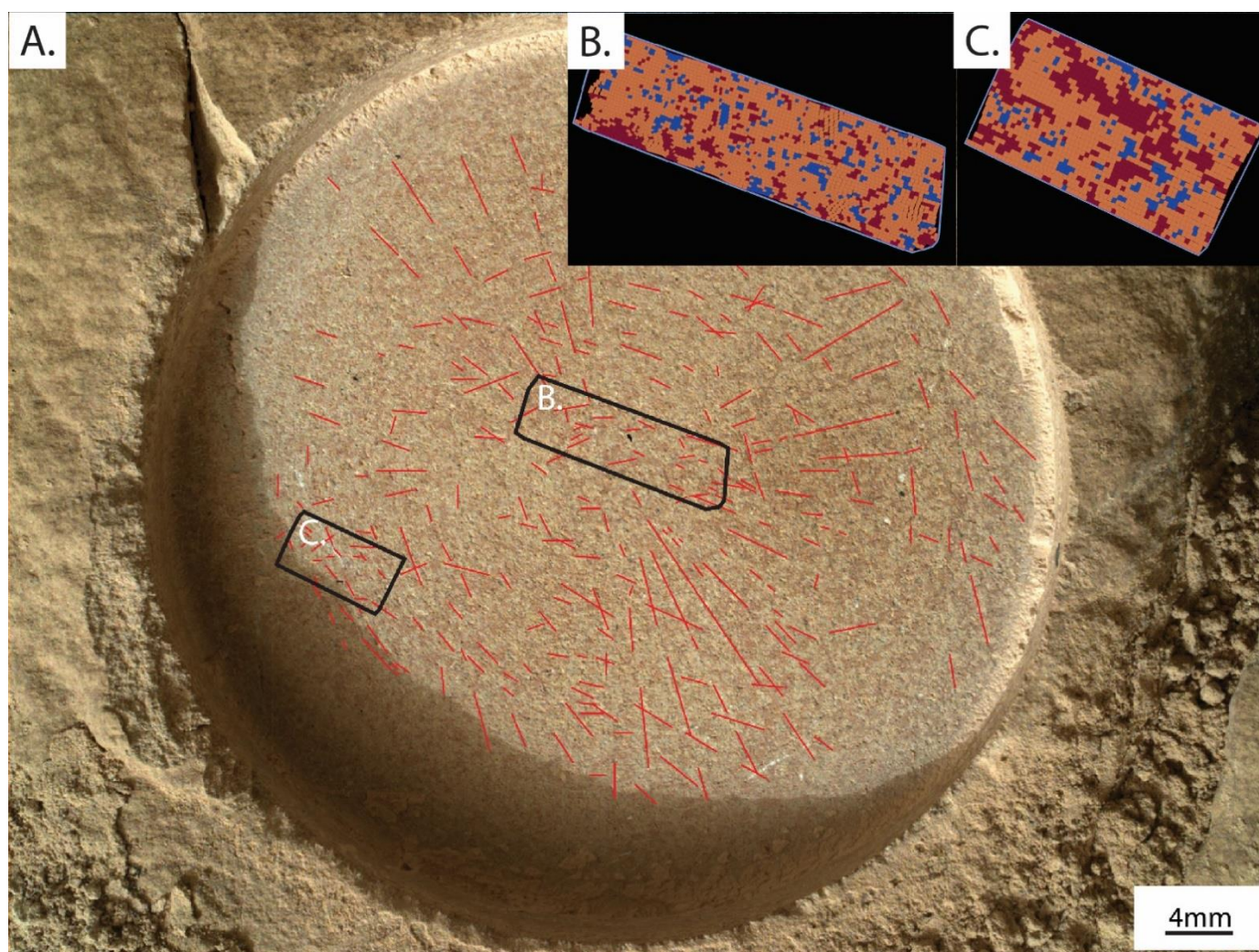


Figure 5-14: (A). SHERLOC-WATSON image SI1_0504_0711704525_972FDR_N0261222SRLC00033_000095J02 of the Berry Hollow abrasion patch. All abrasion marks are traced in red and the PIXL FOVs are outlined in black. Mineral maps of Berry Hollow 1 (B.) and Berry Hollow 2 (C.) are displayed at the top right. Regions with “Low Salt High,” “High Salt” and “Alteration” are coloured blue, red, and yellow respectively.

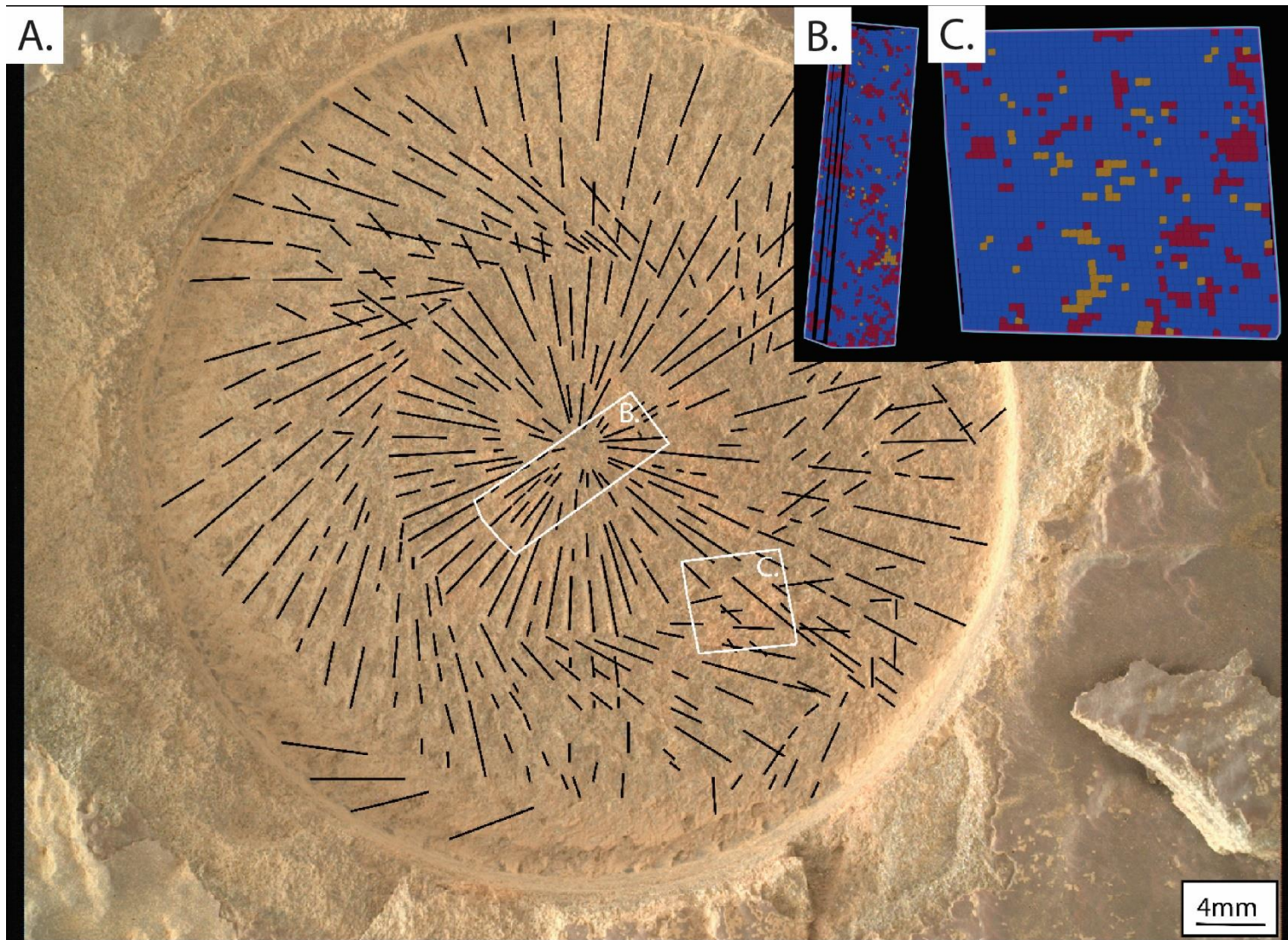


Figure 5-15: (A.) SHERLOC-WATSON image SIF_0568_0717381433_183FDR_N0290000SRLC01031_0000LMJ01 of the Novarupta abrasion patch. Mineral maps of Novarupta 2 (B.) and Novarupta 3 (C.) are displayed at the top right. Regions with “Low Salt High,” “High Salt” and “Alteration” are coloured blue, red, and yellow respectively.

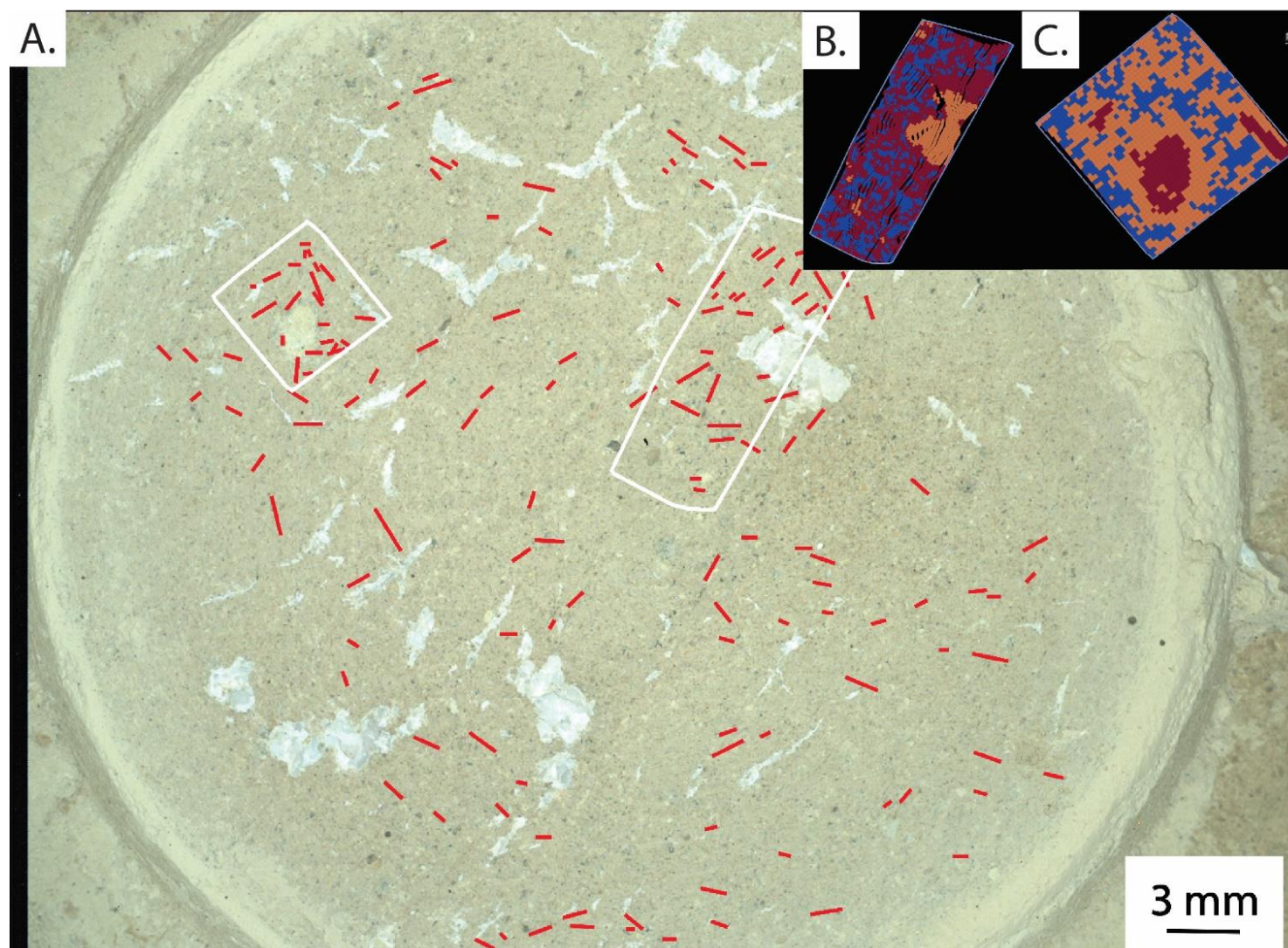


Figure 5-16: (A). SHERLOC-WATSON image SIF_0617_0721745943_003FDR_N0301172SRLC08027_0000LMJ01 of the Uganik Island abrasion patch. Mineral maps of Uganik Island 2 (B.) and Uganik Island 3 (C.) are displayed at the top right. Regions with “Low Salt High,” “High Salt” and “Alteration” are coloured blue, red, and yellow respectively.

5.4.1 Abrasion Mark Measurements

Abrasion marks are variably distributed in abraded patches along the M2020 traverse. Abrasion mark counts are higher in crater floor targets and lower in targets along the delta front. Crater floor targets also generally yielded the longest total abrasion lengths (Table 5-4); however, the Novrarupta (sol 570 and 573; Figure 5-15) abrasion patch contained the second highest total abrasion length (Table 5-4). Median abrasion mark lengths for the crater floor patches were generally shorter than those preserved in the flatter abrasion patches produced along the delta front. Clipping the abrasion mark lengths to their respective PIXL FOVs preserved these relationships (Table 5-5). The Alfalfa abrasion patch (sol 367; Figure 5-12) was comparatively flatter and preserved the longest median abrasion length amongst the crater floor targets. The highest median abrasion length amongst the delta front targets was Novarupta (Table 5-4). Maximum abrasion lengths were statistically insignificant ($p > 0.05$), however the longest abrasion mark was recorded in Berry Hollow (Figure 5-14). Higher prodapt levels were required for crater floor targets as they contained greater proportions of hard, primary igneous minerals. Higher proportions of softer alteration and high salt materials in Thornton Gap (Figure 5-13), Berry Hollow (Figure 5-14), and Uganik Island (Figure 5-16) required lower prodapt levels during abrasion as these surfaces were less resistant to abrasion. Novarupta contained the highest abundance of primary igneous materials amongst the delta front targets, requiring a higher prodapt level (Figure 5-15; Table 5-4). Maximum and minimum grain sizes were relatively consistent amongst the crater floor targets (Table 5-4), however their predominant grain sizes were larger than those in the Shenandoah formation. Maximum grain sizes from the Shenandoah formation varied from coarse sand to pebble-sized grains, however the predominant and minimum grain sizes were below the resolving power of SHERLOC-WATSON ($\sim 13\mu\text{m}/\text{pixel}$; Bhartia et al., 2021) and could not be measured. Abrasion patches from the delta front campaign were generally flatter than those sampled during the crater floor campaigns.

5.4.2 Geochemistry and Mineralogy

Crater floor targets contained higher abundances of low salt, or primary igneous minerals ($\sim 75\%$; Figure 5-7), with varying amounts of high salt ($\sim 15\%$) and alteration materials ($\sim 5\%$). Targets from the Shenandoah formation were primarily alteration and high salt products with

variable low salt abundances (Figure 5-7). While Novarupta is a sedimentary rock, the Novarupta 2 and 3 PIXL scans (Figure 5-15) revealed its mineralogy contained predominantly detrital igneous minerals (Figure 5-7).

5.4.3 Comparison between Abrasion Marks and Geochemistry/Mineralogy

Total abrasion lengths within each PIXL FOV were positively correlated with low salt or primary igneous abundances. Delta front targets contained lower abundances of primary igneous minerals, preserved fewer abrasion marks overall, and lower total abrasion lengths within their respective PIXL FOVs (Figure 5-17; Table 5-5). Mááz and Séítah contained greater abundances of primary igneous minerals, preserved more abrasion marks, and longer total abrasion lengths within their respective FOVs. While Novarupta 2 and 3 appear as outliers in Figure 5-17, Novarupta preserved the most abrasion marks, and the longest total length of abrasion amongst the delta front targets. While the abrasion marks were prevalent overall, only a few crossed the PIXL FOVs (Figure 5-15), and made Novarupta appear as outliers. Dourbes 1 and 2 also plot as outlier in Figure 5-17 but are similar to Novarupta in that these PIXL FOVs contained minimal abrasion marks despite the overall abrasion surface preserving many more (n=973; Table 5-4).

5.4.4 Prodapt Level and Primary Igneous Mineral Abundance

Plotting primary igneous mineral abundances of targets against the average prodapt levels used during abrasion revealed (Figure 5-18) that these two variables were positively correlated. Crater floor targets, which have an average primary igneous mineral abundance of approximately 75%, used prodapt levels between 7 and 16. Delta Front targets, which had primary igneous mineral abundances range from 9% to 80%, used prodapt levels between 3 and 12. Novarupta, which had the highest abundance of primary igneous minerals amongst the delta front targets (Figure 5-7), required the highest prodapt level during abrasion (12 Table 5-4). Dourbes (Figure 5-9), Bellegarde (Figure 5-8), and Alfalfa (Figure 5.12), which had the highest abundances of primary igneous minerals amongst the crater floor targets, also required the highest prodapt levels during abrasion. These results suggest that primary igneous minerals are more resistant to abrasion, requiring higher prodapt levels when being abraded.

Table 5-5: Abrasion mark statistics clipped to PIXL FOVs in each abrasion patch.

Geologic Formation	Sol	Target Name	FOV Total Area (mm ²)	Total Abrasion Length (mm)	Length/Area (mm ⁻¹)
Máaz	167	Guillaume	47.189	56.138	1.190
	187	Bellegarde	47.199	74.901	1.587
	364	Montpezat	56.322	94.693	1.681
	367	Alfalfa	55.976	60.931	1.090
Séítah	257	Dourbes 1	59.458	55.935	0.939
	270	Dourbes 2	36.018	34.878	0.968
	294	Quartier 1	50.591	46.516	0.919
	301	Quartier 2	54.718	66.037	1.207
Shenandoah	484	Thornton Gap	64.021	51.436	0.803
	505	Berry Hollow 1	47.909	26.752	0.558
	507	Berry Hollow 2	23.784	14.589	0.613
	570	Novarupta 2	39.431	39.753	1.008
	573	Novarupta 3	29.417	21.849	0.743
	614	Uganik Island 2	66.279	22.862	0.345
	617	Uganik Island 3	28.83	15.14	0.52

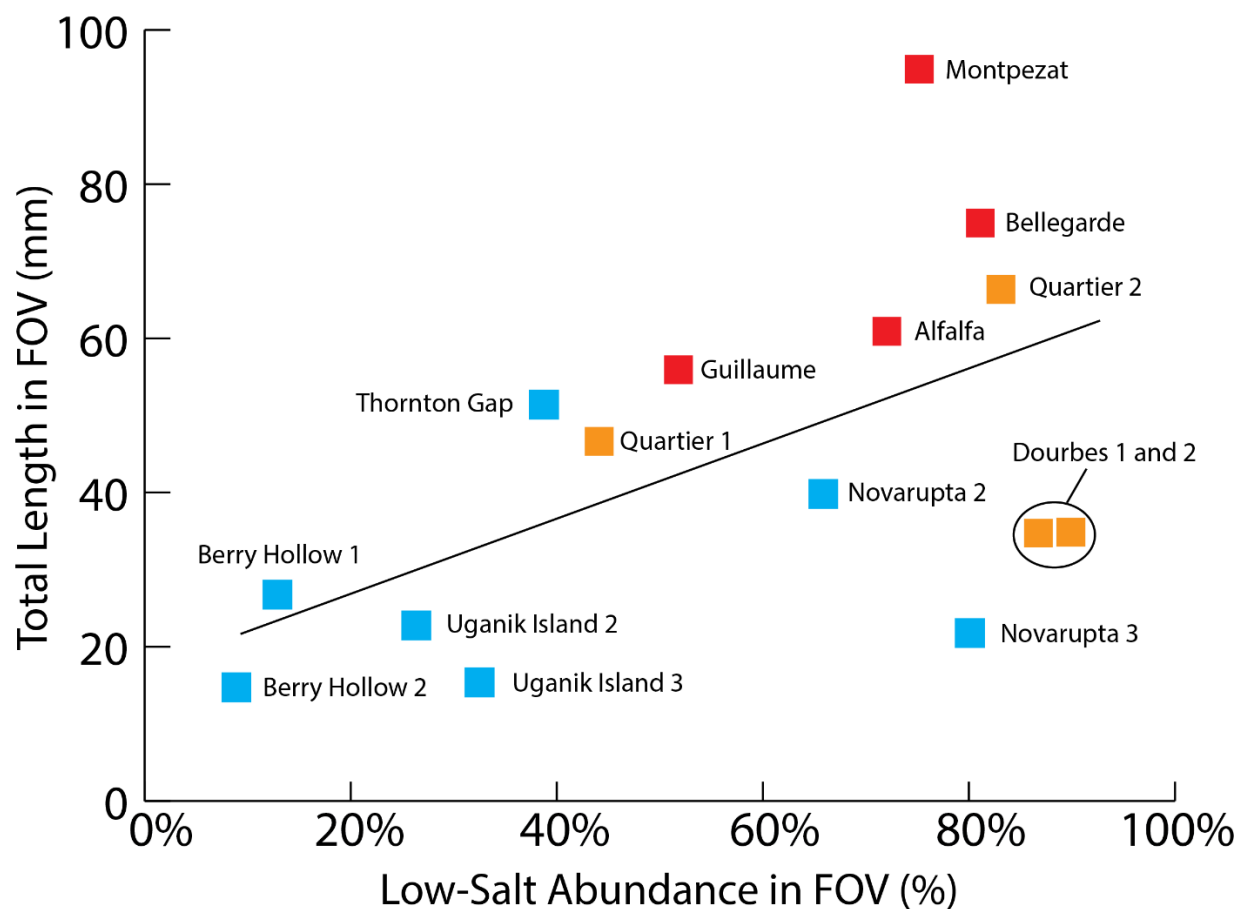


Figure 5-17: Scatter plot comparing the total abrasion lengths within each PIXL FOV from the Shenandoah (blue), Máaz (orange) and Séítah (red) formations against their respective abundances of low salt materials.

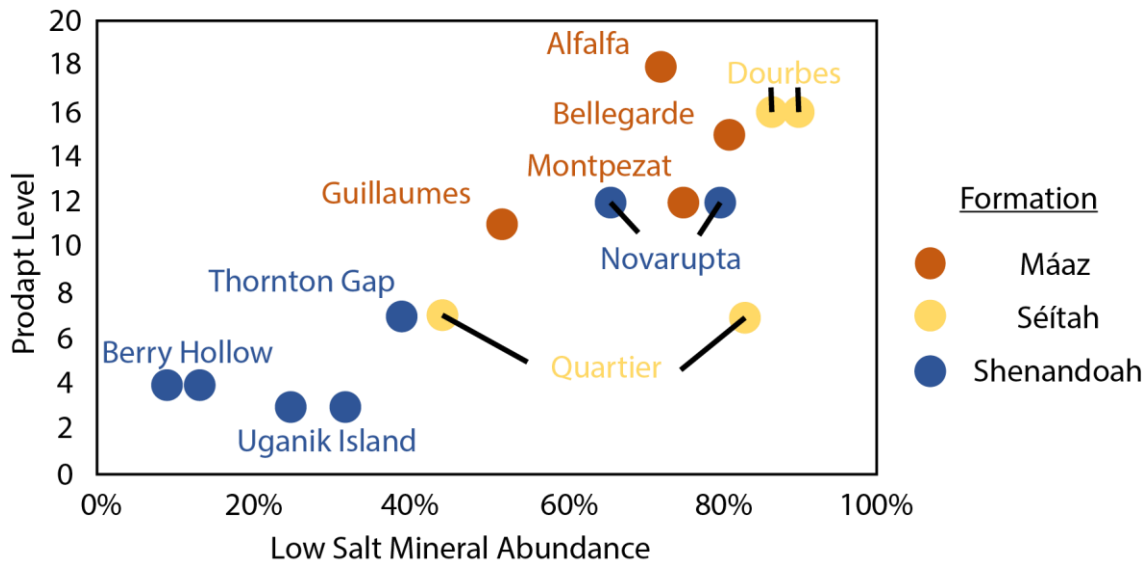


Figure 5-18: Scatterplot comparing the Prodapt Levels used during the production of each abrasion patch. Points are colored based on formation: Máaz (Orange), Séítah (Yellow) and Shenandoah (Blue).

5.5 Discussion

This study measured abrasion marks in 10 abrasion patches produced during the M2020 Crater Floor and Delta Front campaigns to understand how target mineralogy affects the abrasion process. Other Mars missions have used rock abrasion to remove surface layers of dust and weathered materials to study the Mars surface (Rock Abrasion Tool for the Mars Exploration Rovers mission; Gorevan et al., 2003; and Dust Removal Tool; Davis et al., 2012), however this work represents the first attempt to characterize and quantify the quality of abrasion surfaces in Jezero crater. While PIXL quantifications and other instruments provide incredible details about target surface, Geologists use all of their senses, including taste in some instances, to assess and characterize rock properties in the field. These observations also include the sound a rock makes when struck by a hammer, to the way a rock breaks and fracture. This work demonstrates how target mineralogy and lithology affect abrasion patch production and tool mark preservation.

The mineral maps produced in this study concur with previously published work (Liu et al., 2022; Schmidt et al., 2022; Tice et al., 2022). While the expressions from this study do not separate PIXL scans into unique minerals, they were designed to sort geochemical data into primary igneous minerals (also referred to in this study as Low Salt materials), high salt or salty materials, and alteration products (see Table 5-2 for mineral examples each expression may

select). These expressions showed that Máaz and Séítah targets were predominantly primary igneous minerals, and contained finer proportions of alteration and secondary salt materials. These results, paired with the observations of autochthonous, well-formed, angular grains in both formations, and an igneous poikilitic texture in Séítah (Liu et al., 2022), indicate that the Máaz and Séítah formations are igneous. Compared to Máaz and Séítah, the delta front materials of the Shenandoah formation were sedimentary, as they were more fine-grained, contained smaller proportions of primary igneous minerals (excluding Novarupta, Figure 5-7; Figure 5-15), and were often carbonate- or sulfate-cemented.

Primary igneous mineral abundance affected tool mark preservations and the prodapt level required during abrasion. The positive correlations in Figure 5-17 and 5.18 are likely attributed to the higher Mohs hardness of primary igneous minerals; these minerals include, but are not limited to: olivine (Hardness, H: 6-6.5), plagioclase (H: 6-6.5), pyroxene (H: 5-7), magnetite (H= 5.6-6.5) and titanomagnetite (H: 5-5.6; Table 3). Salty materials, such as gypsum (H:2) and anhydrite (H:3.5), and alteration materials, such as magnesite (H: 3.5-4.5) and serpentine (H: 3-6), have lower Mohs hardness, are easier to abrade, and require lower prodapt levels during abrasion. The harder primary igneous minerals are more resistant to abrasion, and preserve fewer abrasion marks from a single impact. Repeated impacts must therefore be required to imprint more abrasion marks and create fractures, which eventually join and remove material. Softer materials require lower prodapt levels and fewer impacts to remove material, and thereby preserve fewer abrasion marks overall. Once the abrasion process has finished and the gDRT clears the abrasion fines, only those abrasion marks that have not joined will remain. Primary igneous minerals require more impacts from the SCS to break, and is consistent with our finding that surfaces rich in primary igneous minerals preserve more abrasion marks overall (Table 5-4).

With abrasion surfaces hosting diverse minerals, bit progression and the associated prodapt level are likely limited by the hardest and most abundant minerals present. For target like Guillaumes (Figure 5-6), Quartier (Figure 5-10) and Montpezat (Figure 5-11), which had jagged abrasion surfaces and diverse minerals, lower prodapt levels were used (7-12; Table 5-4). Alfalfa (Figure 5-12) had a similar primary igneous mineral abundance to these targets, however the abrasion surface was noticeably smoother, required a higher prodapt level (18; Table 5-4),

and preserved the lowest abrasion mark abundance amongst the crater floor targets. The abrasion mark count and total length are likely under represented in our measurements however, due to an accumulation of abrasion fines along the edges of the abrasion patch. Similar prodapt levels were used when abrading the Bellegarde and Dourbes targets (15.3 and 16, respectively; Table 5-4), produced flatter abrasion surfaces, however these targets recorded the highest abrasion mark counts amongst the targets included in this study. Since these targets (Guillaumes, Quartier and Montpezat) possess similar mineralogies to Bellegarde, Dourbes and Alfalfa, these results suggest that the abrasion surfaces may have been smoother if a higher prodapt level had been used.

Delta front targets, like Thornton Gap (Figure 5-13) and Berry Hollow (Figure 5-14), also contained diverse mineralogies, however these targets contained abundant carbonate and sulfate-cement. Igneous mineral grains were still present in delta front targets, and are relatively more resistant to abrasion, however the fine-grained matrix and cement are softer and less resistant to abrasion. As softer and finer grained materials are abraded, the larger and more resistant grains are removed. These surfaces therefore required less force to remove material, and produced flatter abrasion surfaces overall.

A flatter abrasion patch would maximize the contact area between the abrasion bit and the target surface, and best explains why flatter abrasion patches preserved longer abrasion marks. This is not to say however that flatter abrasion marks produce more abrasion marks. Of the abrasion patches included in this study, Alfalfa (Figure 10) required the highest prodapt level, despite having a composition similar to other crater floor targets, and produced the flattest abrasion patch amongst the igneous targets. Alfalfa also preserved the longest abrasion marks amongst any of the igneous targets. While a portion of the Quartier (Figure 8) and Montpezat (Figure 9) abrasion patches are unobservable due to a thin layer of abrasion fines, these targets likely contain more abrasion marks than their overall counts in Table 5. This also means that Alfalfa likely contains the lowest overall abrasion mark count amongst the crater floor targets. Likely preserving the fewest and longest abrasion marks amongst the igneous targets, the Alfalfa abrasion patch best demonstrates how flatter abrasion patches preserve longer abrasion marks.

The Novarupta abrasion patch (Figure 5-15) is compositionally similar to abraded targets from the crater floor campaign. In contrast, its grain size (Table 5-4) and abrasion surface is more similar to other targets from the delta front. With a composition rich in primary igneous minerals, Novarupta was more resistant to abrasion, requiring the highest prodapt level amongst the delta front targets (Table 5-4). The same prodapt level was used for Guillaumes despite having lower abundances of primary igneous minerals, and produced a jagged abrasion surface. Novarupta's finer grain size and cement likely made it easier to abrade compared crater floor targets, but easier compared to delta front targets. Containing detrital igneous minerals, Novarupta preserved the most abrasion marks amongst the delta front targets, while its grain size and flatter abrasion surface allowed it to preserve longer abrasion marks as well.

5.6 Conclusion

The effect mineralogy has on tool mark preservation in abrasion surface was investigated using SHERLOC-WATSON images of the 10 abrasion patches produced during the crater floor and delta front campaigns. Crater floor abrasion targets from the Máaz and Séítah formation contained abundant hard, primary igneous minerals that were more resistant to abrasion and required higher prodapt levels. These targets preserved more abrasion marks overall, however these tool marks were generally shorter. Materials from the western delta front's Shenandoah formation contained softer sulfate and carbonate cemented materials that were less resistant to abrasion and required lower prodapt levels. These surfaces preserved fewer but longer abrasion marks than crater floor targets. The Novarupta target from the Shenandoah formation was an intermediate between the crater floor and delta front. With a composition rich in primary igneous minerals but overall smaller grain sizes than igneous targets, Novarupta recorded the highest count of abrasion marks amongst the delta front targets. Novarupta's composition made it more resistant to abrasion, preserved the most and longest total abrasion lengths, and required the highest prodapt level amongst all the delta front targets. This study found that abrasion mark lengths and abundance provide another perspective to rock composition, and that the prodapt level can be used to infer overall rock composition.

5.7 Acknowledgements

I wish to express my sincerest gratitude to my supervisor and Canadian Space Agency M2020 Participating Scientist Dr. Mariek Schmidt, for her unwavering support throughout this research. I would also like to thank the incredibly brilliant, and hardworking PIXL team for their expertise and collaboration throughout this study.

5.8 References

- Bhartia, R., Beegle, L. W., DeFlores, L., Abbey, W., Razzell Hollis, J., Uckert, K., Monacelli, B., Edgett, K. S., Kennedy, M. R., Sylvia, M., Aldrich, D., Anderson, M., Asher, S. A., Bailey, Z., Boyd, K., Burton, A. S., Caffrey, M., Calaway, M. J., Calvet, R., ... Zan, J. (2021). Perseverance's Scanning Habitable Environments with Raman and Luminescence for Organics and Chemicals (SHERLOC) Investigation. *Space Science Reviews*, 217(4), 58. <https://doi.org/10.1007/s11214-021-00812-z>
- Brown, A. J., Hook, S. J., Baldrige, A. M., Crowley, J. K., Bridges, N. T., Thomson, B. J., Marion, G. M., de Souza Filho, C. R., & Bishop, J. L. (2010). Hydrothermal formation of Clay-Carbonate alteration assemblages in the Nili Fossae region of Mars. *Earth and Planetary Science Letters*, 297(1), 174–182. <https://doi.org/10.1016/j.epsl.2010.06.018>
- Brown, A. J., Viviano, C. E., & Goudge, T. A. (2020). Olivine-Carbonate Mineralogy of the Jezero crater Region. *Journal of Geophysical Research: Planets*, 125(3), e2019JE006011. <https://doi.org/10.1029/2019JE006011>
- Carr, M. H. (2007). *The Surface of Mars*. Cambridge University Press.
- Carr, M. H. (2012). The fluvial history of Mars. *Philosophical Transactions of the Royal Society A: Mathematical, Physical and Engineering Sciences*, 370(1966), 2193–2215. <https://doi.org/10.1098/rsta.2011.0500>
- Farley, K. A., Williford, K. H., Stack, K. M., Bhartia, R., Chen, A., de la Torre, M., Hand, K., Goreva, Y., Herd, C. D. K., Hueso, R., Liu, Y., Maki, J. N., Martinez, G., Moeller, R. C., Nelessen, A., Newman, C. E., Nunes, D., Ponce, A., Spanovich, N., ... Wiens, R. C. (2020). Mars 2020

- Mission Overview. *Space Science Reviews*, 216(8), 142. <https://doi.org/10.1007/s11214-020-00762-y>
- Fassett, C. I., & Head, J. W. (2008). Valley network-fed, open-basin lakes on Mars: Distribution and implications for Noachian surface and subsurface hydrology. *Icarus*, 198(1), 37–56. <https://doi.org/10.1016/j.icarus.2008.06.016>
- Goudge, T. A., Mohrig, D., Cardenas, B. T., Hughes, C. M., & Fassett, C. I. (2018). Stratigraphy and paleohydrology of delta channel deposits, Jezero crater, Mars. *Icarus*, 301, 58–75. <https://doi.org/10.1016/j.icarus.2017.09.034>
- Liu, Y., Tice, M. M., Schmidt, M. E., Treiman, A. H., Kizovski, T. V., Hurowitz, J. A., Allwood, A. C., Henneke, J., Pedersen, D. A. K., VanBommel, S. J., Jones, M. W. M., Knight, A. L., Orenstein, B. J., Clark, B. C., Elam, W. T., Heirwegh, C. M., Barber, T., Beegle, L. W., Benzerara, K., ... Zorzano, M.-P. (2022). An olivine cumulate outcrop on the floor of Jezero crater, Mars. *Science*, 377(6614), 1513–1519. <https://doi.org/10.1126/science.abo2756>
- Moeller, R. C., Jandura, L., Rosette, K., Robinson, M., Samuels, J., Silverman, M., Brown, K., Duffy, E., Yazzie, A., Jens, E., Brockie, I., White, L., Goreva, Y., Zorn, T., Okon, A., Lin, J., Frost, M., Collins, C., Williams, J. B., ... Biesiadecki, J. (2020). The Sampling and Caching Subsystem (SCS) for the Scientific Exploration of Jezero crater by the Mars 2020 Perseverance Rover. *Space Science Reviews*, 217(1), 5. <https://doi.org/10.1007/s11214-020-00783-7>
- Mustard, J. F., Ehlmann, B. L., Murchie, S. L., Poulet, F., Mangold, N., Head, J. W., Bibring, J.-P., & Roach, L. H. (2009). Composition, morphology, and stratigraphy of Noachian crust around the Isidis basin. *Journal of Geophysical Research: Planets*, 114(E2).
- Mustard, J. F., Poulet, F., Head, J. W., Mangold, N., Bibring, J.-P., Pelkey, S. M., Fassett, C. I., Langevin, Y., & Neukum, G. (2007). Mineralogy of the Nili Fossae region with OMEGA/Mars Express data: 1. Ancient impact melt in the Isidis Basin and implications for the transition from the Noachian to Hesperian. *Journal of Geophysical Research: Planets*, 112(E8). <https://doi.org/10.1029/2006JE002834>

- Phillips, R. J., Zuber, M. T., Solomon, S. C., Golombek, M. P., Jakosky, B. M., Banerdt, W. B., Smith, D. E., Williams, R. M. E., Hynek, B. M., Aharonson, O., & Hauck II, S. A. (2001). Ancient Geodynamics and Global-Scale Hydrology on Mars. *Science*, 291(5513), 2587–2591. <https://doi.org/10.1126/science.1058701>
- Rummel, J. D., Beaty, D. W., Jones, M. A., Bakermans, C., Barlow, N. G., Boston, P. J., Chevrier, V. F., Clark, B. C., de Vera, J.-P. P., Gough, R. V., Hallsworth, J. E., Head, J. W., Hipkin, V. J., Kieft, T. L., McEwen, A. S., Mellon, M. T., Mikucki, J. A., Nicholson, W. L., Omelon, C. R., ... Wray, J. J. (2014). A New Analysis of Mars “Special Regions”: Findings of the Second MEPAG Special Regions Science Analysis Group (SR-SAG2). *Astrobiology*, 14(11), 887–968. <https://doi.org/10.1089/ast.2014.1227>
- Schmidt, M. E., Allwood, A., Christian, J., Clark, B., Flannery, D., Hennecke, J., Herd, C. D. K., Hurowitz, J. A., Kizovski, T. V., Liu, Y., McLennan, S. M., Nachon, M., Pedersen, D. A. K., Shuster, D. L., Simon, J. I., Tice, M., Tosca, N., Treiman, A. H., Udry, A., ... Wadhwa, M. (2022). Highly Differentiated Basaltic Lavas Examined by PIXL in Jezero crater. In *Proceedings of the 53rd Lunar and Planetary Science Conference (LPSC)*. Lunar and Planetary Science Conference, United States of America. Lunar and Planetary Institute. <https://www.hou.usra.edu/meetings/lpsc2022/pdf/1530.pdf>
- Soffen, G. A. (1976). Scientific Results of the Viking Missions. *Science*, 194(4271), 1274–1276. <https://doi.org/10.1126/science.194.4271.1274>
- Tice, M. M., Hurowitz, J. A., Allwood, A. C., Jones, M. W. M., Orenstein, B. J., Davidoff, S., Wright, A. P., Pedersen, D. A. K., Henneke, J., Tosca, N. J., Moore, K. R., Clark, B. C., McLennan, S. M., Flannery, D. T., Steele, A., Brown, A. J., Zorzano, M.-P., Hickman-Lewis, K., Liu, Y., ... THE PIXL TEAM. (2022). Alteration history of Séítah formation rocks inferred by PIXL x-ray fluorescence, x-ray diffraction, and multispectral imaging on Mars. *Science Advances*, 8(47), eabp9084. <https://doi.org/10.1126/sciadv.abp9084>
- Tice, M. M., O'Neil, L. P., Clark, B. C., Ganly, B. P., Jones, M. W., Orenstein, B. J., . . . Hurowitz, J. A. (2023). PIXL on Perseverance as a Complete X-Ray Spectroscopic Instrument: ANALyzing X-Ray Fluorescence, Scattering, and Diffraction of Martian Rocks. *54th Lunar*

and Planetary Science Conference 2023, (p. 2). The Woodlands, Texas. Retrieved from chrome-extension://efaidnbmnnnibpcajpcgiclfndmkaj/https://www.hou.usra.edu/meetings/lpsc2023/pdf/2659.pdf

Verma, V., Maimone, M., Graser, E., Rankin, A., Kaplan, S., Myint, S., . . . Lashore, M. (2023). Results from the First year and a Half of Mars 2020 Robotic Operations. *2023 IEEE Aerospace Conference*.

Williams, A., Russell, P. S., Sun, V., Shuster, D., Stack, K. M., Farley, K., . . . Wadhwa, M. (2023). Exploring the Jozero delta front: Overview of results from the Mars 2020 Perseverance rover's second science campaign. *54th Lunar and Planetary Science Conference 2023*.

Chapter 6: Thesis Conclusion

6.1. Overview

High-resolution microscopic images from Gale crater and Jezero crater provide alternative perspectives for studying the Martian surface. After introducing the premise and literature review in Chapter 1 and 2, Chapter 3 detailed the methods used in Chapters 4 and 5. Chapter 4 presented ~6years of airfall dust measurements atop horizontal rock surfaces in Gale crater and discussed the effects seasonal winds, changes in elevation and proximity to aeolian sand dune deposits have on dust abundance. Chapter 5 measured and compared abrasion mark abundances in 10 abrasion patches produced during the M2020 mission to their associated mineralogy to understand how mineralogy is impacting the abrasion process and tool mark production. This chapter will summarize the main findings from Chapters 4 and 5, discuss their significance, and suggestions for future work.

6.2. Surficial dust accumulation in Gale crater

The Martian surface is buried beneath a thin, variegated layer of airfall dust (Schmidt et al., 2018). Seasonal winds mobilize, suspend, and deplete surface deposits of dust (Haberle et al., 2017), and have also been observed to mobilize sand-sized particles during the southern summer season in Gale crater (Baker et al., 2018). Our dust measurements of 697 horizontal rock surfaces, which spanned four complete and two partial Mars Years, was amongst the first studies to measure surface dust deposits. Our results were inversely related to atmospheric dust measurements that have been documented in previous literature (e.g., Clancy et al., 2000; Haberle et al., 2017; Lemmon et al., 2015), and showed dust abundances decreasing at higher elevations, and in proximity to aeolian sand dune deposits.

This work demonstrated the highly variable nature of dust, where adjacent targets that were separated by only a few meters, had dust coverages vary by >40%. These variations are caused by small surface features such as voids, cracks and eroded diagenetic veins shield dust particles from wind and allow them to persist on the surface for extended periods of time. Despite this, our measurements of airfall dust deposits atop horizontal rock surfaces are inversely related to published studies of atmospheric dust.

Our surficial dust measurements and other published atmospheric dust studies are inversely related (e.g., Douté, 2014; Haberle et al., 2017; Vicente-Retortillo et al., 2018). Surface dust deposits are greatest during the atmospheric “Non-Dusty” season (Ls 0-135°), and lowest during the “Dusty” season (Ls 135-360°), when dust particles are suspended in the atmosphere. Due to the size of this study’s dataset ($n = 697$), seasonal variability was most apparent in maximum dust coverages. These values increased, and were greatest, at each Mars New Year when seasonal winds are understood to be weakest and atmospheric dust is least abundant. Mirroring atmospheric measurements, maximum dust coverages were lower during the “Dusty” season when seasonal winds are strongest. Contrary to globally averaged dust opacities that only show dust activity during the “Dusty” season (e.g. Haberle et al., 2017; Korablev et al., 2005), the maximum dust coverages gradually decreased shortly after each New Year. This observation suggests: (1) dust particles are mobile in Gale crater during the “Non-Dusty” season, (2) dust mobility is not limited to the “Dusty” season, (3) seasonal winds capable of mobilizing dust are not limited to the “Dusty” season, and (4) dust particles are mobilized locally before detectable changes in global atmospheric opacity.

We attribute the abnormally low dust coverages (between 1.7% and 6.9%) recorded during Phase 2 of the Bagnold Dunes traverse (P2BD) to mobilized, saltating sand particles in Bagnold Dunes. Baker et al. (2018) observed impact ripple migration during this length of Curiosity’s traverse, features that confirm sand-sized particles are mobilized and saltating during this period. While small surface features shield dust from winds elsewhere in Gale crater, sheltered dust particles are likely be ejected through collisions with saltating sand particles, decreasing thir overall dust coverages. While dust particles were noticeably absent during P2BD traverse, sand particles were present in nearly all the associated MAHLI images, often filling small surface features that may have otherwise sheltered dust particles. Seasonal dust mobility and removal is likely comparable to other regions in Gale crater, but accelerates once sand-sized particles are mobilized, leading to further dust removal.

Dust coverage have remained highly variable throughout MSL, however the maximum dust coverage spikes and overall dust coverages have gradually decreased since MY31 as Curiosity has increased in elevation. Additionally, the rate at which maximum dust coverages

decrease have increased with elevation gain. These results suggest that dust mobilization and deposition is not uniform throughout Gale crater, and that it is influenced by local topography and atmospheric conditions. The increased rate at which maximum dust coverages decrease at higher elevations suggests wind speeds are stronger at higher elevations. However, the annually decreasing maximum dust coverages that we document following the ascent of Vera Rubin Ridge suggest dust particles are less abundant at higher elevations along Mt Sharp. We propose katabatic and adiabatic winds, dense parcels of cool air descending and ascending the slopes of Mt Sharp, are mobilizing dust particles during the “Non-Dusty.” These winds enable the long-term suspension of dust particles at higher elevations, producing the lower dust coverages recorded at higher elevations in Gale crater. Combining with seasonal winds, these adiabatic and katabatic winds would also explain the enhanced rate of dust removal observed in the seasonal maximum dust coverage declines of MY34-36.

The second series of low dust covered targets encountered along the southern, downwind edge of the Sands of Forvie (SoF; another aeolian sand dune deposit in Gale crater) were similar, yet slightly higher (6.6% to 26.3%) than those recorded during P2BD traverse. The southern autumn and winter timing of this traverse complicated the interpretation of this data, as it seasonally aligns with Phase 1 of the Bagnold Dunes traverse when there was no resolvable ripple migration or sand-particle mobility. However, the results suggested these dust covered surfaces were still influenced by their proximity to the SoF. The associated increase in elevation as Curiosity traverse the southern edge of the SoF may have further contributed to these lower dust coverages as well. Without the remaining MY36 dust data and associated wind speed measurements (inhibited by damage to the Rover Environmental Monitoring Station during landing; Gómez-Elvira et al., 2014), it is difficult to know how each variable(s) contributed to these lower dust coverages. Since our results suggest each variable contributes to dust removal, we suggest that seasonal winds, elevation gain, and proximity to aeolian dunes are likely contributing to these decreased dust coverages.

6.3. Abrasion mark mapping Jezero crater

We mapped and measured abrasion marks preserved in 10 abrasion patches that were produced during the Crater Floor and Delta Front campaigns of the M2020 mission using high-resolution SHERLOC-WATSON images. Igneous targets from the Máaz and Séítah formations (Crater Floor Campaign) preserved higher abrasion mark counts than sedimentary targets from the sedimentary Shenandoah formation (Delta Front Campaign; $n = 153\text{--}422$). However abrasion marks in igneous targets were noticeably shorter than those preserved in sedimentary surfaces. These observations indicate target mineralogy and mineral abundances strongly influence tool mark abundances and length.

Separating Planetary Instrument for X-ray Lithochemistry (PIXL) scans into primary igneous (low salt), high salt and alteration minerals revealed that primary igneous minerals preserved higher abrasion mark counts. Being harder materials, primary igneous minerals are more resistant to abrasion, requiring greater force (prodapt levels) during abrasion to remove materials. Because of this resistance, igneous surfaces were often jagged, limiting points of contact with the abrasion bit and produced shorter abrasion mark lengths. Targets with higher abundances of salter, salt-rich and alteration minerals were easier to abrade, required lower prodapt levels, and produced flatter abrasion surfaces. This flatter surface points of contact between the target surface and abrasion bit and produced longer abrasion marks. Since sedimentary targets are made of softer minerals, these materials are more easily removed but less likely to preserve abrasion marks.

6.4. Significance of this Research

Decades of Mars research has expanded our knowledge of our neighboring planet and other planetary bodies, while also teaching us more about our own. Satellite, lander, and rover missions enable researchers to study the Martian surface from a variety of perspectives and resolutions. The works detailed in Chapters 4 and 5 study areas of ongoing research from new perspectives thanks to high-resolution microscopic cameras and other instrumentation delivered with rover payloads.

6.4.1. Chapter 4: Dust Coverages from Gale crater

Previous research that have measured Martian dust and seasonal variations have used orbital atmospheric opacity measurements to quantify the volume of dust suspended in the atmosphere, however very few have sought to quantify dust abundances at the planet's surface. As a generalization, these surface studies have quantified dust accumulation atop solar arrays and rover equipment (e.g., Lorenz et al., 2020; Yingst et al., 2016), only a select few have quantified dust abundances atop natural surfaces (e.g., (Schmidt et al., 2018)). This study continued the methods of Schmidt et al. (2018) and provides the single, longest recording of surficial dust deposits to date.

As discussed in Section 4.5.1, our dust measurements align and agree with the seasonal dust patterns documented in previous work. Despite the decades of research that have observed and studied Mars dust, the precise mechanisms which mobilize and suspend dust particles are not well quantified (Newman et al., 2022). These mechanisms were further obstructed by damage to Curiosity's Rover Environmental Monitoring Station during landing (Gómez-Elvira et al., 2014) and complicates surface measurements of wind speeds in Gale crater. We compared our results to orbital detections of atmospheric opacity, such as those described by Haberle et al. (2017), to understand when dust particles are mobilized in the Martian atmosphere, as wind speeds during these periods are mobilizing dust particles. Our results show consecutive decreases to maximum dust coverages following each New Year, and before changes are seen in atmospheric opacity. These results suggest dust particles are being mobilized in Gale crater, and likely in other localities, earlier in the year. It is my hope that these observations will aid in our understanding of dust mobility on Mars, and help to further constrain the mechanisms which suspend dust particles.

Remember that our dust coverages are measurements of dust clumps, accumulations of sticky dust particles, that are resolvable by MAHLI ($>14\mu\text{m}/\text{pixel}$; Edgett et al., 2012). Measurements of atmospheric opacity are capable of detecting dust particles that are only a few micrometers in diameter (Guzewich et al., 2014). The results from this study suggest there is a lag in time between when dust clumps are mobilized and when dust particles are detected in the atmosphere. Counterintuitively, larger dust clumps require lower wind speeds to be mobilized

since individual dust particles possess electrostatic forces that adhere them to surfaces. The wind speeds required to overcome both the electrostatic and gravitational forces are higher for individual dust particles than those needed to mobilize dust clumps, assuming all other parameters are quasi-equal (e.g., density, texture, drag etc.). This relationship best explains why there is an offset between our results and orbital detections of dust particles in the atmosphere.

6.4.2. Chapter 5: Abrasion Mark Mapping

During weekly science discussion meetings with the M2020 team, other members commented on how abrasion marks distract or interfere with their interpretations of rock textures. However, chapter 5 demonstrates that abrasion marks are the product of a target's mineralogy, and the associated hardness. While they may be distracting for some, this work demonstrates that they can be rather informative.

Despite the prodapt level autonomously adjusting the drilling parameters of the SCS, Perseverance has failed to produce five abrasion patches throughout M2020. The Perseverance rover's onboard computer details and records these complications during abrasion, however subsequent proximity science, such as PIXL quantification, is not performed to avoid damage to rover instrumentation. The results from this study show that some information may still be extracted from these failed abrasion patches. Since target mineralogy was found to affect both abrasion mark abundances and lengths, mapping the abrasion marks preserved in the failed abrasion surface can be used to infer its mineralogy.

Since the failed Rose River Falls abrasion patch (sol 452), M2020 has seeded the prodapt levels in an attempt to prevent further failed abrasions. Unfortunately, two more abrasion attempts have since failed. Mapping the abrasion marks preserved in these surfaces and assessing the quality of these failed abrasion surfaces may aid in choosing more appropriate seed values in future targets. It is my hopes that this work will aid in improving the prodapt algorithm and provide observations which will aid in reducing the number of failed abrasion attempts in the future.

6.5. Future Work

The research from chapter 4 includes the longest, continuous recording of surface dust deposits on Mars. These results were temporally and spatially investigated using Curiosity's geospatial data, however an abundance of information remains in the associated MAHLI images. While the funding for this work and my time as a graduate student are approaching their terminus (dun dun dun!), there are a number of directions future research can continue this work. This study focused on quantifying the surface areal abundance of airfall dust but did not collect particle size or diameter measurements. Combining particle diameter measurements with the dust dataset would help constrain the parameters and mechanisms that suspend Martian dust. Assessing the target height above the surrounding surface, and the inclination of the target surfaces would further refine this data and may further explain the dust coverage variability between adjacent targets. Dust may be ubiquitous across the surface of Mars, however this research has quantified dust abundance from single Martian crater that, with its own unique variables that are locally influencing dust abundances. The methods used in this study, developed by Schmidt et al. (2018), can be applied to other rover mission to quantify dust abundances elsewhere on Mars. Observations from other mission would further constrain our understanding of dust mobility and suspension on Mars and would allow for regional comparisons to be made between sites.

The observations from chapter 5 describe material properties for both the Martian surface and samples to be returned to Earth in the near future. These observations may help in improving both the current prodapt algorithm of M2020 and reduce the number of failed abrasion attempts. These observations may also aid in designing abrasion tool designs to be included in future missions. With the sample return mission costing billions of dollars, it is imperative that these materials reach the Earth's surface safely and intact. The results from this study demonstrate how each target have responded differently to the applied forces during abrasion. Since these samples will undergo immense force as they are launched from the Martian surface, and upon-re-entry to Earth's atmosphere, engineering may use our observations to ensure these delicate samples safely survive their delivery to Earth.

References

- Clancy, R. T., Sandor, B. J., Wolff, M. J., Christensen, P. R., Smith, M. D., Pearl, J. C., Conrath, B. J., & Wilson, R. J. (2000). An intercomparison of ground-based millimeter, MGS TES, and Viking atmospheric temperature measurements: Seasonal and interannual variability of temperatures and dust loading in the global Mars atmosphere. *Journal of Geophysical Research: Planets*, 105(E4), 9553–9571. <https://doi.org/10.1029/1999JE001089>
- Douté, S. (2014). Monitoring atmospheric dust spring activity at high southern latitudes on Mars using OMEGA. *Planetary and Space Science*, 96, 1–21. <https://doi.org/10.1016/j.pss.2013.12.017>
- Edgett, K. S., Yingst, R. A., Ravine, M. A., Caplinger, M. A., Maki, J. N., Ghaemi, F. T., Schaffner, J. A., Bell, J. F., Edwards, L. J., Herkenhoff, K. E., Heydari, E., Kah, L. C., Lemmon, M. T., Minitti, M. E., Olson, T. S., Parker, T. J., Rowland, S. K., Schieber, J., Sullivan, R. J., ... Goetz, W. (2012). Curiosity's Mars Hand Lens Imager (MAHLI) Investigation. *Space Science Reviews*, 170(1), 259–317. <https://doi.org/10.1007/s11214-012-9910-4>
- Gómez-Elvira, J., Armiens, C., Carrasco, I., Genzer, M., Gómez, F., Haberle, R., Hamilton, V. E., Harri, A.-M., Kahanpää, H., Kemppinen, O., Lepinette, A., Martín Soler, J., Martín-Torres, J., Martínez-Frías, J., Mischna, M., Mora, L., Navarro, S., Newman, C., de Pablo, M. A., ... Zorzano, M.-P. (2014). Curiosity's rover environmental monitoring station: Overview of the first 100 sols. *Journal of Geophysical Research: Planets*, 119(7), 1680–1688. <https://doi.org/10.1002/2013JE004576>
- Guzewich, S. D., Wilson, R. J., McConnochie, T. H., Toigo, A. D., Banfield, D. J., & Smith, M. D. (2014). Thermal tides during the 2001 Martian global-scale dust storm. *Journal of Geophysical Research: Planets*, 119(3), 506–519. <https://doi.org/10.1002/2013JE004502>
- Haberle, R. M., Clancy, R. T., Forget, F., Smith, M. D., & Zurek, R. W. (2017). *The Atmosphere and Climate of Mars*. Cambridge University Press.

- Korablev, O., Moroz, V. I., Petrova, E. V., & Rodin, A. V. (2005). Optical properties of dust and the opacity of the Martian atmosphere. *Advances in Space Research*, 35(1), 21–30. <https://doi.org/10.1016/j.asr.2003.04.061>
- Lemmon, M. T., Wolff, M. J., Bell, J. F., Smith, M. D., Cantor, B. A., & Smith, P. H. (2015). Dust aerosol, clouds, and the atmospheric optical depth record over 5 Mars years of the Mars Exploration Rover mission. *Icarus*, 251, 96–111. <https://doi.org/10.1016/j.icarus.2014.03.029>
- Lorenz, R. D., Lemmon, M. T., Maki, J., Banfield, D., Spiga, A., Charalambous, C., Barrett, E., Herman, J. A., White, B. T., Pasco, S., & Banerdt, W. B. (2020). Scientific Observations With the InSight Solar Arrays: Dust, Clouds, and Eclipses on Mars. *Earth and Space Science*, 7(5), e2019EA000992. <https://doi.org/10.1029/2019EA000992>
- Newman, C. E., Hueso, R., Lemmon, M. T., Munguira, A., Vicente-Retortillo, Á., Apestigue, V., Martínez, G. M., Toledo, D., Sullivan, R., Herkenhoff, K. E., de la Torre Juárez, M., Richardson, M. I., Stott, A. E., Murdoch, N., Sanchez-Lavega, A., Wolff, M. J., Arruego, I., Sebastián, E., Navarro, S., ... Guzewich, S. D. (2022). The dynamic atmospheric and aeolian environment of Jezero crater, Mars. *Science Advances*, 8(21). <https://doi.org/10.1126/sciadv.abn3783>
- Schmidt, M. E., Perrett, G. M., Bray, S. L., Bradley, N. J., Lee, R. E., Berger, J. A., Campbell, J. L., Ly, C., Squyres, S. W., & Tesselaar, D. (2018). Dusty Rocks in Gale crater: Assessing Areal Coverage and Separating Dust and Rock Contributions in APXS Analyses. *Journal of Geophysical Research: Planets*, 123(7), 1649–1673. <https://doi.org/10.1029/2018JE005553>
- Vicente-Retortillo, Á., Martínez, G. M., Renno, N., Newman, C. E., Ordonez-Etxeberria, I., Lemmon, M. T., Richardson, M. I., Hueso, R., & Sánchez-Lavega, A. (2018). Seasonal Deposition and Lifting of Dust on Mars as Observed by the Curiosity Rover. *Scientific Reports*, 8(1), Article 1. <https://doi.org/10.1038/s41598-018-35946-8>

Yingst, R. A., Edgett, K. S., Kennedy, M. R., Krezoski, G. M., McBride, M. J., Minitti, M. E., Ravine, M. A., & Williams, R. M. E. (2016). MAHLI on Mars: Lessons learned operating a geoscience camera on a landed payload robotic arm. *Geoscientific Instrumentation, Methods and Data Systems*, 5(1), 205–217. <https://doi.org/10.5194/gi-5-205-2016>